



## Nonlinear Finite Element Analysis of Steel Fiber Reinforced Concrete Deep Beams With and Without Opening

Hayder Qais Majeed  
Asst. lecturer, College of engineering  
Baghdad University, Iraq  
E-mail: hayderqs@yahoo.com

### Abstract

This paper presents a nonlinear finite element modeling and analysis of steel fiber reinforced concrete (SFRC) deep beams with and without openings in web subjected to two- point loading. In this study, the beams were modeled using ANSYS nonlinear finite element software. The percentage of steel fiber was varied from 0 to 1.0%. The influence of fiber content in the concrete deep beams has been studied by measuring the deflection of the deep beams at mid- span and marking the cracking patterns, compute the failure loads for each deep beam, and also study the shearing and first principal stresses for the deep beams with and without openings and with different steel fiber ratios. The above study indicates that the location of openings and the amount steel fiber are affects to the behavior and strength of deep beams. And also when the results of the experiments taken from the literature were compared with the results obtained from the beam modeled with ANSYS finite element program, it was shown that the results of computer model gave similar results to the experimental behavior.

**Keywords:** Deep beams, Steel fibers, Beam Web openings, SFRC Beams, Ansys

-:

(SFRC)

.1.0% 0

. ANSYS

ANSYS

الكلمات الرئيسية: الجسور العميقة، الاليف الفولاذية، الفتحات الجذعية، الجسور المسلحة المقواة بالاليف الفولاذية، الانسز

## 1. Introduction

For reinforced concrete, improvement of calculation methods and analysis of behavior by either creating a model on computer or counting with analytical calculation methods are used extensively in recent years. The behavior of a reinforced concrete element is generally observed by conducting experiment on laboratory environment; but this process considerably takes up much time. The studies are limited due to the problems in providing the materials and the proper conditions to conduct the experiments and scarcity of usage of materials which are constituted according to certain size and number of elements. Modeling of all these processes unlimitedly in computer is dependent on the capacity of the computer being used. While modeling on the computer, properties and limit conditions of materials should be defined properly and completely [Lawrance KL 2002].

ANSYS finite element program is chosen for this study. Finite element method is a numeric method which can solve complex and difficult physical problems) with acceptable approximation.

As concrete is a material showing nonlinear behavior during loading, it is modeled in such a way that it will show a nonlinear behavior with ANSYS finite element program [Barbosa AF, Riberio 2004].

Deep beams are often used as structural members in Civil Engineering works. In many cases, web openings are required to provide for services or for access. Because of the geometric proportions of deep beams, their strength is usually controlled by shear rather than flexure, if normal amounts of reinforcements are provided. A proliferation of new developments in steel fiber reinforced concrete technology has greatly extended the range of applications. The application currently depends on the ingenuity of the designer and builder taking advantage of the improved static and dynamic tensile strength, ductility, energy – absorbing characteristics, abrasion resistance, and fatigue strength of this material of construction [Mansur,

M.A1982, and Vengatachalapathy.V 2010].

The uniform dispersion of steel fiber throughout the concrete provided isotropic strength properties which are not exhibited by conventionally reinforced concrete. A number of investigations are being carried out on the behavior of fiber reinforced composites. Since 1972, a number of experimental and analytical investigations have been carried out to study the behavior and collapse loads of deep beams with and without web opening [Leonhardt, F 1972].

The openings are usually provided in such beams to have an access for utility ducts without further increases in ceiling head room. As the usage of those beams with or without openings increases, it becomes imperative that the design criteria of such beams is widely tested and established [Vengatachalapathy.V 2010].

## 2. Experimental Study

Vengatachalapathy et al. (2010) [Vengatachalapathy.V 2010] modeled of simply supported nine concrete deep beams of dimensions 750mm × 350mm × 75mm thickness were tested to destruction by applying gradually increased load. The percentage of steel fiber was varied from 0 to 1.0.

## 3. Finite Element Modeling of Steel Reinforcement and Steel Fiber

Tavarez discusses three techniques that exist to model steel reinforcement in finite element models for reinforced concrete is shown in figure 1 the discrete model, the embedded model, and the smeared model [Tavarez (2001)]. In this study the main and web steel reinforcement are modeled as discrete and embedded, and the steel fiber modeled as smeared model.

## 4. The Finite Element Model

The material models used for transferring material properties of the specimen to the designed computer program are given in this section. ANSYS 11, finite element program is used for modeling. Material properties of concrete, reinforcement and

adhesive are defined and entered as data in the model. Some criteria given below are based on to define the material properties:

#### 4.1. Reinforced Concrete

The solid element (Solid 65) has eight nodes with three degrees of freedom at each node and translations in the nodal x, y, and z directions. The element is capable of plastic deformation, cracking in three orthogonal directions, and crushing. The geometry and node locations for this element type are shown in figure 3. Smeared cracking approach has been used in modeling the concrete in the present study [ANSYS, Inc 2006].

The geometry and node locations for Link 8 element used to model the steel reinforcement are shown in figure 4. Two nodes are required for this element. Each node has three degrees of freedom, translations in the nodal x, y, and z directions. The element is also capable of plastic deformation [ANSYS, Inc 2006].

#### 4.2. Steel Plates

An eight-node solid element, Solid45, was used for the steel plates at support and load locations. The element is defined with eight nodes having three degrees of freedom at each node and translations in the nodal x, y, and z directions. The geometry and node locations for this element type are shown in Figure 4. Steel plate modeled using Solid45 elements, was added at the support locations in order to avoid stress concentration problems and to prevent localized crushing of concrete elements near the supporting points and load application locations. This provided a more even stress distribution over the support area [ANSYS, Inc 2006].

### 5. Real Constant and Material Properties:-

The real constants for these models are shown in Table 1. Note that individual elements contain different real constants. No real constant set exists for the Solid45 element. In this study the volume ratio of the real constant for solid 65 element varying from 0% - 1.0% depending on the steel fiber ratio imbedded in concrete, and

the material number of steel fiber indicated in table 2.

Parameters needed to define the material models can be found in Table 2. The Solid65 element requires linear isotropic and multi-linear isotropic material properties to properly model concrete. The multi-linear isotropic material uses the von Mises failure criterion along with the Willam and Warnke (1975) model to define the failure of the concrete. EX is the modulus of elasticity of the concrete ( $E_c$ ), and PRXY is the Poisson's ratio ( $\mu$ ). The compressive uniaxial stress-strain relationship for the concrete model was obtained using the following equations to compute the multi-linear isotropic stress-strain [Saifullah, et al 2011].

$$f = \frac{E_c \varepsilon}{1 + \left(\frac{\varepsilon}{\varepsilon_o}\right)^2} \quad (1)$$

$$\varepsilon_o = \frac{2f_c^-}{E_c} \quad (2)$$

$$E_c = \frac{f}{\varepsilon} \quad (3)$$

Where:

$f$  = stress at any strain  $\varepsilon$ , N/mm<sup>2</sup>

$\varepsilon$  = strain at stress  $f$

$\varepsilon_o$  = strain at the ultimate compressive strength,  $f_c$ .

The multi-linear curve is used to help with convergence of the nonlinear solution algorithm. Figure 5 shows the stress-strain relationship used for this study and is based on work done by Vengatachalapathy et al. (2010). Nonlinear model curve Point 1, defined as  $0.3 f_c$  is calculated in the linear range Equation 3. Other points are calculated from Equation 1 with  $\varepsilon_o$  obtained from Equation 2. Last point is defined at  $f_c$  and  $\varepsilon_o=0.003$  mm/mm indicating traditional crushing strain. Figures 6 and 7 show the stress- strain curves for the main steel reinforcement and web reinforcement respectively.

**6. Modeling:-**

The beam specimen consists of 350 x 75mm section of 750 mm long. The geometry of these samples and the location of the openings are shown in figure 8. Due to symmetry half of the beam is modeling as shown in figure 9. The bond between steel reinforcement and concrete was assumed as perfect in the modeling of RC control beam specimen. Each beam contained two steel rods of 16mm diameter of 415 N/mm<sup>2</sup> yield strength were used as the main tension, and web reinforcement consisting of two layers of welded wire fabric of 3.3mm diameter and 50mm on centers having yield strength of 300 N/mm<sup>2</sup>, as shown in figure 10. The FE mesh for the beam model is shown in figure 11.

**7. Non-Linear Solution**

In this study the total load applied was divided into a series of load increments (or) load steps. Newton -Raphson equilibrium iterations provide convergence at the end of each load increment within tolerance limits. The automatic time stepping in the ANSYS program predicts and controls load step sizes for which the maximum and minimum load step sizes are required. After attempting many trials the number of load steps, minimum and maximum step sizes was determined. During concrete cracking, steel yielding and ultimate stage in which large numbers of cracks occur the loads were applied gradually with smaller load increments.

**8. Discussions of Results****8.1 Load Deflection Curves**

The experimental carried by Vengatachalapathy et al. (2010) and ansys load-deflection curves obtained for the beams are illustrated in figures 12, 13, and 14. The curves show good agreement in finite element analysis with the experimental results throughout the entire range of behavior and failure mode. Figure 15 shows deferent ratios of steel fiber content, in this study the ratios of 0.25% and 0.5% are added to the results to make comparison with more steel fiber ratios, for all beams the finite element model is stiffer than the actual beam in the

linear range. Several factors may cause the higher stiffness in the finite element models. The bond between the concrete and steel reinforcing is assumed to be perfect (no slip) in the finite element analyses, but for the actual beams the assumption would not be true slip occurs, therefore the composite action between the concrete and steel reinforcing is lost in the actual beams. After the initiation of flexural cracks, the beam stiffness was reduced and the linear load –deflection behavior ended when the internal steel reinforcement began to yield.

**8. 2 Crack Pattern**

The ANSYS program records a crack pattern at each applied load step. Figure 16 shows evolutions of crack patterns developing for each beam at the last loading step. ANSYS program displays circles at locations of cracking or crushing in concrete elements. Cracking is shown with a circle outline in the plane of the crack, and crushing is shown with an octahedron outline. The first crack at integration point is shown with a red circle outline, the second crack with a green outline, and the third crack with a blue outline [ANSYS, Inc 2006].

**8. 3 Failure Load**

The failure load obtained from the numerical solution for all beams is slightly smaller than experimental load. The final loads for the finite element models are the last applied load step before the solution diverges due to numerous cracks and large deflections. Table 1 shows comparison between the ultimate loads of the experimental beams and the final loads from the finite element models for deep beams with deferent ratios of steel content with and without opening, and also show the percentage of increase in the final load with the different values of steel fiber.

**8.4 Shearing and Principal Stresses**

Figures (17-25) show the shearing and 1<sup>st</sup> principal stress at first crack for the deep beams with and without opening and with steel fiber ratios varying from (0- 1.0%). For the solid deep beam the bearing load at the 1<sup>st</sup> crack increase with increases in the steel fiber percentage as shown in figures





(17-19 a), whereas for deep beam with openings the bearing load at 1<sup>st</sup> crack is remained constant with increase in the steel fiber ratios as shown in figures (20-25 a). For the solid deep beam the shearing stress transfer from the point load to the support as fusiform shape, when the way between loading point and support intersects with the opening the shearing stress transform to the support come around the opening as shown in figures (17-25 b). For the solid deep beam the largest stress appears at the mid-span at the 1<sup>st</sup> crack happened as shown in figures (17-19 c), and for deep beam with opening the big stress appears at the edges of the opening along loading point as shown in figures (20-25 c).

## 9. Conclusions

- The general conclusion is that 3D ANSYS modeling is able to properly simulate the nonlinear behavior of the steel fiber reinforced concrete Deep Beams With and Without Openings.
- In simple, ANSYS is a rapid way compared with experimental test.
- The general behavior of the finite element models shows good agreement with observations and data from the experimental beam tests of the others.
- The results obtained demonstrate that web openings may be provided in the compression zone of the beams and fiber content of 0.75% by volume may be added to improve the strength of the structure. The openings in the tension zone weaken the beam. And Fiber content of 0.75% by volume of the beam improves the ultimate load.
- The percentage of increase in load capacity at the 1<sup>st</sup> crack for the solid deep beam is 32.3% when 0.75% steel fiber added, and 33.3% for 1.0% steel fiber added therefore use 0.75% fiber give good strength and more economic than 1.0% steel fiber.
- No significant increase in the load capacity at the 1<sup>st</sup> crack for the deep beam with opening.

## 10. References

- ANSYS, Inc., "ANSYS Help", Release 11.0, Documentation, Copyright 2006
- Bangash, M.Y.H. (1989), Concrete and Concrete Structures: Numerical Modeling and Applications, London, England: Elsevier Science Publishers Ltd.
- Barbosa AF, Riberio GO (2004). Analysis of reinforced concrete structures using ANSYS nonlinear concrete model. Computer. Mech. 1(8): pp. 1-7.
- Barzegar, F., Maddipudi, S. (1997), "Three – Dimensional Modeling of Concrete structures. I". Plain Concrete Journal of Structural Engineering, pp.1339-1346.
- Leonhardt, F. H.A.R.de Paiva and C.P.Siess 1972, Discussion of :Strength and behavior of deep beams in shear. Proceedings of the American Society of Civil Engineers. Vol.92, No. 2
- Lawrance KL (2002). ANSYS Tutorial Release 7.0 and 6.1, SDC Publications, Canonsburg, 1.1- 2.25.
- Mansur, M.A, and Alwis, W.A.M., 1982, Reinforced fiber concrete deep beams with web openings, The international journal of cement composites and lightweight concrete, Vol.6., No.4.
- Saifullah, M.A. Hossain, (2011) " Nonlinear Analysis of RC Beam for Different Shear Reinforcement Patterns by Finite Element Analysis". International Journal of Civil & Environmental Engineering IJCEE-IJENS Vol: 11 No: 01 pp.86-98.
- Tavarez, F.A., (2001), "Simulation of Behavior of Composite Grid Reinforced Concrete Beams Using Explicit Finite Element Methods," Master's Thesis, University of Wisconsin-Madison, Madison, Wisconsin.-
- Vengatachalapathy.V, Ilangoan.R 2010, A Study on Steel Fibre Reinforced Concrete Deep Beams With and without Openings. International Journal of Civil and Structural Engineering Volume 1, No 3, 2010 pp.509-517.

Table 1. Real constant for model

Real Constant set	Element Type				
1	Solid 65		Real Constant for Rebar 1	Real Constant for Rebar 2	Real Constant for Rebar 3
		Material Number	0	0	0
		Volume Ratio	0	0	0
		Orientation Angle	0	0	0
		Orientation Angle	0	0	0
2	Link8	Cross-Sectional Area (mm <sup>2</sup> )	201		
		Initial Strain (mm/mm)	0		
3	Link8	Cross-Sectional Area (mm <sup>2</sup> )	8.56		
		Initial Strain (mm/mm)	0		

Table 2. Material Models for the Calibration Model

Material Model Number	Element Type	Material Properties	
		Linear Isotropic	
		EX (MPa)	29,715
		PRXY	0.2
		Multilinear Isotropic	
		Strain (mm/mm)	Stress (MPa)
		0.0002736	8.13
		0.0004	11.34
		0.0008	20
		0.0012	24.89
		0.0016	26.87
		0.001824	27.1
		0.003	27.1
		Concrete	
		ShrCf-Op	0.2
		ShrCf-Cl	0.8
		UnTensSt	2.57
		UnCompSt	-1
		BiCompSt	0
		HydroPs	0
		BiCompSt	0



		UnTensSt	0
		TenCrFac	0
2	Link 8	Linear Isotropic	
		EX (MPa)	200,000
		PRXY	0.3
		Bilinear Isotropic	
		Yield Stress (MPa)	415
		Tangent Modulus (MPa)	0
3	Link 8	Linear Isotropic	
		EX (MPa)	200,000
		PRXY	0.3
		Bilinear Isotropic	
		Yield Stress (MPa)	300
		Tangent Modulus (MPa)	0
4	Solid 45	Linear Isotropic	
		EX (MPa)	200,000
		PRXY	0.3
5	Link 8	Linear Isotropic	
		EX (MPa)	200,000
		PRXY	0.3
		Bilinear Isotropic	
		Yield Stress (MPa)	1100
		Tangent Modulus (MPa)	0

Table 3. Experimental and Analytical Ultimate Loads for Deep beams

Opening Position	Fiber 0%			Fiber 0.75%				Fiber 1.0%			
	Experimental [Vengatachalapathy, V 2010] load(kN)	Analytical load(kN)	% Difference	Experimental [Vengatachalapathy, V 2010] load(kN)	Analytical load(kN)	% Difference	% Increase in the Ultimate Load	Experimental [Vengatachalapathy, V 2010] load(kN)	Analytical load(kN)	% Difference	% Increase in the Ultimate Load
Without web opening (WWBO)	204.50	183.56	10.2	238.14	218.62	8.20	<b>16.04</b>	220.23	212.76	3.39	<b>13.72</b>
Web opening at A (WBOA)	173.00	163.76	5.34	234.36	211.23	9.87	<b>22.47</b>	209.44	187.26	10.6	<b>12.55</b>
Web opening position at B (WBOB)	165.30	150.23	9.12	190.51	183.11	3.88	<b>17.96</b>	180.99	167.77	7.3	<b>10.45</b>

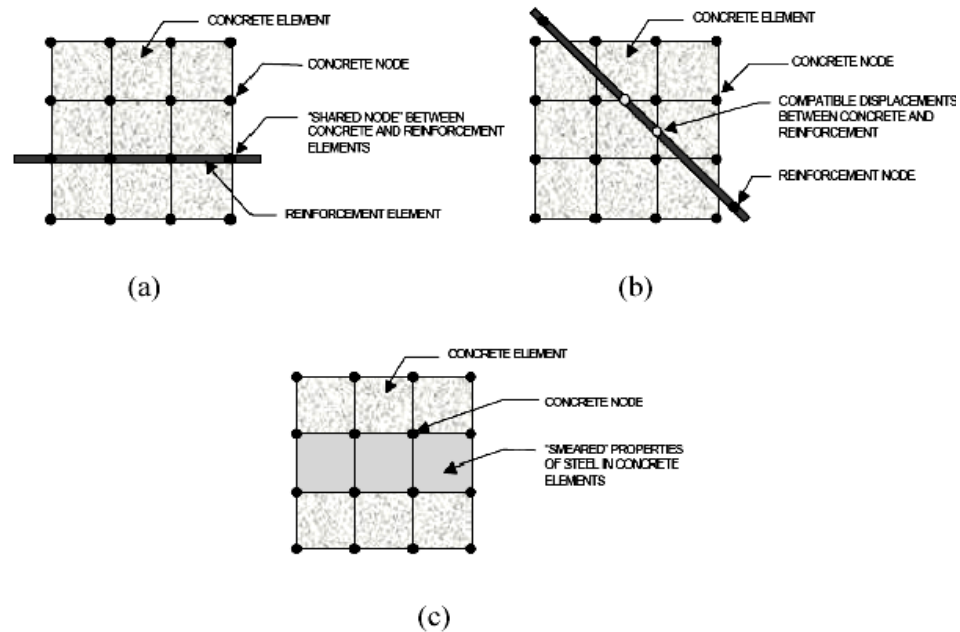


Fig. 1: Models for Reinforcement in Reinforced Concrete (Tavarez 2001):  
(a) discrete; (b) embedded; and (c) smeared

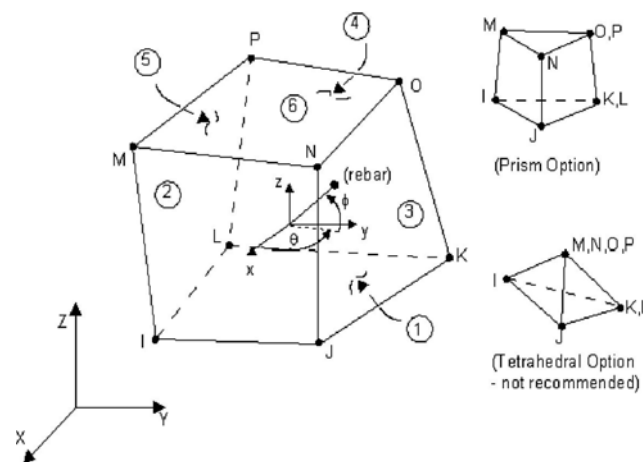


Fig. 2: Solid 65 – 3-D reinforced concrete solid

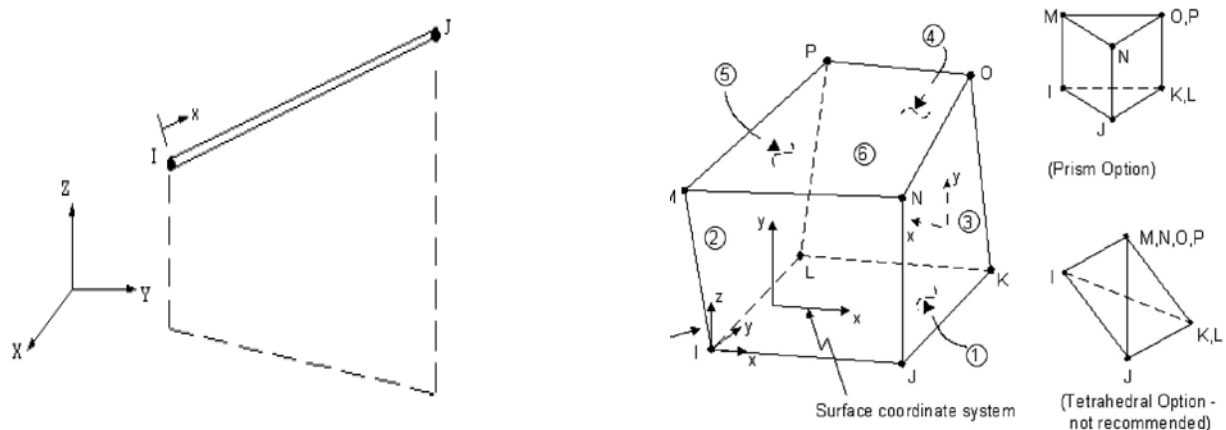


Fig. 3 Link 8 Element

Fig. 4 Solid45 – 3D solid

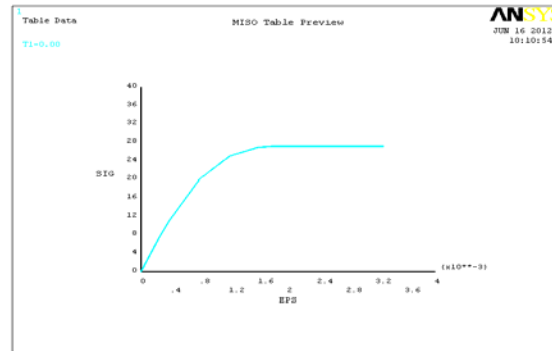


Fig. 5. Uniaxial Stress-Strain Curve of Concrete

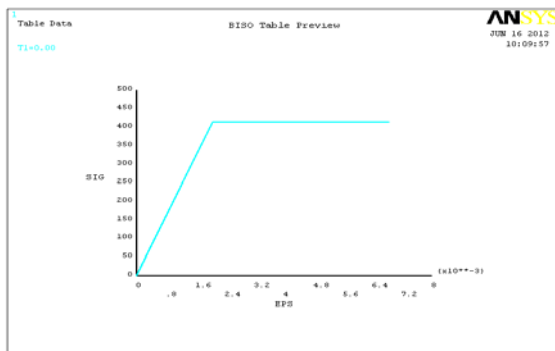


Fig. 6: Idealized Stress-Strain Curve of Main Reinforcing Steel

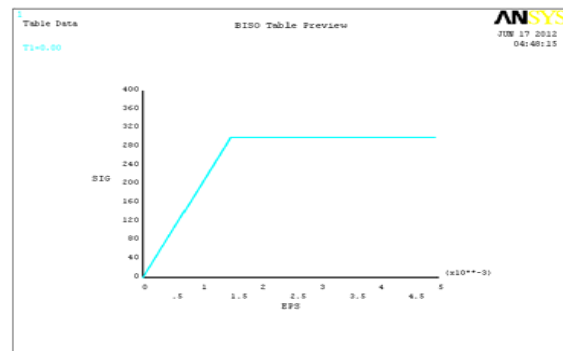


Fig. 7: Idealized Stress-Strain Curve of Web

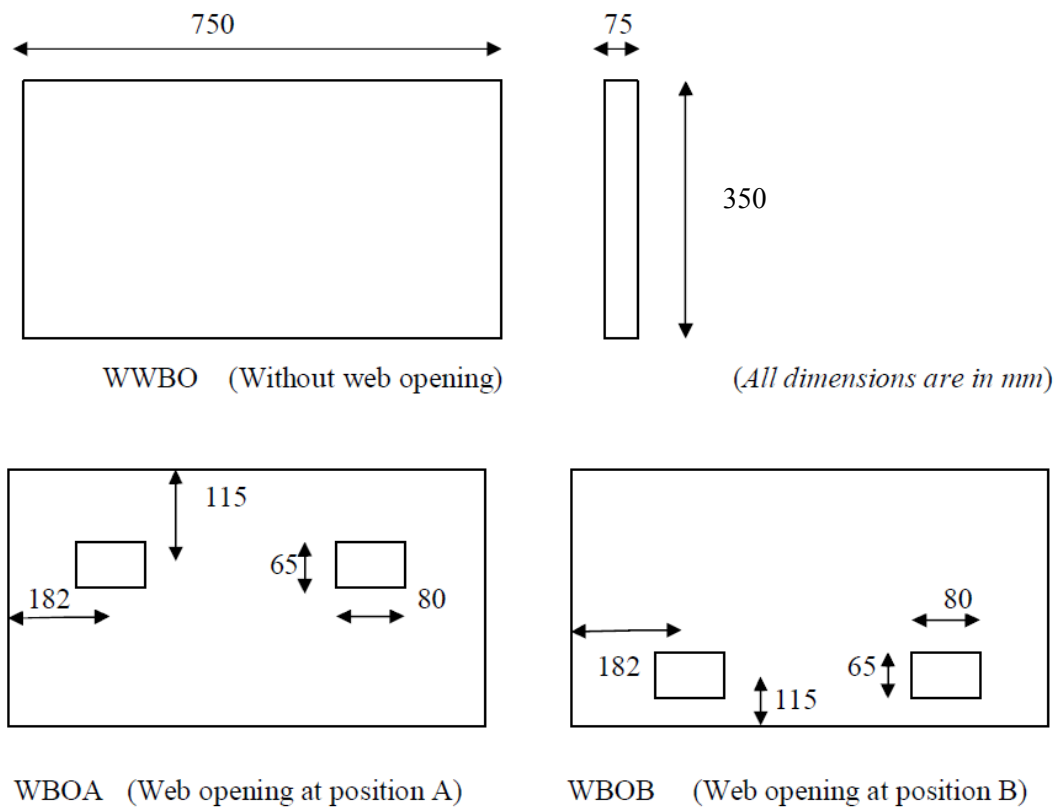


Fig.8 Location Of The Web Opening

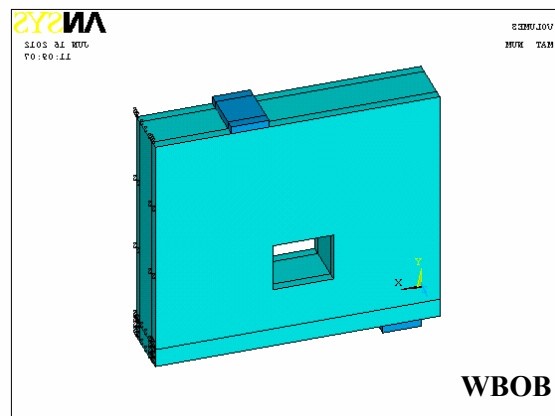
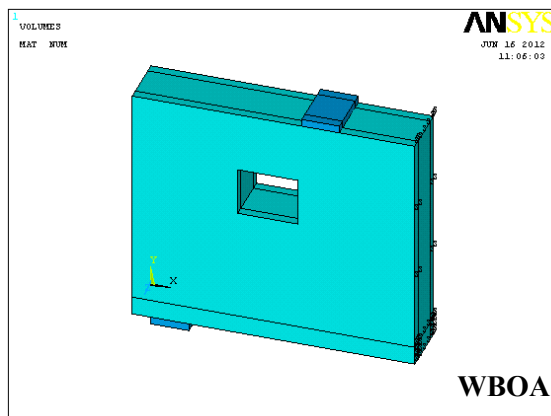
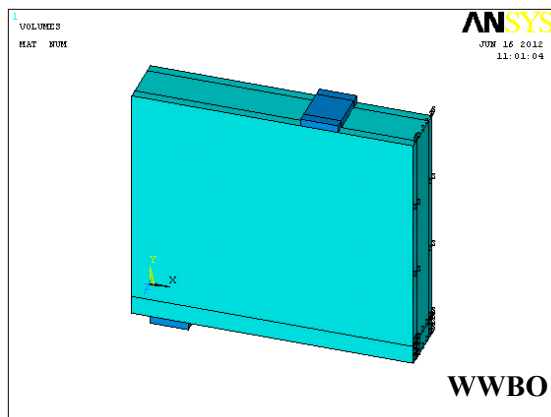


Fig. 9 Modeling Of The Reinforced Concrete Deep Beam

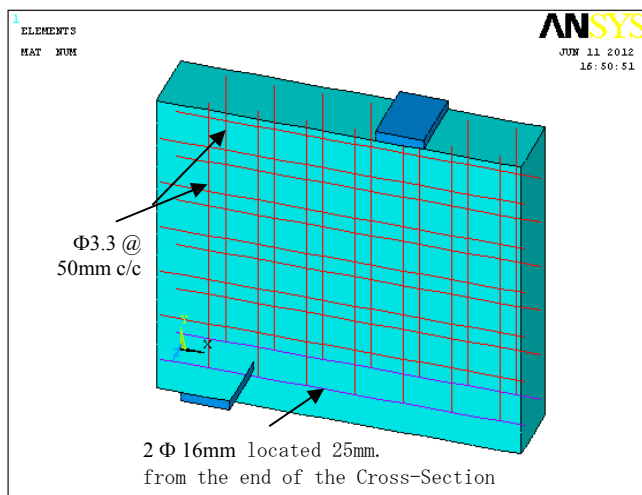


Fig10. Reinforcement Configuration

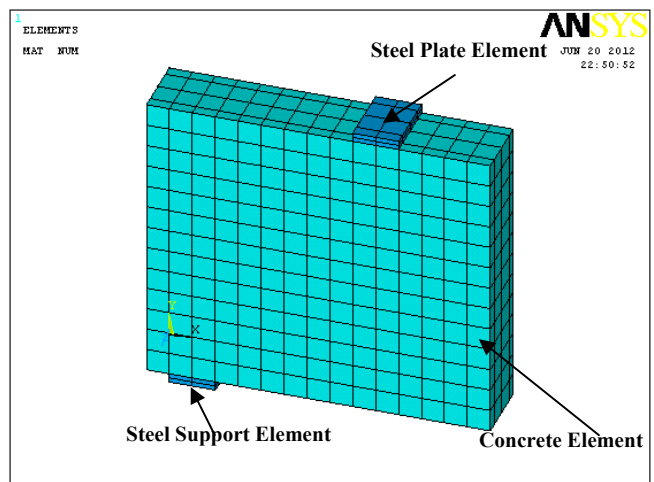


Fig. 11 Mesh of the Concrete, Steel Plate, and Steel Support

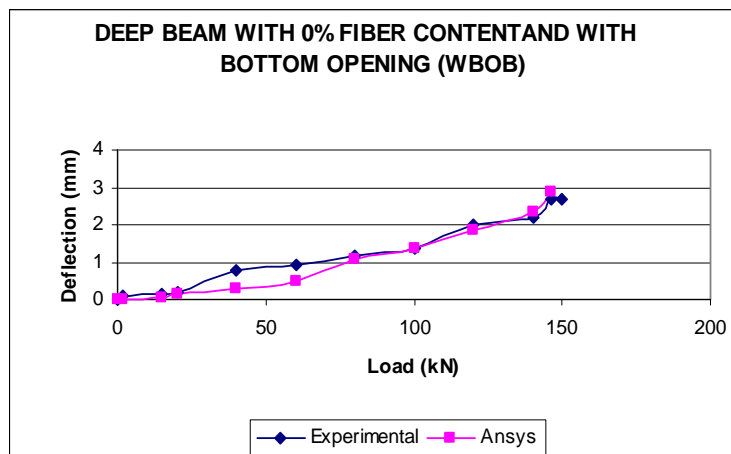
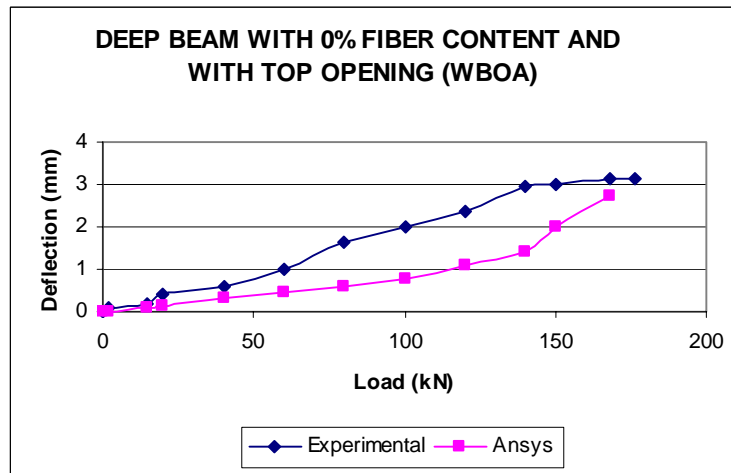
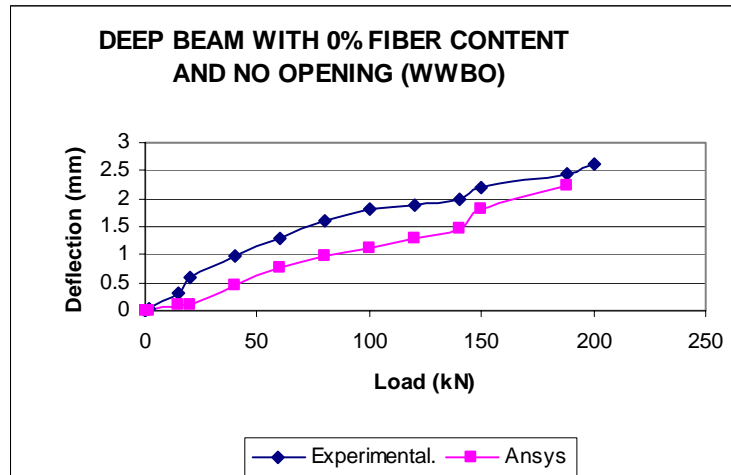


Fig.12 Deep Beam With 0% Fiber Contents With and Without Opening

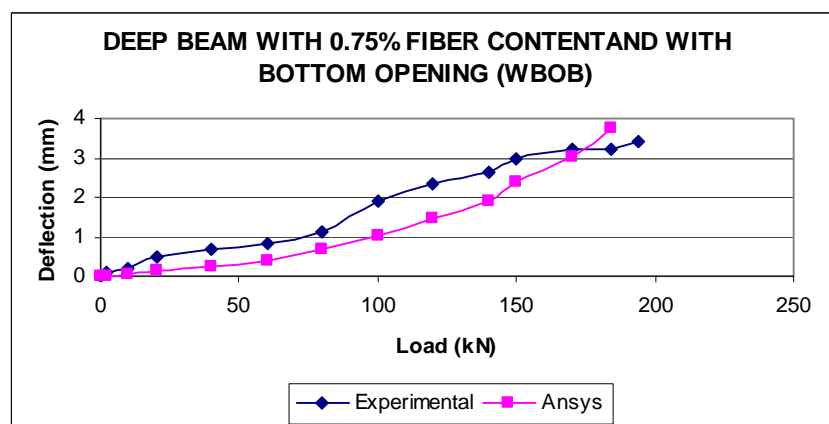
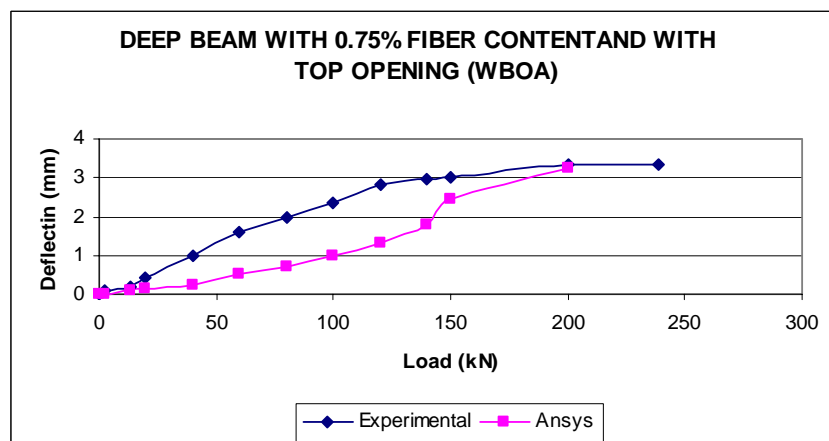
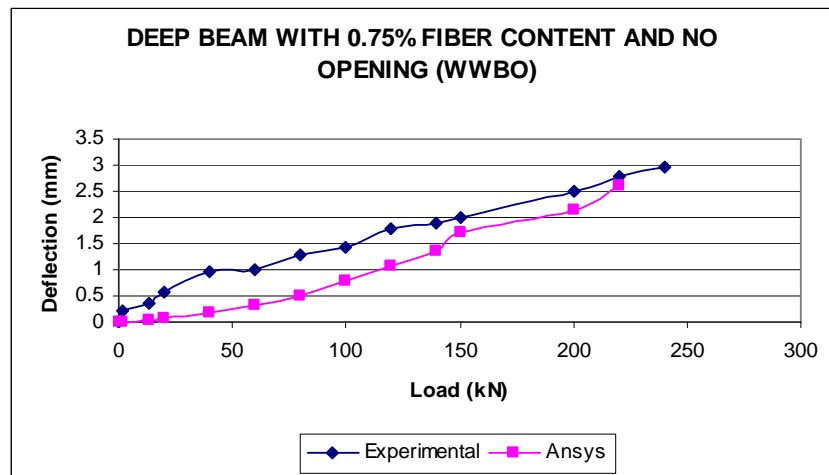


Fig. 13 Deep Beam With 0.75% Fiber Contents With and Without Opening



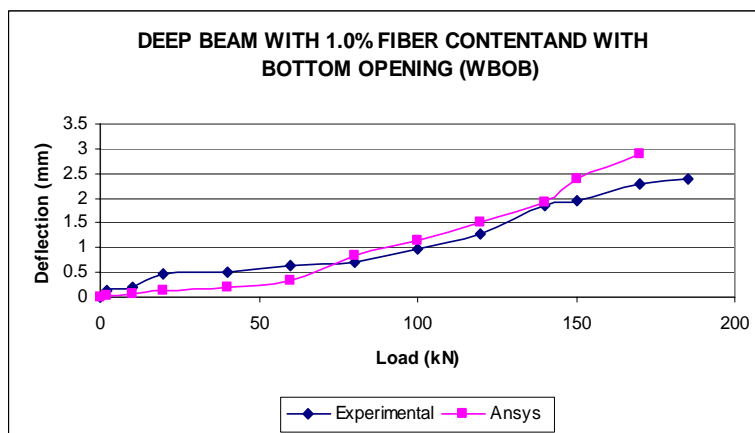
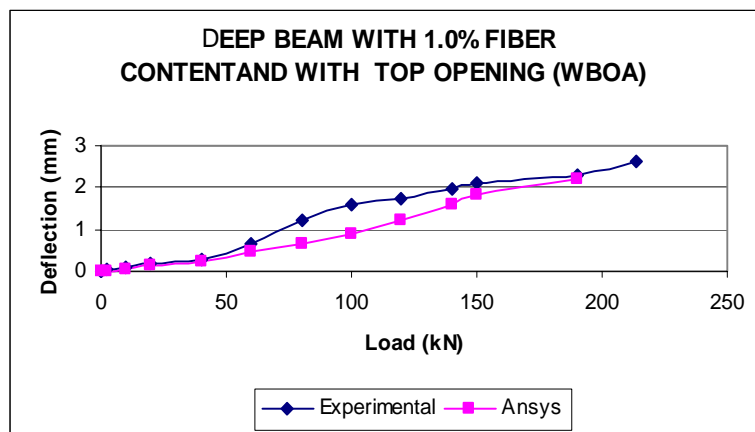
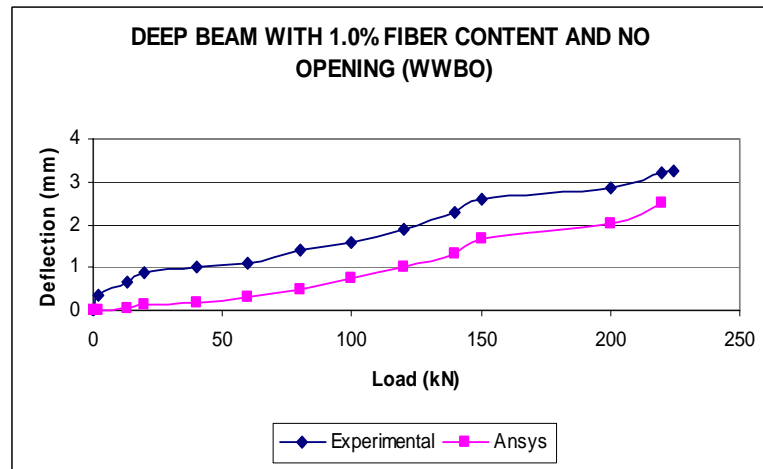


Fig.14 Deep Beam With 1.0% Fiber Contents With and Without Opening

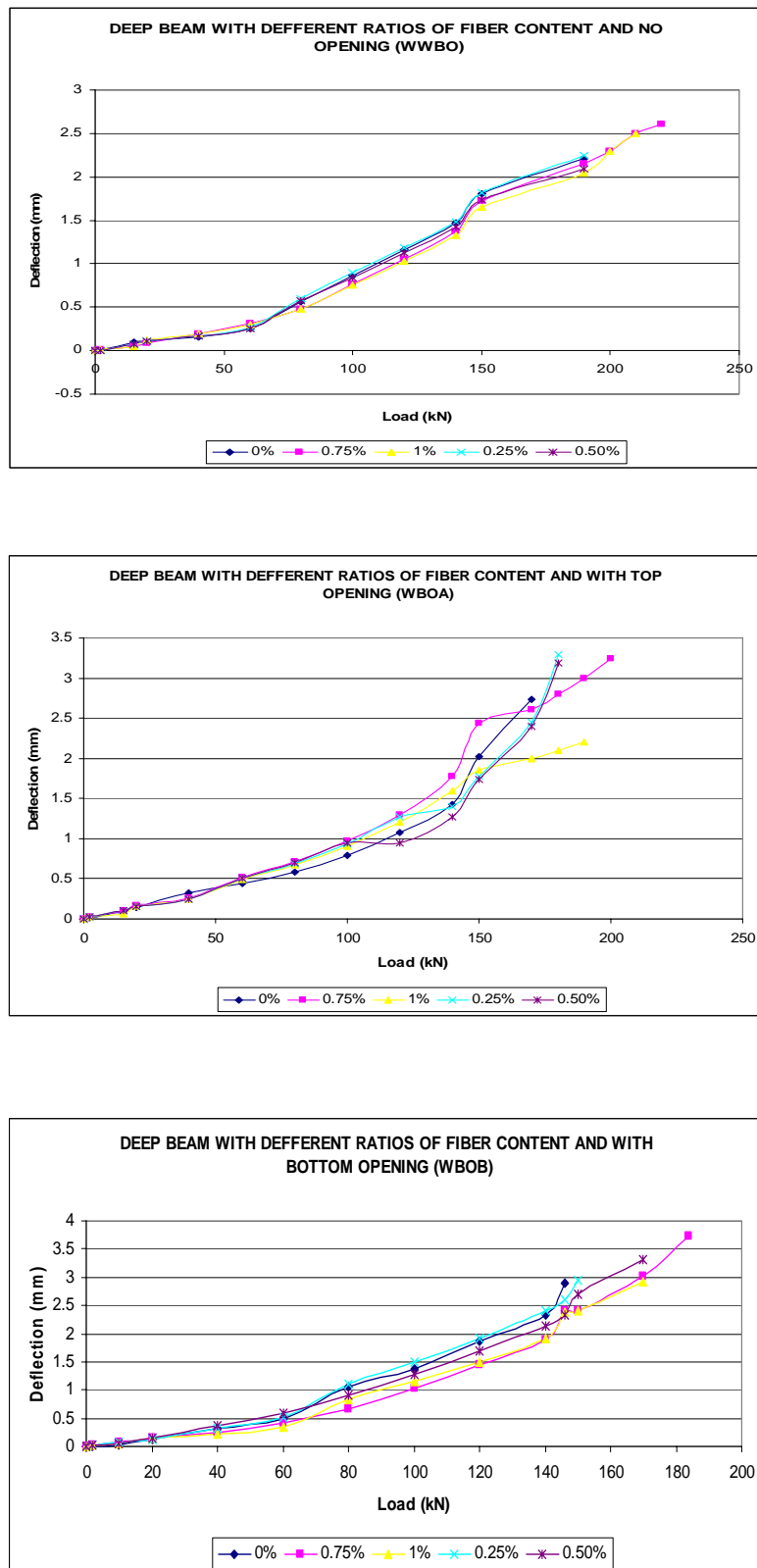


Fig.15 Deep Beam with Different Ratios of Fiber Contents With and Without Opening

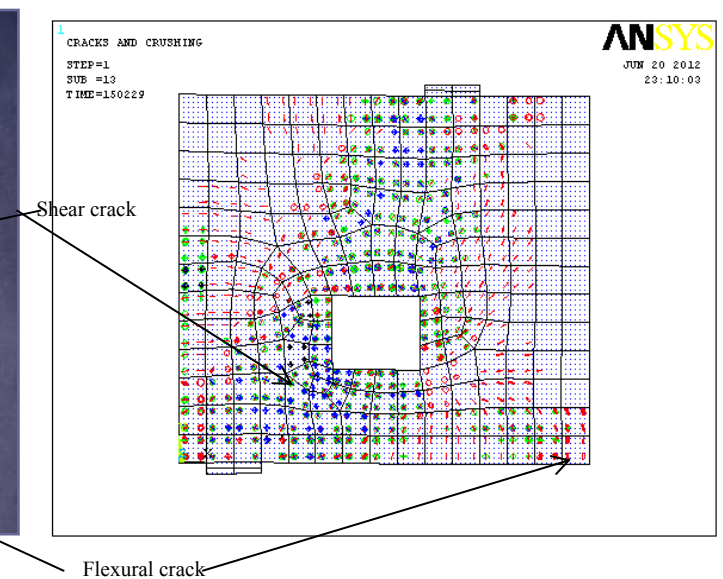
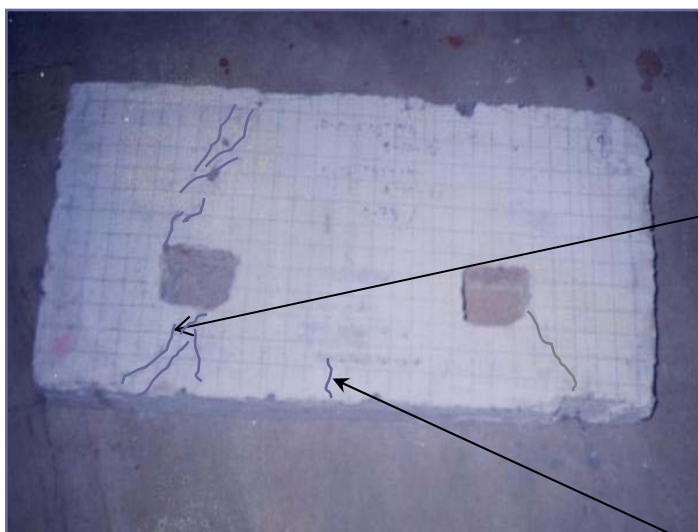
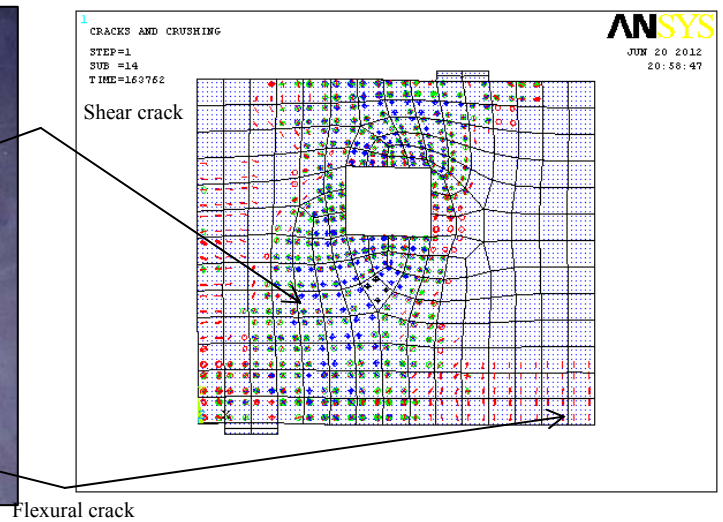
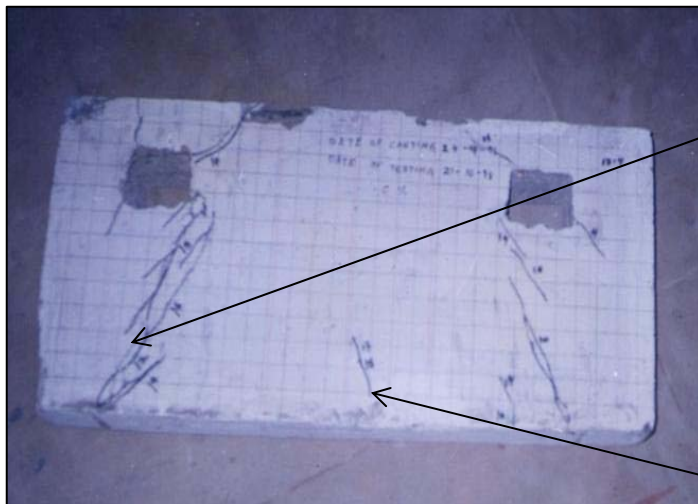
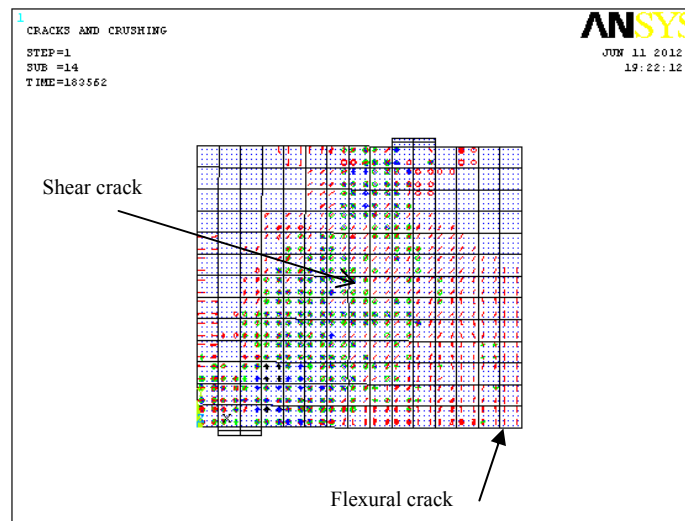
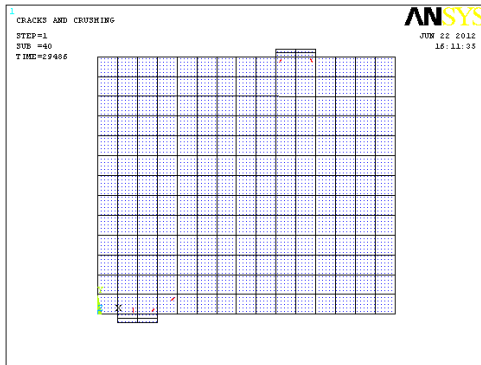
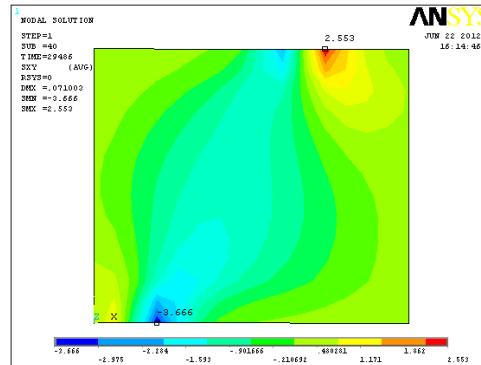


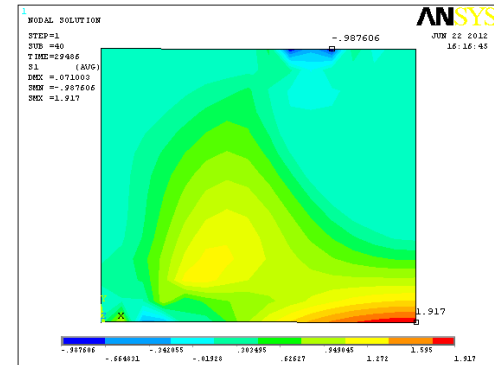
Fig.16 Cracks and Crushing at Ultimate load



a) 1<sup>st</sup> Crack of WWBO

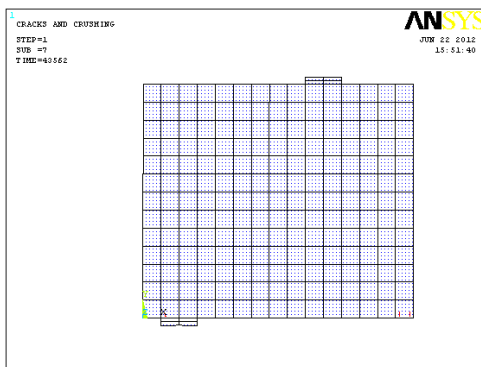


b) Shearing stress of WWBO  
along XY

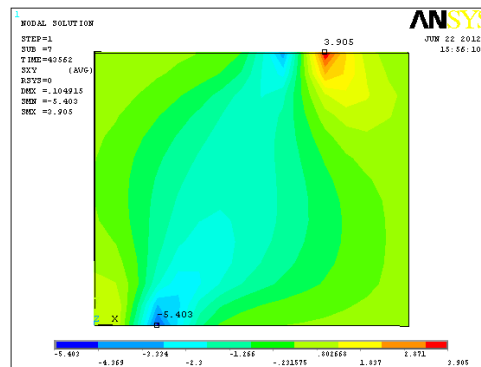


c) The first principal stress of WWBO

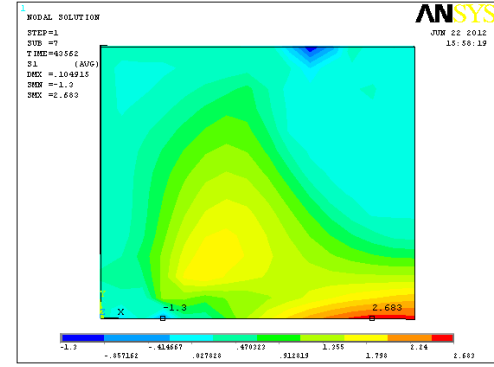
Fig. (17) 1<sup>st</sup> Crack, Shearing and Principal Stresses for WWBO at 0% Steel Fiber



a) 1<sup>st</sup> Crack of WWBO

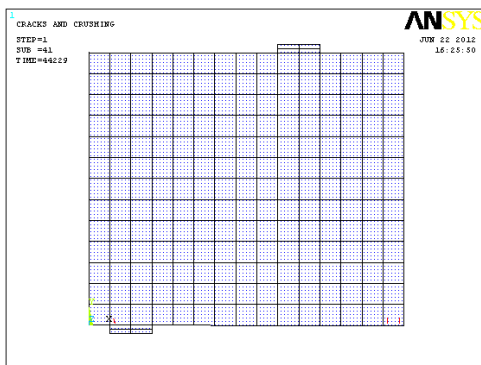


b) Shearing stress of WWBO  
along XY

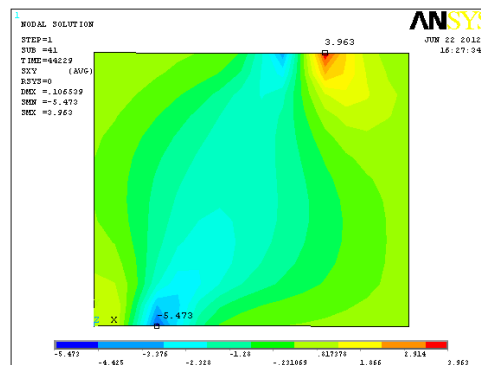


c) The first principal stress of WWBO

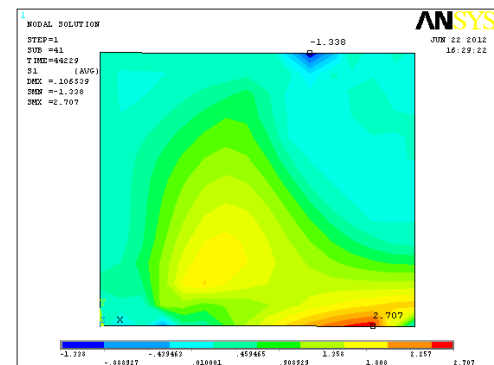
Fig. (18) 1<sup>st</sup> Crack, Shearing and Principal Stresses for WWBO at 0.75% Steel Fiber



a) 1<sup>st</sup> Crack of WWBO

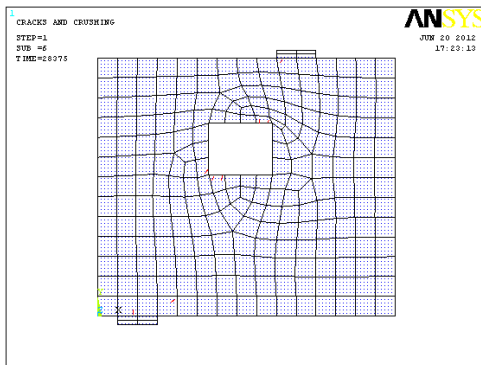


b) Shearing stress of WWBO  
along XY

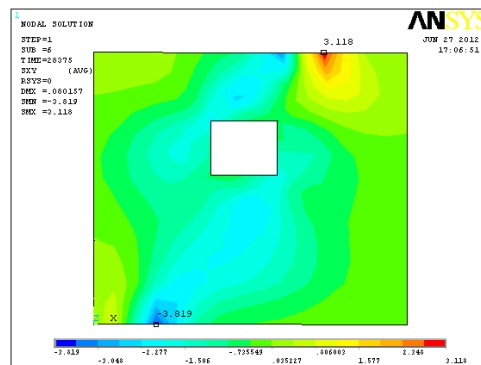


c) The first principal stress of WWBO

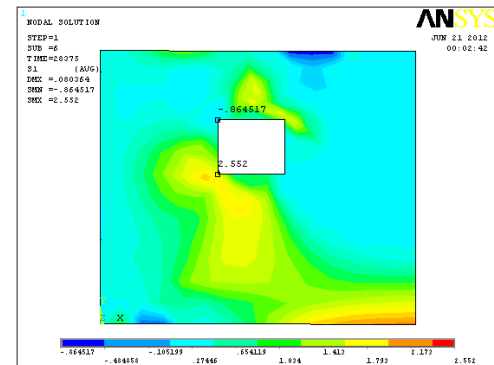
Fig. (19) 1<sup>st</sup> Crack, Shearing and Principal Stresses for WWBO at 1.0 % Steel Fiber



a) 1<sup>st</sup> Crack of WBOA

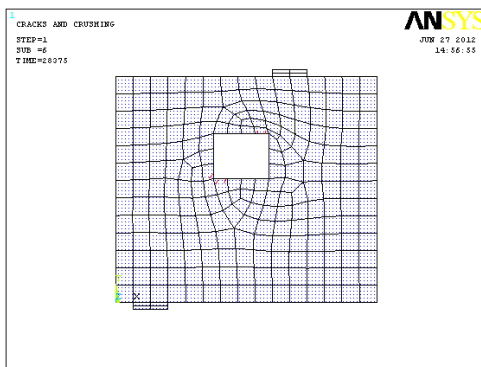


b) Shearing stress of WBOA along XY

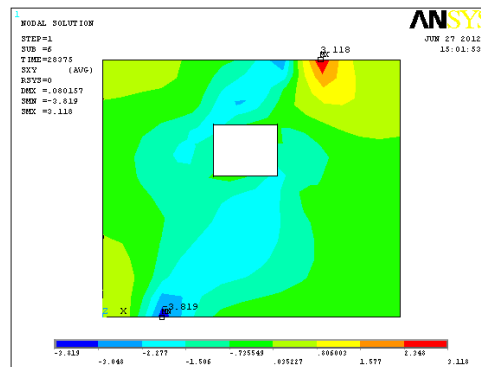


c) The first principal stress of WBOA

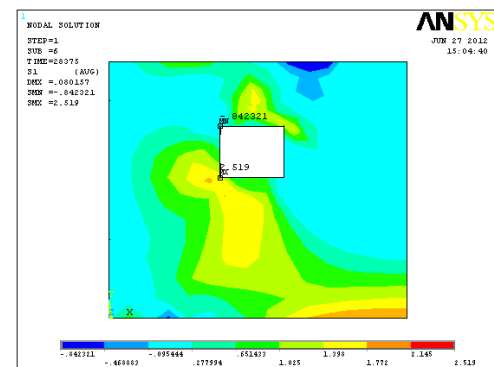
Fig. (20) 1<sup>st</sup> Crack, Shearing and Principal Stresses for WBOA at 0 % Steel Fiber



a) 1<sup>st</sup> Crack of WBOA

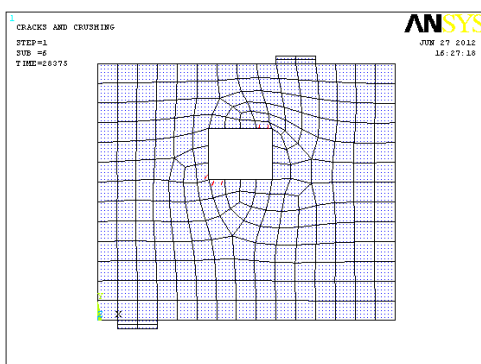


b) Shearing stress of WBOA along XY

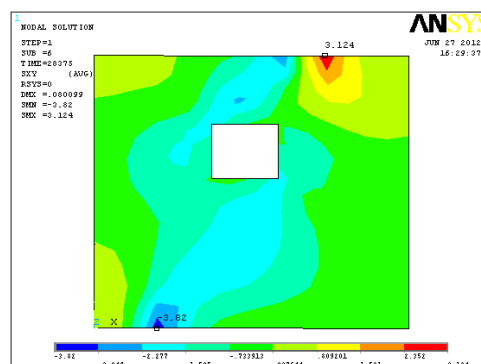


c) The first principal stress of WBOA

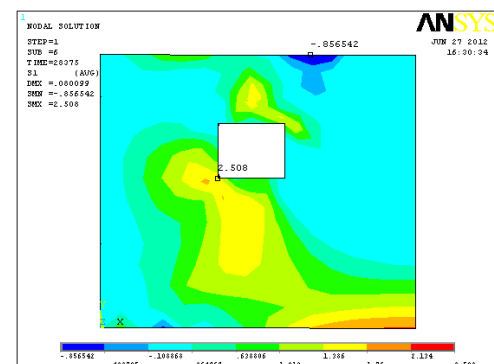
Fig. (21) 1<sup>st</sup> Crack, Shearing and Principal Stresses for WBOA at 0.75 % Steel Fiber



a) 1<sup>st</sup> Crack of WBOA

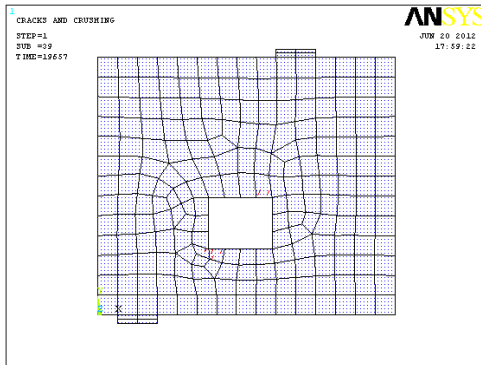


b) Shearing stress of WBOA along XY

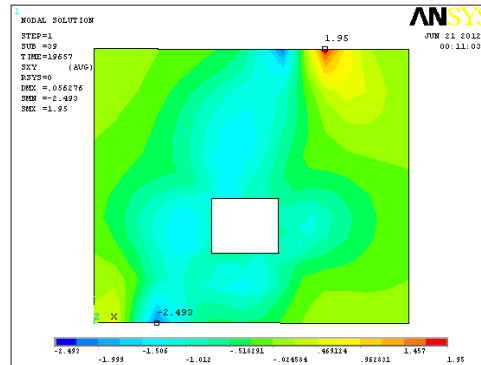


c) The first principal stress of WBOA

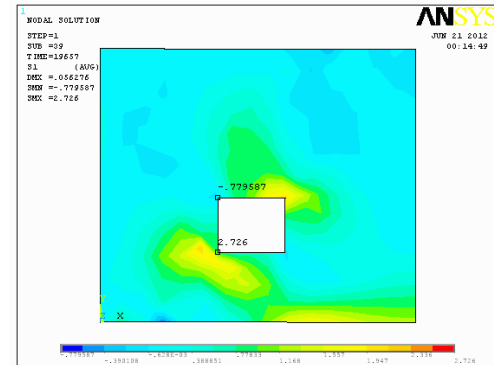
Fig. (22) 1<sup>st</sup> Crack, Shearing and Principal Stresses for WBOA at 1.0 % Steel Fiber



a) 1<sup>st</sup> Crack of WBOB

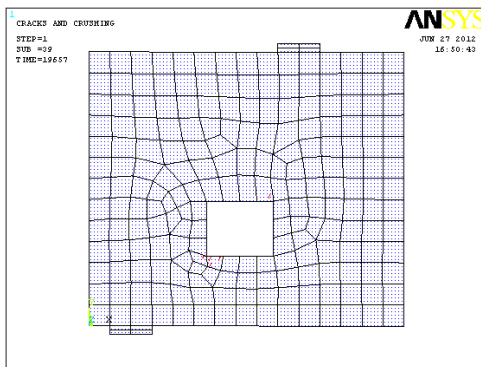


b) Shearing stress of WBOB  
along XY

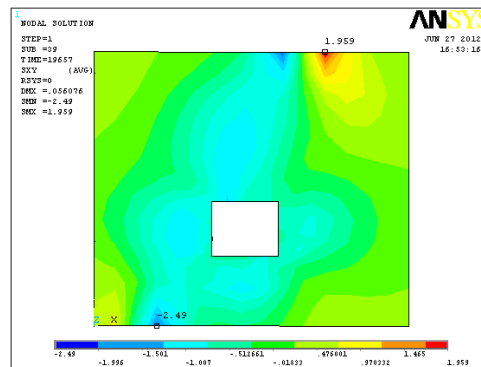


c) The first principal stress of WBOB

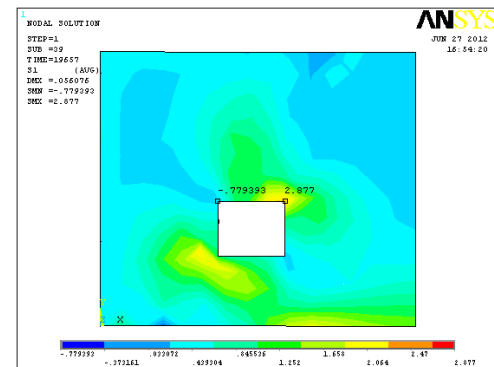
Fig. (23) 1<sup>st</sup> Crack, Shearing and Principal Stresses for WBOB at 0 % Steel Fiber



a) 1<sup>st</sup> Crack of WBOB

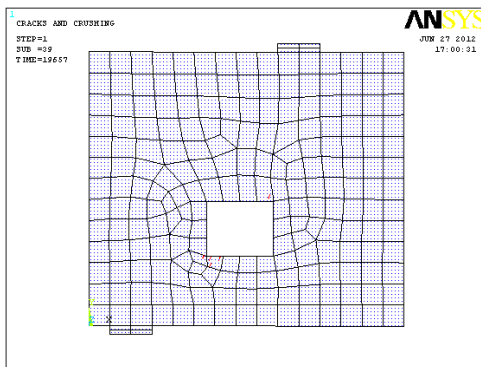


b) Shearing stress of WBOB  
along XY

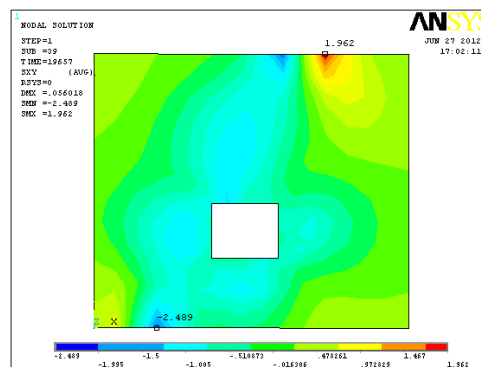


c) The first principal stress of WBOB

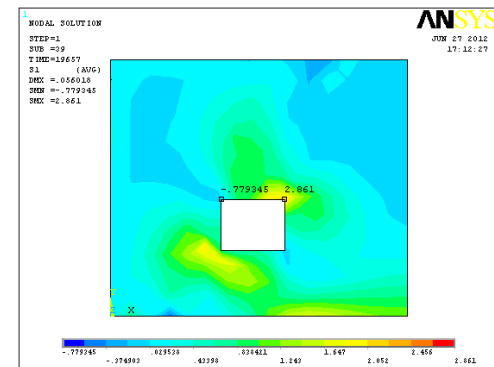
Fig. (24) 1<sup>st</sup> Crack, Shearing and Principal Stresses for WBOB at 0.75 % Steel Fiber



a) 1<sup>st</sup> Crack of WBOB



b) Shearing stress of WBOB  
along XY



c) The first principal stress of WBOB

Fig. (25) 1<sup>st</sup> Crack, Shearing and Principal Stresses for WBOB at 1.0 % Steel Fiber

## Mathematical Model for BOD in Waste Water Discharges from Al Dora Refinery in Baghdad

Shatha Dh. AL Khazraji

Civil Engineering Department

College of Engineering

Dr.Nawar O.A.Nasser

Civil Engineering Department

College of Engineering

### Abstract

This research consists of two parts, the first part concern with analyzing the collected data of BOD and COD values in discharge waste water from Al-Dora refinery during 2010 to find the relationship between these two variables. The results indicates that there is a high correlation between BOD and COD when using a natural logarithm model ( $0.86 \ln(\text{COD})$ ) with correlation coefficient of 0.98. This relationship is useful in predicting the BOD value using the COD value. The second part includes analyzing collected data from the same site in order to find a relationship between BOD and other parameters COD, Phenol(phe), Temperature(T), Oil, Sulphat( $\text{SO}_4$ ), pH and Total dissolved solids( TDS) discharged from the refinery. The results indicated that the best mathematical model is

$$\text{BOD} = 0.786 (\ln(\text{COD}))^2 - 3.077\text{E}83/\text{Exp}(10T) + 1.76\text{E}+48/\text{Exp}(0.1\text{TDS}) - 5.6507/\text{Exp}(100\text{Phe})$$

With correlation coefficient of 0.873. The presented research demonstrates many conclusions regarding the relation between BOD and other pollutions, it is clear that the relation between BOD and COD is a direct relation, while it's a reverse relation with other pollutions and it's also clear that a linear model can be used to represent the relation between BOD and COD for a value of COD approximately less than (50 mg/L).

**Key Words:** BOD, COD, Al- Dora refinery, mathematical model, waste water.

### الخلاصة:

تضمن هذا البحث جزئين، الجزء الاول تناول تحليل البيانات التي جمعت خلال سنة 2010 من مصفى الدورة الذي يقع الى الجنوب الغربي من مدينة بغداد، من اجل ايجاد نموذج رياضي يصف العلاقة بين المتطلب الحيائي للاوكسجين والمتطلب الكيمائي للاوكسجين في مياه المخلفات المطروحة من المصفى. تبين من النتائج ان افضل معامل ارتباط ينتج عند استخدام النموذج الرياضي اللوغارتمي الطبيعي ( $0.86 \ln(\text{COD})$ ) وبمعامل ارتباط مقداره 0.98 ، وباستخدام هذه العلاقة اصبح من الممكن التنبؤ بقيمة المتطلب الحيائي للاوكسجين بالاعتماد على قيمة المتطلب الكيمائي للاوكسجين.

اما الجزء الثاني فقد تضمن تحليل البيانات التي جمعت من نفس المكان لاجاد افضل نموذج رياضي لتمثيل العلاقة بين المتطلب الحيائي للاوكسجين و بقية العناصر مثل المتطلب الكيمائي للاوكسجين ،الفينول، درجة الحرارة، الزيت، الكبريتات، pH، المواد الصلبة الذائبة الكلية، حيث تبين من النتائج ان افضل معامل ارتباط هو عند استخدام النموذج الرياضي

$$\text{BOD} = 0.786 (\ln(\text{COD}))^2 - 3.077\text{E}83/\text{Exp}(10T) + 1.76\text{E}+48/\text{Exp}(0.1\text{TDS}) - 5.6507/\text{Exp}(100\text{Phe})$$

وبمعامل ارتباط مقداره 0.873 .

لقد اظهرت الدراسة المقدمة العديد من الاستنتاجات فيما يخص طبيعة العلاقة بين المتطلب الحيائي للاوكسجين و بقية العناصر. فيمكننا القول بان العلاقة بين المتطلب الحيائي للاوكسجين و المتطلب الكيمائي للاوكسجين هي علاقة طردية ، في حين ان العلاقة عكسية مع بقية العناصر. كما بينت الدراسة امكانية استخدام النموذج الخطي في



تمثيل العلاقة بين المتطلب الحياتي للاوكسجين و المتطلب الكيميائي للاوكسجين على ان لا تتجاوز قيم المتطلب الكيميائي للاوكسجين ( 50 mg/L ) تقريبا .

## Introduction

It is quite clear that air, water and soil are among vital elements of the life on earth (Rose, 1998). During certain period in the past, human being and other living animals enjoyed clear and clean water and air, but industrial revolution during 19<sup>th</sup> century and its perfection in 20<sup>th</sup> century, gradually caused air, water and soil to become polluted. Nowadays, environmental pollution has already reached to a certain scale that it threatens and endangers the health of human beings and survival of other living things. Rivers are the valuable echo- system, besides playing a crucial role in providing great portion of water demanded for agriculture, industry and drinking water, are also considered vital, social, economical problems in different societies (Jenkins, 2001). The environment around us should be exploited in such a way both to provide our reasonable daily needs and at the same time not to be confronted by damage, loss or intimidation by our side. Otherwise in long-term and sometimes short- term, the damage will not only affect us, but also will damage our future. (Sadat pour et al.2004)

The industrial and municipal waste water effluents may contain very high amounts of organic matter and if discharged directly into natural water bodies, it can cause complete depletion of dissolved oxygen leading to the mortality of aquatic organisms.

The oxygen required for the degradation of the organic matter biologically is called the Biochemical Oxygen Demand (BOD), the amount of oxygen needed to consume the organic and inorganic materials is called the Chemical Oxygen Demand (COD). There exists a definite correlation between the COD and BOD under certain conditions and by determining the COD, the information about the BOD of the water/waste water can be derived.( Walters et al,2009)

In the first part of this research some mathematical models are used to find the best relationship between BOD and COD

In the waste water discharges from Al-Dora refinery in Baghdad which is an important center for fuel in Iraq, while in

the second part, computer program using the software (Matlab 09) was used to detect the constants of the mathematical model, in order to find the relationship between BOD and other pollutants like phenol, temperature, and total dissolved solid.

## Al - Dora Refinery:

Al- Dora refinery is one of the biggest refineries in Iraq, it lies at the south west side of Baghdad city, this refinery initiated at 1953 and started its work at 1955, its capacity now 180000 barrel/day and it's an imported center for fuel, medical vaseline, grease, and wax (Al- Dora Refinery web site, 2012).

There is a treatment plant unit in Al Dora refinery for the industrial waste water before discharging it to the Tigris River.

The refinery wastewater generally includes oil, hydrocarbon materials and chemical additives. The following parameters, such as oil and grease, Phenol, BOD, COD, TDS, SO<sub>4</sub>, Ph and Temperature are determined in the wastewater of the refinery.

## Biochemical Oxygen Demand (BOD) and Chemical Oxygen Demand (COD)

Biochemical oxygen demand (BOD) is a measure of the amount of oxygen that bacteria will consume while decomposing organic matter under aerobic conditions. Biochemical oxygen demand is determined by incubating a sealed sample of water for five days and measuring the loss of oxygen from the beginning to the end of the test. Samples often must be diluted prior to incubation or the bacteria will deplete all of the oxygen in the bottle before the test is complete.

Chemical oxygen demand (COD) does not differentiate between biologically available and inert organic matter, and it is a measure



of the total quantity of oxygen required to oxidize all organic material into carbon dioxide and water. COD values are always greater than BOD values, but COD measurements can be made in a few hours while BOD measurements take five days. (NGRDC,2000)

Pedro et al.2004 Made a research on Evaluation of Organic Load Measurement Techniques in a Sewage and Waste Stabilization Pond Biochemical Oxygen Demand (BOD) and Chemical Oxygen Demand (COD) are the major parameters used as routine surrogate tests for measuring the load of organic carbon into the environment. In their research, evaluations of possible replacement of BOD and COD for Dissolved Organic Carbon (DOC) measurements are presented for different wastewaters. For anaerobic pond effluent, the following correlations were obtained:

$COD = 1.08 DOC + 79$	$BOD = 0.82 DOC + 12.1$
For facultative pond effluent	
$COD = -0.29DOC + 109$	$BOD = 0.14DOC + 26.2$
For raw sewage	
$COD = 4.18DOC - 2$	$BOD = 0.46COD + 5.3$
For aerated pond effluent	
$COD = 3.57DOC + 6$	$BOD = 0.27COD + 3.4$
For sedimentation pond effluent	
$COD = -1.34DOC + 138$	$BOD = 0.73DOC + 16.5$

It was found that the determination of COD was not appropriate for substituting classical alternatives in tested samples in despite of the limitations of the samples.

Chemical oxygen demand fractions of municipal wastewater for modeling of wastewater treatment is a research done by I. Pasztor;etal. 2010 , They showed that when a new wastewater treatment plant is being designed by computer simulation, detailed data about organic fractions of influent wastewater (measured as chemical oxygen demand) are usually not available, but knowledge of the typical ranges of these fractions is indispensable. The

influent chemical oxygen demand fractions can substantially influence the results of simulation-based design such as reactor volumes, solids residence time, effluent quality, oxygen demand, sludge production, etc. This research attempts to give an overview of wastewater organic fractions as modeling parameters and presents new chemical oxygen demand fractionation results from Hungary. According to the data from literature, the ratio of chemical oxygen demand components in raw wastewater is very different and the average composition is as follows: Inert particulate =17.1%, slowly biodegradable = 57.9 %, inert soluble =7.8 % and readily biodegradable = 17.5 %. The Hungarian wastewater samples were analyzed according to STOWA (Dutch foundation for applied water research) the obtained results were not much different from those of literature

( inert particulate = 23.7 %, slowly biodegradable = 49.8 %, inert soluble = 4.6 % and Readily biodegradable = 21.9 %), but some typical characteristics were observed.

Sadatipour et al. 2004 made a research on investigation on Kangan gas refinery wastewater , this research is carried out on March 2002 at Kangan refinery, which is located in Kangan city, southern part of Iran. The gas refinery wastewater generally includes oil, hydrocarbon materials and chemical additives, which are in the form of emulsion in water. The following parameters, such as oil and grease, PAHs, BOD, TH, turbidity, COD, EC, pH, TSS, SiO<sub>2</sub>, PO<sub>4</sub> are determined in wastewater of the refinery in order to determine the amount of pollutants, which are affecting the area where the refinery is located. The oil and grease are analyzed by FTIR and PAHs are determined by UV-Luminance and physico-chemical parameters are determined according to the Standard Methods. The results showed that although pollution of the refinery wastewater is within world permissible limits (EPA), but since the area is affected by the wastewater and surrounding area is confined with river basin it could be concluded that pollutants, which are

discharged to the echo environment, are not in the permissible limits of the similar Industries.

Determination of inert chemical oxygen demand (COD) fractions of Cumhuriyet University wastewater is a research made by F. Ciner and M. Sarioglu 2005, Some amounts of inert products are given into environment due to biological degradation of substrate in activated sludge system. The effluent of biological wastewater treatment consists of inert substrate in influent flow, soluble microbial products and non degradable or slowly degradable organic products. Soluble inert COD (SI) must be determined for discharge standards since it did not give any reaction in activated sludge system and was given with wastewater discharge. However particular inert COD (XI) accumulated in system depending on sludge retention time due to it is only wasted from system by wasted sludge.

This study focused on inert fractions of Cumhuriyet University campus wastewater which consists of domestic, hospital and laboratory wastewaters. Experimental method was used suggested by Orhon et al. and modified by Germirli et al. in order to determine directly influent particulate and soluble inert fractions. According to the experimental procedure three aerobic batch reactors, two with the wastewater and the third with glucose were run parallel. In the reactors, the change in the soluble COD profiles is observed for a period during which all degradable COD is entirely depleted, in other words, the COD profiles reach a plateau and remain unchanged. Wastewater samples were taken equalization tank in wastewater treatment plant. The conventional parameters of campus wastewater characterization were as follows:

Total COD  
(CT0) = 372 mg l-1, total soluble COD  
(STO) = 124 mg l-1,  
total suspended solids (TSS) = 177 mg l-1,  
ammonia (NH3) = 31.2 mg l-1,  
ortho-phosphate (PO4-P) = 11.3 mg l-1  
and pH=7,4 .

In this study, in order to determine inert COD fractions in Cumhuriyet University campus wastewater, three aerobic batch

reactor systems were used. At the end of approximately 381 h operation, COD composition of campus wastewater were found to be CT0=372 mg l-1, XS0=56 mg l-1, SS0=104 mg l-1, CS0=149 mg l-1, SI=12 mg l-1, XI=211 mg l-1, respectively

An application study in Al Dora refinery made by Abood,2004. The aim of that experimental work was for studying the Furfural removal from Al Dora refinery waste water by the adsorption process using a continuous system (fixed activated carbon bed). The equilibrium data were determined experimentally and the equilibrium isotherm was found to be of a favorable type and fit well by Langmuir and Freundlich isotherm while experimental and theoretical results were compared by estimating the deviation absolute mean error (7%, 6.8%) and root mean square (0.0119, 0.0169) respectively for the results. Regeneration process of exhausted activated carbon was carried out by three different methods(washing with dilute Alcohol, washing with boiled distilled water and the thermal process) in order to find the regeneration efficiencies which was found to be (60-90)%

Al azzawi 2007 made a research on Evaluation of the performance of the Dora refinery waste water treatment plant, comparisons were made between the actual and the designed performance for various potential pollutants. For long term evaluation of (2004 and 2005) years the test measurements were collected and analyzed. His results indicated that the annual percentage removal of sulfide, oil, COD, BOD, and TSS, were found acceptable except for the TSS value which shows relatively low removal percent 67.58%. and the monthly percentage removal of sulfide, oil, COD, BOD and TSS shows considerable changes among different months of the years, which may reflect considerable variation in influent water properties and treatment process.

## Building Of the Mathematical

### Models:

In order to find a suitable relationship between BOD and COD concentration,

and BOD with other pollutants, the following points must be achieved:

- 1- Removing all the data that can be consider as irregular.
- 2- Separating the data in to two parts. The first part which represent 60% of the total data are used to find the optimum model for the relationship between BOD and COD, and the second part of ratio 40% of the total data that used to evaluate the estimated relationship.
- 3- Using of correlation coefficient and T-test in order to select the suitable relationship.
- 4- Calculating the constants corresponding to each term in the selected model so that the error between the real values and the calculated values minimized. A computer program using the software (Matlab 09) was used to detect the constants of the mathematical model.
- 5- Evaluating the resulting model by using the second part of data, which is 40% of the total data?

## Results:

**Step one:** The mathematical models that used in describing the relationship between BOD and COD are shown in table 1, where  $Y=BOD$  and  $X=COD$  Figur 1 and figure 2 indicated that the relationship between BOD and COD is liner for the values below 50mg/lit, this relationship is

$$BOD=0.901X+5.214 \quad 6$$

with correlation factor 0.965.

**Step two:** The mathematical models that were used in describing the relationship between BOD and other pollutants are shown in table 2, where:

$$Y=BOD, x = T, TDS \text{ or Phe}$$
$$z = 10x \text{ for } T, 0.01x \text{ for TDS, } 100x \text{ for Phe, } x \text{ for } SO_4 \text{ \& PH, } 0.01x \text{ for Oil}$$
$$f = 10x \text{ for } T, 0.1x \text{ for TDS, } 100x \text{ for Phe, } , x \text{ for } SO_4 \text{ \& PH, } 0.01x \text{ for Oil}$$

**Step three:** Selected the best mathematical models that used to describe the relationship between BOD and other pollutants are shown in table 3  
Figure 3 and figure 4 indicated that the modeled data and the origin data has the same trend.

## Discussion and Conclusions

The industrial and municipal waste water effluents may contain very high amounts of organic matter and if discharged into natural water bodies, it can cause complete depletion of dissolved oxygen leading to the mortality of aquatic organisms.

The two parts considered in the presented research demonstrated the major conclusions given hereafter:

-The best correlation coefficient between BOD and COD is 0.980, based on natural logarithm model, Table 1. Hence, the best relationship between BOD and COD is:

$$BOD = A \ln(COD)^2 \quad 7$$

Where A is a constant of the model.

- The relation between BOD and COD is a direct relation and can be relatively represented using a linear model ( $0.901X + 5.214$ ) with correlation factor 0.965, for a value of COD approximately less than (50mg/L), as shown in figures 1 and 2.

- The estimated natural logarithm relationship can use in predicting the value of BOD according to the value of COD, COD values are always greater than BOD values, but COD measurements can be made in a few hours while BOD measurements take five days.

- In part two of the research there were many pollutants were examined in order to find the suitable mathematical model, these pollutants are COD, phe ,T,Oil,SO<sub>4</sub> and TDS.

- The correlation coefficient show that there is weak correlation between BOD and Oil and between BOD and SO<sub>4</sub> and BOD and pH, therefore, these values were neglected, table 2, and the mathematical model was build according to the values of TDS,T,Phe.

- The relation between BOD and Phe, TDS, and T is a reverse relation, table 3

- The magnitude of BOD is more sensitive to the change in the COD contains rather than to the change in the Phe, TDS, and T contains.

- the modeled data and the origin data has the same trend as shown in figures 3,4.

## References

**Abood, 2004**, Waleed Mohammed,  
"Designing of Pilot Plant for Treatment  
of Waste Water Contaminated with  
Furfural by The Adsorption Method", a  
thesis submitted to the Environmental  
Engineering, College of Engineering  
,University of Baghdad.

**Al-Azzawi, 2007**,Muwafaq Ahmed  
Abed, "Evaluation of The Performance  
of The Dora Refinery Waste Water  
Treatment Plant", a thesis submitted to  
the Environmental Engineering,  
College of Engineering, University of  
Baghdad.

**Al Dora Refinery web site,2012**,  
<http://www.dauramrc.com>

**CINER ,F., SARIOGLU, M.**  
**,2005**, "DETERMINATION OF INERT  
CHEMICAL OXYGEN DEMAND  
(COD) FRACTIONS OF CUMHURIYET  
UNIVERSITY WASTEWATER",  
Cumhuriyet University, Department of  
Environ. Eng. 58140,Sivas,  
Turkey,Selected from papers presented in  
9<sup>th</sup>, International Conference on  
Environmental, Science and Technology  
(9CEST2005), 1-3 September 2005,  
Rhodes island, Greece

**I. Pasztor;etal. 2010**, I. Pasztor; P.  
Thury; J. Pulai, " Chemical oxygen  
demand fractions of municipal wastewater  
for modeling of wastewater  
treatment",Department of Environmental  
Engineering and Chemical Technology,

University of Pannonia, Veszprem,  
Hungary.

**Jenkins, S. H., 2001**, " Water quality  
management",Pergamon Press, NewYork.

**NGRDC,2000**, Northeast Georgia  
Regional Development Center, Appendix  
B, Description Of Commonly Considered  
Water Quality Constituents, Watershed  
Protection Plan Development Guidebook

**Pedro ,2004**, Pedro Sérgio Fadini a,  
Wilson F. Jardimb and José Roberto  
Guimarães J. , " Evaluation of Organic  
Load Measurement Techniques in a  
Sewage and Waste Stabilisation  
Pond",Braz. Chem. Soc., Vol. 15, No. 1,  
131-135, 2004. Printed in Brazil - ©2004  
Sociedade Brasileira de Química, 0103 -  
5053 \$6.00+0.00

**Rose, J., 1998**, "Water and the  
environment". Gordn and Breach Science  
Publishers, Philadelphia, USA, 1-15

**S. M. T. Sadatipour, L. Mirzaie and A.**  
**A.Rezaei,2009**, " An investigation on  
Kangan gas refinery wastewater",  
Department of Marine Science and  
Technology, Islamic Azad University,  
Tehran North Branch, Tehran, Iran  
National Iranian Gas Company, Research  
and Development Division, Tehran, Iran  
Int. J. Environ. Sci. Tech., 6 (1), 51-56.

**Walters, M.,2009**, Munde Walters,  
Ganesh Raj Osti, Nguyen Diem Hang, "  
Determination of Chemical Oxygen  
Demand (COD) of Waste Wate

**Table 1: The mathematical models for BOD-COD relationship**

Mathematical Model	Correlation Coefficient
$Y = x^2$	0.846
$Y = x^3$	0.807
$Y = 1/x$	-0.682
$Y = \exp(0.12x)$	0.804
$Y = (\ln(x))^2$	0.980
$Y = \log(x)$	0.953
$Y = x^{1.8}$	0.857
$Y = \exp(x^{0.5})$	0.804
$Y = \exp(1/x)$	-0.675
$Y = 1/\exp(x)$	0.439
$Y = x^6$	0.804
$Y = (\exp(x))^{0.5}$	0.804
$Y = (\exp(x))^{0.75}$	0.804

**Y=BOD , x=COD**

**Table 2: The mathematical models for BOD - other pollutants relationship**

Mathematical Model	Correlation Coefficient					
	T	TDS	Phe	SO4	PH	Oil
$Y = x^2$	0.105	0.022	0.529	-0.195	-0.054	0.052
$Y = x^3$	0.128	0.054	0.500	-0.225	-0.058	-0.001
$Y = 1/x$	0.003	0.111	-0.552	0.078	0.043	----
$Y = x^{0.5}$	0.057	0.043	0.561	-0.139	-0.049	0.259
$Y = (1/x)^{0.5}$	-0.018	0.009	-0.555	0.099	0.045	-0.093
$Y = \log(x)$	0.038	-0.061	-----	-0.119	-0.047	----
$Y = \exp(z)$	0.007	0.149	-0.058	-0.055	-0.076	0.180
$Y = 1/\exp(f)$	0.800	0.811	0.877	-0.130	0.019	-0.155
$Y = (\exp(x^{0.5}))^2$	0.156	0.029	----	-0.235	-0.059	-0.021
$Y = \exp(1/x)$	0.005	0.038	-0.353	0.078	0.043	-0.124
$Y = \ln(x)$	0.038	-0.061	----	-0.119	-0.047	----
$Y = 1/\ln(x)$	-0.012	-0.002	----	0.103	0.043	----

**Table 3: The selected mathematical models for BOD - other pollutants relationships**

Mathematical Model	$(\ln(\text{COD}))^2$	$1/\exp(10T)$	$1/\exp(0.1\text{TDS})$	$1/\exp(100\text{Phe})$
<b>Correlation Coefficient</b>	0.980	0.800	0.811	0.877

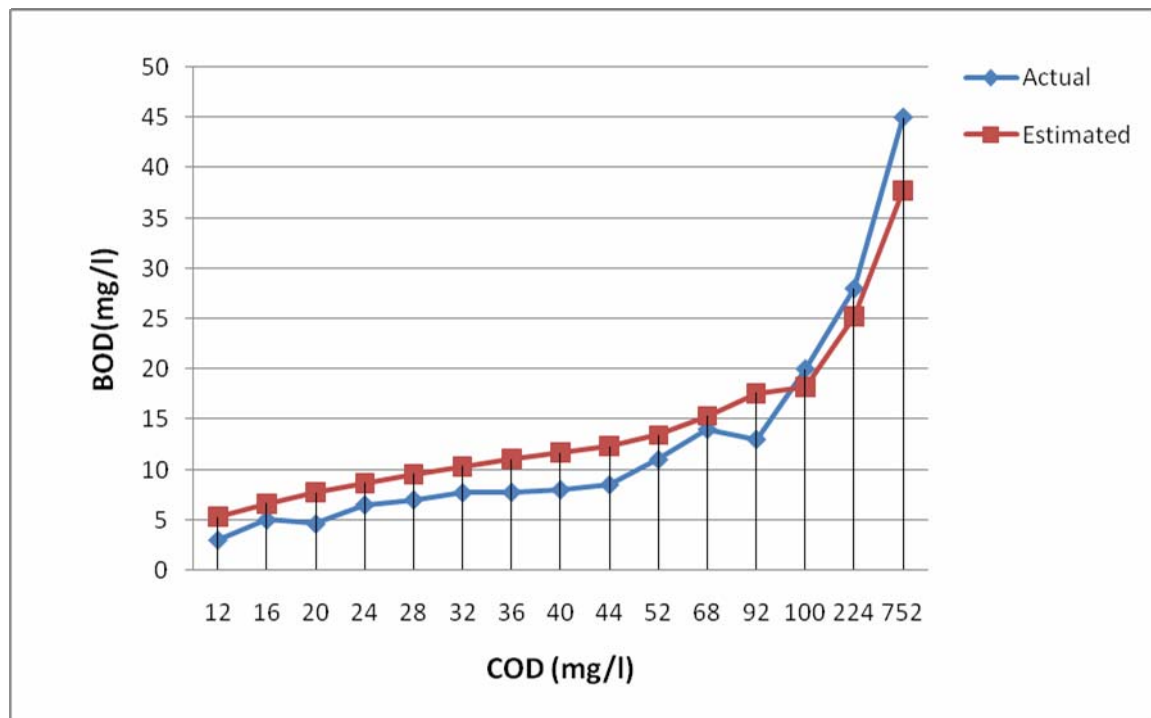


**Figure 1: BOD versus COD during the period under study  
(First set of data - Modeling)**

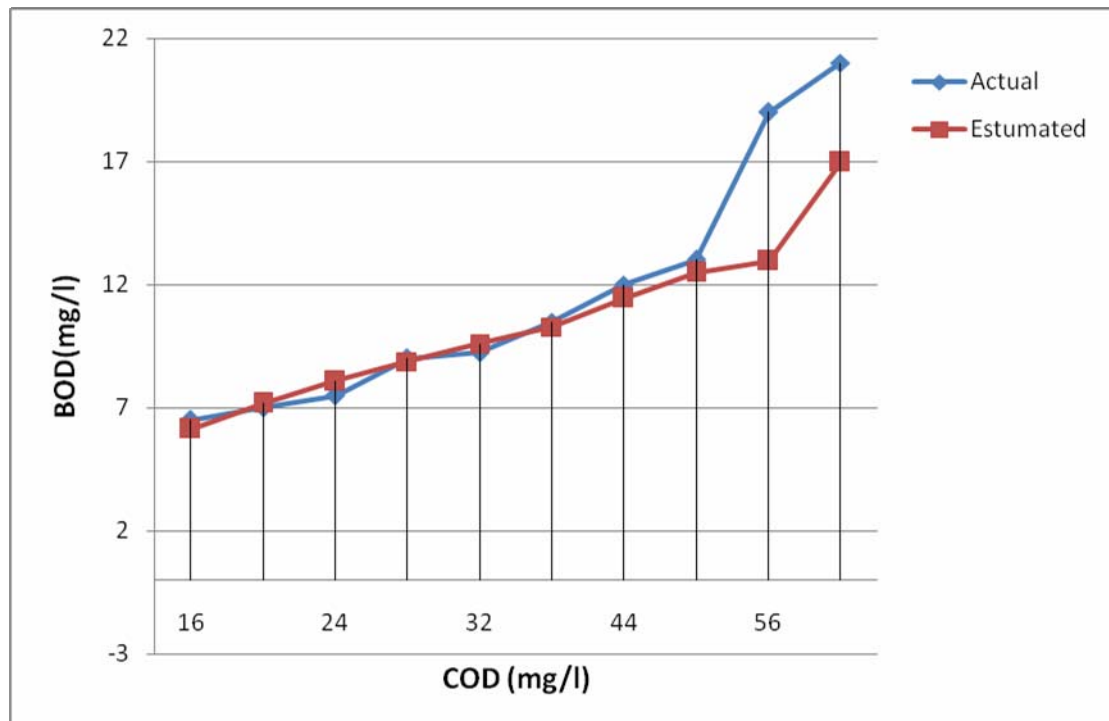


**Figure 2: BOD versus COD during the period under study  
(Second set of data - Evaluation)**

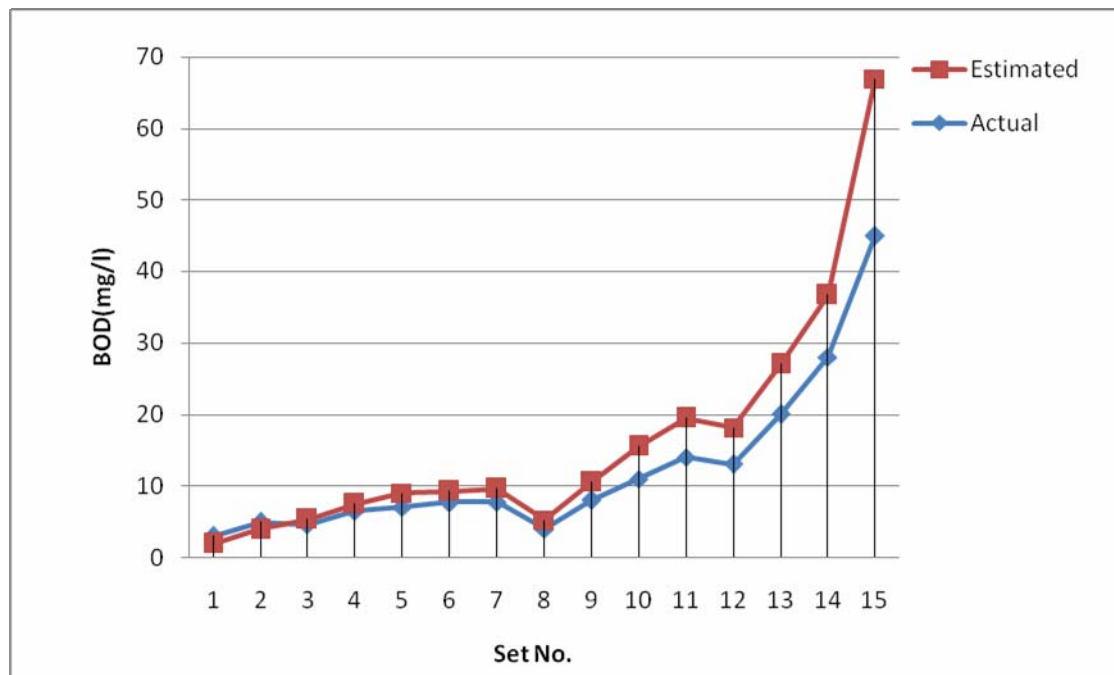


**Figure 3: BOD evaluation during the period under study  
(First set of data - Modeling)**

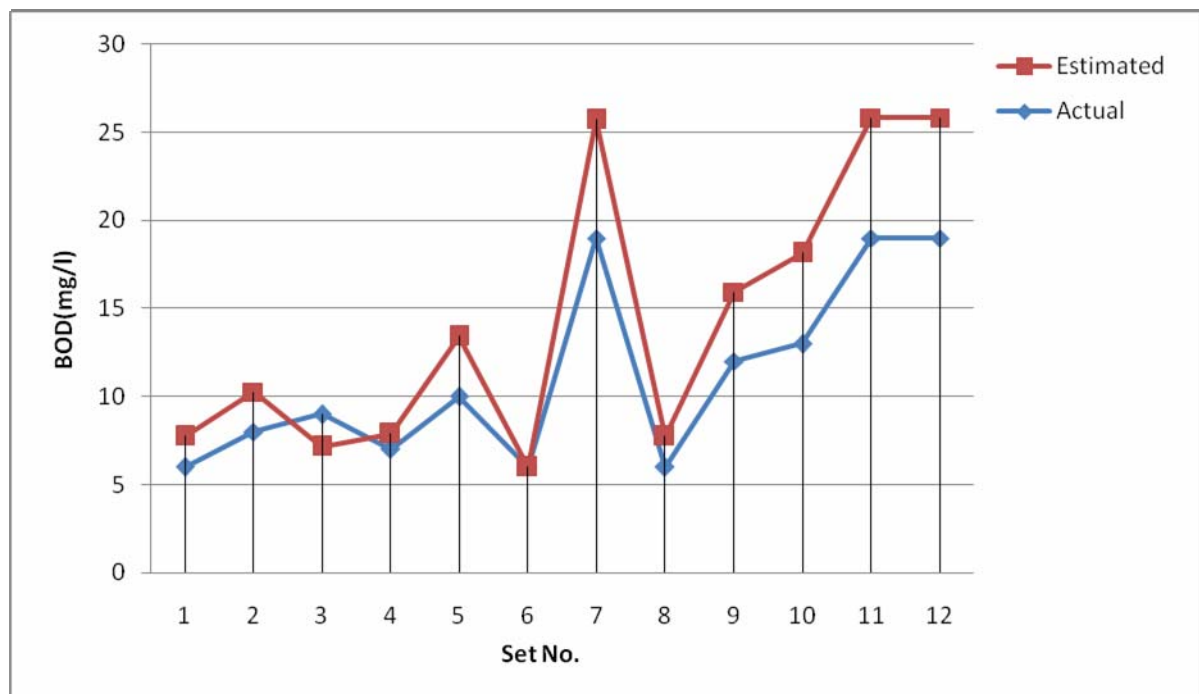


**Figure 4: BOD evaluation during the period under study  
(Second set of data - Evaluation)**





## Database for Baghdad Soil Using GIS Techniques

Athraa Hashim Mohammed

[athraram2004@yahoo.com](mailto:athraram2004@yahoo.com)

Lecturer

Asmaa Younus Yahya

[asmayounis2004@yahoo.com](mailto:asmayounis2004@yahoo.com)

Lecturer

Balqees Abdulwahid Ahmed

[baahe7@yahoo.com](mailto:baahe7@yahoo.com)

Lecturer

Civil Engineering Dept., College of Engineering, University of Baghdad, Iraq.

### Abstract

In this paper, assessing underground conditions and the engineering properties of the various strata of fourteen sites Baghdad are made. The sites are divided into two groups, one in Karkh and the other in Rusafa. Assessing the underground conditions can be occurred by drilling vertical holes called exploratory boring into the ground, obtaining soil (disturbed and undisturbed) samples, and testing these samples in a laboratory (civil engineering laboratory /University of Baghdad). From disturbed, the tests involved the grain size analysis and then classified the soil, Atterberg limit, chemical test (organic content, sulphate content, gypsum content and chloride content). From undisturbed samples, the test involved the consolidation test (from this test, the following parameters can be obtained: initial void ratio  $e_0$ , compression index  $c_c$ , swelling index  $c_s$ , coefficient of consolidation  $c_v$ , coefficient of volume change  $m_v$ , maximum preconsolidation stress  $\bar{P}_c$ , Effective overburden pressure  $\bar{P}_0$ ) and shear test (the following parameters can be obtained: undrained cohesion  $c_u$ , angle of friction  $\phi$ ).

In-situ testing was carried out by the standard penetration test in order to obtain the penetration resistance of the soil strata in a bore hole.

Database for Baghdad soils is made using different GIS techniques connecting the spatial locations of those soils with their properties (Atterberg Limits, Specific Gravity, Grain size Analysis, Shear Strength parameters, Consolidation parameters), Borehole log, Site profile using the attribute tables, hyperlinks, metadata and SQL (System Query Language), so GIS techniques give the facilities for adding, editing and analyzing the existing data as well as the any future data of Baghdad soils.

**Keywords:** Properties, Baghdad, soil, GIS, attribute table, hyperlinks, metadata.

### قاعدة البيانات لتربة بغداد باستخدام نظم المعلومات الجغرافية

بلقيس عبد الواحد احمد

مدرس

أسماء يونس يحيى

مدرس

عذراء هاشم محمد

مدرس

### الخلاصة:

في هذه المقالة، تم دراسة وتقييم الخواص الهندسية لطبقات التربة الخاصة لاربعة عشر موقعا في بغداد. المواقع قسمت الى مجموعتين احدها في الكرخ والآخرى في الرصافة. هذا التقييم حدث بحفر شاقولية تسمى بالحفر الاستكشافية في الارض، ومنها تم الحصول على نماذج مخلخلة وأخرى غير مخلخلة، ومن ثم أجرينا فحص هذه النماذج مختبريا (في مختبر العائد الى قسم الهندسة المدنية / جامعة بغداد). من فحص النماذج المخلخلة تم الحصول على تدرج الحبيبي للتربة، حدود الاتريبرك، الفحوص الكيماوية (محتوى المواد العضوية، محتوى املاح الكبريتات، محتوى الجبس ومحتوى الكلوريد) ومن فحص النماذج غير مخلخلة والتي يضم فحص الانضمام (من هذا الفحص تم استخراج نسبة الفراغات الابتدائية، مؤشر الانضغاط، مؤشر الانتفاخ، معامل الانضمام، معامل التغير الحجمي، اعلى اجهاد مسبق، ضغط الثقل الفعال) وفحص القص (من هذا الفحص تم الحصول على التماسك الغير مبزول، وزاوية الاحتكاك). في الموقع تم فحص الاختراق القياسي للحصول على مقاومة اختراق طبقات التربة في الحفرة.

لقد تم عمل قاعدة البيانات لتربة بغداد باستخدام نظم المعلومات الجغرافية والذي تم من خلاله الربط بين المواقع المكانية لحفر الاختبار وكافة المعلومات الخاصة بالتربة والتي تتضمن ( حدود الاتريبرك، الوزن النوعي، التدرج الحبيبي، معاملات قوى القص، ومعاملات الانضغاط)، وحفر الاختبار التي تمثل طبقات التربة ومواصفاتها، ومقطع لطبقات الارض باستخدام جداول الخاصية، الارتباطات التشعبية، وبيانات الميتا وتقنية لغة استفسار النظام، ولهذا فان نظام المعلومات الجغرافية يقدم التسهيلات والامكانيات لاضافة وتعديل وتحليل المعلومات الموجودة حاليا والمعلومات المستقبلية لكل ما يخص تربة بغداد.

#### الكلمات الرئيسية:

الخواص، بغداد، تربة، نظم المعلومات الجغرافية، جدول الخاصية، الارتباطات التشعبية، وبيانات الميتا.

## Introduction

Engineers classify earth materials into two broad categories: rock and soil. Although both materials play an important role in foundation engineering, most foundations are supported by soil. In addition, foundations on rock are often designed much more conservatively because of the rock's greater strength, whereas economics prevents overconservatism when building foundations on soil. Therefore, it is especially important for the foundation engineer to be familiar with soil mechanics.

One of the fundamental differences between soil and most other engineering material is that it is a particulate material. This means that it is an assemblage of individual particles rather than being a continuum (a continuous solid mass). The engineering properties of soil, such as strength and compressibility, are dictated primarily by the arrangement of these particles and the interactions between them, rather than by their internal properties (Coduto, 2001).

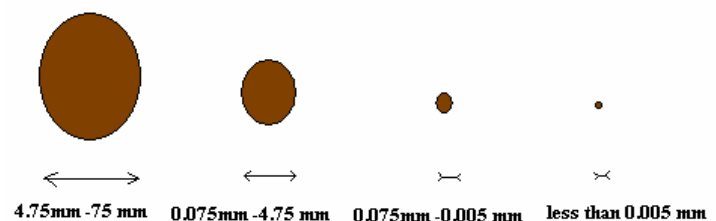
A geographic information system (GIS) is a computer-based tool for mapping and analyzing spatial data. GIS technology integrates common database operations such as query and statistical analysis with the unique visualization and geographic analysis benefits offered by maps. These abilities distinguish GIS from other information systems and make it valuable to a wide range of public and private enterprises for explaining events, predicting outcomes, and planning strategies. GIS is considered to be one of the most important new technologies, with the potential to revolutionize many aspects of society

through increased ability to make decisions and solve problems

## Soil Classification Systems

Soil classification systems divide soils into groups and subgroups based on common engineering properties such as the grain-size distribution, liquid limit, and plastic limit. The two major classification systems presently in use are (1) the American Association of State Highway and Transportation Officials (AASHTO) system and (2) the Unified Soil Classification System (USCS) (Das, 2007).

According to the Unified Soil Classification System, Soils are classified as follows (University of St. Thomas, 2009):



Generally, soils consist of a mixture of different particle types, such as "sandy clay", or a "silty sand".

## Atterberg Limit

When a clayey soil is mixed with an excessive amount of water, it may flow like a semi-liquid. If the soil is gradually dried, it will behave like a plastic, semisolid, solid material, depending on its



moisture content. The moisture content, in percent, at which the soil changes from a liquid to a plastic state is defined as the liquid limit (LL). Similarly, the moisture content, in percent, at which the soil changes from a plastic to a semisolid state and from a semisolid to a solid state are defined as the plastic limit (PL) and the shrinkage limit (SL), respectively. These limits are referred to as Atterberg limits. The difference between the liquid limit and the plastic limit of a soil is defined as the plasticity index (PI) (Das, 2007).

$$PI = LL - PL$$

### Consolidation

In the field, when the stress on a saturated clay layer is increased- for example, by the construction of a foundation- the pore water pressure in the clay will increase. Because the hydraulic conductivity of clays is very small, some times will be required for the excess pore water pressure to dissipate and the increase in stress to be transferred to the soil skeleton.

From consolidation test, three parameters necessary for calculating settlement in the field can be determined. They are preconsolidation pressure ( $\bar{P}_c$ ), compression index ( $C_c$ ) and the swelling index ( $C_s$ ) (Das, 2011)

### Classification of Foundation

The term foundation is used to describe the structural elements that connect a structure to the ground. These elements are made of concrete, steel, wood, or perhaps other materials. Foundations will be divided into two board categories: shallow foundations and deep foundations, as shown in figure 1 (Coduto, 2001).

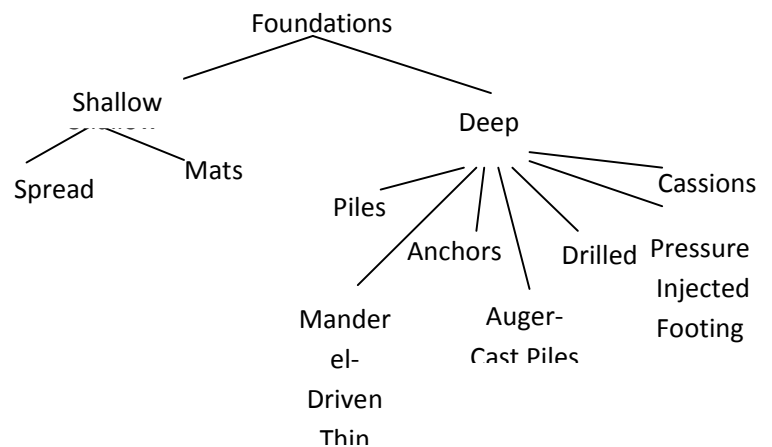


Figure 1 Classification of Foundations

### Effect of the Salts on The Soil

Sabkha soil is a rich soil with salt deposited which result from evaporation of water; it is one of the many types of the collapsible soils and in turn is one of the many types of problematic soils. This soil totally has good engineering properties when dry, i.e, moderately bearing capacity with low settlement. But once is wetted it loses its entire structure (collapse) and undergoes very large instantaneous settlement (Abbas, 2012).

### Estimation of Settlements from Standard Penetration Test (Spt)

Menzenbach, 1967 arrived at the conclusion of a relationship between the results of standard penetration tests to the deformation modulus of the soil. This relationship is shown in figure 2.

This relationship is shown for different values of the effective overburden pressure  $\bar{P}_o$  at the level of test. The values of deformation modulus are then used to calculate the immediate settlement. The Poisson's ratio ( $m$ ) should be taken as 0.15 for coarse- grained soils and 0.25 for fine- grained soils.

The calculations of net immediate settlement  $\Delta I$  (elastic settlement) beneath the corner of a flexible

loaded area is calculated from the following equation (Ghosh, 2010):

$$\Delta l = q_n \times B \times (I - m^2) (E_d \times I_p)$$

Where:

B= width of foundation ,  $E_d$ = deformation modulus,  
m= Poisson's ratio,  $q_n$  = net foundation pressure,  
 $I_p$  = influence factor.

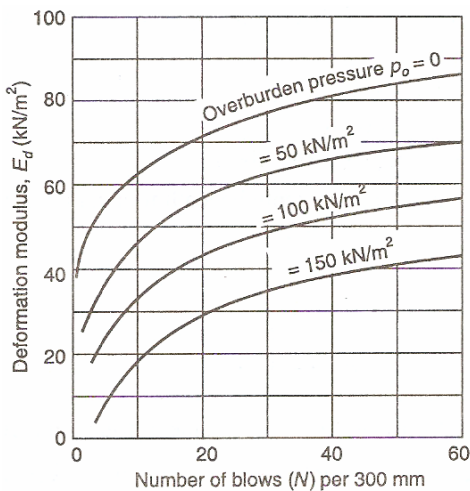


**Figure 2 Curves Showing the Relationship between Deformation Modulus and Standard Penetration Resistance (Prepared By Menzenbach)**

### Standard Penetration Test Correlations

The SPT has been used in correlations for unit weight  $\gamma_{wet}$ , relative density  $Dr$ , angle of internal friction  $\Phi$ , and undrained compressive strength  $qu$ , and that can be seen in tables 1 and 2 (Bowles,1996).

**Table 1 Empirical Values For  $\Phi$ ,  $Dr$  And Unit Weight of Granular Soils Based on the SPT at about 6 M Depth and Normally Consolidated**

Description	Very	Loose	Medium	dense	Very
Relative	0	0.15	0.35	0.65	0.85
SPT: fine	1-2	3-6	7-15	16-30	----
$\Phi$ : fine	26-28	28-30	30-34	33-38	< 50
$\gamma_{wet}$ ,kN/m3	11-16	14-18	17-20	17-22	20-23

**Table 2 Consistency of saturated cohesive soils**

consistency	Spt	$q_u$ ,kPa	Remarks
Very soft	0-2	< 25	Squishes between fingers when squeezed
Soft	3-5	25-50	Very easily deformed by squeezing
Medium	6-9	50-100	-----
Stiff	10-16	100-200	Hard to deform by hand squeezing
Very stiff	17-30	200-400	Very hard to deform by hand squeezing
Hard	> 30	> 400	Nearly impossible to deform by hand

### Components Of A Geographic Information System

A working Geographic Information System seamlessly integrates five key components: hardware, software, data, people, and methods.

**H A R D W A R E** Hardware includes the computer on which a GIS operates, the monitor on which results are displayed, and a printer for making hard copies of the results. Today, GIS software runs on a wide range of hardware types, from centralized computer servers to desktops computers used in stand-alone or networked configurations. The data files used in GIS are relatively large, so the computer must have a fast processing speed and a large

hard drive capable of saving many files. Because a GIS outputs visual results, a large, high-resolution monitor and a high-quality printer are recommended.

**S O F T W A R E** GIS software provides the functions and tools needed to store, analyze, and display geographic information. Key software components include tools for the input and manipulation of geographic information, a database



management system (DBMS), tools that support geographic query, analysis, and visualization, and a graphical user interface (GUI) for easy access to tools. The industry leader is ARC/INFO, produced by

Environmental Systems Research, Inc. The same company produces a more accessible product, ArcView, that is similar to ARC/INFO in many ways.

#### **D A T A**

Possibly the most important component of a GIS is the data. A GIS will integrate spatial data with other data resources and can even use a database management system, used by most organizations to organize and maintain their data, to manage spatial data. There are three ways to obtain the data to be used in a GIS. Geographic data and related tabular data can be collected in-house or produced by digitizing images from aerial photographs or published maps. Data can also be purchased from commercial data provider. Finally, data can be obtained from the federal government at no cost.

#### **P E O P L E**

GIS users range from technical specialists who design and maintain the system to those who use it to help them perform their everyday work. The basic techniques of GIS are simple enough to master that even students in elementary schools are learning to use GIS. Because the technology is used in so many ways, experienced GIS users have a tremendous advantage in today's job market (Chang, 2006).

#### **.How A GIS Works**

A GIS stores information about the world as a collection of thematic layers that can be linked together by geography. This simple but extremely powerful and versatile concept has proven invaluable for solving many real-world problems from modeling global atmospheric circulation, to predicting rural land use, and monitoring changes in rainforest ecosystems.

#### **GIS Tasks**

General purpose GIS's perform seven tasks.

- Input of data
- Map making
- Manipulation of data
- File management
- Query and analysis
- Visualization of results

#### **Input of Data**

Before geographic data can be used in a GIS, the data must be converted into a suitable digital format. The process of converting data from paper maps or aerial photographs into computer files is called digitizing. Modern GIS technology can automate this process fully for large projects using scanning technology; smaller jobs may require some manual digitizing which requires the use of a digitizing table

Today many types of geographic data already exist in GIS-compatible formats. These data can be loaded directly into a GIS.

#### **Map Making**

Maps have a special place in GIS. The process of making maps with GIS is much more flexible than are traditional manual or automated cartography approaches. It begins with database creation. Existing paper maps can be digitized and computer-compatible information can be translated into the GIS. The GIS-based cartographic database can be both continuous and scale free. Map products can then be created centered on any location, at any scale, and showing selected information symbolized effectively to highlight specific characteristics. The characteristics of atlases and map series can be encoded in computer programs and compared with the database at final production time. Digital products for use in other GIS's can also be derived by simply copying data from the database. In a large organization, topographic databases can be used as reference frameworks by other departments.

#### **Manipulation of Data**

It is likely that data types required for a particular GIS project will need to be transformed or manipulated in some way to make them compatible with your system. For example, geographic information is available at different scales (street centerline

files might be available at a scale of 1:100,000; census boundaries at 1:50,000; and postal codes at 1:10,000). Before this information can be integrated, it must be transformed to the same scale. This could be a temporary transformation for display

purposes or a permanent one required for analysis. GIS technology offers many tools for manipulating spatial data and for weeding out unnecessary data.

### File Management

For small GIS projects it may be sufficient to store geographic information as simple files. There comes a point, however, when data volumes become large and the number of data users becomes more than a few, that it is best to use a database management system (DBMS) to help store, organize, and manage data. A DBMS is nothing more than computer software for managing a database--an integrated collection of data.

### Query and Analysis

Once you have a functioning GIS containing your geographic information, you can begin to ask simple questions such as

- How far is it between two places?
- How is this particular parcel of land being used?
- What is the dominant soil type for oak forest?
- Where are all the sites suitable for relocating an endangered species?
- Where are all of the sites possessing certain characteristics?
- If I build a new highway here, how will animals in the area be affected? GIS provides both simple point-and-click query capabilities and sophisticated analysis

tools to provide timely information to managers and analysts alike. GIS technology really comes into its own when used to analyze geographic data to look for patterns and trends, and to undertake "what if" scenarios. Visualization For many types of geographic operations, the end result is best visualized as a map or graph. Maps are very efficient at storing and communicating geographic information. While cartographers have created maps for millennia, GIS provides new and exciting tools to extend the art and science of cartography. Map displays can be integrated with reports, three-dimensional views, photographic images, and with multimedia (Sutton, 2009).

### The Importance of Geographic Information Systems

The ability of GIS to search databases and perform geographic queries has revolutionized many areas of science and business. It can be invaluable during

a decision-making process. The information can be presented succinctly and clearly in the form of a map and accompanying report, allowing decision makers to focus on the real issues rather than trying to understand the data. Because GIS products can be produced quickly, multiple scenarios can be evaluated efficiently and effectively. For this reason, in today's world, the ability to use GIS is increasingly important (DeMers, 2005).

### Using GIS to Make the Database for Baghdad Soils

To make the database for Baghdad soils, the latest aerial photo of the city of Baghdad is prepared and Georeferenced as shown in figure (3). The boreholes locations are divided into two groups, one in Karkh (Ameriah, Arabjbour, , Sa'ediyah , Ghazaliyh, Mamoon , Bayaa, Kamalyah ,Dura-refinery and Mansour ) and the other in Rusafa (Wazeriya , Baladiat, , Sadr city, Aljaderiyah, , Zayuna) . Presentation for the locations is made in the arcmap by making two layers for boreholes, one in Karkh side and the other in Rusafa side.

Figure (4) shows the two layers as well as the layer of Baghdad aerial photo.

Description of each site location is represented in GIS techniques by metadata which is the part of the system where the detailed description for the abstract, purpose, status of the data, time period for the data is relevant, etc. the description of the site location can be seen in figures (5) and (6).

### Laboratory Test

After drilling the vertical holes into the ground, the disturbed and undisturbed samples are obtained. From disturbed samples, the tests involved the grain size analysis and then classified the soil (according to BS 1377), Atterberg limit is performed according to (BS 1377:1975, Test 2(B)) , chemical test (organic content (OR %), sulphate content (SO<sub>3</sub>%), chloride content (CL%) (according to BS 1377) ((Head, 1980), gypsum content (according to the following equation (gypsum content = SO<sub>3</sub>% ×





2.15) (Al-Mufti , 1997) and Total soluble salts content (T.S.S%) (Earth Manual,E8) (Earth Manual, 1974). From undisturbed samples, the test involved the consolidation test (from this test, the following parameters can be obtained: initial void ratio  $e_0$ , compression index  $c_c$ , swelling index  $c_s$ , coefficient of consolidation  $c_v$ , coefficient of volume change  $m_v$ , maximum preconsolidation stress  $\bar{P}_c$ , Effective overburden pressure  $\bar{P}_o$ ) (according to BS 1377:1975) (Head, 1982) and shear test (the following parameters can be obtained: undrained cohesion  $c_u$ , angle of friction  $\phi$  (ASTM , D2166) (Head, 1982). For example, the soil properties of Al- Ghazaliyah (in Karkh group) are shown in tables (3), (4), (5) and (6).

All the above is represented in the GIS technique as shown in figure (7), (8), and (9). These figures show the potentials and facilities that GIS produce to connect between the spatial location of the boreholes and their computations, analyses and results, so by clicking any point which represents the location of any borehole in any site of the fourteen test sites, all the information about Atterberg Limits, Specific Gravity, Grain size Analysis, Shear Strength parameters, Consolidation parameters, Borehole log, Site profile can be obtained by using the hyperlink technique.

By analyzing the above parameters, the design parameters of Ghazaliyah site are concluded and these parameters can be presented in table (7)

Managing the table above in the system in figure (10) which shows the attribute table containing the table information but in this case it is spatially connected.

Another example in Rusafa group is Al-Baladiat site, the soil properties, borehole log, the site profile and the design parameters are represented by GIS in figures (11), (12), (13) and (14).

By using the SQL (System Query Language), the sites those have bearing capacity less than 100 kpa

are obtained in Karkh and Rusafa as shown in figures (15) and (16)

#### NOTE:

- The detailed applications of the research using the GIS are in the attendant CD. Uploading of the ARCGIS 9.3 or 10 is needed.
- The information in CD must be placed in D partitions in the hard disk of the computer.

#### Conclusion

From the previous results, the parameters design for Baghdad soils in general can be shown as the following:

- Bearing capacity (1.0-3.0) m equal to (90-110) kpa
- Compression Index = 0.106 – 0.465
- Swelling Index = 0.005- 0.046
- Initial Void Ratio = 0.68 -1.068
- Saturated Unit Weight = 20 kN/m<sup>3</sup>
- Submerged Unit Weight = 10 kN/m
- Undrained cohesion,  $c_u$  = 40 -55 kPa
- Angle of friction = (28 -30) degree
- Factor of safety for bearing capacity = 3
- The above conclusions can be represented in GIS in figure 17
- In Karkh, Ghazaliyh and Al- Sa'ediyah have bearing of capacity less than 100 kpa
- In Rusafa, Al-Baladiat has bearing of capacity less than 100 kpa

#### References

- Al-Mufti, A.A., "Effect of Gypsum Dissolution on the Mechanical Behavior of Gypseous Soils" Ph.D. Thesis, Civil Engineering Department, University of Baghdad, 1997.
- Abbas, H. O., "Improvement of Sabkha Soil by Using Geomesh and Addition of Poly Coat, 2012.
- Bowels, J. E., "Foundation Analysis and Design", Fifth Edition, the McGraw- Hill Companies.
- Chang, K. T., "Introduction to Geographic Information Systems", Third Edition. McGraw, 2006.

- Coduto, D. B., "Foundation Design, Principles and Practices", second Edition, 2001.
- Das, B.M., "Principles of Geotechnical Engineering", fifth edition, 2007.
- Das, B. M., "Principles of Foundation Engineering", Seven edition, 2011.
- Das, B. M., "Principles of Foundation Engineering", Six edition, 2007.
- DeMers, M. N., "Fundamentals of Geographic Information System", Third Edition, Wily, 2005.
- Earth Manual, U.S., "Department of the Interior Bureau of Reclamation" Second Edition, Washington, 1974.
- Ghosh, M. G., "Foundation Design Practice", 2010.

- Head, K.H., "Manual of Soil Laboratory Testing". Vol. 1, Prentch, press, London, 1980.
- Head, K.H., "Manual of Soil Laboratory Testing". Vol. 2, Prentch, press, London, (1982)
- Menzenbach, E., Le Capacidad soportante de pilotes y grupos pilotes, Tecnologia (Ingenieria Civil) series 2, No. 1, pp. 20-21, Aavana University, Cuba, 1967.
- Sutton, T., "a Gentle Introduction to GIS", 2009.
- University of Thomas, "an Introduction to Soils", 2009.

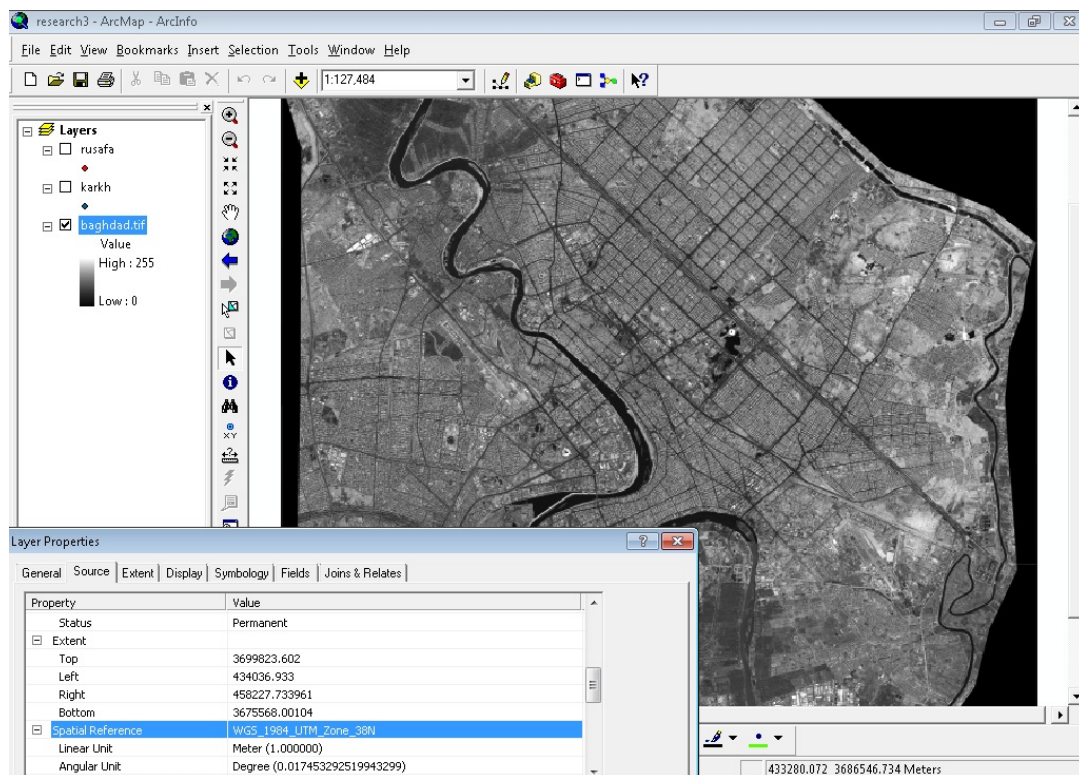


Fig.3 Latest Georeferenced Aerial Photo of Baghdad city





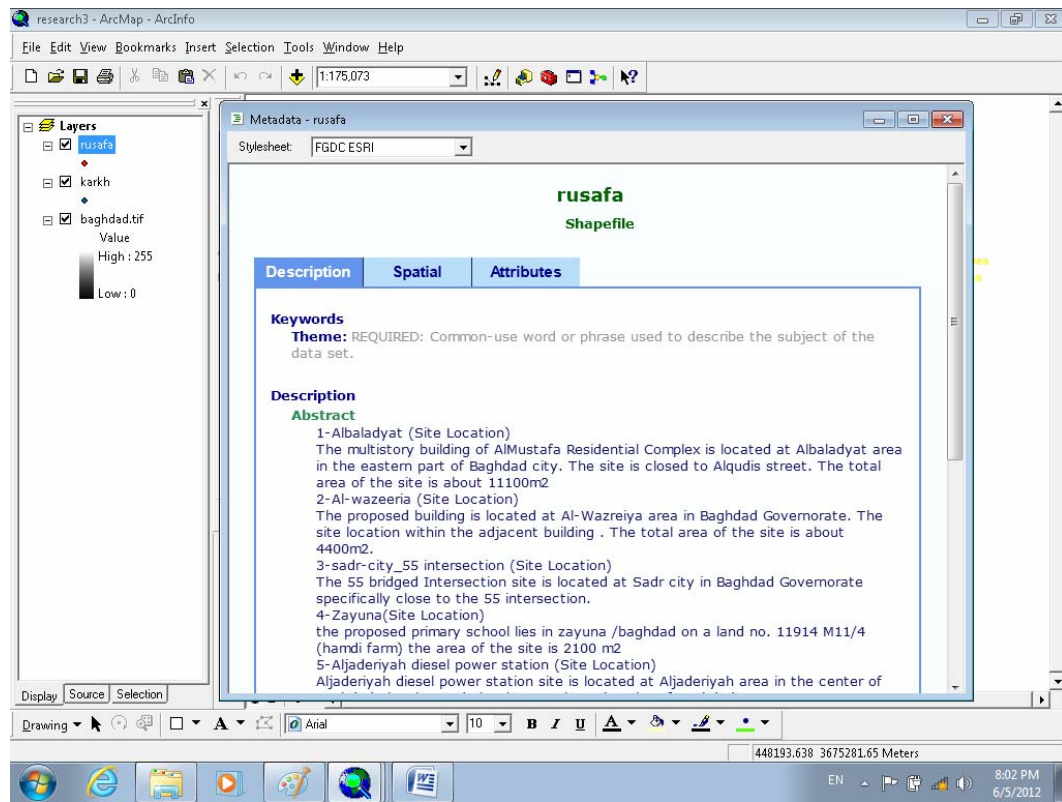


Fig. 6 Metadata of Rusafa

Table 3: Results of Atterberg Limits, Specific Gravity & Grain size Analysis

B.H. No.	Depth (m)		Soil Classification and Identification											
	From	To	$\omega_n$ %	Gs	Atterberg Limits			Consistency		USCS	Sieve and Hydrometer			
					LL	PL	PI	A	LI		Gravel	Sand	Silt	Clay
1	0.0	1.5		2.76	40	18	22	0.523		CL	0	10	37	53
	1.5	2.0	26.00											
	2.0	2.5	20.33	2.72	42	19	23		0.058	CL				
	4.5	5.0	22.22											
	5.0	5.5	26.14		45	20	25		0.246	CL				
	5.5	7.0			40	19	21			CL				
	7.0	7.5	23.20											
	7.5	8.0	31.42	2.73	39	20	19	2.111	0.601	CL	0	25	59	16
	9.5	10.0	33.17											
2	0.0	1.5		2.70										
	2.0	2.5	23.92	2.76	45	19	26	0.742	0.189	CL	0	11	40	49
	4.5	5.0	25.10	2.75										
	5.0	5.5	22.78		44	20	24		0.116	CL				
	5.5	7.0		2.77	38	18	20	0.909		CL	0	22	46	32
	7.0	7.5	23.61											



B.H. No.	Depth (m)		Soil Classification and Identification											
	From	To	$\omega_n$ %	Gs	Atterberg Limits			Consistency		USCS	Sieve and Hydrometer			
					LL	PL	PI	A	LI		Gravel	Sand	Silt	Clay
	9.5	10.0	24.70											
3	0.0	1.5		2.77	57	26	31	0.596		CH	0	10	28	62
	1.5	2.0	25.71											
	2.0	2.5	22.95	2.74	40	18	22		0.225	CL				
	4.5	5.0	24.04	2.78										
	5.0	5.5	25.92		46	20	26		0.228	CL				
	5.5	7.0			38	19	19			CL				
	7.0	7.5	24.90											
	7.5	9.5			38	18	20			CL				
	9.5	10.0	26.75	2.70	NP	NP	NP				0	35	59	6

Where:

LI: Liquidity Index 
$$L.I. = \frac{\omega_n - P.L.}{P.I.}$$

A: Activity 
$$A = \frac{P.I.}{\text{clay fraction}}$$

LL: Liquid Limit

PL: Plastic Limit

PI: Plasticity Index

$\omega_n$  : Natural Water Content

Table 4: Results of Shear Strength Tests

BH No.	Depth (m)	$\gamma_t$ kN/m <sup>3</sup>	$\omega_n$ %	Shear Test		
				UCS kPa	Triaxial (UU)	
					C	$\phi^\circ$
1	1.5-2.0	21.27	26.00	211.0	-	-
	4.5-5.0	19.76	22.22	-	72.5	0.0
2	4.5-5.0	19.87	25.10	-	60.0	0.0
3	1.5-2.0	19.96	26.00	327.5	-	-
	4.5-5.0	19.38	24.03	-	50.1	4.25

**Table 5: Results of Consolidation Test**

BH No.	Depth (m)	Parameters of Consolidation Test									
			$\omega_n$	$e_o$	$c_c$	$c_s$	$m_v$	$c_v$	$\bar{P}_c$	$\bar{P}_o$	OCR
2	4.5-5.0	19.68	25.10	0.747	0.200	0.028	0.264	6.03	125	49.98	2.50
3	4.5-5.0	19.96	24.04	0.726	0.182	0.030	0.100	9.93	250	55.31	4.52

**Table 6 Results of Chemical Analysis**

BH No.	Depth (m)		Soil					Water			
	From	To	O.C.	Cl	TSS	SO <sub>3</sub>	Gypsum	pH	Cl	SO <sub>4</sub>	TDS
1	0.0	1.5	2.7	400	6.1	1.8	3.87	6.9	600	2600	4276
	2.0	2.5	3.1	400	3.5	0.9	1.94				
	7.5	8.0	1.3	200	1.2	0.3	0.65				
2	0.0	1.5	2.9	400	5.7	1.7	3.66	6.8	400	2800	4156
	2.0	2.5	1.9	300	2.7	0.8	1.72				
	5.5	7.0	1.8	400	2.4	0.7	1.51				
3	0.0	1.5	2.6	400	5.1	1.6	3.44	7.0	450	2250	3108
	2.0	2.5	1.8	300	3.3	1.2	2.58				
	9.5	10.0	1.6	200	3.9	0.6	1.29				

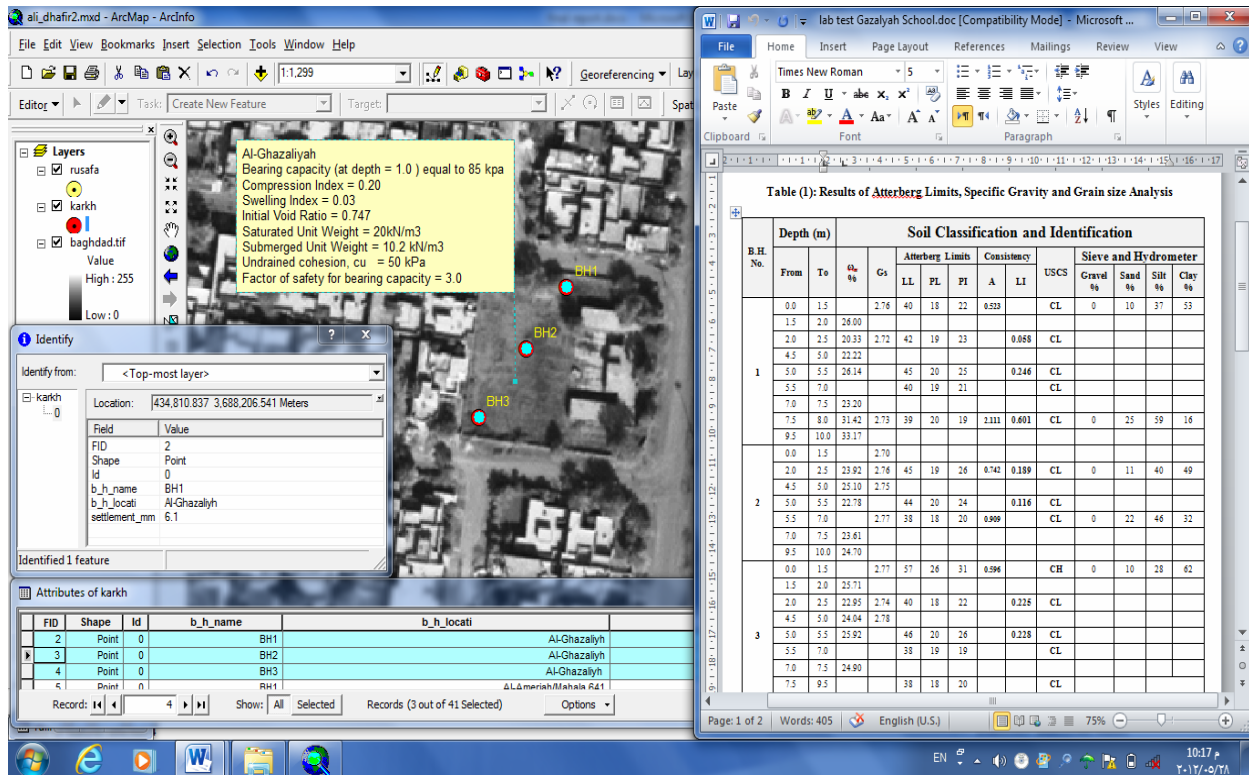


Fig. 7 Laboratory Test by GIS in Ghazaliyah

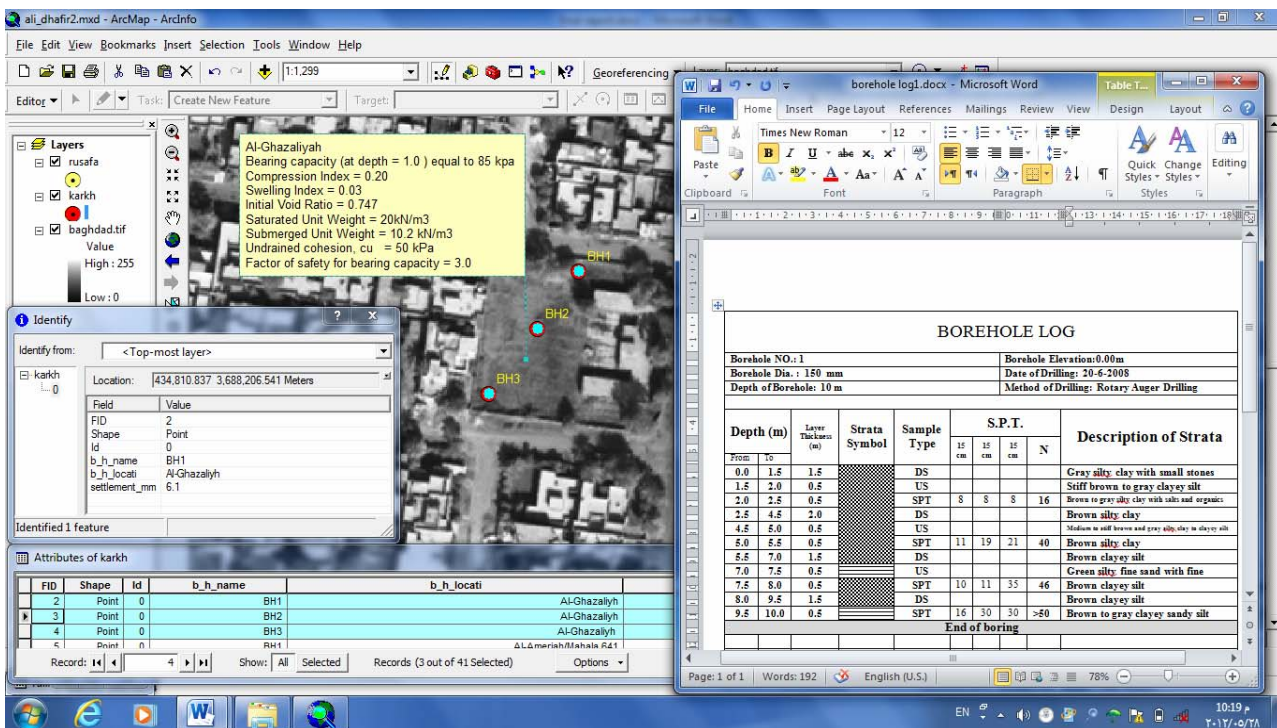


Fig. 8 Borehole Log by GIS in Ghazaliyah



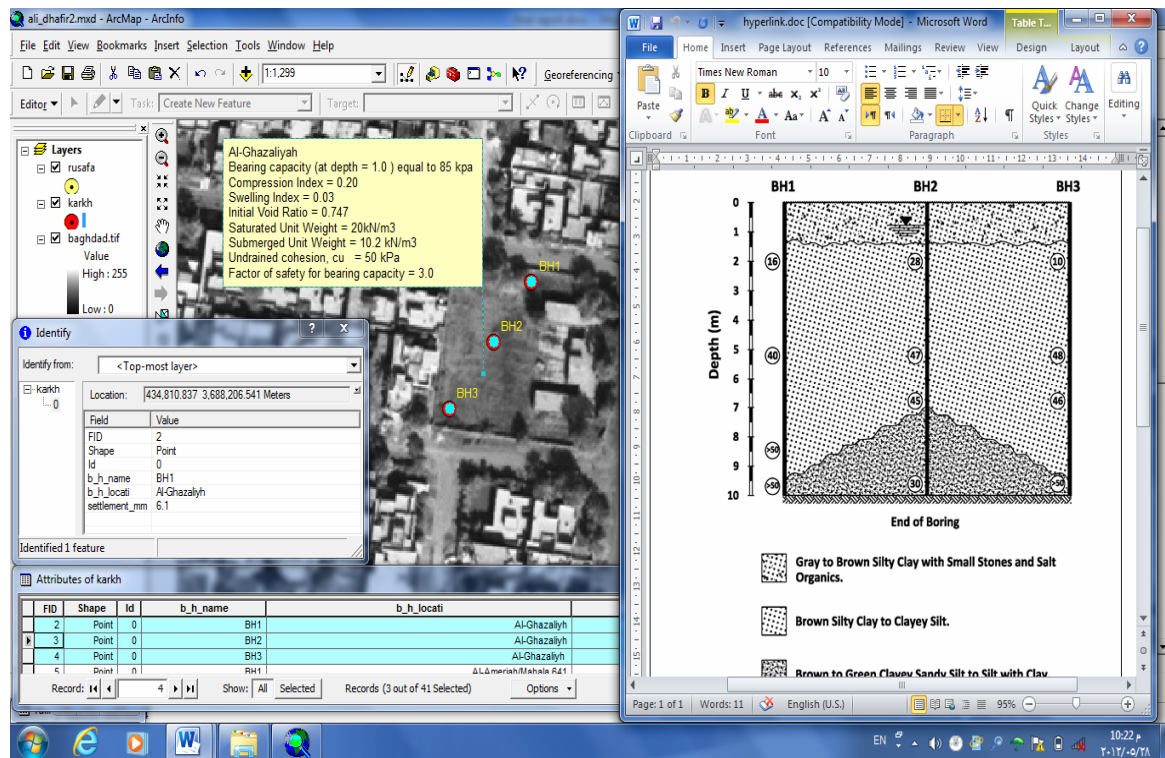


Fig. 9 Site Profile by GIS in Ghazaliyah

Table (7) Values of the Design Parameters for Ghazaliyah site

Bearing capacity (at depth = 1.0 )	85 kpa
Compression Index	0.20
Swelling Index	0.03
Saturated Unit Weight	0.747
Submerged Unit Weigh	20kN/m <sup>3</sup>
Undrained cohesion, $c_u$	50 kPa
Factor of safety for bearing capacity	3.0
Settlement	6.6mm

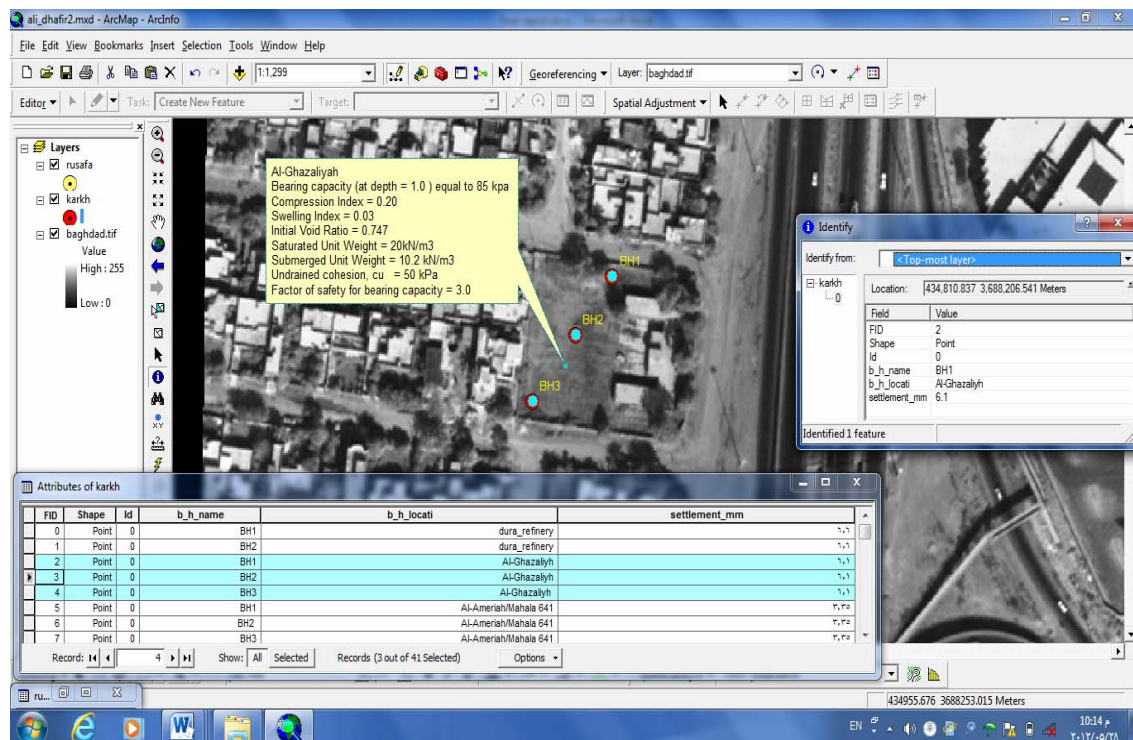


Fig.10 Values of the Design Parameters by GIS in Ghazaliyah

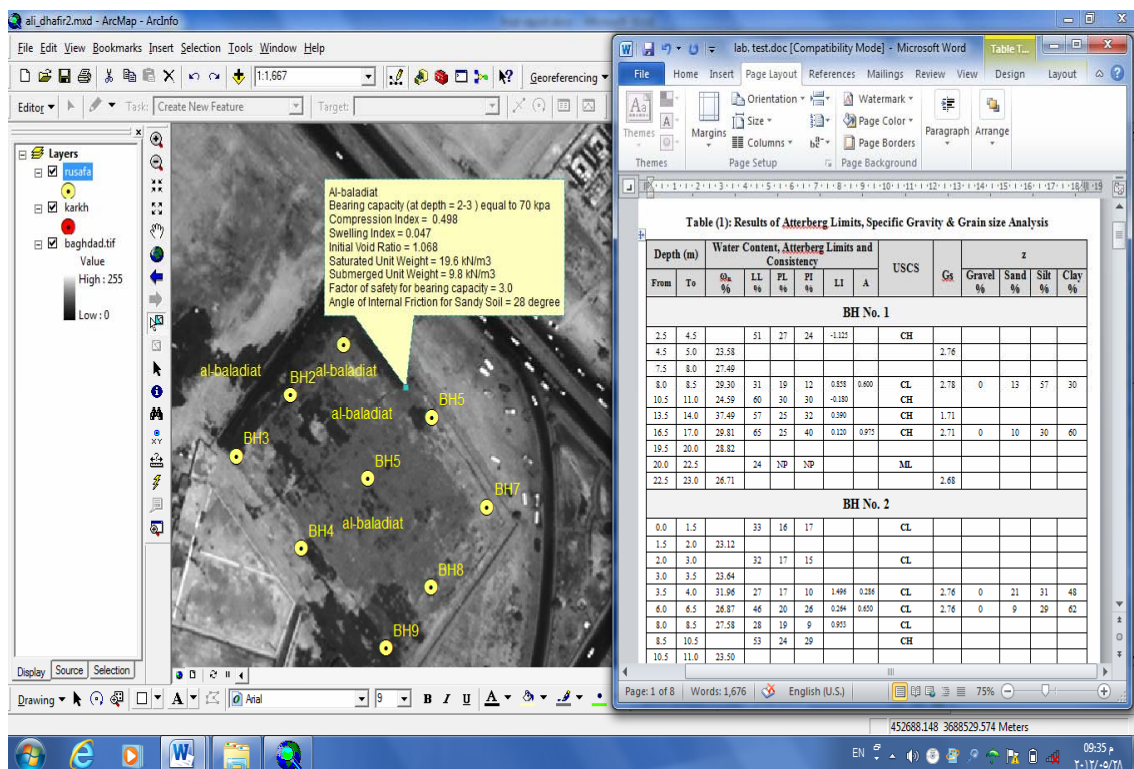


Fig. 11 Laboratory Test by GIS in Al-Baladiat

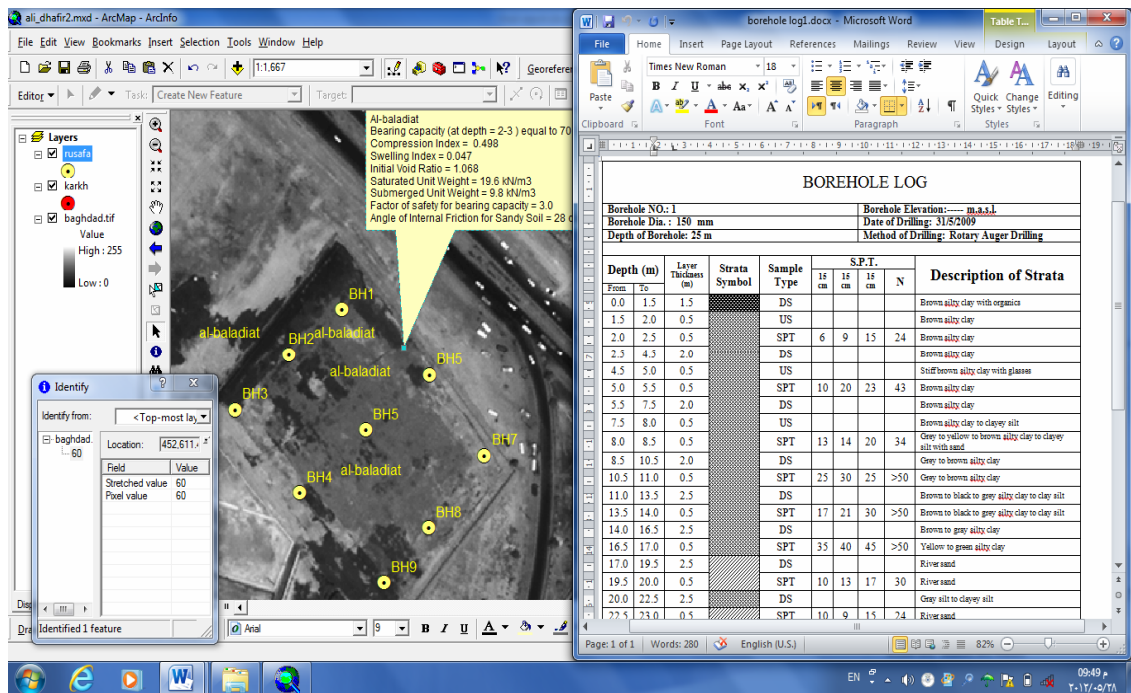


Fig. 12 Borehole Log by GIS in Al-Baladiat

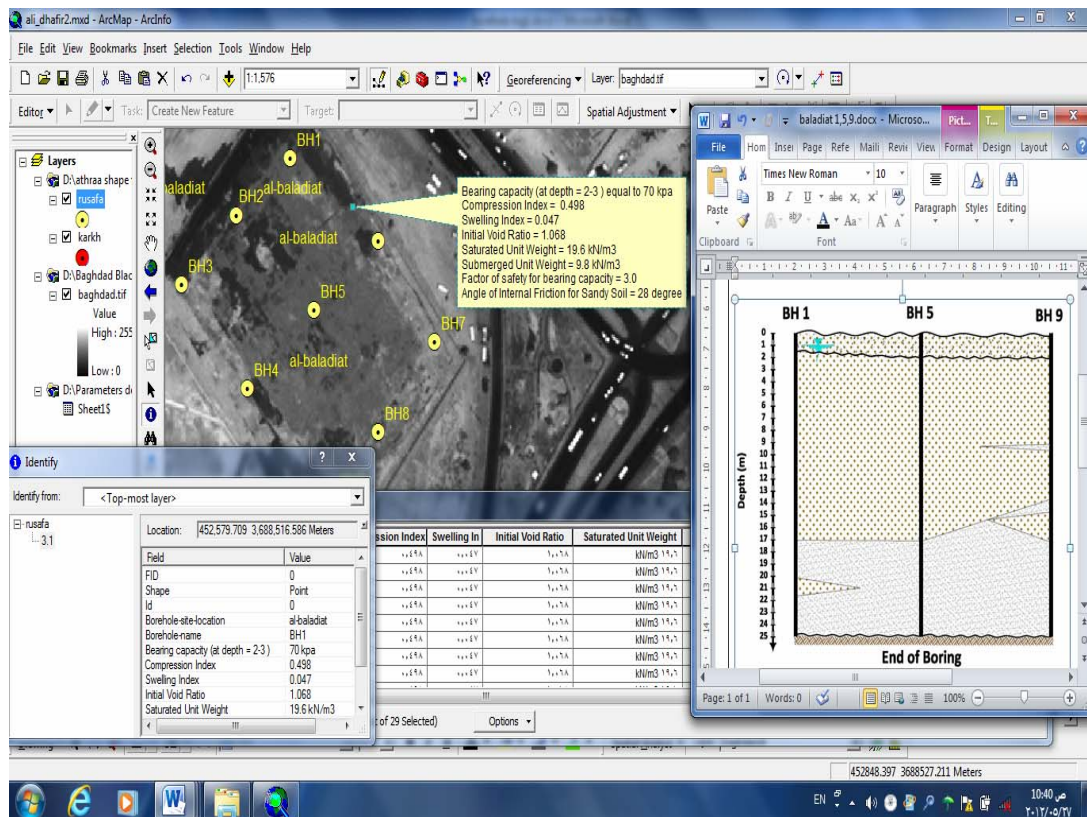


Fig. 13 SiteProfile by GIS in Al-Baladiat



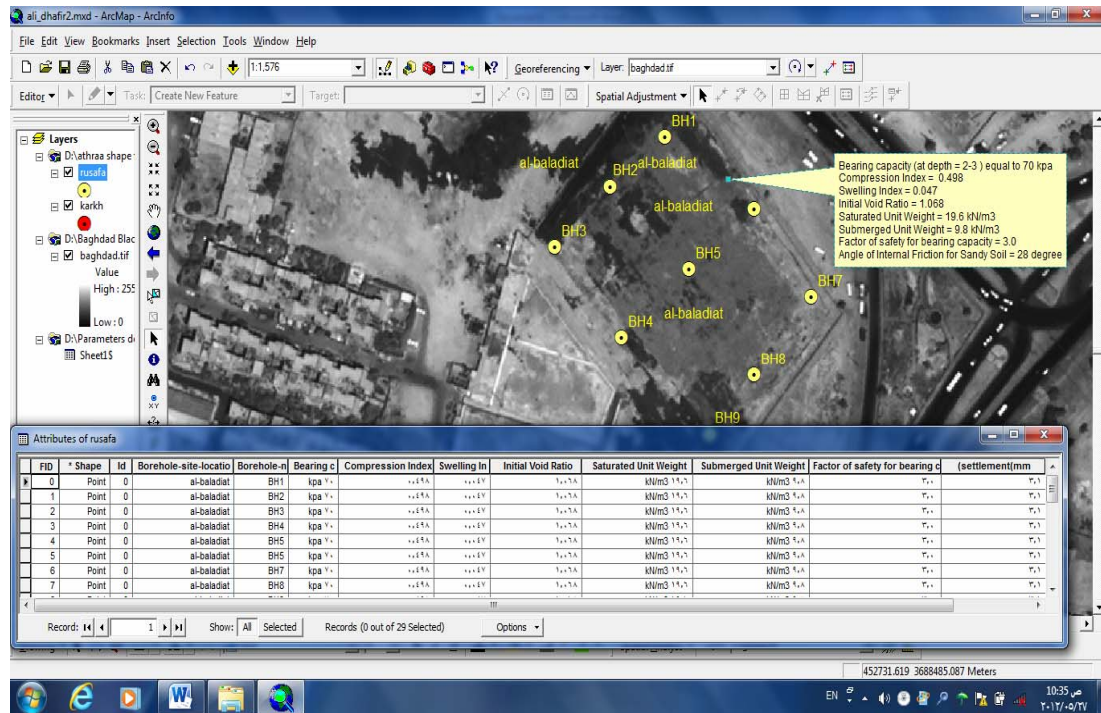


Fig. 14 Values of the Design Parameters by GIS in Al-Baladiat

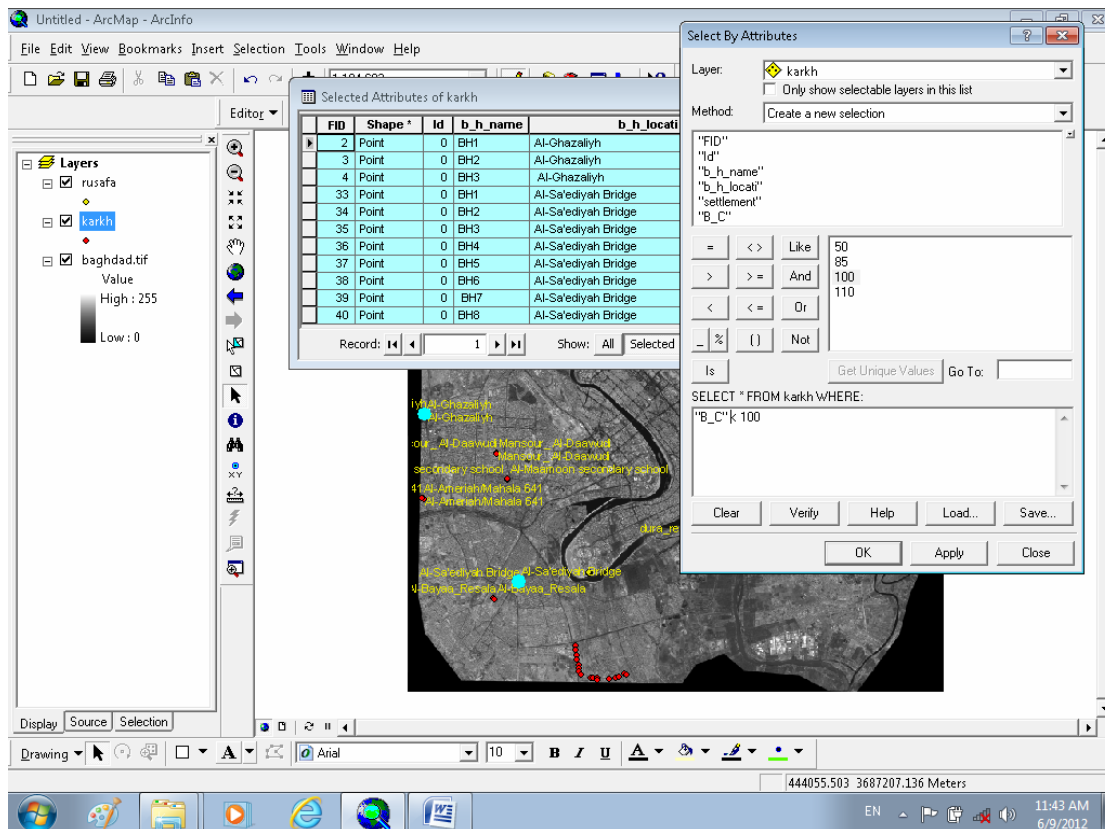


Fig. 15 Bearing Capacity Less than (100) kpa in Karkh

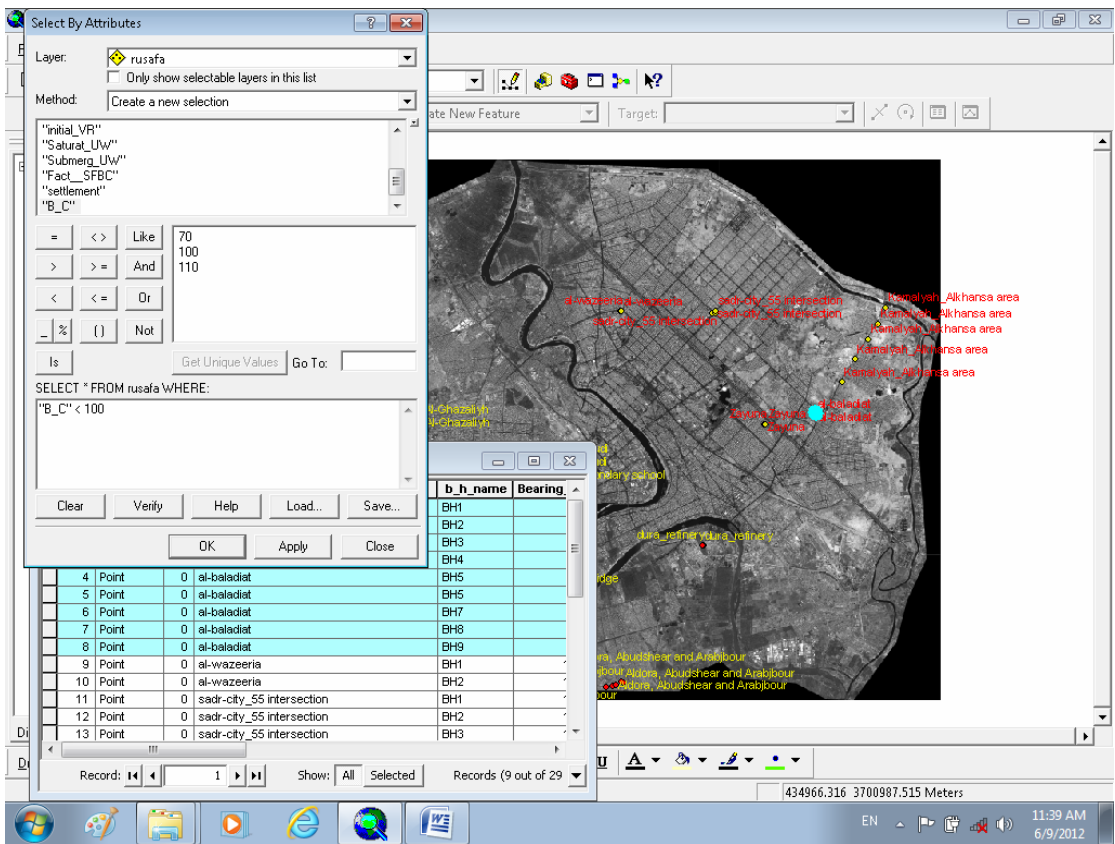


Fig. 16 Bearing Capacity Less than (100) kpa in Rusafa

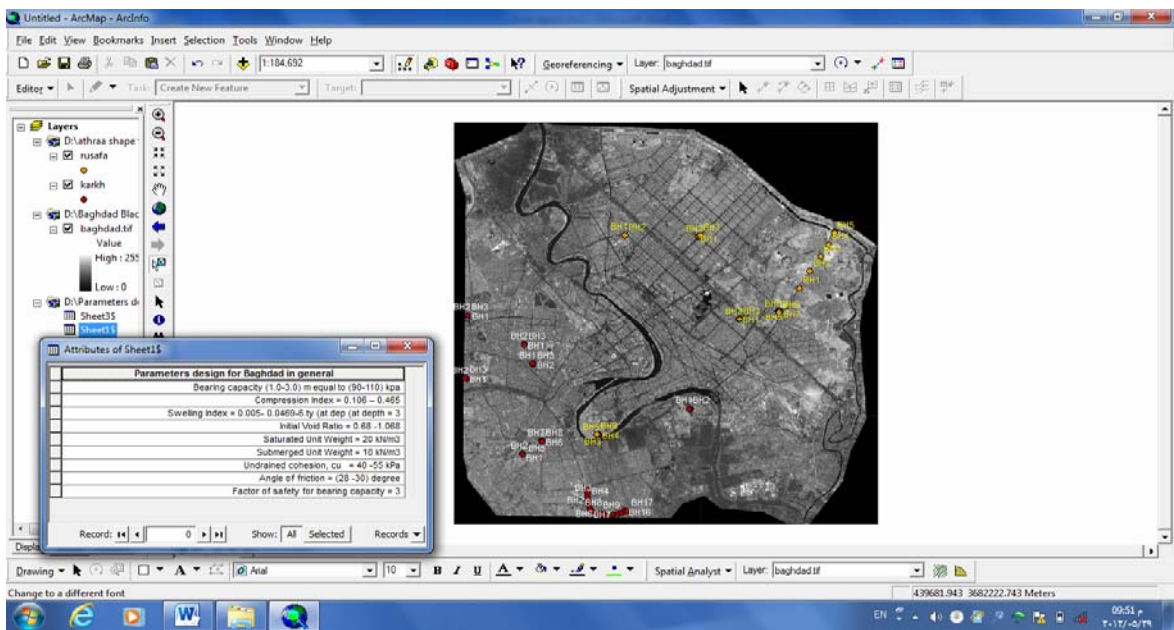


Fig.17 Design for Baghdad Soils in General



## Artificial Neural Network Model to Predict Sodium Adsorption Ratio for Tigris River in Amara

Zeren Jamal Ghafour and Prof. Dr. Rafa Hashim Al-Suhaili

### Abstract:

Water quality evaluation is important for its proper use. Water use for irrigation depends on its quality. One of the important factors that evaluate the suitability use of water for irrigation is the sodium adsorption ratio. In this research an attempt is tried to develop an ANN model to estimate the sodium adsorption ratio of Tigris river in Amara using Chloride (CL), Salinity (EC), and total dissolved solid (TDS).

Many ANN models are investigated with different subdivision of the data sets training, testing and holdout subsets, different number of nodes in the hidden layer, and different values of the learning rate and momentum term. The network model with the highest correlation coefficient between the predicted SAR and observed SAR values is selected. This network is with correlation coefficient of 0.963 with 4 nodes in the hidden layer, learning rate of 0.4, momentum term of 0.9, hyperbolic tangent and identity activation functions for the hidden and output layers respectively, and 47%, 26%, 27 % data subests division for training, testing and holdout respectively. The model then is considered capable to predict SAR values for the selected region. A normalized importance analysis was also done to investigate the effect of each independent variable on the dependent variable SAR, which shows that chloride has an effect of 100%, while EC and TDS have 20.4% and 12.8% respectively. The sequence of importance is found in accordance with the values of correlation coefficients obtained between SAR and these variables as, 0.961, 0.929, and 0.91 respectively.

**Key Words:** Artificial Neural Networks, Sodium Adsorption Ratio, Chloride, Electrical Conductivity, Total Dissolved Solids

### الخلاصة

ان تحليل نوعية المياه مهم جدا لتحديد الاستخدامات الملائمة له فاستخدام الماء لأغراض الري يعتمد على نوعيته . أن احد اهم محددات نوعية المياه هو نسبة امتزاز الصوديوم (Sodium Adsorption Ratio SAR) في هذا البحث تم نمذجة هذا المحدد باستخدام تقنية الشبكات العصبية الصناعية لتقدير كميته لمياه نهر دجلة في مدينة العمارة وباستخدام قياسات الكلوريد (Cl) و التوصيلية الكهربائية (EC) و الأملاح الذائبة الكلية (TDS) كمدخلات للنموذج.

تم اجراء العديد من محاولات النمذجة باستخدام مختلف النسب لتقسيم البيانات الى مجموعات التدريب ،الأختبار والبرهنة ومختلف القيم لعدد العقد العصبية في الطبقة المخفية و قيم معدل التعلم ومعامل الزخم ونوع دالتي التنفيل للطبقة المخفية وطبقة المعطيات.

تم اختيار القيم اعلاه للشبكة النهائية التي تعطي اعلى معامل ارتباط بين قيم المخمنة وتلك المقاسة. ان قيمة معامل الارتباط هذا كانت 0.963 مع عدد عقد للطبقة المخفية 4 ، معدل تعلم 0.4 ، معامل زخم 0.9 ونسبة تقسيم البيانات 47%، 26%، 27% الى مجموعة التدريب، الاختبار والبرهنة على التوالي. وعليه اعتبر النموذج هذا قادرا على تخمين قيم نسبة الأمتزاز للصوديوم في مياه دجلة عند مدينة العمارة. كما اجري التحليل القياسي لأهمية كل من متغيرات الأمدخال ووجد ان نسبة تأثير الكلوريد (Cl) 100% ونسبة تأثير التوصيلية الكهربائية (EC) والأملاح الذائبة الكلية (TDS) هي 12.8%، 20.4% على التوالي حيث تتطابق تسلسل الأهمية هذا مع قيم معامل الارتباط بين هذه المتغيرات ونسبة الأمتزاز للصوديوم والبالغة (0.91, 0.929, 0.961) على التوالي

## Introduction:

The sodium adsorption ratio classification of irrigation water is important to indicate the ability and extent of using this water for irrigation. In view of the water quality deterioration specially at the lower region of Tigris river , the water quality evaluation is an essential factor in the strategy of water use for irrigation projects. Nowadays , the role of water resources, and particularly rivers, as vital artery of each region is considered as one of the main bases for stable development (Oliai et. al, 2011). Hence, the prediction and evaluation of water quality parameters should be considered in a river. Knowledge of water quality provides the availability and possibility to use water in different ways in order to reduce the damages to the water resource.

The most important irrigation water quality parameters are the sodium adsorption ratio SAR and the electrical conductivity Ec. High SAR values causes undesirability of irrigation water (Michael et al 2008).

In recent years the ANN modeling had proved its capability to model many engineering phenomenon. Many prediction models had been used utilizing the technique of artificial intelligence. One of the most used artificial neural network models used in water resources and hydrology, is the multi-layers perceptron MLP model with feed- forward process and Back propagation algorithm for error adjustment. (Sarani et al 2012 ), had made a comparison of such model with multivariate linear regression modeling to predict SAR values using EC, Cl, pH, and TDS

values for Kohak Dam , located on river Sistan. They concluded that the MLP neural network model Had performed better than the multiple linear regression MLR model. (Palani et. Al 2009 ), had used artificial neural network model to predict the Dissolve Oxygen in Singapore sea water at the mouth of the east Johor Strait. The model used many water quality parameter as input for predicting the DO values. These variables are Salinity, pH, Nitrate, phosphate ....etc. They concluded that the model can predict the DO values with satisfactory accuracy. (Kanani et. al. 2008 ), had used artificial neural networks to model the total dissolved solids in Achechy River basin in east Azerbaijan. The model predict future TDS values using past TDS values and Discharge values as input data. ( Talib et. al, 2009 ) had used artificial neural network model to predict the Biochemical Oxygen Demand BOD of Sungai Pinang river in Malaysia. The input data are the physical and chemical properties of the river water. The model had proved its capability of prediction, with Phosphate as the most important variable that has an effect on BOD. (Hore et. al 2008 ) , had investigated the effect of water channel parameters on river contamination in India. The model had been a successful tool for prediction.

The most architecture of the MLP neural network model used in water quality prediction is the three layers neural network. The input layer, one hidden layer and the output layer. In these models the input layer has a number of nodes that equal to the input variables, while the output layer has a number of nodes that equal to the output variables. The number of nodes in the hidden layer is usually obtained by a trial and error procedure. The



available data set should be divided into training, testing and holdout subsets. The percent of division is also a matter of a trial and error procedure. The training set is used for training the network. The variables between the layers are connected by a weight matrices. These matrices are assumed first and the corrected. Using the assumed weight matrices and the training data set the input variables are assembled using linear weighted summation process and a bias term is added. Then this sum of each node in the hidden layer is processed using an activation function to result an output from the hidden nodes, which a similar linear summation with the bias term is used, but using the weight matrix between the hidden layer and the output layer to produce inputs to the nodes of the output layer which then processed with activation function to produce outputs. This process is known as the feed forward process. The outputs are then compared with the measured values and error is obtained. These errors are then used to adjust the weight matrices and the process is then repeated for another set of the input output variables of the training set using certain optimization algorithm, such as steepest gradient method. The weight matrices are further adjusted using the testing set to obtain the final weight matrices of the model. Then the model is evaluated using the hold out test to obtain the correlation coefficient between the predicted and observed values (Sarani et al 2012).

So many types are available for the activation function such as linear(identity), sigmoid, and hyperbolic tangent....etc. It is not necessary that the hidden layer and the output layer has the same activation functions, the most suitable combination is to be obtained using a trial and error procedure (Sarani et al 2012). Moreover the weight correction procedure equations in the back propagation algorithm has coefficients known as learning rate and momentum term, which also are changed using a trial and error procedure. The final value of the model parameters that to be obtained

by trial and error solution are the measure of the accuracy of the predicted values obtained by the correlation coefficient or the mean square error MSE. Fig (1) shows a three layer neural network model with three input variables ( $X_1, X_2, \dots, X_n$ ,  $n=3$ ), and four hidden nodes ( $Z_1, Z_2, \dots, Z_p$ ,  $P=4$ ), and one output node in the output layer ( $Y_1, \dots, Y_m$ ), where  $n$  is the number of hidden nodes in the input layer,  $P$  is the number of hidden nodes in the hidden layer and  $m$  is the number of the output nodes in the output layer.  $X_i$  is input variables vector ( $i=1, n$ ) and  $Y_k$  is the output variables vector ( $k=1, m$ ) and  $Z_j$  is the hidden node vectors ( $j=1, p$ ). The hidden node vector is subdivided into two vectors  $Z_{in j}$  which is the vector input to the hidden nodes and  $Z_{out j}$  which is the vector output from the hidden nodes. Using these notations the weight matrices between the input and the hidden layers and that between the hidden and output layers, are  $V\{n, p\}$  and  $W\{p, m\}$  respectively. The matrix equations for the feed forward process will be:

$$Z_{in}\{p, 1\} = V_o\{p, 1\} + V\{n, p\}^T X\{n, 1\} \quad (1)$$

Where  $V_o$  is the assumed bias matrix of the input layer, and

$$Z_{out}\{p, 1\} = F_1(Z_{in}\{p, 1\}) \quad (2)$$

Where  $F_1$  is the activation function of the input layer

$$Y_{in}\{m, 1\} = W_o\{m, 1\} + W\{p, m\}^T Z_{out}\{p, 1\} \quad (3)$$

Where  $Y_{in}$  is the vector input to the nodes of the output layer

$$Y_{out}\{m, 1\} = F_2(Y_{in}\{m, 1\}) \quad (4)$$

Where  $Y_{out}$  is the output vector,  $F_2$  is the activation function of the output layer

For the correction of the weight matrices the following steps and equations can be used:

$$\Delta y\{m, 1\} = [t\{m, 1\} - Y_{out}\{m, 1\}] \cdot F_2'(Y_{in}) \quad (5)$$



Where  $F_2'$  is the first derivative of the output layer activation function and the multiplication process is an element by element one, then

$$WoCorr\{m,1\}=Woass\{m,1\}+\alpha. Dy\{m,1\} \quad (6)$$

Where  $Wocorr$  and  $Woass$  are the corrected and assumed bias matrices of the input layer respectively, and  $\alpha$  is the learning rate.

$$Dw\{p,m\}=\alpha. Zout\{p,1\} Dy\{m,1\}^T \quad (7)$$

Where  $Dw$  is the correction matrix of the weight matrix between the input and the hidden layers, and  $T$  hold for transpose matrix operation, then

$$W\{p,m\}corr=W\{p,m\}ass + Dw\{p,m\} \quad (8)$$

Where  $Wcorr$  and  $Wass$  are the corrected and assumed matrices between the input and hidden layers.

$$Din\{p,1\}=W\{p,m\}ass.Dy\{m,1\} \quad (9)$$

And

$$Dz\{p,1\}=Din\{p,1\}.F_1'(Zin)\{p,1\} \quad (10)$$

Where  $Dz$  is output layer correction matrix and  $F_1'$  is the first derivative of the hidden layer activation function. The multiplication process is an element by element one, then

$$DVo\{p,1\}=\alpha.Dz\{p,1\} \quad (11)$$

$$Vocorr\{p,1\}=Voass\{p,1\}+DVo\{p,1\} \quad (12)$$

Where  $Vocorr$  and  $Voass$  are the corrected and assumed bias vector of the input layer, and

$$DV\{n,p\}=\alpha.X\{n,1\}.DZ\{p,1\}^T \quad (13)$$

$$V\{n,p\}corr=V\{n,p\}ass+DV\{n,p\} \quad (14)$$

Where  $Vcorr$  and  $Vass$  are the corrected and assumed weight matrices between the input and hidden Layer.

## **Artificial Neural Network Model To Predict Sodium Adsorption Ratio for Tigris River in Amara**

Each pass of a set of input-output through the listed equation above is called an epoch.

### **Study Area and Data Analyzed:**

The data for water quality used in this research is that of Tigris river in AMMARA city located south of Iraq. The water quality is deteriorated and characterized by high salinity due to upstream agricultural and municipal activities. Many disposal points of these pollution sources exist upstream of the point of measurement. The set of data used for analysis extend for 30 years (1979-2009) and measured by the Ministry of water Resources in Iraq. Water quality parameters were measured such as pH, EC, TDS, Ca, Mg, Na, K, Cl, SO<sub>4</sub>, Th, NO<sub>3</sub>, CO<sub>3</sub>, and HCO<sub>3</sub>, i.e, Acidity, electrical conductivity, total dissolved solids, calcium, magnesium, sodium, potassium, chloride, sulphate, total hardness, nitrate, carbonate, and hycarbonate, respectively.

The Sodium adsorption ratio is calculated from eq. (15) as:

$$SAR = [Na+] / \{([Ca^{2+}] + [Mg^{2+}]) / 2\}^{1/2} \quad (15)$$

The neural network model used for predicting the SAR values utilize only input values of EC, Chloride Cl and TDS. The Spss Version 19 software is used for the modeling process. Using this software many neural networks are investigated with different data subdivision, different types of activation functions for the hidden and output layers, different numbers of nodes in the hidden layer and different values of the learning rate and momentum term. The network with the highest correlation coefficient is selected for prediction of SAR values.

### **Results and Discussion:**

Before application of the ANN modeling, the data are checked and reduced to full measurements cases only, i.e., if any set of the data of the water quality parameters measured in a certain date has missing value or values the whole set is removed and only



the complete sets are considered in the analysis. The complete data set reached 140. Table(1) shows the descriptive statistics of the data for those variables used in the ANN model. The highest variance obtained is for the EC, while the lowest is for the SAR values. The differences in means between the variables is relatively high, hence this will justify the use of standardized variables instead of the original in the ANN modeling in order to avoid the order of magnitude effect. The standardization process of each variable is obtain by subtracting the mean value and dividing by the standard deviation of this variable, which transform the data to a zero mean and unit variance sets.

Table (2) shows the correlation matrix of all measured water quality parameters. The last column in this table indicates the correlation coefficients between the dependent variable SAR with the other variables. It is shown that the highest correlations with SAR are (0.961,0.957,0.929,and 0.91) with chloride (CL),sodium (Na),electrical conductivity(EC), and Total Dissolved Solids(TDS), respectively. These results justify the use of these variables as input variables to the ANN model for predicting the SAR values. However the sodium (Na) was removed as it is originally used for SAR estimation in Equation (15), while the aim is to estimate SAR values from EC, TDS and Cl , without the need of Measuring Na,Mg and Ca.

Many trials had been conducted for obtaining the best ANN model to predict the SAR values from the selected input variables. The trials adopt different data subsets division, different numbers of hidden nodes in the hidden layer, different types of activation functions for the hidden and output layers, and different learning rates and momentum terms. The Final Network selected gave the highest correlation coefficient between the Observed and Predicted SAR values, of 0.963. The best performance of the network was found to have a data subsets division of 47%,26%,27 % for the

training, testing and holdout with 4 nodes in the hidden layer, learning rate of 0.4 ,momentum term of 0.9, and hyperbolic tangent and identity activation functions for the hidden and output layers respectively.

Figure(2) shows the architecture of the final neural network obtained. Figure(3) shows the 45° line of comparison between the predicted and observed SAR values, which indicates the good capability of the model for prediction. The sum of square error and the relative error for the training set are 3.45,and 0.108 ,respectively. These values for testing data are found to be 1.62,and 0.08,respectively, while the relative error for the hold out is found to be 0.035.

Figure(4) shows the normalized relative important analysis of the input variables on the output variable SAR, indicates the highest importance of Chloride 100%,then the Electrical conductivity 20.4%,and the Total dissolved solids 12.8%. These values are found in the same order of the correlation coefficients of these variables with SAR, as (0.961,0.929,and 0.91),respectively.

### Conclusions:

From this analysis the following conclusions could be deduced of this study:

- 1- The developed ANN model that is capable of predicting SAR values from EC,TDS,and Cl as input values with correlation coefficient of 0.963.
- 2- The most variable affecting SAR values among the selected input variables is the Chloride as 100% normalized importance analysis, followed by EC with 20.4%,and TDS with 12.8%.
- 3- The importance normalized analysis are found in the same order of the correlation coefficient between the SAR variable and the other variables.

- 4- The training, testing and holdout relative errors of the network are found all to be small and acceptable (less than 5%), however the relative error of the holdout set is the lowest which is more important in such a model.
- 5- The number of the hidden nodes required to obtain an acceptable model is relatively low only 4, which let the weight matrix coefficients of small dimensions ,hence reduce the calculations required for prediction.

### References:

Hore A, Dutta S, Datta S and Bhattacharjee C 2008.” Application of an artificial neural network in wastewater quality monitoring: prediction of water quality index International. Journal of Nuclear Desalination (IJND) 3: 160 - 74.

Kanini S,Asadollahfaradi G, and Ghanbari A,2008, “ Application of Artificial Neural Network to predict Total Dissolved Solid in Achechay River Basin”, World Applied Sciences Journal 4(5):646-654,2008 ISSN 1818-4952,IDOSI Publications

Michael AM, Kherpar SD, Sondhi SD, 2008,” Water wells and pumps”,McGraw-Hill, New Delhi.

Oliai A, Banejad H, Samadi MH, Rahmani A, Saghi MH, 2011,”Performance evaluation of artificial neural network in predicting BOD and DO water quality criteria Darreh Hamadan River”. Journal of Science water and soil / Vol 20.1(3).

### Artificial Neural Network Model To Predict Sodium Adsorption Ratio for Tigris River in Amara

Palani S,Liong S,Tkalich P, and Palinichamy J, 2009,”Development of a Neural Network Model for Dissolved Oxygen in Seawater”, Indian Journal of Marine Sciences ,Vol. 38(2) ,June, pp 151-159.

Sarani N,Soltani J, Sarani S, and Moasheri A, 2012 ,”Comparison of Artificial Neural Networks and Multivariate Regression Models to Predict Sodium Adsorption Ratio SAR (Case Study: Sistan River,Iran)”, International Conference on Chemical ,Ecology, and Env. Sciences (ICEES 2012), Mar 17-18,2012,Bangkok.

Talib A,Abu Hassan Y, and AbdulRahman N,2009,”Predicting Biochemical Oxygen Demand as Indicator of River Pollution Using Artificial Neural Networks”,18<sup>th</sup> World IMACS/MODSIM Congress,Cairns,Australia,13-17 July.

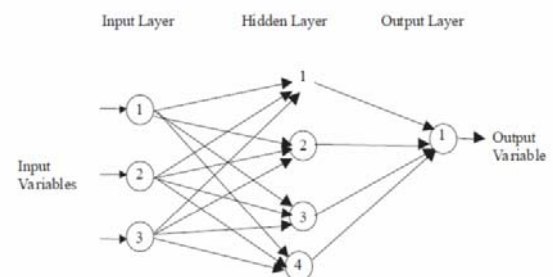
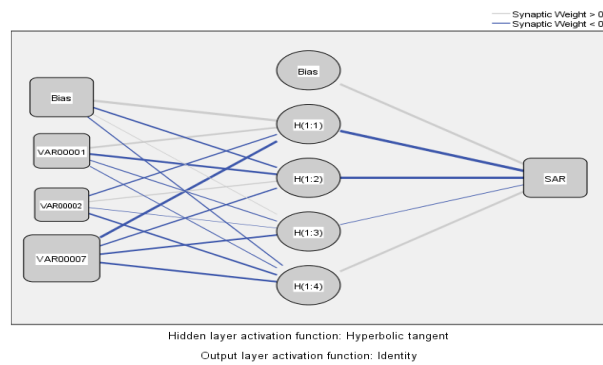
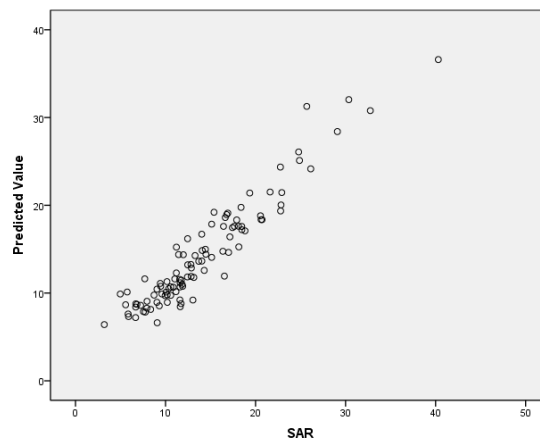


Fig. 1: A 3-layer ANN architecture used for Monthly precipitation prediction





**Fig. 2 The architecture of the Neural network used for predicting SAR values at Tigris River in AMMARA(VAR0001=EC,VAR0002=TDS,VAR0007=CI).**



**Fig. 3 The predicted SAR values Vs. The Observed SAR Values of Tigris River At AMMARA.**

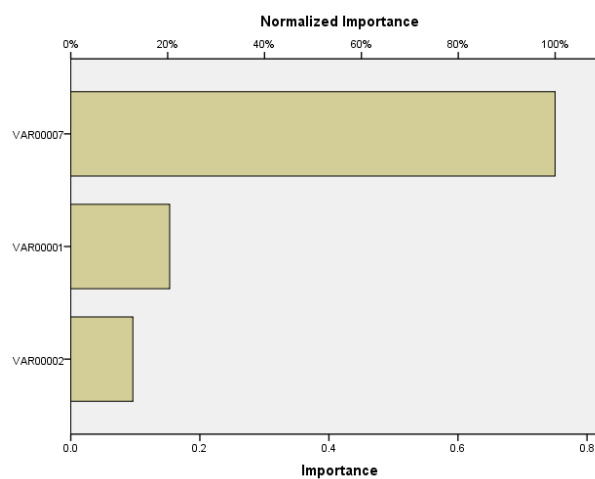


**Fig. 4 The normalized Importance Analysis on SAR Values of Tigris River in AMMARA.**

**Table (1) Descriptive Statistics of The Data Used in Modeling.**

-	Min	Max	Mean	Stand. Dev.	Skewness	Kurtosis
SAR	40.3	320	14.68	6.846	1.32	2.09
Ec	290	3000	1122.2	581.669	1.035	0.547
TDS	200	4000	783.3	384.582	0.973	0.45
CL	26	630	173.5	112.68	1.579	3.116

**Table (2) Correlation Matrix between Water Quality Parameters in Tigris River at AMMARA.**

-	EC	TDS	Ca	Mg	Na	K	CL	SO <sub>4</sub>	TH	CO <sub>3</sub>	HCO <sub>3</sub>	SAR
EC	1	0.981	0.764	0.721	0.957	0.427	0.967	0.88	0.874	-0.464	0.297	0.929
TDS		1	0.78	0.78	0.944	0.41	0.952	0.903	0.882	-0.436	0.298	0.91
Ca			1	0.517	0.686	0.317	0.686	0.841	0.834	-0.287	0.28	0.567
Mg				1	0.674	0.331	0.662	0.717	0.774	-0.236	0.910	0.583
Na					1	0.408	0.974	0.822	0.812	-0.44	0.246	0.957
K						1	0.418	0.352	0.314	-0.035	-0.057	0.379
CL							1	0.808	0.806	-0.421	0.231	0.961
SO <sub>4</sub>								1	0.9	-0.429	0.329	0.757
TH									1	-0.401	0.322	0.773
CO <sub>3</sub>										1	-	-



											0.543	0.549
HCO <sub>3</sub>											1	0.198
SAR												1



## Development an Anomaly Network Intrusion Detection System Using Neural Network

**Prof. Dr. Kais Said Al-Sabbagh**  
Electric engineering dept.  
University of Baghdad

**Assist.prof. Hamid M. Ali**  
Computer engineering dept.  
University of Baghdad

**Elaf Sabah Abbas**  
M.Sc. student  
Computer engineering dept.

### Abstract

Most intrusion detection systems are signature based that work similar to anti-virus but they are unable to detect the zero-day attacks. The importance of the anomaly based IDS has raised because of its ability to deal with the unknown attacks. However smart attacks are appeared to compromise the detection ability of the anomaly based IDS. By considering these weak points the proposed system is developed to overcome them.

The proposed system is a development to the well-known payload anomaly detector (PAYL). By combining two stages with the PAYL detector, it gives good detection ability and acceptable ratio of false positive.

The proposed system improve the models recognition ability in the PAYL detector, for a filtered unencrypted HTTP subset traffic of DARPA 1999 data set, from 55.234% in the PAYL system alone to 99.94% in the proposed system; due to the existence of the neural network self-organizing map (SOM). In addition SOM decreases the ratio of false positive from 44.676% in the PAYL system alone to 5.176% in the proposed system.

The proposed system provides 80% detection ability of smart worms that are meant to invade the PAYL detector in the PAYL system alone, due to the existence of the randomization stage in the proposed system.

**Keywords:** Intrusion Detection Systems (IDS), PAYL, SOM, Randomization.

### الخلاصة

معظم الـ (Intrusion Detection Systems) هي من نوع (Signature based) والتي تعمل بشكل مشابه الى مضادات الفيروسات ولكنها غير قادرة على التعرف على الهجمات التي تظهر لأول مره (الهجمات غير المدرجه في قاعده بياناتها) وقد ظهرت اهميه الـ (anomaly based IDS) نتيجة لقدرتها على اكتشاف مثل هذه الهجمات بالرغم من ذلك فانه ظهور الهجمات الذكيه اصبح يمثل تهديد الى الـ (Anomaly based IDS). تم تطوير النظام المقترح للتغلب على نقاط الضعف المذكوره سابقا.

النظام المقترح هو تطوير الى نظام الـ (PAYL) المعروف. بدمج مرحلتين مع كاشف الـ (PAYL) يتم الحصول على قدره كشف جيده و نسبه ايجابيه كاذبه (False positive) حسن النظام المقترح قابليه الـ (PAYL) للتعرف على الانماط، من 55.234% في الـ (PAYL system alone) الى 99.94% في النظام المقترح، نتيجة لوجود الشبكة العصبية. وكذلك قلل وجود الـ (SOM) الـ (False positive) من 44.676% في الـ (PAYL system alone) الى 5.176% في النظام المقترح.

بسبب وجود مرحلة الـ (randomization) اظهر النظام المقترح قابليه على اكتشاف الـ (smart worms) والمصمم لغزو كاشف الـ (PAYL) في الـ (PAYL system alone) بنسبة 80%.

## I. Introduction

Network Intrusion detection system (NIDS) is a type of security management system for computers and networks; it inspects all network activity and identifies suspicious patterns that may indicate a network or system attack from someone attempting to break into or compromise a system.

The Internet and computer networks are exposed to an increasing number of security threats. With new types of attacks appearing continually, developing flexible and adaptive security oriented approaches is a severe challenge. In this context, anomaly-based intrusion detection techniques are a valuable technology to protect target systems and networks against malicious activities [P. Garci'a-Teodoro et. al., 2009]. PAYL detector is statistical model that detects anomalies by capturing features of data payload in an efficient way -automatic and unsupervised-, it has been used before in the context of computer security in many researches and gave such a good results [S. Zanero, 2005, KeWang, 2006, Ke Wang et. al., 2004, D. Bolzoni et. al., 2006].

The PAYL detector alone is considered a successful system to detect the abnormalities in the incoming traffic, of course after it has a proper training phase. In recent time, smart attacks [C. Mao et.al., 2010] have been dedicated to invade the PAYL detector, such as the mimicry attacks [KeWang, 2006]. To avoid such attacks, on the PAYL detector the randomized testing technique [KeWang, 2006] is used. This technique provides diversity on the packet payload that confuses the attacker about which byte positions to pad his exploit code in order to appear normal.

Instead of using the clustering technique that follows the PAYL detector (we call PAYL detector followed by clustering technique PAYL system alone), which is used to reduce the number of models that varies by one byte and the models that don't have enough training samples, a neural network Self-organizing map SOM is used. SOM is used for classification of the incoming traffic (data) into clusters. There are multiple reasons for choosing a SOM for classification purpose. The algorithm is robust

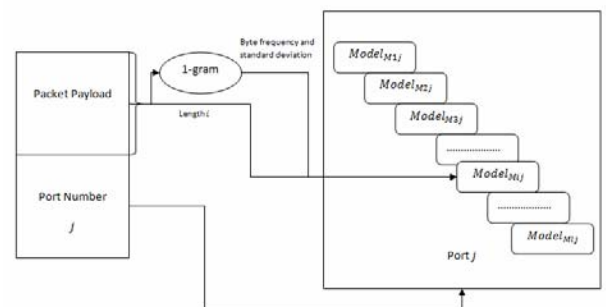
with regard to the choice of the number of classes to divide the data into, and it is also resistant to the presence of outliers in the training data, which is a desirable property. In addition, the SOM have the best performance trade-off between speed and classification quality [S. Zanero, 2005].

To build a highly performance anomaly based intrusion detection system, it is necessary that the proposed system consists of several stages where the combination of these stages is responsible for eliminating weak points that faces the PAYL system alone

## II. Background

### i. PAYL Detector: 1-gram Payload Modeling and Anomaly Detection

PAYL detector detects anomalies by combining an n-gram analysis algorithm with a classification method based on clustering of



packet payload. PAYL detector computes a set of models. One for each specific observed length  $i$  of each port  $j$  as shown in figure 1

Figure 1: Internal structure of PAYL detector

The distance between models is measured by using simplified Mahalanobis distance. The advantage of simplified Mahalanobis distance is that it takes into account not only the average value but also its variance and the covariance of the variables measured. Instead of simply computing the distance from the mean values, it weights each variable by its standard deviation and covariance, so the computed value gives a statistical measure of how well the new example matches (or is

consistent with ) the training samples. And the whole computation time is linear in the length of the payload with a small constant to compute the measure. This produces an exceptionally fast detector [KeWang, 2006].

## ii. Self-organizing Map (SOM)

A Self-organizing Map (also called Self-Organizing Feature Map or Kohonen map), is a kind of artificial neural network. It works by emulating the cognitive classification process typical of the human brain and it is based on competitive learning [S. Zanero, 2005]. SOM learns to classify input vectors according to how they are grouped in the input space. They differ from competitive layers in that neighboring neurons in the self-organizing map learn to recognize neighboring sections of the input space. Thus, self-organizing maps learn both the distribution (as do competitive layers) and topology of the input vectors they are trained on [Mat Lab Help].

The goal of learning in a SOM is accomplished by modifying the weight vector of neurons in a certain manner. To select which weight vectors must be updated and how, two parameters are used: the learning rate that controls the “influence” of the input on the neuron weight array components, and the update radius, that controls which neurons to modify. To accomplish the classification, a SOM goes through three phases: initialization, training, and classification [S. Zanero, 2005, D. Bolzoni, 2009].

## iii. Randomized Testing

Randomization is necessary to avoid mimicry attacks. Instead of modelling and testing the whole packet payload, the packets are randomly partitioned into several (possibly interleaved) substrings or sub sequences S1, S2, ..., SN, and model each of them separately against the same single normal model as shown in figure 2 (to make sure that partitions will produce different models from the one built using the whole payload) [KeWang, 2006].

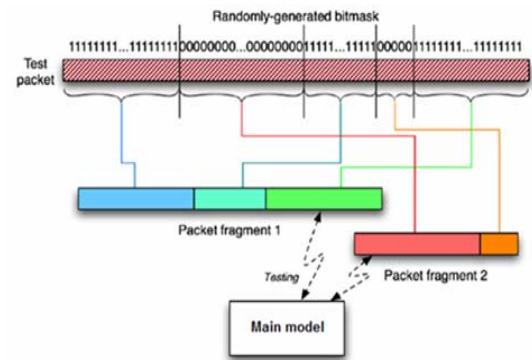


Figure 2: Randomized Testing.

To perform this randomization it is necessary to provide appropriated random binary bit mask which must be a purely random binary string, so that the following two criteria must be satisfied [W. Stallings, 2005]:

- 1- Uniform distribution.
- 2- Independence.

There are several advantages come from using this type of randomization, first all the calculations are liner that take a very short time to performed so it gives an ability to provide this system directly on line for training and testing. Second, because of using a pure binary random mask only two sub-models appeared and need to be compared with the model extracted from the entire packet payload, each of these models has distribution different from the original model. Third when the binary mask changed there is no need to retrain the entire system (because of the properties of the pure random binary mask). Still, there is the disadvantage of the false positive increment, but the false positive rate is usually much higher when the partitions have extremely unbalanced lengths [KeWang, 2006].

## III. The Proposed System Architecture

Each anomaly-based NIDS must consist of two phases, training phase and testing phase. Input data for both phases must pass through the same stages to get comparable information, which can be used for detecting any abnormalities.

The general structure of the proposed anomaly based NIDS is shown in figure 3, and the detailed structure are shown in figure 4.

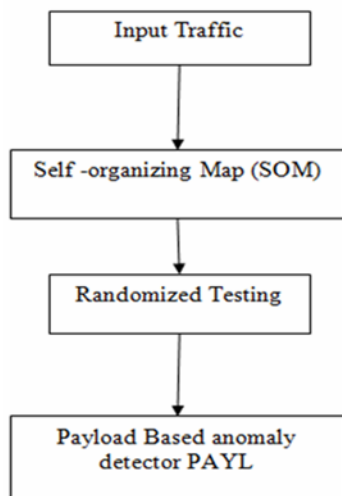


Figure 3: general structure of the proposed system

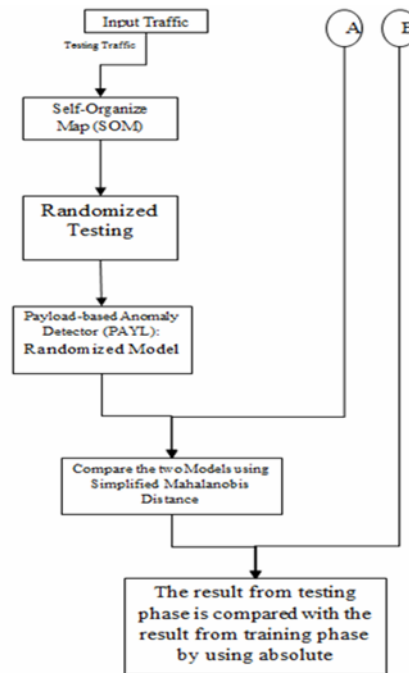


Figure 4 (b): Training Phase.

Figure 4: detailed structure of the proposed Anomaly NIDS.

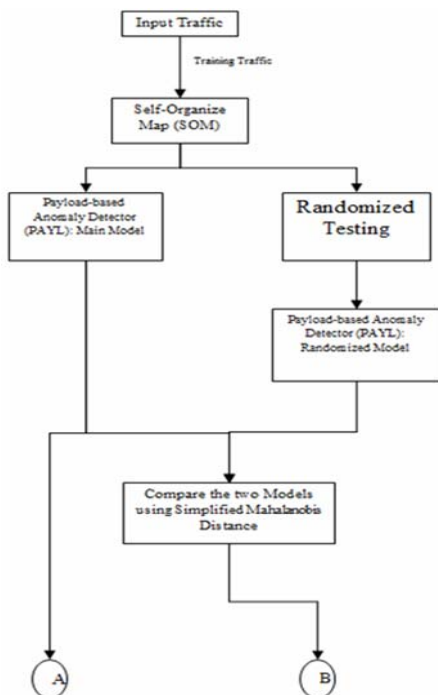


Figure 4 (a): Testing Phase.

## Proposed Anomaly NIDS Implementation

### A. Input Traffic

The input traffic that is used in this work is DARPA 1999 data set. The data set contains five weeks of collected data that are provided for IDS evaluation, three of them for training phase and two of them for testing phase. The first and third weeks of the training data do not contain any attacks. This data was provided to facilitate the training of anomaly detection systems. The second week of the training data contains a select subset of attacks from the 1998 evaluation in addition to several new attacks. The inside network traffic data is used which was captured between the router and the victims. Because most public applications on the Internet use TCP (web, email, telnet, and ftp), and to reduce the complexity of the work due to the huge amount of data, only the inbound TCP traffic at the port 80 of the hosts 172.016.xxx.xxx which contains



most of the victims at the first four weeks is examined. The traffic is filtered using Wireshark program, the filter is:  
`http && (ip.dst >= 172.16.0.0 && ip.dst <= 172.16.255.255) && data.`

This filter provides all the conditions that are required:

- Hosts ip address in the range of 172.016.xxx.xxx
- The port number is 80 for HTTP
- The packets must contain data between 1 byte to 1460 bytes

All filtered packet payloads copied into a file. Then MATLAB program is used to transfer them from hexadecimal format into the decimal format of ASCII characters. After the extraction and transformation of all packets payloads, the training and testing phases can be started.

## B. PAYL detector

The practical work of the PAYL detector is described in the following segments:

At first a program segment that describes the simplified Mahalanobis distance within the PAYL detector is:

$P_{new}$  = is the incoming packet payload.

$fv_{new}$  = is the feature vector of the incoming packet. It is a vector of length 256.

$mean_{ij}$  = is the mean of the byte value distribution of the training model.

/\* averaged feature vector of length 256 computed from the training examples \*/

$\sigma_{ij}$  = is the standard deviation of the byte value distribution of the training model;

/\* standard deviation of length 256 computed from the training examples \*/

$\alpha$  = is the smoothing factor determined previously.

$Thr$  = is a previously defined threshold from training phase.

$d$  = is the initial distance equal to zero;

/\* Now to compute simplified Mahalanobis distance between the new incoming packet and the previously calculated model \*/

For  $k = 0$  to 255

$$d = d + \frac{fv_{new}(k) - mean_{ij}(k)}{\sigma_{ij}(k) + \alpha}$$

End

If ( $d > Thr$ )

Then generate an alert;

End

Compute one model  $M_{ij}$  for each observed length  $i$  of payloads sent to port  $j$ . Such model might introduce several problems. First, the total size of the model can become very large. (The payload lengths are associated with media files that may be measured in gigabytes and many lengths may be defined causing a large number of centroids to be computed.) Further, the byte distribution for payloads of length  $i$  can be very similar to that of payloads of lengths  $i - 1$  and  $i + 1$ ; after all they vary by one byte. Another problem is that for some lengths, there may not be enough training samples. Sparseness implies the data will generate an empirical distribution that will be an inaccurate estimate of the true distribution leading to a faulty detector.

The solution for these problems is to “borrow” data from neighboring lengths to increase the number of samples. Two



neighboring models will be computed by using the simple Manhattan distance to measure the similarity of their average byte frequency distributions [KeWang, 2006].

Then, a program segment that describes the work of the Clustering technique is:

```

FV= relative byte frequency values for a
payload of length l.

/* feature vector is double vector between
0.0 and 255.0)*/

Thr=previously defined threshold

l= length of the longest packet payload

PAYLOAD= array [1 ..l] of [0 ..255 ]

MODELS = [M1,M2,M3 ...ML]

/* There are a model for each length */

For k = 1 to infinity

  IF Manhattan distance between two

    neighboring models < Thr

  Then
  
```

### *Merge them*

```

/* the operation repeated until no more
models can be merged*/
  
```

We call The PAYL detector followed by clustering technique PAYL system alone. PAYL system alone is used as comparison system with the proposed Anomaly NIDS.

### C. Self-organizing Map

A Self-organizing Map (also called Self-Organizing Feature Map or Kohonen map), is a kind of artificial neural network. It works by emulating the cognitive classification process typical of the human brain and it is based on competitive learning. To accomplish the classification, a SOM goes through three phases: initialization, training, and classification.

- **Initialization:** First of all, some parameters (number of neurons, learning rate, radius, and number of training samples) have to be fixed. The following segment shows the work of initialization phase:

```

 $\alpha_0$ : is the initial learning rate.
 $\alpha = \alpha_0$  is the current learning rate
 $Red_0$ : is the initial radius size.
 $Red = Red_0$  is the current radius.
T: is the number of training samples
(epochs).
D: is the input data, its range lies
between [d1 .....dn].
L: is the maximum length of the input
data.
N: is the total number of neurons that
arranged in two dimension array.
Wi: is the weight vector for i'th neuron
To initialize the weight vector for each
neuron
  
```



```
For i = 1 to N
```

```
Wi = random values of length L in the  
range of D
```

```
End
```

- **Training:** The training phase consists of a number of iterations (also called epochs). Each training sample is used for one iteration only, thus the number of samples determines the number of iterations. The following segment shows the work of training phase:

```
For i = 1 to T
```

```
To find the winning neuron (BMU):
```

```
Win-distance = mathematical distance  
(Neuroni, x)
```

```
Win - neuron = Neuron1
```

```
for j = 1 to N
```

```
Distance = mathematical distance  
( Neuronj, x)
```

```
if (Distance ≤ Win - distance)
```

```
then
```

```
Win - distance = Distance
```

```
Win - neuron = Neuronj
```

```
End
```

```
To find the neighboring neurons to the  
winner neuron:
```

```
for j = 1 to N
```

```
If (trigonometric distance(win - neuron,  
neuronj) < Red)
```

```
then
```

```
Neuronj is a neighbor to the Win-neuron
```

```
End
```

```
To update the weight vectors of the  
neighboring neurons:
```

```
for j = 1 to number of neighboring  
neurons
```

```
for k = 1 to L
```

```
Wj[k] = Wj[k] + α * (x[k] - Wj[k])
```

```
End
```

```
End
```

```
To update the learning rate and the radius  
values:
```

```
Red = Red0 * e- $\frac{1}{\#i}$ 
```

```
α = α0 * e- $\frac{1}{\#i}$ 
```

```
End
```

- **Classification:** To classify an input  $x$ , the SOM proceeds similarly to the training phase. The following segment shows the work of classification phase:

```
Win-distance = mathematical distance  
(Neuron1, x)
```

```
Win - neuron = Neuron1
```

```
for j = 1 to N
```

```
Distance = mathematical distance  
( Neuronj, x)
```

```
if (Distance ≤ Win - distance)
```

```
then
```

```
Win - distance = Distance
```

```
Win - neuron = Neuronj
```

```
End
```

#### D. Randomized Testing

The following segment shows the randomization stage in the proposed anomaly NIDS:

```
Mask is input packet length;  
Mod1 is the vector [b, m, d, l]  
Mod2 = is the second sub-model  
/* Mod1 and Mod2 are vectors [1.... l]  
*/
```

```
For i = 1 to l
```

```

If (Mask (i) == 0)

then

Mod1 (i) = P (i)

else

Mod2 (i) = P (i)
to make the length of Mod1 and
Mod2 ==L the rest of the packet will
Stuffed by Null */

```

#### IV. The Proposed System versus the PAYL System Alone

The proposed system is applied and tested on subset of the DARPA 1999 dataset. This is because of the huge size of the data set which takes very long time and effort to extract payload from the packet. Accordingly the proposed system is compared with the well-known PAYL system alone. The same training and testing subsets of DARPA 1999, used in this work are applied to the PAYL system alone.

Each stage from the proposed system has its own strength that can eliminate a weakness faces the PAYL system alone:

1- Self-Organizing Map (SOM): this stage classifies the input traffic into several types. SOM classification reduces the calculation and time required to cluster the models resulted from the PAYL detector. SOM stage can perform better classification than the clustering in the PAYL system alone. Because SOM classification is based on the bytes distribution of the input traffic (not only the length of the incoming packets) and its ability to learn from that traffic. Using the same training traffic for

both systems, the proposed system and the PAYL system alone, the clustering in the PAYL system alone shows less ability to recognize models compared to the SOM stage in the proposed system.

In the practical work of this dissertation the testing traffic consisting of 5081 packets. The number of packets that are appeared for the first time in the PAYL system alone are 2270 from 5081 packets (in the PAYL system alone the packet is considered appearing for first time if its payload length never appear during the training phase). There are 33 unique lengths within the 2270 packets that are appeared for the first time. By comparing these 33 unique lengths with the packets from the training phase, it is found that none of these 33 packets match any packet from the training data.

In the proposed system, the number of packets that appears for the first time are 3 from 5081 packets (in the proposed system the packet is considered appearing for the first time if it is classified by the SOM network into a neuron that doesn't have a model). In fact there is one packet in the testing data that is repeated three times and classified by the SOM network into neuron number 81. During the training phase no packet is classified into neuron number 81, which has no model. For this reason the packet in the testing phase which is classified into neuron 81 is considered appearing for the first time. By comparing these 3 packets with the packets from the training phase no match has been found, and this proves the accuracy and classification efficiency of the SOM stage in the proposed system.

From the above discussion, we conclude that the SOM stage decreases the ratio of false positive because of its efficiency in classification (the classification operation is an important stage in any network intrusion detection system). The clustering in the PAYL system alone, which is based on the length of the packet payload, is less accurate than the SOM stage in the proposed system. Where, the PAYL system alone is giving 2270 packets appearing for the first time from the testing traffic of 5081 packets. The false positive ratio of the PAYL system alone is  $(2270/5081)*100$  equal 44.676%. While the SOM stage in the proposed system shows more accuracy in classification. The SOM stage gives



only 3 packets appearing for the first time from the testing traffic of 5081 packets. The false positive ratio of the proposed system is  $(3/5081)*100$  equal 0.5988%.

Even if we compare the unique packets appearing for the first time for both systems as a measurement for the ratio of the false positive, the SOM stage in the proposed system gives a better performance (the number of unique packets is 1 from 3 first time appearing packets) than the clustering in the PAYL system alone (the number of unique packets is 33 from 2270 first time appearing packets).

2- Randomization: this stage is used to prevent smart worms from blinding the PAYL system alone and evade the protected systems. However the randomization stage will increase the ratio of false positive, but the existence of the SOM stage decreases the ratio of false positive; the resulting ratio of false positive for the proposed system become reasonable and acceptable.

3- Finally the PAYL detector stage of the proposed work is using the 1-gram and the same mathematical model of the PAYL system alone. The main difference is that the proposed system is working on already classified and randomized input data and there is no need to cluster anything after the PAYL detector computations.

For the training traffic extracted from weeks one and three from DARPA 1999 dataset, the number of training packets is 2148. The PAYL system alone required 1minutes to be trained, while the proposed system required 29minutes to be trained

For the testing traffic that are extracted from weeks two and four from DARPA 1999 data set, the number of testing packets are 5081. PAYL system alone required 3 minutes to end its testing phase, while the proposed system required 48 minutes to end its testing phase.

For the PAYL system alone, the total number of testing packets that generate an alert is 2452 from 5081 packets. 2270 out of 2452 packets are appeared for the first time and 182 out of 2452 packets are false positives and attacks. For the proposed system the total number of testing packets that generate alerts is 263 from 5081 packets. 3 out of 263 packets are

appeared for the first time and 260 out of 263 packets are false positives and attacks.

Table 1 shows performance comparison between the proposed system and PAYL system alone.

**Table 1: The performance comparison between the PAYL system alone and the proposed system.**

	Number of models that appear for the first time	Total number of packets that generate alerts	False positive and the attacks ratio	Training time in minutes	Testing time in minutes
PAYL System alone	2270	2452	44.676%	1	3
The Proposed System	3	263	5.176%	29	48

## V. Conclusions

During the study and development of the proposed system, several points were observed and noticed.

- There are two phases for each anomaly based IDS, training phase and testing phase, to make the data classified correctly during the testing phase the same stages must be used for both phases. The data in the proposed system is passing through three stages, first the SOM network stage; second the Randomized testing stage and finally the PAYL detector stage.

- Because the traffic payload of the same length can be classified into several categories, and the traffic is belong to a relatively small number of services and protocols. A good learning algorithm can classify the traffic into small number of clusters; a neural network the self-organizing map SOM network has been used. So instead of using the clustering technique that follows the work of the PAYL detector, SOM network is used by the proposed system to classify the input traffic (before it enters to any stage) into a certain number of types. SOM learn both the distribution (as competitive layers do) and the topology of the input traffic that is trained on. So for the proposed system the SOM network has been used to classify any input data to a specific

neuron. To accomplish the classification, the SOM network goes through three phases: initialization, training and classification.

- The PAYL system alone is considered a successful system to detect the abnormalities in the incoming traffic, of course after it has a proper training phase. In recent time, attacks have been dedicated to invade the PAYL system alone, such as the mimicry attacks. To avoid such attacks, on the PAYL system alone, we used the randomized testing technique that randomly partition packet payload into several subsets by using a randomly-generated bitmask. This technique provides diversity on the packet payload that confuses the attacker about which byte positions to pad his exploit code in order to appear normal.

- The proposed system is applied on subset of DARPA 1999 dataset for the training and testing phases, the same subset has been applied to the PAYL system alone. The proposed system is showing a better performance than the PAYL system alone. Where the clustering operation in the PAYL system alone is replaced by using the SOM network, the mimicry attacks are overcome by using the randomization method, and the same PAYL detector is used for the proposed system.

- The PAYL system alone require less time in training phase and testing phase than the proposed system. The time consumption in the proposed system, which is represent a drawback in it, is attributed to the existence of the SOM stage and the randomization stage that increase the amount of calculations required to train and test the proposed system.

#### IV. References

Ching-Hao Mao, En-Si Liu, Kuo-Ping Wu and Hahn-Ming Lee: "Web Mimicry Attack Detection Using HTTP Token Causal Correlation", International Journal of Innovative Computing Information and Control (IJICIC), Volume 7, 2010.

Damiano Bolzoni: "Revisiting Anomaly-based Network Intrusion Detection Systems", Ph.D. Thesis, University of Twente, 2009.

Damiano Bolzoni, Sandro Etalle, Pieter Hartel and Emmanuele Zamboni: "POSEIDON: a 2-tier Anomaly-based Network Intrusion Detection System", Fourth IEEE International Workshop, 10 pp. - 156, 2006.

Ke Wang, Salvatore J. Stolfo: "Anomalous Payload-based Network Intrusion Detection", Recent advances in intrusion detection: 7th international symposium, Sophia-Antipolis, France, September 15-17, volume 3224, pp. 203-222, 2004.

KeWang: "Network Payload-based Anomaly Detection and Content-based Alert Correlation", Ph.D. Thesis, School of Arts and Sciences, Columbia University, 2006.

"Self-Organizing Feature Map toolbox", Mat Lab Help.

Stefano Zanero: "Analyzing TCP Traffic Patterns Using Self Organizing Maps", 13th International Conference on Image Analysis and Processing (ICIAP), Cagliari (Italy), September 6-8, volume 3617 of LNCS, pp. 83-90, 2005.

P. Garcí'a-Teodoro, J. Dí'az-Verdejo, G. Macía'-Fernández and E. Va'zquez: "Anomaly-based network intrusion detection: Techniques, systems and challenges", Computers Security, Volume 28, pp. 18-28, 2009.

William Stallings: "Cryptography and Network Security Principles and Practices", Prentice Hall, 2005.

## Effect Of Technology Based Learning As A Supplement To Traditional Technology On Student's Achievement

**Dr. Ahmed A. Hashim**  
Computer Science Department  
College of Science for Women, Baghdad  
University  
Baghdad, Iraq  
dreng.ahmed@yahoo.com

**B.Sc. Nada K. Kareem**  
Computer Science Department  
College of Science for Women, Baghdad  
University  
Baghdad, Iraq  
nada\_prof1@yahoo.com

### Abstract

This paper describes a practical study on the impact of learning's partners, Bluetooth Broadcasting system, interactive board, Real – time response system, notepad, free internet access, computer based examination, and interaction classroom, *etc*, had on undergraduate student performance, achievement and involving with lectures. The goal of this study is to test the hypothesis that the use of such learning techniques, tools, and strategies to improve student learning especially among the poorest performing students. Also, it gives some kind of practical comparison between the traditional way and interactive way of learning in terms of lectures time, number of tests, types of tests, student's scores, and student's involving with lectures.

This paper studies the effect of using relatively new technology appearing in classroom today which is real time response system (voting system), that serves as real – time windows into each students understand of concepts. These devices can provide a foundation decision making based on data at scale never before possible as well as increasing students learning and engagement with each other as well with the lecturer, also, another new technology the "Bluetooth broadcasting system" is applied which is one of the moderate technique towards M- learning, this tool is used to transfer audio, video, text, notes, etc to the mobile of the students as well as laptop.

The computer based examination, interactive board, and notepad as well as free wire and wireless internet access are used to close the digital divide and increasing technology literacy in all students which was one of the challenges, additional challenges include “social loafing,” characterized by students who work less diligently than they otherwise might, or who become frustrated by course material or technology and thus less engaged. Finally the other colleague's resistance to the use of technology in learning and its effect on students learning is discussed based on practical situations.

**Keywords-** e-learning, m-learning, voting system, automated examination, smart board, bluetooth broadcasting system

### تأثير التعليم القائم على استعمال التكنولوجيا كمتعمم للتعليم التقليدي على تعليم الطلبة

د. احمد عبد الصاحب هاشم  
قسم علوم الحاسوب  
كلية العلوم للبنات/جامعة بغداد

م. مبرمج ندى خليل كريم  
قسم علوم الحاسوب  
كلية العلوم للبنات/جامعة بغداد

### الستخلص

يصف هذا البحث دراسة عملية لتأثير شركاء التعلم، انظمة البث بواسطة تقنية البلوتوث، السبورة التفاعلية، نظام التصويت، اللوح التفاعلي، الوصول المجاني إلى الإنترنت، الامتحانات المؤتمته بواسطة الحاسوب، ونظام الفصول الدراسية التفاعلية، على أداء الطالب الجامعي ومشاركته بالتكنولوجيا، الهدف من البحث هو اختبار الفرضية القائلة بأن استخدام مثل هذه التقنيات، والأدوات، والاستراتيجيات في التعليم تؤدي إلى تحسين تعلم الطالب وخصوصاً الطلاب الأقل أداءاً، كما إنه يعطي نوعاً من المقارنة العملية

بين الطريقة التقليدية والطريقة التفاعلية في التعلم من حيث الوقت المستغرق للمحاضرات، وعدد الاختبارات وأنواع الاختبارات، ودرجات الطلبة، ومدى مشاركة الطلبة في المحاضرات.

درس البحث أثر إستعمال تقانات جديدة نسبياً والتي بدأت تظهر في الفصول الدراسية اليوم والذي هو جهاز الاستجابة اللحظي (نظام التصويت) ، والتي هي بمثابة نافذة – حقيقية لقياس مدى إستيعاب كل طالب للمفاهيم. يمكن لهذه الأجهزة أن تكون أساساً لتنمية القدرة على صنع القرار إستناداً إلى البيانات على نطاق واسع لم يكن بالسابق ممكناً كذلك يزيد من قدرة التعلم والتفاعل للطلاب مع بعضهم البعض من جهة ومع المحاضر من جهة ثانية، كما تم تطبيق تقانه البث بواسطة البلوتوث والتي تعد من أحدث التقانات في مجال التعليم الإلكتروني، هذه الأداة تستعمل لنقل الصوت، الفيديو، النص، الملاحظات، إلخ إلى هواتف الطلاب الخليوية والحاسبات المحمولة.

إن الإمتحانات المؤتمته بواسطة الحاسوب، السبورات التفاعلية ، اللوح التفاعلي ، وكذلك خدمة الإنترنت السلكية واللاسلكية المجانية المستخدمة هي تقانات تم إستخدامها لردم الهوة الرقمية وزيادة الإلمام بالتكنولوجيا لجميع الطلبة والذي كان واحداً من التحديات التي تعامل معها البحث، من التحديات الأخرى التي تناولها البحث "التواني الاجتماعي"، والذي يصف الطلاب الذين يعملون بدأب أقل، أو الذين يشعرون بالاحباط بسبب المادة الدراسية أو بسبب استعمال التكنولوجيا، ويعمل بالتالي بإهتمام أقل. وأخيراً تمت مناقشته أثر الرأي المعارض للزملاء الآخرين لإستعمال التقانات الحديثة في التعليم على الطلاب لما يحدثه ذلك من إرباك لدى الطلاب وبالإعتماد على حالات واقعية فعلية.

الكلمات الرئيسية- التعليم الإلكتروني، التعليم المتنقل (الموبايل)، نظام التصويت، الاختبارات المؤتمته، السبورة الذكية، البث بواسطة البلوتوث

## I. Introduction

There is an argument that the best way of maintaining a learning process is traditional learning. Other models are always considered to be inferior or less efficient. There is no finding to support this argument, and researches show that technology learning models are at least as good as traditional learning if not better [Sven G. Bilén, M. Tutunea]. When comparing learning of an identical course in a traditional framework to a computer mediated learning framework, students have expressed higher satisfaction from the computer mediated learning, and rated the learning as more effective than in the traditional framework. In other studies, too, it was argued that technology – based learning is more effective and interactive. Technology – based Learning includes advantages which are not found in traditional learning, such as: time for digesting the information and responding, enhanced communication among the learners, both as regards quality and as regards urgency, knowledge being acquired and transferred among the learners themselves, the ability to conduct an open discussion, where each learner gets more of an equal standing, a higher motivation and involvement in the process on the part of the learners [Sue Pieper and Kathleen Thatcher].

Organization: This paper is organized as follows:

Section 2 describe a brief comparison between the traditional learning and technology based learning

Section 3 states the problem and promises of improving the student interaction via involving technology in learning

Section 4 describe the employed solution including the controls and type of data collected

Section 5 contains the evaluation based on several parameters

Section 6 is the results obtained which was divided into Two categorize, positive findings and negative findings, based on the effect of the applied technology. Finally section 7 which include the conclusions.

## I. Traditional Learning versus Technology Based Learning

The very use of technology for learning has been found to have a positive effect on the student's commitment to the learning process. Also, use of technology creates a greater commitment on the students' part to learn. Too many points have to be taken under consideration when evaluating the technology based learning as compared with the traditional learning, in terms of reaction for example, gathering feedback continuously, recording a meaningful statistics automatically, in terms of learning, in technology – based learning, tests can be automatically administered, scored, recorded, and reported. Automatic testing reduces the difficulty, effort, and costs of creating and administering tests, which means one can use them more widely. With pretests, you can determine whether learners are ready to begin a course or module [Giuseppe Favretto]. Diagnostic tests will help identify the specific modules or learning objects learners should take. Post-tests will confirm learning or shunt learners to remedial learning experiences, and within-course modules help learners to monitor their accomplishment of the learning objectives [Jason Harloww].

Technology based learning provides learners with inexpensive and easy-to-use testing tools to create tests and standards-based reporting mechanisms to record and report scores. Many tools include



components to create test questions and administer real time tests [Mofreh A. Hogo].

The advantage for evaluation is that the tedious, time consuming and expensive process of distributing, conducting, gathering, grading, and recording tests is automated from start to finish. The effort and costs of tests are reduced, and the results of testing are available for immediate analysis.

The following table summarizes several opinions regarding the comparison between traditional learning and technology based learning [Kimberle Koile]:

**TABLE 1** A brief comparison between traditional learning and technology based learning

	Traditional Learning	Technology Based Learning
<b>Classroom Discussions</b>	The teacher usually write more than talking	The teacher discussion more than writing
<b>Subject Matter</b>	The teacher conducts the lesson according to the study program and the existing curriculum	The student participates in determining the subject matter; the studying is based on various sources of information, including web data banks and net-experts located by the student.
<b>Emphases in the Learning Process</b>	The students learn “what” and not “how”; the students and the teachers are busy completing the required subject matter quota; the students are not involved in inquiry-based education and in solving problems, but rather in tasks set by the teacher.	The students learn “how” and less “what”; the learning includes research study which combines searching for and collecting information from web data banks and authorities on the communications network; the learning is better connected to the real world, the subject matter is richer and includes material in different formats.
<b>Motivation</b>	The students’ motivation is low, and the subject matter is “distant” from them.	The students’ motivation is high due to the involvement in matters that are closer to them and to the use of technology.
<b>Teacher’s Role</b>	The teacher is the authority	The teacher directs the student to the information

## I. Problem Statement and Context

A promise for improving student interaction and learning, a work has focused on development and deployment of Voting systems, automated examination, interactive board, notepad, and multimedia in the classroom, as well as a free access to wire and wireless internet inside and outside the classroom. Also and as a step towards m-learning, the Bluetooth broadcasting system was used. As with any other kind of technology, it is required to investigate whether the promised benefits can be realized. Our hypothesis has been that such a system will improve student learning, especially among students who might otherwise be left behind. Our goal has been to test this hypothesis by rigorously

assessing student learning in controlled studies involving deployment of the system. We report here the findings from our most recent and most valid study till the time of this writing.

## I. Solution Employed

We conducted a study in Baghdad University – College of Science for Women – Computer Department – First Year – logic design subject and Third Year – modeling and simulation subject in 2010 – 2011. The course had an enrollment of 32 first year students and 25 third year students taking the course met in 2 hours classes one time a week—lecture plus 2 hours laboratory for both subjects. The technology used in the study consisted of PCs in a network connected Classroom with free access to internet, interactive board, notepad, voting system, multimedia, automated examinations, Bluetooth broadcasting system. The PCs is used for wire and wireless internet access as well as for automated examination using "Quiz Creator" software as well as using other software or tools in the exams like the MATLAB, calculator, etc. The interactive board gives a very wide options never been available in the white board, which intern increases the interactivity, ability to explain some difficult ideas with easier way and less time which intern gives more time for the lecturer for contacting with the students and the ability to give more material within the same lecture time, no mention for the ability to store the lectures as text or as a video file where the audio is taken from the tutor and students discussion and the video captured from what is written on the interactive board, it is important here to add the curiosity of the student to use the interactive board and the effect of that on his skills. Notepad, on the other hand allows students to wirelessly and anonymously submit digital ink answers to in-class exercises. The instructor chooses student submissions—both correct and incorrect—to be used as the basis for class discussion. Automated examination gives an excellent way testing the students with different kinds of questions for any time with the ability to each students to know his/her score immediately, there are two important thinks; first, the right answer, second, his/her level of understanding among the other students. Voting system, from the other hand is one of the most promising interesting systems to be used in the classrooms. The system enables real-time performance tracking (real – time windows into each student's understand of concepts), immediate feedback and review. These devices can provide a foundation decision making based on data at scale never before possible as well as increasing students learning and engagement with each other as



well with the lecturer, the wireless design saves time, paper and investment costs in networking or purchasing, student PC, with this total solution, teaching environment can be more interactive and be different from traditional presentation style. Finally, the wire/ wireless free internet access is used to close the digital divide and increasing technology literacy in all students which was one of the challenges.

#### **A. Controls**

The study was run with one control class and one experimental class. Students in the experimental class used technology based learning; students in the control class used paper handouts as well. The study employed the following strict controls[Graham Attwell, Philip S. Anto'n].

- **Teaching style:**

We controlled for teaching style by having the same instructor teach both the control and experimental classes. The instructor began each class with a review of material, lecturing and writing on an interactive board,..., or referring to class handouts. The instructor spent the majority of class time (between 75% and 90%) engaged in high levels of teacher-student interaction: Students asked and answered oral questions, worked written problems individually or in small groups, participated in class discussions of problem-solving approaches and solutions, and worked at their own pace on extra problems when they want. As a result, the students spent most of class time in two ways:

processing information by solving problems and answering questions, and getting immediate feedback on responses to problems and questions. The voting system greatly facilitated both processing, by letting students easily handwrite answers, wirelessly and anonymously submitting them to the instructor; and feedback, by allowing an instructor to choose submissions for public display and class discussion, often "inking" directly on the submissions. In the control class, the students spent the same amount of time processing information and getting feedback, but at the loss of anonymity and/or discussion of incorrect answers (since students were reluctant to share incorrect answers).

- **Class material and exams:**

For the first Year class, in the experimental class, the students received the same information and problems (with 2 hours per week and with much more quizzes and

#### **Effect Of Technology Based Learning As A Supplement To Traditional Technology On Student's Achievement**

exams compared with control class of 3 hours per week and less quizzes and exams). For the third Year class, the students in the experimental class receive approximately 40% more information and much more quizzes and exams compared with the control class students.

- **Time of day:**

The control and experimental classes met at approximately the same time of day. In this way, we expected to mitigate the problem of students not attending early morning or late classes.

- **Student characteristics:**

We only included students who were taking the class for a grade; no listeners included, since such students may not have been as motivated as for-grade students. No graduate students or upperclassmen were included because we felt that they might have had better study habits or might have taken other courses that would have benefited them in the current course.

- **Attendance:**

It is included in the study, just as a reflection of student's interest and involving with the subject without making it as factor affecting the students score.

- **Other colleague's resistance:**

The other colleague's resistance against the use of new technology in learning, prefer the traditional ways, and their effect on students learning are discussed based on practical situations

#### **B. Types of Data Collected**

- **Amount of technology use:**

The number of minutes that technology was used in the experimental class was recorded. Inherent in our hypothesis of improve in learning is the idea that the amount of time spent learning a task is correlated with the amount learned [Sue Pieper and Kathleen Thatcher].

- **Performance metric:**

Exam score was used, percentage of attendance, student's involvement with lecture, gradual interest and involvement of the students with technology (mainly the increased number of internet users out of the lecture time, their curiosity about updating their knowledge about technology) as the performance metric.

- **Interaction metric:**

In the experimental class, we used the number of answers submitted by each

student for each problem within the specified time as a quantitative measurement of interaction in the class, as well as the student interest, rush, and passion.

We compared the number of answers expected with the number actually submitted and computed an average daily submission fraction for each student. Our goal is to see if this measure of interaction would correlate with performance scores. No such metric was easily computed in the control class, so our analysis was limited to the experimental class.

- Learning preferences and interests:

Data on learning preferences, self-perceptions, and levels of interest and satisfaction was collected by evaluating questions asked of students in two surveys, one survey given at the beginning of the term, a second at the end. We only considered “disagree” and “agree”; we insured that the learning preferences were more validly reflected in the statistical results.

Multiple timed few-minutes observation periods of students and short after-class interviews with students validated or clarified observed learning preferences and individual surveys.

## II. Evaluation

- Technology use [Jason Harloww, Mofreh A. Hogo]

The technology was used in 2 of 4 classes by both design and circumstance. During each class that technology was used, we did not count the minutes used for administrative procedures, such as login; or time spent fixing technology glitches, such as interference with wireless connectivity. At the end of the Year, we tallied approximately 900 minutes of technology use for the third class over the 30 days, which accounted for 35% of available class time and approximately 1600 minutes of technology use for the first class over the 30 days, which accounted for 66% of available class time, the reason for this time difference was mainly for the other colleague's resistance and social loafing.

- Attendance:

As mentioned above, the attendance in the study was included to reflect the student's interest with subject because of the use of technology. We started with 80-90% attendance at beginning of the Year and ended with normally zero absence students (without

excuse) at the end of the Year, comparing that with normal 80-90% attendance in the controlled class.

Performance metric:

When comparing exam scores for the experimental and control classes, we saw highly statistically significant differences in the scores of the experimental class compared with controlled one. We looked at this performance data in several different ways.

## II. Results

To see the impact of education technology on student's achievement (regarding the case studied), the results of this work divided into two categorizes based on the effect of applying these technologies:

### C. Positive findings

- 1) On average, students who used technology in learning scored at the 75th percentile on tests compared to students in the conditions without computers who scored at the 55th percentile
- 2) Students learn more in less time and the lecturer can give more in less time
- 3) When the technology used, the contact between the lecturer and all students and each student so that each student know that he may be the focus point at any time during the lecture
- 4) Students like their class more and develop more positive attitudes when their class include technology and their own self-concept improved consistently
- 5) Through the use of technology – based learning students surpass students in traditional classroom on measures of depth of understanding, maximizing their reflection and encourages progressive thought, taking multiple perspectives, and independent thinking

### D. Negative findings

- 1) A lot of students think about the technology first and the education later
- 2) Technology resistive colleagues
- 3) Technology resistive student
- 4) Class level at which the technology employed
- 5) Lecturer experience in the used technology and how to get use of it perfectly towards his subject.
- 6) Drill, practices, home works, and some materials that required focusing and more time for understanding is better done with traditional way, otherwise it will require professional technology user to make it more understandable

The higher performance of the students in the experimental class was evident when we looked at the performance distribution, (Fig 1 and Fig 2).

When we ranked final exam scores for both classes, we saw that eight of ten scores in the control class were below the lowest, two scores in the experimental class (Fig 3 and Fig 4).

## **VII. Conclusions**

This work makes important contributions: a sound assessment methodology and validation of learning gains among students using technology-based classroom interaction system, especially among the low performing students. The instructor's teaching style matched the technology well in that it emphasized student problem-solving and immediate feedback. The goal of the study was to test the hypothesis that the use of technology based learning system improves student learning, especially among the poorest performing students, as well as increase their engagement with each other and with the lecturer, no mention for the increase of attendance. This paper describes our validation of that hypothesis, and the controls, performance metric, and assessment methodology that we developed in the course of our study. The study shows that the students with better basic computer and Internet skills prefer the moderate learning methods. On the other hand, the concern should not be just with whether moderate learning methods is conducted successfully using the technological tools available, but more on whether the institutions did what they set out to do, i.e., educating students.

However, Technology – based learning should not be used as a replacement for traditional learning. It should be considered as a supplement to traditional learning, as an added-value for the learners, and the optimal system would be the integration of traditional learning and technology based learning.

## **References**

Giuseppe Favretto, Giovanna Caramia and Matteo Guardini, "E-learning measurement of the learning differences between traditional lessons and online lessons", University of Verona (Italy), 2003, [www.eurodl.org/?article=187](http://www.eurodl.org/?article=187)

Graham Attwell, Pontydysgu, "Personal Learning Environments - the future of eLearning?", elearning papers, vol 2, no. 1, January 2007, ISSN 1887-1542, [www.elearningpapers.eu](http://www.elearningpapers.eu)

Jason Harloww, David M. Harrison and Ruxandra Serbanescu, "Blackboards, power point, and tablet PCs in the classroom", Department of Physics University of Toronto, 2008

Kimberle Koile, MIT, "Assessing the Impact of a Tablet-PC-based Classroom Interaction System", To appear in proceedings of workshop on the impact of pen – based technology on education (WIPTE) 2008

Mofreh A. Hogo, "Evaluation of E-Learners Behaviour using Different Fuzzy Clustering Models: A Comparative Study", Benha University, Egypt, IJCSIS International Journal of computer science and information security, vol 7, no. 2, 2010

M. Tutunea, R. V. Rus, and V. Toader, "Traditional Education vs. E-learning in the vision of Romanian business students", International Journal of education and information technologies, volume 3, No. 1, 2009

Philip S. Anto'n, Richard Silberglitt and James Schneider, "The global technology revolution Bio/Nano/Materials Trends and their Synergies with information technology by 2015", prepared for the national intelligence council RAND national defense research institute, 2010

Sue Pieper and Kathleen Thatcher, "Creative Ways to Evaluate Classroom and Clinical Performance", Northern Arizona University, 2010

Sven G. Bilén, Dongwon Lee...*et.al*, "Tablet PC use and impact on learning in technology and engineering classrooms: A preliminary study", The Pennsylvania State University, 2006

Distribution of performance average score for traditional (controlled) and technology based (experimental) students

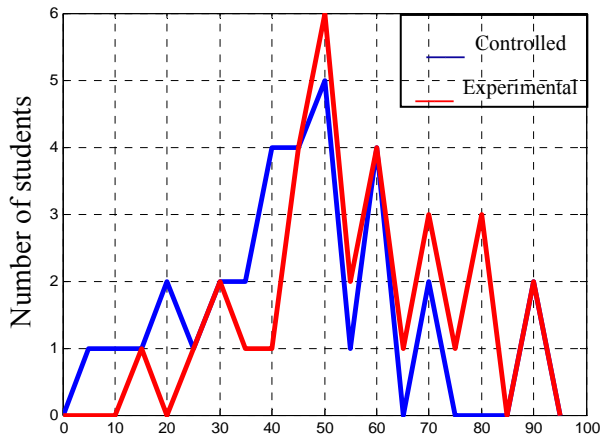


Figure 1 Distribution of 1<sup>st</sup> Year average students ranks

Ranked performance average score for traditional (controlled) and technology based (experimental) students

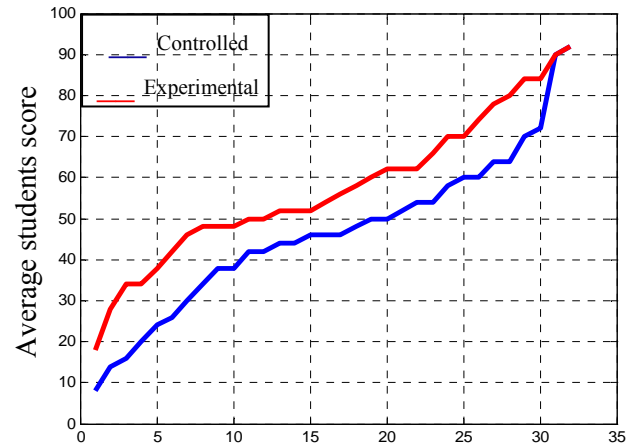


Figure 3 average rank ordering of 1<sup>st</sup> Year students

Distribution of performance average score for traditional (controlled) and technology based (experimental) students

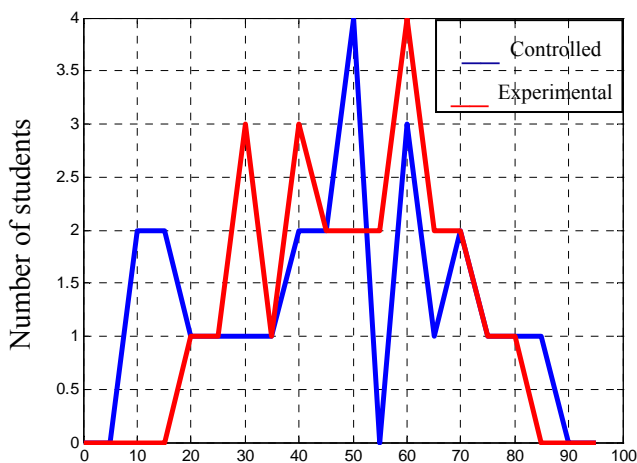


Figure 2 Distribution of 3<sup>rd</sup> Year average students ranks

Ranked performance average score for traditional (controlled) and technology based (experimental) students

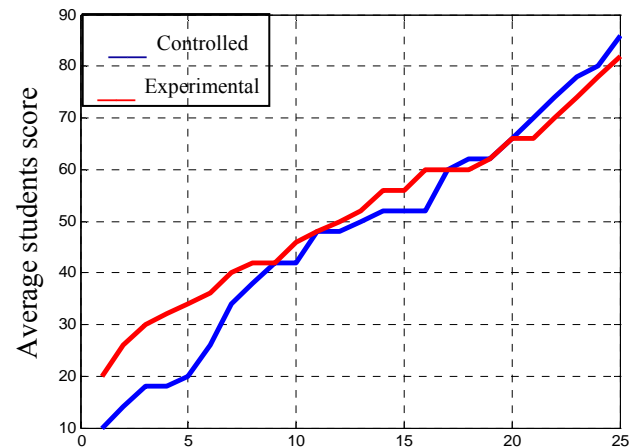


Figure 4 average rank ordering of 3<sup>rd</sup> Year students

## Different Resolution Merging Methods For Environmental Areas Extraction

Husham Abd Munaf Atta

Assistant Lecturer in Computer Center\ University of Baghdad

[husham@uobaghdad.edu.iq](mailto:husham@uobaghdad.edu.iq)

### Abstract

The usage of remote sensing techniques in managing and monitoring the environmental areas is increasing due to the improvement of the sensors used in the observation satellites around the earth. Resolution merge process is used to combine high resolution one band image with another one that have low resolution multi bands image to produce one image that is high in both spatial and spectral resolution.

In this work different merging methods were tested to evaluate their enhancement capabilities to extract different environmental areas; Principle component analysis (PCA), Brovey, modified (Intensity, Hue, Saturation) method and High Pass Filter methods were tested and subjected to visual and statistical comparison for evaluation.

Both visual and statistical comparison showed that High Pass Filter method have highest visual enhancement and highly maintained the quantitative information of the original image, Modified (Intensity, Hue, Saturation) method showed good visual and statistical results in comparison with PCA and Brovey method which had the lower results respectively.

**Keywords:** Environmental Areas, Resolution merge, High Pass Filter method, PCA, Visual inspection and statistical comparison.

هشام عبدمناف عطا

إن استخدام تقنيات التحسس النائي في ادارة ومراقبة المناطق البيئية المختلفة في ازدياد مستمر وذلك بسبب التحديث الحاصل في المتحسسات المستخدمة في أنظمة المراقبة الفضائية حول الأرض. تستخدم عملية دمج الصور بين صورتين، الأولى تكون ذات قدرة تمييزية عالية ومتكونة من حزمة موجية واحدة، أما الثانية فهي اقلقدرة تمييزية نسبياً من الأولى ولكنها متعددة الحزم الموجية، لينتج لنا صورة واحدة تحتوي على قدرة تمييز عالية ومتعددة الأطياف.

في هذا العمل، تم اختبار مجموعة من طرق دمج الصور لمعرفة قابليتها على تعزيز القدرة في استخلاص وتحديد المناطق البيئية المختلفة، وهذه الطرق هي تحليل المركب الرئيسي، بروفي، طريقة (الكثافة، الدرجة، التشبع) المعدلة، مرشح الترددات العالية تم اختبارها من حيث التباين الظاهري ومن خلال المقارنة الأحصائية لمجموعه من المعاملات.

اوضح اختبار التباين الظاهري و الاختبارات الأحصائية ان طريقة مرشح الترددات العالية لديها اعلى تباين لحدود المناطق البيئية كما وانها حافظت بشكل كبير على المعلومات الكمية الأحصائية للصورة الأصلية، تليها طريقة طريقة (الكثافة، الدرجة، التشبع) المعدلة والتي اظهرت تحسين ظاهري ونتائج احصائية جيدة مقارنة بطريقة تحليل المركب الرئيسي وبروفي الذين اظهروا اقل النتائج على التوالي.

الكلمات الرئيسية

المناطق البيئية، دمج الصور، طريقة مرشح الترددات العالية، تحليل المركبات الأساسية، اختبار التباين الظاهري والمقارنة الأحصائية .

## Introduction

The Remote sensing technologies is a valuable tool for Environmental purposes it have been used for decades for land changes detection and for different areas monitoring from environmentally side of view (Marcus Borengasser, 2008).

The early attempts to resolution merging or enhancement were related to merging the bands (4, 6, 7) which have a 240 m resolution with the fifth band which have a 80 m resolution for the Landsat MSS (Nikolakopoulos, 2004).

The reason beyond resolution merge process is to increase the interpretability of the high spectral resolution ( multi bands ) images with the aid of the high spatial resolution images, which will enhance the recognition of the exact limits of objects and shapes, maintaining as much as possible the spectral signature of these objects and shapes (Steven M. and De Jong, 2005).

After the merging process, the resulted images must be tested against the original images, the evaluation includes in most cases a statistical and visual interpretation comparison between the images (Is. Parcharidis, 2000).

The objective of this work is to compare the efficiency of four different techniques of merging high spatial resolution image with multispectral image in improving the extraction and identification of different environmental areas.

## Area Of Study

The study area lies in the south of Basrah governorate, in the southern part of Iraq. This area includes Um-Qasser, the border city between Iraq and Kuwait and One of the largest Iraqi harbors which surrounded by Desert, crop and palm fields and lies in the mouth of Al-Zubair estuary (Khawr Az-zubair), the area includes as well the northern part of Bubian island. The diversity of environmental areas of this location is what makes it suitable for this research.

## Methodology

LandSat7 ETM+ Images took in 27<sup>th</sup> of January 2002 is used in this work. Two images have been used, the first one with (4, 3, 2) bands with a 30 meter resolution displayed in **Figure1**, The second image is panchromatic band with resolution 15 meters, displayed in **Figure 2**.

The results of this work were achieved by using ERDAS Imagine 9.3 software. In the beginning all the images were accurately corrected and geo-referenced, in order to start the merging process.

The merging process was done with four different methods:

### 1- Principal Component Analysis

Some of the merging methods can be used with only three bands, the Principle component analysis can be used with more than three bands which is one of the main advantages of this method (Zhijun Wang, 2005).

The PCA highly maintain the original scene radiometry in the output file, this advantage come with longer time for processing; also this method tend to keep the data range in the output file same as the multispectral file (ERDAS Field Guide, 2008) .

This method uses the equation below for remapping the fused images

$$\begin{bmatrix} DN_{MS1}^h \\ DN_{MS2}^h \\ \dots \\ DN_{MSn}^h \end{bmatrix} = \begin{bmatrix} DN_{MS1}^l \\ DN_{MS2}^l \\ \dots \\ DN_{MSn}^l \end{bmatrix} + (DN_{PAN}^{h'} - DN_{PAN}^l) \begin{bmatrix} v11 \\ v21 \\ \dots \\ vn1 \end{bmatrix}$$

Where

$DN_{PAN}^l = PC1$  and  $DN_{PAN}^{h'}$  is  $DN_{PAN}^h$  (Zhijun Wang, 2005)

### 2- High Pass Filter Method

In this method, the injection of high frequency information (spatial details) extracted by the high pass filter from the High resolution Panchromatic image into the multi band low resolution image, which will produce a fused image with sharp high frequency characteristics ( Haixia liu and Xia Zhang, 2009).The model used in this method is

$$DN_{MS}^h = DN_{MS}^l + (DN_{PAN}^h - DN_{PAN}^l)$$

Where  $DN_{PAN}^l = DN_{PAN}^h * h_0$

and  $h_0$  is low pass filter such as boxcar filter. (Zhijun Wang, 2005)

### 3- Brovey Method

This method uses a direct intensity modulation; it was developed to increase the visual contrast in the ends of the image histogram. The limitation of this method is only three bands can be used in



each merging process (Jian Guo Liu, 2009) as represented in the equation below

$$\begin{aligned} [DN_{B1} / DN_{B1} + DN_{B2} + DN_{B3}] \times \\ [DN_{high \text{ res. image}}] &= DN_{B1\_new} \\ [DN_{B2} / DN_{B1} + DN_{B2} + DN_{B3}] \times \\ [DN_{high \text{ res. image}}] &= DN_{B2\_new} \\ [DN_{B3} / DN_{B1} + DN_{B2} + DN_{B3}] \times \\ [DN_{high \text{ res. image}}] &= DN_{B3\_new} \end{aligned}$$

(ERDAS Field Guide, 2008)

#### 4- Modified IHS ( Intensity, Hue, Saturation ) method

The modified IHS have an improvement over the traditional IHS method when working in merging images that have relatively high differences in spectral response (Siddiqui, 2003) .

This method like the Brovey method can be used with three bands only in each merging process as represented in this equation

$$\begin{bmatrix} DN_{MS1}^h \\ DN_{MS2}^h \\ DN_{MS3}^h \end{bmatrix} = \begin{bmatrix} DN_{MS1}^l \\ DN_{MS2}^l \\ DN_{MS3}^l \end{bmatrix} + (DN_{PAN}^h - DN_{PAN}^l) \begin{bmatrix} 1 \\ 1 \\ 1 \end{bmatrix}$$

Where

$$DN_{PAN}^l = (1/3)(DN_{MS1}^l + DN_{MS2}^l + DN_{MS3}^l)$$

And  $DN_{PAN}^h$  is  $DN_{PAN}^h$  (Zhijun Wang, 2005).

In all methods the merging process used the cubic convolution as the resampling method.

The merged images were put in comparison from two stand of view;

- 1- The visual inspection
- 2- Statistics

#### Visual Inspection

In order to evaluate the visual enhancement of each method, general and specific comparisons for the images have been done.

In **Figure 3** the original and the merged images were put together for the general inspection.

The spatial resolution is clearly improved for the resulted images in compare with the original multi bands image. All the images highly preserved the color composite of the original multi band image, although the Brovey image were darker than others.

**Figure 4** illustrates the comparison for the coastal area. The coastal area appears highly distinguishable in the HPF image, the high brightness of the shore line in the IHS image give it some advantage over the PCA and Brovey images which had less capability of extraction for the coastal area respectively.

**Figure 5** shows the agricultural zone, the same results as the coastal area were obtained; the visual enhancement was higher in HPF and IHS than PCA and the Brovey which has the least enhancement; the same result appeared in desert and urban zones as well.

#### Statistical Comparison

The statistical parameters comparison is used to identify the effect of different merging techniques on the original image in quantitative terms.

**Table1** shows the statistical information (Min, Max, Mean, Median, Mode and Standard deviation) for the images participated in this work.

The first parameter for comparison is Mean, which describes the central location of the data or where the DN histogram curve is positioned horizontally. **Figure 6** illustrate a graphical comparison among the four techniques and the original multi band image. The figure shows that Brovey method image have a lower mean values than other images, HPF and IHS images a very close values to the original multi band image and the PCA image was less closer to the original image, this means that the Brovey image is expected to be darker than other images which approve the result obtained from the visual inspection.

The other tested parameter was the standard deviation, shows how much variation or exists from the mean value. The importance of standard deviation is expressing the brightness values variation of the image.

**Figure 7** representing the standard deviation of the merged and original images.

In this figure we notice that the Brovey image has less standard deviation than the original image, this resulted in less brightness contrast and less environmental boundaries definition. PCA has standard deviation values higher than Brovey but less than original image. The IHS scored higher values than the original image except the third

Band and the HPF have approximately the same values of the original image.

### Conclusion

In this work, four merging methods were tested for their suitability for different environmental areas extraction. Visual enhancement and statistical comparison took place for the evaluation process.

In General, all the methods enhance the image spatial resolution. The visual inspection showed that the HPF and Modified IHS methods had better image quality, although HPF method preserved the natural colors of the original multi spectral image more than other images.

The statistical comparison showed that HPF method maintained the quantitative information of the original image, Modified IHS method showed good statistical results in comparison with PCA and Brovey method, which had the lower results respectively.

### Bibliography

ERDAS Field Guide. (2008). ERDAS Inc.

Haixia liu and Xia Zhang. (2009). Comparison of Data Fusion Techniques for Beijing-

1.2009 Joint Urban Remote Sensing Event, 1-6.

Is. Parcharidis, L. M.-T. (2000). Landsat TM and ERS Data Fusion :A Statistical Approach Evaluation for Four Different Methods.

Geoscience and Remote Sensing Symposium, 5, 2120-2122.

Jian Guo Liu, P. J. (2009). "Essential Image Processing and GIS for Remote Sensing". Oxford,UK: John Wiley & Sons Ltd.

Marcus Borengasser, W. S. (2008)" Hyperspectral remote sensing : principles and applications. "CRC Press Taylor & Francis Group.

Nikolakopoulos, K. G. (2004). Comparison of four different fusion techniques for IKONOS data. Geoscience and remote sensing symposium , 4, 2534-2537.

Siddiqui, Y. (2003). "The Modified IHS Method for Fusing Satellite Imagery". ASPRS 2003 Annual Conference Proceedings. Alaska,USA.

Steven M. and De Jong, F. D. (2005). "Remote Sensing and Digital Image Processing". Kluwer Academic Publishers.

Zhijun Wang, D. Z. (2005)." A Comparative Analysis of Image Fusion Methods". IEEE TRANSACTIONS ON GEOSCIENCE AND REMOTE SENSING, 43(6), 1391-1402.

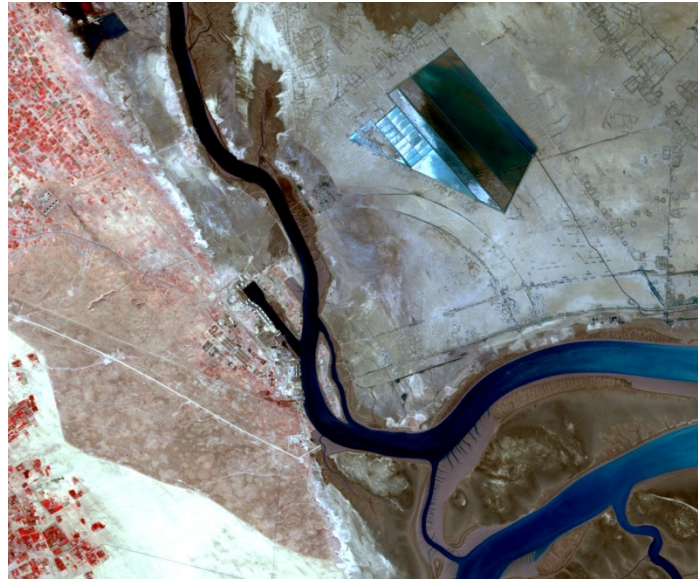


**Figure 1 A 4, 3, 2 RGB image with 30 meter resolution for the study area, nearly in the middle of the image is Um-Qasser city.**



**Figure 2 The panchromatic image with 15 meter resolution of the study area**



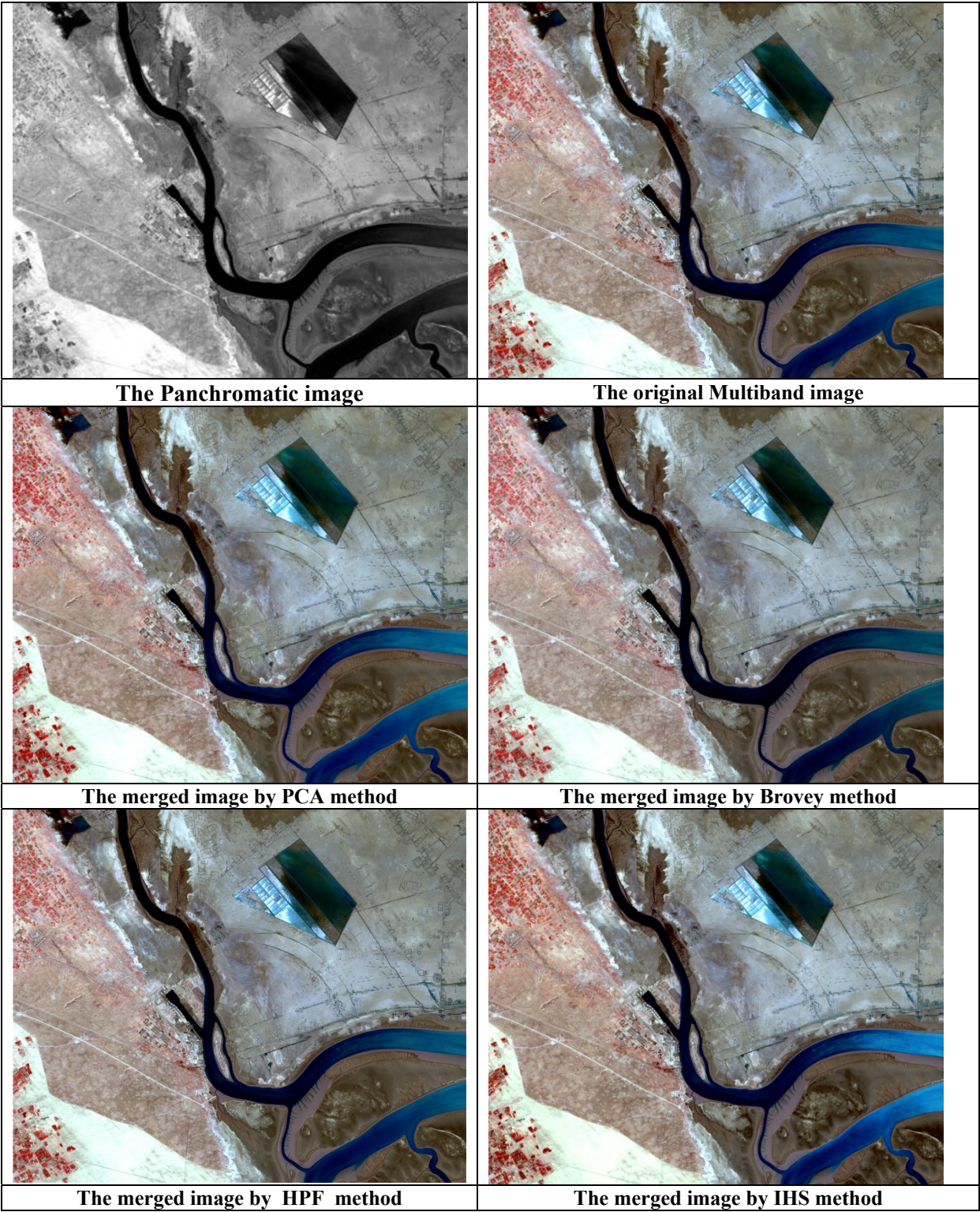


Figure 3 The original (panchromatic and multi bands) and the different methods merged images.



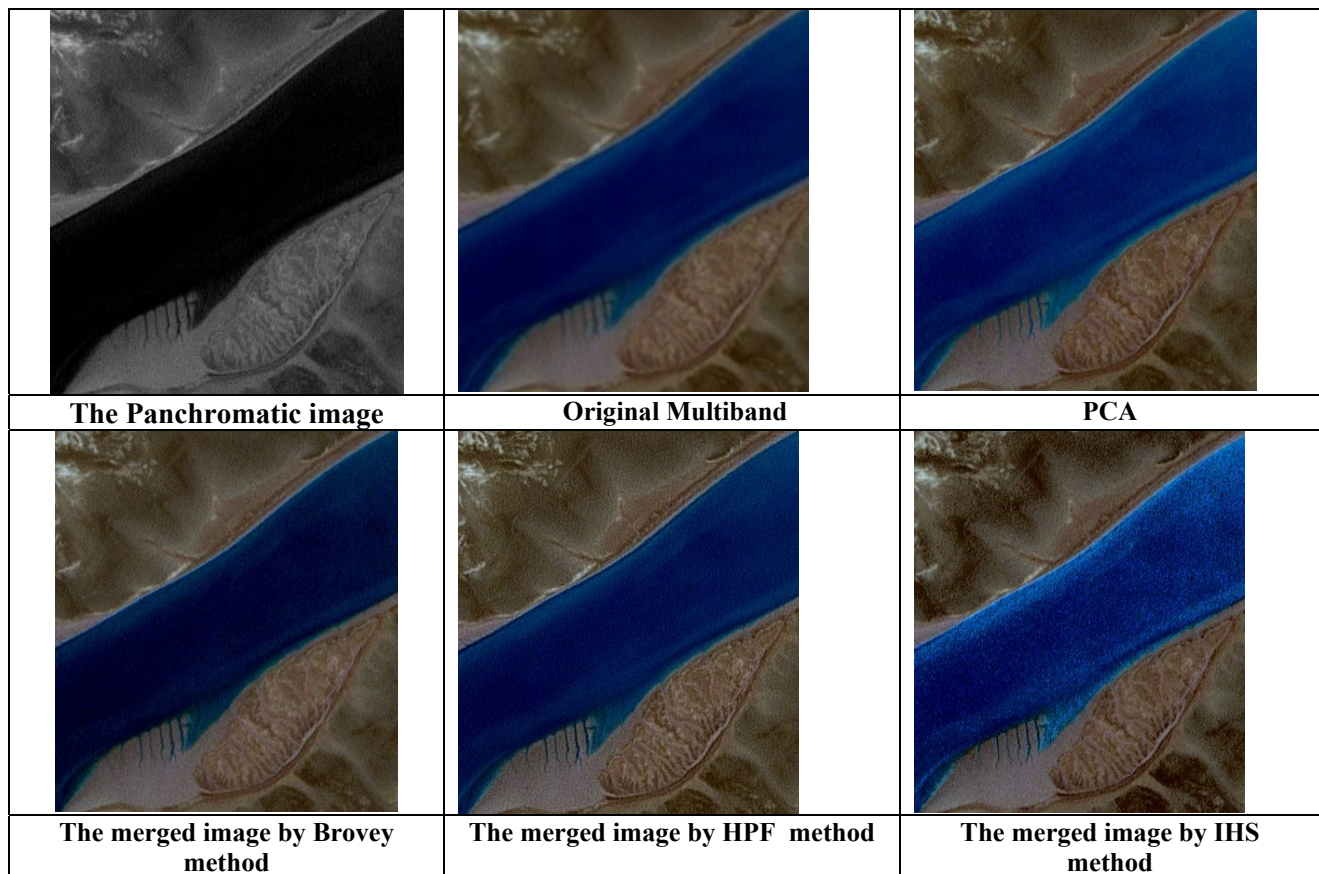


Figure 4 Sub scenes of the original and resulted images, to compare the coastal zone extraction.

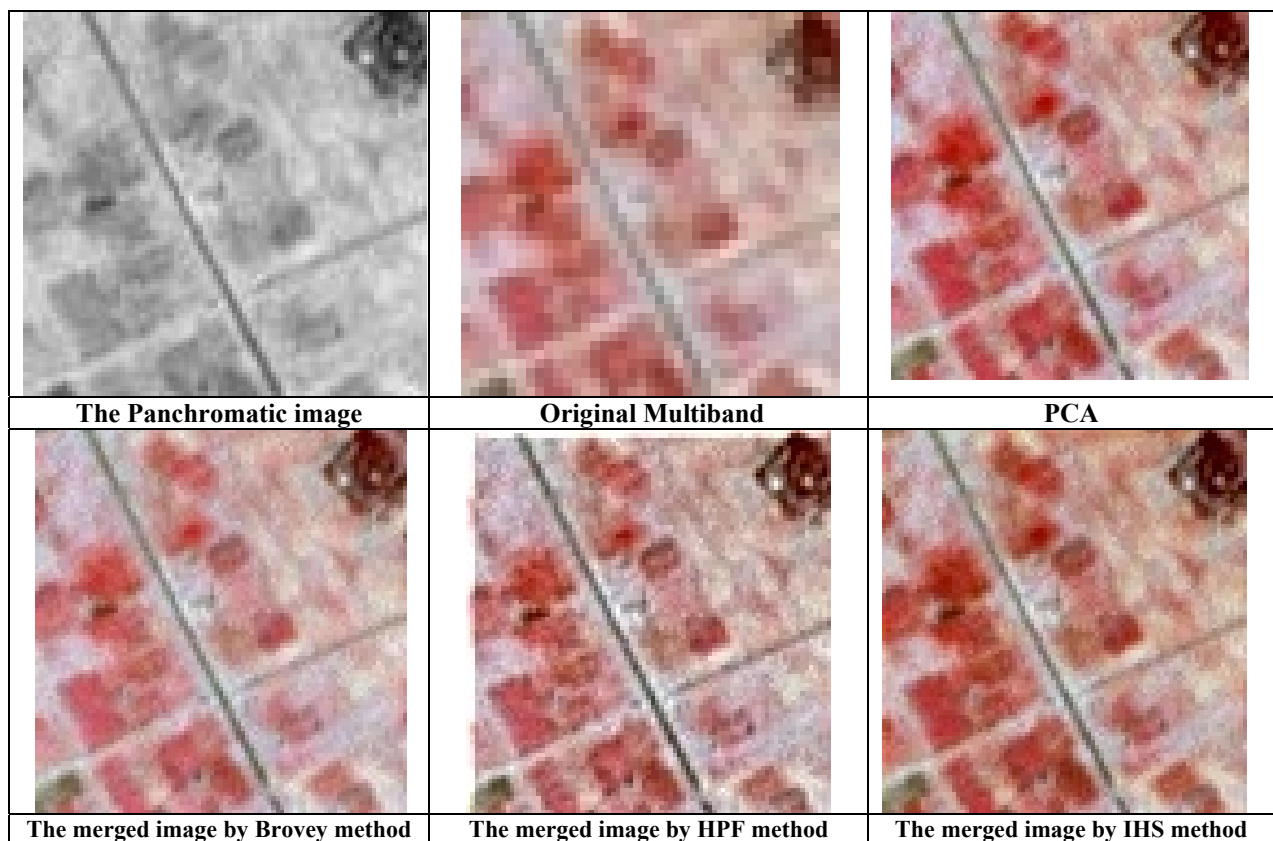


Figure 5 Sub scenes of the original and resulted images, to compare the agricultural zone extraction.

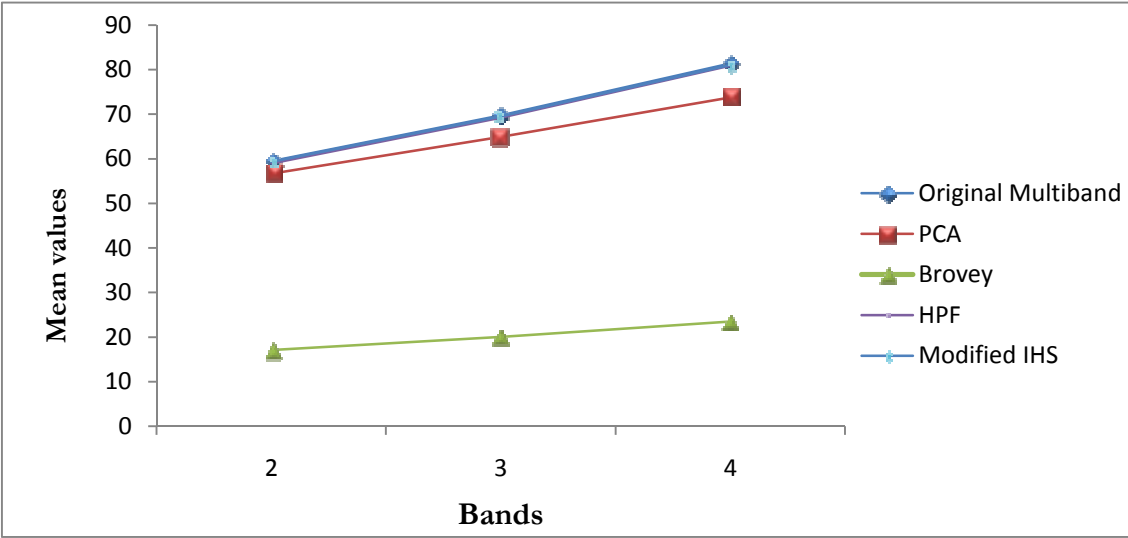


Figure 6 A graphical comparisons among the four techniques and the original multi band image

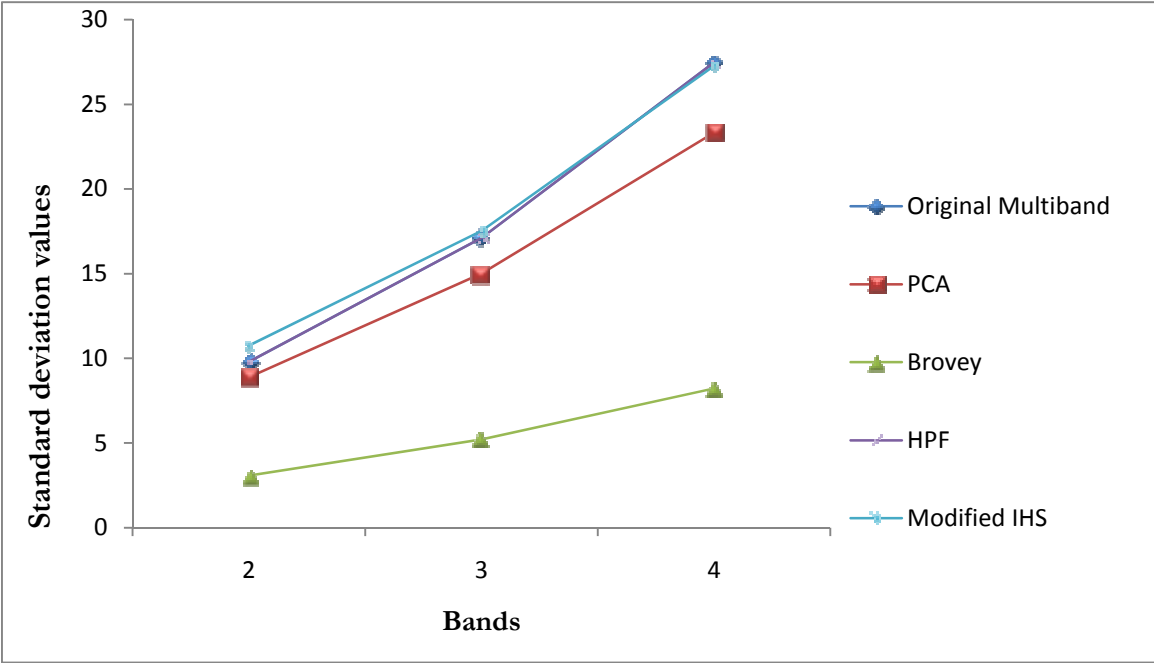


Figure 7 Representation of standard deviation values for the merged and original images.



**Table 1 Statistical information of the Panchromatic, Original Multi band and merged images**

Image	Band	Min	Max	Mean	Median	Mode	Standard Deviation
Panchromatic		13	141	60.695	63	68	16.068
Original Multiband	2	23	129	59.486	60	61	9.787
	3	18	150	69.734	71	76	17.104
	4	14	165	81.368	84	81	27.450
PCA	2	22	130	56.717	56.594	57.859	8.881
	3	6	158	64.937	65.969	68.938	15.003
	4	12	165	73.794	75.949	74.754	23.323
Brovey	2	5.0801	41.837	17.098	17.284	17.572	3.079
	3	3.8371	50.276	20.085	20.526	22.159	5.216
	4	3.3241	49.296	23.512	24.334	23.437	8.216
HPF	2	18	156	58.985	59	60	9.791
	3	5	208	69.234	71	73	17.107
	4	0	248	80.869	84	82	27.450
Modified IHS	2	16	129	59.360	60	61	10.756
	3	9	150	69.527	71	70	17.526
	4	14	165	81.007	85	95	27.251



## Numerical and experimental investigation on the performance of the capillary tube using R-134a and R-600a

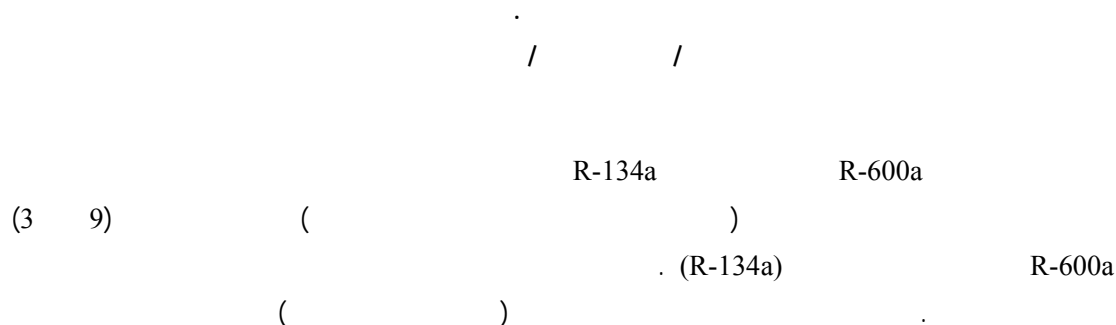
Prof.Dr.Qasim Saleh Mehdi  
Mech. Eng. Dept.  
College of Engineering  
AL-Mustansiriya University  
E-mail:qasim60@yahoo.com

Baydaa Jaber Nabhan  
Mech. Eng. Dept  
College of Engineering  
AL-Mustansiriya University  
E-mail:Baydaa1971@yahoo.com

### Abstract

In this paper, isobutane (R-600a) is used as a suitable substitute for (R-134a) when changing the length of capillary tube. And the experimental data on capillary tube are obtained under different conditions such as (subcooling and ambient temperatures) on domestic refrigerator (9ft3 size), this data shows that (R-600a) a suitable substitute for (R134a). The test presented a model for a steady state, two-phase flow in capillary tube for vapour compression system. The numerical model depends on conservation equations (mass, energy and momentum) as well as the equation of state for refrigerant. The solution methodology was implemented by using finite difference techniques. The system results indicate that it is possible to change the refrigeration system using (R-134a) by shorter capillary tube length about (28.6%) when using (R-600a). The theoretical results for different variables such as (subcooling and ambient temperatures) showed a good agreement with the "ASHRAE" tables and experimental results.

**Key Word:** Refrigeration; Capillary Tube; Domestic refrigerator; R-134a; R-600a.



R-600a (28.6%)  
"ASHRAE"  
(  
R-134a  
R-600a R-134  
:

## Introduction

The capillary tube is one type of expansion device used in small vapour compression refrigerating and air conditioning systems. The capillary tube is made from an extremely small-bore hollow copper tube (in the order of 0.5-1.5mm diameter) of about 2-5m length [Bansal and Rupasinghe, 1998]. Liquid refrigerant enters the capillary tube, and as it flow through the tube, the pressure drops because of friction and acceleration of the refrigerant. Its simplicity, low initial cost and low starting torque of compressors are the main reasons for its use.

The flow enters the capillary tube in a subcooled condition, while in a subcooled the pressure drop is linear and the temperature is constant. Once the pressure drops down to saturation condition, a superheated liquid flow is realized for a short distance (metastable region). In this region vapour bubbles appear and pressure suddenly drops. However, this is a metastable region because of the existence of superheat liquid together with saturated liquid and vapour fluid. After this region the local thermodynamic equilibrium state, liquid-vapour two phases is reached as shown in Fig.

(1).Choked flow usually is encountered at the tube exit.

Especially in the past 20 years or so, the flow characteristics of refrigerant passing through capillary tubes have been widely studied experimentally or analytically with alternative and common traditional refrigerants.

Koizumi and Yokoyama (1980), measured pressure and temperature distributions for refrigerant R-22 flow in adiabatic capillary tubes, verifying the occurrence of the delay of vaporization. The authors proposed a simple calculation method to find the length of the liquid region. Such method was developed for adiabatic flow, based on integration of the momentum equation and assuming two-phase homogeneous flow. The experimental results showed a delay of vaporization ranging from 2°C to 4°C and the average length of the metastable flow was 0.39m. The maximum length was 0.6m, and calculations agree with experimental data within  $\pm 3\%$ .

Li et al. (1990), investigated the effects of the diameter, back pressure, subcooling degree and mass flow rate on metastability for R-12. It was found that a decrease in the length of



metastable flow region as the capillary tube diameter increases. The mass flow rate increased as consequence of a larger underpressure of vaporization  $\Delta P_{\text{vap}}$ , and an increase in  $\Delta T_{\text{sub}}$  caused a decrease in  $\Delta P_{\text{vap}}$ . It was also verified that the position of the flashing inception was not affected by backpressure variations.

**Chen et al. (1990)**, developed a correlation for the delay of vaporization for R-12 flow through capillary tube based on the nucleation theory initially developed by Alamgir and Lienhard (1981) and with experimental data of Li et al. (1990). For instance, Dirik et al. (1994) verified that Chen's correlation was suitable for R-134a flow through capillary tubes, and Bittle and Pate (1996) used such correlation for R-22, R-134a, R-152a and R-410A.

**Valladares et al. (2002)**, showed that the importance of considering the metastable region in the mathematical model gives more accurate mass flow rate predictions. Results presented included both metastable flow modeling and non-metastable flow modeling. Also homogeneous and separated flow model for metastable flow was presented using different empirical correlation which was essential in the numerical model.

**Li Yang and Wen Wang (2007)**, studied a generalized correlation for predicting the refrigerant mass flow rate through the adiabatic capillary tube with approximate

analytic solutions based on the extensive data for R-12, R-22, R-134a, R-290, R-600a, R-410A, R-407C, and R404A, in which a homogeneous equilibrium model for two-phase flow was employed. The predicted values from the correlation agree well with the experimental data for those seven refrigerants.

The aim of this paper is to evaluate the overall performance of the refrigeration system, in the steady state condition through experimental and theoretical modeling using R-134a and R-600a. The work will also include the following points:

1. Investigating the performance of alternative refrigerant R-600a to be used in the same system.
2. Analyzing the experimental data for various conditions for flow in an adiabatic capillary tube using Bourdon gauge to measure pressure, and using thermocouple type (T) to monitor temperature, along the capillary tube.
3. Comparing the calculation results with experimental results.

### Mathematical Model

The pressure distribution pattern along a tube depends on a many factors such as the tube geometry (i.e. tube length, inner diameter, roughness) and refrigerant entrance conditions (i.e. condensing pressure, degree of sub-cooling and/or quality). The mass flow rate has

Significant influence on the fluid flow, especially in the two-phase region and affects the pressure drop and quality of the refrigerant. The exit condition, either choked or unchoked, also depends considerably on the mass flow rate. For a given condensing pressure and tube length, the mass flow rate through the capillary tube remains constant for evaporating pressure lower than the choke value. **Fig. (2)** shows the schematics of typical capillary tube.

The following assumptions are made in this model:

- Straight horizontal and constant inner diameter and roughness capillary tube,
- One-dimensional flow,
- Adiabatic and homogeneous two-phase flow,
- The flow in the single-phase metastable region is considered,
- Thermodynamic equilibrium through the capillary tube.

According to the assumption above, the governing equations used in describing the flow are presented as follows:

### I. Entrance Region

In this region losses due to sudden contraction and dynamic pressure head losses, magnitude of this drop is calculated from equation: [Fatouh, 2007]

$$\Delta P_c = (G)^2 \left( \frac{1}{2\rho_{SL}} \right) \left( \frac{1}{C_{con}} - 1 \right)^2 \quad (1)$$

The contraction coefficient ( $C_{con}$ ) is correlated as a function of area ratios ( $A_2/A_1$ ) in the following form:

$$C_{con} = 0.6083 + 0.547 \left( \frac{A_2}{A_1} \right) - 0.326 \left( \frac{A_2}{A_1} \right)^2 + 0.168 \left( \frac{A_2}{A_1} \right)^3 \quad (2)$$

Where  $A_1$  and  $A_2$  are the cross section area of the condenser outlet tube and the capillary tube, respectively.

### II. Single -Phase (Sub-Cooled Liquid) Region

In this region, the fluid is assumed to be incompressible and steady. Also pressure drop is linear, and the refrigerant is entirely in the liquid state. The capillary tube length in the single-phase (subcooled) region can be given by: [Bansal and Wang, 2004]

$$L_{s,p,sub} = \left[ \frac{\rho}{G^2} (P_{cond} - P_{sat}) - d_c (k_i + 1) \right] / f_{sp} \quad (3)$$

Where ( $k_i$ ) is the entrance loss coefficient (for square edged,  $k_i=0.5$ ) and ( $f_{sp}$ ) is the single-phase friction factor.

( $k_i$ ) can be determined from: [Bansal and Wang, 2004]



$$k_i = 0.42 \left[ \left( 1 - \frac{d_c}{D_{cond.}} \right)^2 \right] \quad (4)$$

for  $(d_c/D_{cond.}) < 0.76$

$(f_{sp})$  can be determined from:

[Churchill, 1977]

$$f_{sp} = 8 \left[ \left( \frac{8}{Re_{sp}} \right)^{12} + \frac{1}{(A_{sp} + B_{sp})^{3/2}} \right]^{1/12} \quad (5)$$

Where:

$$A_{sp} = \left[ 2.457 \ln \left( \frac{1}{\left( \frac{7}{Re_{sp}} \right)^{0.9} + 0.27 \frac{e}{d_c}} \right) \right]^{16} \quad (6)$$

$$B_{sp} = \left( \frac{37530}{Re_{sp}} \right)^{16} \quad (7)$$

$$Re = \frac{\rho U d_c}{\mu_f} = \frac{G d_c}{\mu_f} \quad (8)$$

$$G = \frac{\dot{m}}{A} = \rho U = \text{constant} \quad (9)$$

### III. Single-Phase Metastable Region

The delay of vaporization has been observed from some experiments [Mikol,

1963], [Koizumi and Yokoyama, 1980] and [Li et al., 1990], which means that vaporization does not occur at  $P_s$  but at some point ( $P_v$ ) below it, which is also known as the non-thermodynamic equilibrium. The capillary length in this region is known as the metastable length. [Chen et al., 1990] studied the flow through capillary tubes and presented a correlation to predict the underpressure ( $P_s - P_v$ ). It is as follows:

$$\frac{(P_s - P_v) \sqrt{k_a T_{sat}}}{\sigma^{1.5}} = 0.679 \left( \frac{v_{g1}}{v_{g1} - v_{f1}} \right) Re^{0.914} \left( \frac{\Delta T_{sub}}{T_c} \right)^{-0.208} \left( \frac{d_c}{D} \right)^{-3.18} \quad (10)$$

Where  $D$  is the reference length.

$$= \sqrt{\frac{k_a T_{sat}}{\sigma}} \times 10^4 \quad (11)$$

The metastable length can then be given by:

$$L_{meta} = (P_s - P_v) \cdot 2 d_c \rho_{sp} / f_{sp} G^2 \quad (12)$$

The metastable length generally decreases with the degree of sub-cooling and increases with increasing condenser temperature, increasing tube inner diameter.

[Bansal and Wang, 2004]

### IV. Region Equilibrium Two-Phase Region

[Stoecker & Jones, 1982] and [Bansal and Rupasinghi, 1998] presented a flow model through the two-phase region based on conservation of mass, energy and momentum.



Their models will be regarded in this study. Consider a control volume in the two-phase region as shown in **Fig. (2)**. The conservation of mass can be expressed as follows:

$$\dot{m} = \rho A U = \text{constant} \quad (13)$$

$$\frac{\dot{m}}{A} = \rho U \quad (14)$$

$$U = \frac{G}{\rho} = G v \quad (15)$$

For steady-state adiabatic with no external work and neglecting the elevation difference, the conservation of energy can be expressed as follows:

$$h + \frac{U^2}{2} = \text{constant} \quad (16)$$

The fluid enthalpy and specific volume are determined by the following equations:

$$h = (1 - \chi)h_f + \chi h_g \quad (17)$$

$$v = (1 - \chi)v_f + \chi v_g \quad (18)$$

Considering the energy balance between point (1) and any point along the capillary tube in two-phase flow region, substituting

equations (17) and (18) into equation (16) gives:

$$h_1 + \frac{U_1^2}{2} = h_f + \chi(h_g - h_f) + \frac{G^2}{2}(v_f(1 - \chi) + v_g \chi)^2 \quad (19)$$

Expanding the right-hand side and rearranging gives:

$$[(v_g - v_f)^2 \frac{G^2}{2} \chi^2 + [G^2 v_f(v_g - v_f) + (h_g - h_f) \chi] + [\frac{G^2 v_f^2}{2} - h_1 \frac{U_1^2}{2} + h_f] = 0 \quad (20)$$

This is in the form of a quadratic equation in which the quality ( $\chi$ ) can be expressed as:

$$\chi = \frac{-h_g - G^2 v_f v_{fg} + \sqrt{(G^2 v_f v_{fg} + h_g)^2 - (2G^2 v_f^2) [\frac{G^2 v_f^2}{2} - h_1 \frac{U_1^2}{2} + h_f]}}{G^2 v_{fg}^2} \quad (21)$$

Where  $h_{fg} = h_g - h_f$  and  $v_{fg} = v_g - v_f$

The conservation of momentum can be expressed by again considering the element of fluid as shown in **Fig. (3)**.

The sum of the pressure forces acting on the left and the right ends and the shear force acting on the inner pipe wall is equal to the time rate of change of linear momentum of the system. Therefore,

$$(P \frac{\pi d_c^2}{4}) - (P + dP) \frac{\pi d_c^2}{4} - \tau_w \pi d_c dL = \dot{m} dU \quad (22)$$

Where  $\tau_w$  is the wall shear stress and defined as:

$$\tau_w = f_{tp} \frac{\rho U^2}{8} \quad (23)$$

On rearranging, we get:

$$dL = -\frac{d_c}{f_{tp}} \left[ \frac{2dp}{\rho U^2} + \frac{2\dot{m} dU}{A \rho U^2} \right] \quad (24)$$

For a constant mass flow rate such that  $d\dot{m} = 0$ , we have:

$$-\frac{dU}{U} = \frac{d\rho}{\rho} \quad (25)$$



Substituting equation (25) into equation (24) gives:

$$dL = \frac{2d_c}{f_{tp}} \left[ \frac{-\rho dp}{G^2} + \frac{d\rho}{\rho} \right] \quad (26)$$

The capillary tube between points (1) and (4) can be divided into numerous sections as shown in **Fig. (4)**.

The two-phase friction factor ( $f_{tp}$ ) can be calculated from [Lin et al., 1990] correlation as given:

$$f_{tp} = \phi_i^2 f_{sp} \left[ \frac{\nu_{sp}}{\nu_{tp}} \right] \quad (27)$$

Where  $f_{sp}$  is calculated from equation (5).

$\phi$ : Friction multiplayer is given by:

$$\phi^2 = \left[ \frac{\frac{8}{\text{Re}_{tp}} + \frac{1}{(A_{tp} + B_{tp})^{3/2}}}{\frac{8}{\text{Re}_{sp}} + \frac{1}{(A_{sp} + B_{sp})^{3/2}}} \right]^{1/2} \left[ 1 + \chi \left( \frac{\nu_g}{\nu_f} - 1 \right) \right] \quad (28)$$

Where: The two-phase Reynolds number is defined by:

$$\text{Re}_{tp} = \frac{U d_c}{\mu_{tp} \nu_{tp}} \quad (29)$$

Where:

$$U = G \nu_{tp} = G(\chi \nu_g + (1 - \chi) \nu_f) \quad (30)$$

Dynamic viscosity ( $\mu_{tp}$ ) can be determined from: [Beattie and Whalley, 1981]

$$\mu_{tp} = \alpha_{tp} \mu_g + \mu_f (1 - \alpha_{tp}) (1 + 2.5 \alpha_{tp}) \quad (31)$$

$$\text{Where: } \alpha_{tp} = \frac{\chi \nu_g}{\nu_f + \chi \nu_{fg}} \quad (32)$$

Thus from equation (26), the two-phase length can be expressed as: [Wongwises and Pirompak, 2001].

$$L_{tp} = d_c \left[ \frac{-2}{G^2} \int_{P_1}^{P_4} \frac{\rho}{f_{tp}} dp + 2 \int_{P_1}^{P_4} \frac{d\rho}{\rho f_{tp}} \right] \quad (33)$$

Thus, total capillary tube length is the summation of the above three lengths in the three different regions as:

$$L_{Tot} = L_{sp,sub} + L_{meta} + L_{tp} \quad (34)$$

The pressure drop in two-phase region can be calculated from the equation: [Ahmed, 2001]

$$P_i - P_{i+1} = \frac{f_{tp} G^2 L_{tp}}{2 d_c} \left[ \nu_f + \frac{\chi_i + \chi_{i+1}}{2} \nu_{fg} \right] + G^2 \nu_{fg} (\chi_{i+1} - \chi_i) \quad (35)$$

## Experimental Apparatus and Measurements

The experimental test rig includes the actual refrigeration system (domestic refrigerator in size 9ft<sup>3</sup>) which was originally manufactured to work with R-134a. A schematic diagram of a single door domestic refrigerator with the instruments and their locations has been shown in **Fig. (5)**.

The apparatus was designed to allow simultaneous control of the pressure and temperature of the liquid entering the capillary tube and also the evaporator pressure. The pressure distribution along capillary tube was measured by precision Borden type gauges. And temperature measurement of the flowing

refrigerant was made by (copper/constantan) thermocouples type's (T). Refrigerant temperatures were measured by mounting thermocouple's probe directly into a groove through the capillary tube wall. The selected capillary tube specifications are (0.82mm) and (2.28mm) inside and outside diameters respectively, with long (2.8m) for R-134a. This length of capillary tube was calculated theoretically, based on a constant inner diameter of the capillary tube. With respect to R-600a, the capillary tube length has been changed several times until the desired evaporator pressure was reached.

As a result to the delay of vaporization phenomenon, and to find the underpressure of vaporization, pressure and temperature sensors must be installed along the capillary tube. In order to measure the pressure drop along the capillary tube, pressure taps were made in the wall of capillary tube using (T) joint. **Fig. (6)** shows a photo of the (T) joint.

The capillary tube cuts into parts, each two parts connected by (T) joint. A (T) joint (Brass covered with chromium) consist of two parts, the first one is a tube with (3.4mm) , (4mm) inside and outside diameters , respectively. This part is connected two parts of capillary tube by solder. The second one is also a tube with (3.4mm), (4mm) inside and outside diameters respectively. This part is constructed with a broad ends contains flair,

which was connected to pressure gauge in order to have a closed chamber.

## **Results and Discussion**

### **1. Computation Results**

The mathematical sample for simulation of capillary tube in adiabatic flow depends on dividing the tube into three regions [liquid (single-phase), delay of vaporization (metastable) and two-phase flow] regions.

**Figs (7), (8), (9) and (10)** show the distribution of pressure and temperature along capillary tube for R-134a and R-600a, respectively. Pressure and temperature distribution for these figures were plotted at variable degree of subcooling. It can be noticed that as subcooling degree increases, then liquid region length increases, while in metastable and two-phase regions are decreases. Also, the liquid region length for R-134a is less than that for R-600a, while metastable region length and two-phase region length for R-134a are higher than that for R-600a.

**Figs (11), (12), (13) and (14)** show the effect of different ambient temperatures on (p-h) diagram at constant subcooling temperature difference of (3°C) and (8°C) for R-134a and R-600a, respectively.

### **2. Experimental Results**

**Fig. (15)** shows increase of COP with superheat (suction temperature) where



subcooling degree is constant. It was observed that COP value for R-134a is lower than that for R-600a.

**Fig.(16)** shows the underpressure of vaporization ( $p_s - p_v$ ) as a function of the mass flow rate. It was observed that at a fixed subcooling condition, the underpressure of vaporization increases with an increase of the mass flow rate. This is because of the specific volume for refrigerant vapour. Also, it can be shown that underpressure of vaporization for R-600a is less than that for R-134a in the same system, where R-600a has specific volume for vapour higher than that for R-134a.

**Fig. (17)** shows that the underpressure of vaporization is a function of the subcooling degree for refrigerant. It can be seen that the underpressure of vaporization decreases with an increase in the subcooling of the refrigerant,  $\Delta T_{\text{sub}}$  ranges (3-13°C). This is because of the pressure drop in a single-phase region.

**Figs (18) and (19)** show the pull down time for R-134a and R-600a in the refrigerator freezer and refrigerator cabin, respectively. Pull down time is defined as the time required for changing the freezer air temperature from ambient condition 303K (30°C) to the desired final temperature 261K (-12°C) and the temperature of the air in the cabin should be maintained at 279K (6°C) according to ISO standard for the considered refrigerator class [Mohanraj et al, 2002].

The time required to reach the required freezer air temperature of nearly (-12°C) for R-134a and R-600a are approximately (110 and 90 min) respectively. Moreover, the time required to reach the required cabin air temperature of nearly (6°C) for R-134a and R-600a are approximately (95 and 83 min) respectively. And as a result, it can be noticed that the pull down time (to reach steady state) for R-600a less than that of R-134a.

**Figs. (20) and (21)** show the difference in COP for refrigerants with ambient temperature and subcooling degree. It can be observed that COP of the system decreases with increasing ambient temperature. However, the COP of the system increases with increasing subcooling degree (and constant superheating degree  $\Delta T_{\text{sup}}$ ). And as a result, it can be concluded that COP of the system using by R-600a is higher than that of R-134a. This is because of the R-600a operating with condensing pressures less than that of R-134a at different ambient temperatures leading to less power consumption for R-600a when compared with R-134a.

## Conclusions

- (1) Through the theoretical results, it was noticed the following:
  - a. R-600a has operating pressures lower than that for R-134a at different working temperatures.

- b. Pressure ratio for R-134a close to pressure ratio of R-600a.
- c. The refrigeration system using R-600a has COP (5%) higher in comparison with R-134a.
- d. The refrigeration system using R-600a has volumetric capacity lower than that for R-134a.
- e. The refrigeration system using R-600a has a discharge temperature lower than that for R-134a and the increase in refrigerant subcooling allows for lowering the discharge temperature which may increase the compressor life

(2) Through the experimental results, it was noticed the following:

- a. COP for the system working by R-600a is higher than that for R-134a at different ambient temperatures and subcooling degrees.
- b. Power consumption for the system working by R-134a is higher than that for R-600a.
- c. Capillary tube used for R-600a must be shorter than that used for R-134a about (28.6%) for the same system.
- d. The underpressure of vaporization decreases with an increase subcooling degree.

**Numerical and experimental investigation on  
The performance of the capillary tube using  
R-134a and R-600a**

- e. The underpressure of vaporization for R-600a during its passage through capillary tube is less in comparison with R-134a.
- f. Pull down time for R-600a is less than that for R-134a.

**References**

- Ahmed Abdul-Nabi Omran, 2001, "Comparative Performance of Refrigerants R-22 & R-290 in Vapour Compression System and Steady the effects on the Capillary tube". M.Sc. Thesis, University of Technology.
- Bansal, P.K., Rupasinghi, A.S., 1998, "A homogeneous model for adiabatic capillary tubes". Applied thermal engineering, vol. 18, pp. (207-219).
- Bansal, P.K., Wang, G., 2004, "Numerical analysis of choked refrigerant flow in adiabatic capillary tubes". Applied thermal engineering, vol. 24, pp. (851-863).
- Beattie, D.R.H. and Whalley, P.B., 1981, "A simple two phase Frictional Pressure Drop Calculation Method". International Journal of Multiphase Flow, vol. 8, pp. 83-87.
- Chen, Z.H., Li, R.Y., Chen, Z.Y., 1990, "A correlation for metastable flow of refrigerant R-12 through capillary tubes". ASHRAE Trans., vol. 96, pp. (550-554).



- Churchill, S.W., 1977, "**Frictional equation spans all fluid flow regions**". Chemical Engineering, vol. 84, pp. (91-92).
- Fatouh, M., 2007, "**Theoretical investigation of adiabatic capillary tubes working with propane/ n-butane/ isobutene blends**". Energy Conversion and Management, vol. 48, pp. (1338-1348).
- Koizumi, H., Yokoyama, K., 1980, "**Characteristics of refrigerant flow in a capillary tube**". ASHRAE Trans., vol. 86, pt. 2, pp. (19-27).
- Li, R.Y., Chen, Z.H., Lin, S., Chen, Z.Y., 1990, "**Metastable flow of R-12 through capillary tubes**". International Journal of Refrigeration, vol. 13, pt. 3, pp. (181-186).
- Li Yang and Wen Wang, 2007, "**A generalized correlation for the characteristics of adiabatic capillary tubes**". International Journal of Refrigeration, pp. (1-7).
- Lin, S., Li, R.Y. and Chen, Z.H., 1990, "**Numerical modelling of thermodynamic non-equilibrium flow of refrigerant through capillary tubes**". ASHRAE Transaction, vol. 96, pt. 1, pp. (542-549).
- Mikol, E.P., 1963, "**Adiabatic Single and Two-Phase Flow in Small Bore Tubes**". ASHRAE Trans., vol. 5, pp. (75-86).
- Mohanraj, M., Jayaraj, S. and Muraleedharan, C., 2002, "**Improved Energy Efficiency for HFC-134a Domestic Refrigerator Retrofitted with Hydrocarbon Mixture HC-290/HC-600a) as Drop in Substitute**". National Institute of Technology, Calicut.
- Stoecker, W.F., and Jones, J.W., 1982, "**Refrigeration and Air Conditioning**". Mc Graw Hill, New York.
- Valladares, O.G., Segarra, C.D. and Oliva, A., 2002, "**Numerical simulation of capillary tube expansion devices behavior with pure and mixed refrigerants considering metastable region**". Applied Thermal Engineering, vol. 22, pp. (379-391).
- Wongwises, S., and Pirompak, W., 2001, "**Flow Characteristics of pure Refrigerants and Refrigerant Mixtures in Adiabatic Capillary Tubes**". Applied Thermal Engineering, vol. 21, pp. (845-861).

#### Nomenclature

$A$  : Area ( $m^2$ )

$\alpha$  : Void fraction

$C_{con}$  : Contraction coefficient (-)

$D^*$  : Reference length (m)

$D_{cond}$  : Condenser inner diameter (m)

$e$  : Inner surface roughness (mm)

$f$  : Friction factor (-)

$G$  : Mass flux ( $kg/m^2.s$ )

$h$  : Specific enthalpy (kJ/kg)

$jd_c$  : Capillary tube inner diameter (m)

$k_a$  : Boltzmann's constant (J/k)



$k_i$  : Entrance loss coefficient (-)

$L$  : Length (m)

$\dot{m}$  : Mass flow rate (kg/s)

$P$  : Pressure (N/m<sup>2</sup> (pa))

$\Delta P_c$  : Pressure drop due to the area contraction  
(N/m<sup>2</sup>)

$Re$  : Reynolds number (-)

$T$  : Temperature (°C )

$U$  : Velocity (m/s )

$v$  : Specific volume (m<sup>3</sup>/kg )

$\chi$  : Dryness fraction (-)

$\phi$  : Friction multiplayer (-)

### Subscripts

$c$  : Critical value

$cond$  : Condenser

$f$  : Liquid phase

$g$  : Vapour phase

$i$  : Present reading according to element  
number

$i+1$  : Next reading

$meta$  : Metastable

$sat,s$  : Saturated

$sp$  : Single-phase

$sub$  : Subcooling

$tp$  : Two-phase

$Tot$  : Total

$v$  : Vapour

### Greek Symbols

$\rho$  : Density (kg/m<sup>3</sup>)

$\mu$  : Dynamic viscosity (kg/m.s )

$\sigma$  : Surface tension (N/m)

$\tau_w$  : Shear stress at wall (N/m<sup>2</sup>)

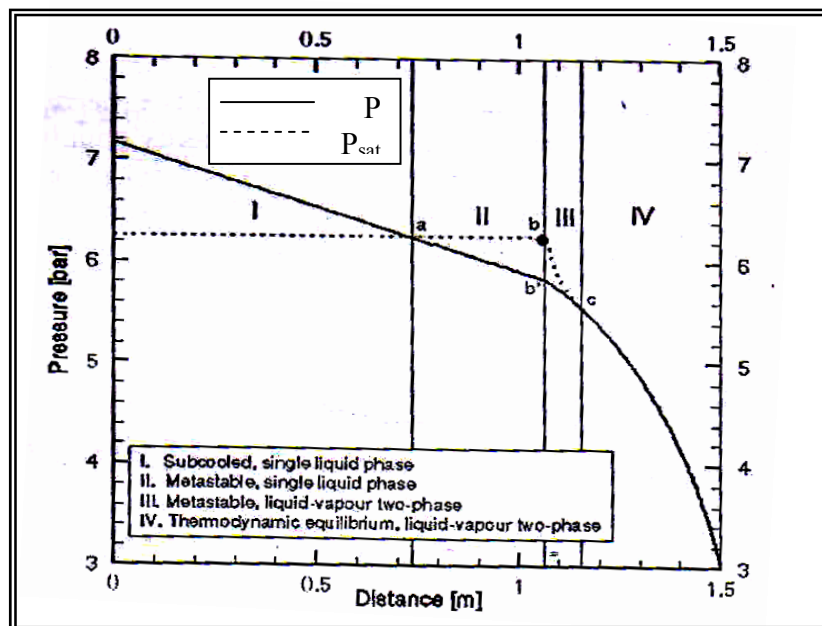


Figure (1): Typical pressure distribution along an adiabatic capillary tube.

[Valladares, 2004]

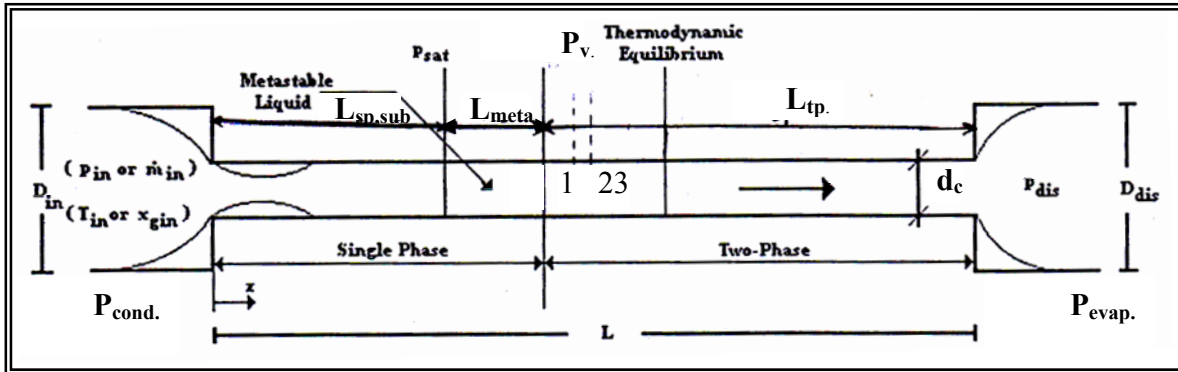


Figure (2): Schematic diagram of a capillary tube [Valladares, 2004]

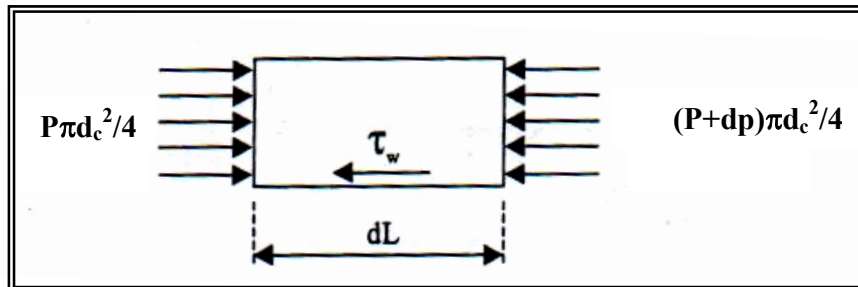


Figure (3): Flow model incremental volume, (two-phase).  
[Wongwises, Pirompak, 2001]

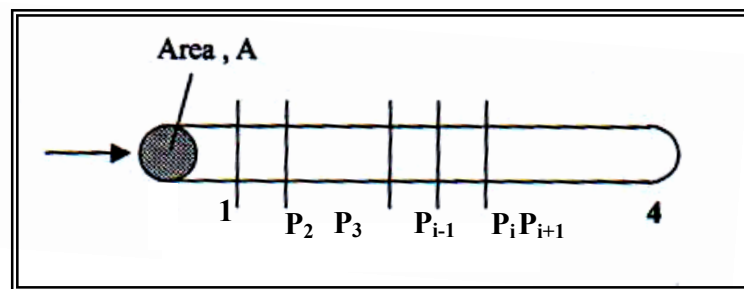
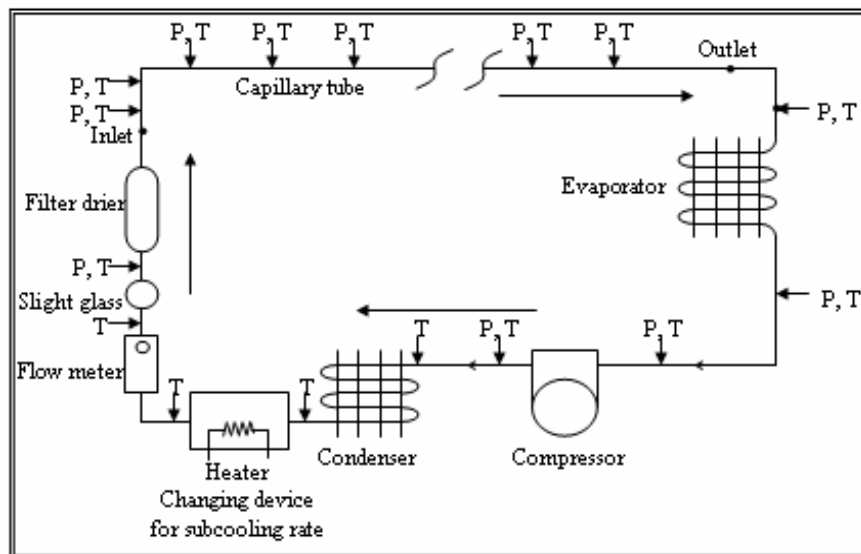
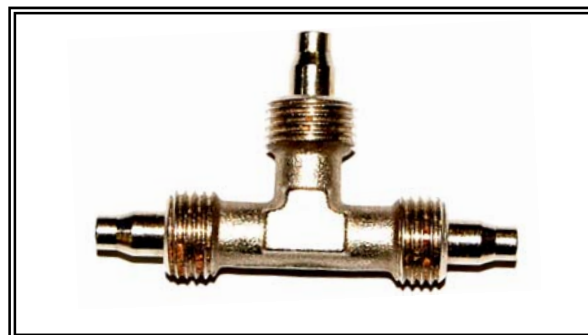


Figure (4): Schematic diagram of simulation approach, (two-phase).  
[Wongwises, Pirompak, 2001]



**Figure (5): Schematic diagram of the experimental set-up. (Domestic refrigerator).Where: P: Pressure gauge & T: Thermocouple.**



**Figure (6): Photo of (T) joint.**

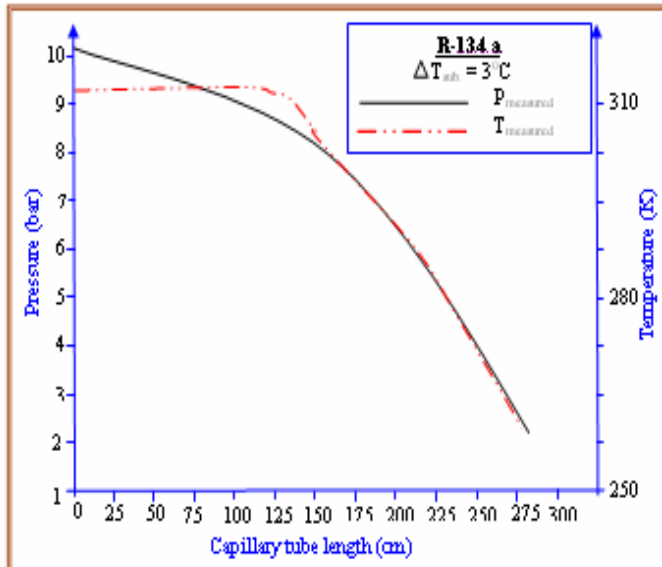


Figure (7): Distribution the pressure and temperature for R-134a along the capillary tube with  $\Delta T_{sub} = 3^{\circ}C$ .

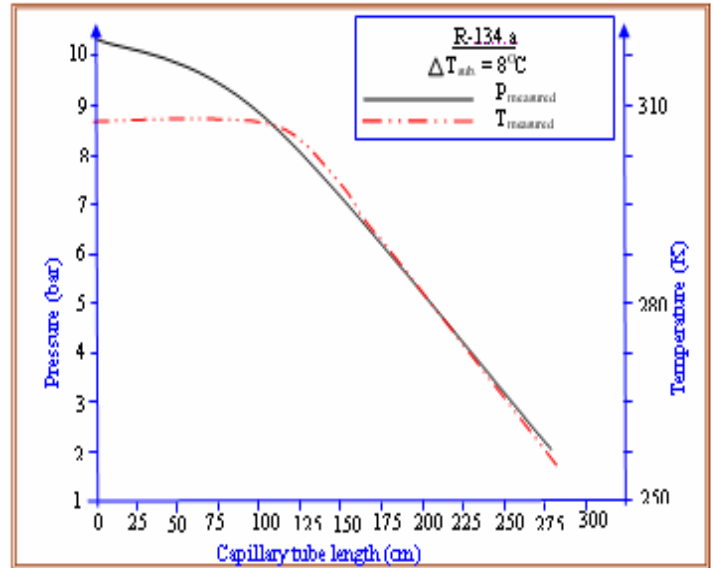


Figure (8): Distribution the pressure and temperature for R-134a along the capillary tube with  $\Delta T_{sub} = 8^{\circ}C$ .

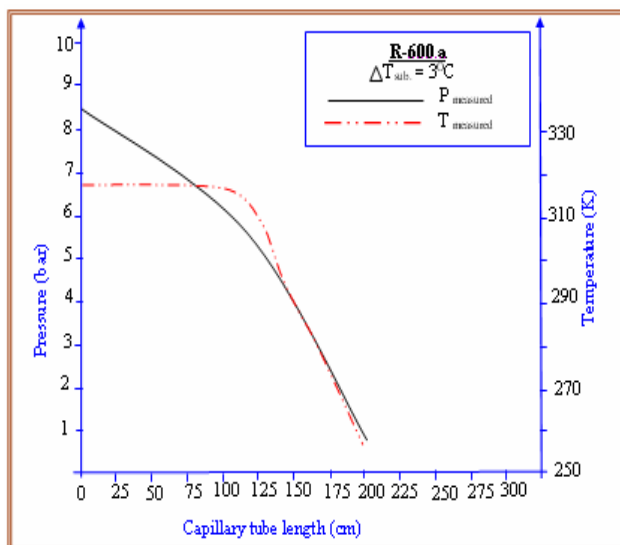
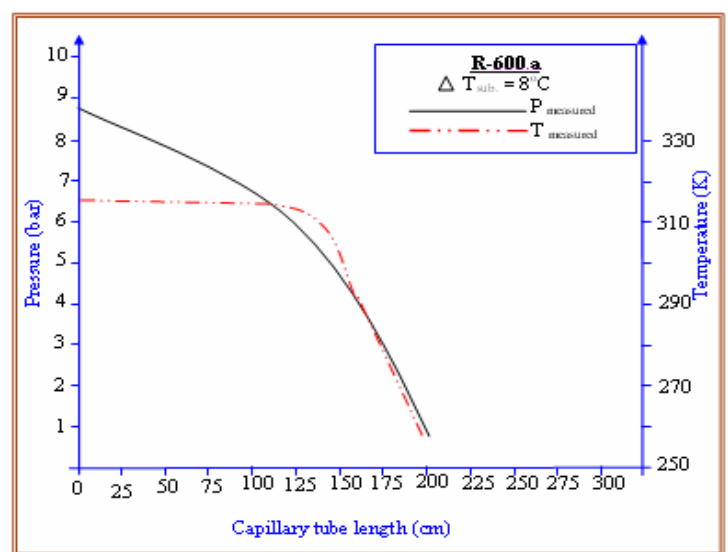


Figure (9): Distribution the pressure and temperature for R-600a along the capillary tube with  $\Delta T_{sub} = 3^{\circ}C$ .



Figure(10): Distribution the pressure and temperature for R-600a along the capillary tube with  $\Delta T_{sub} = 8^{\circ}C$

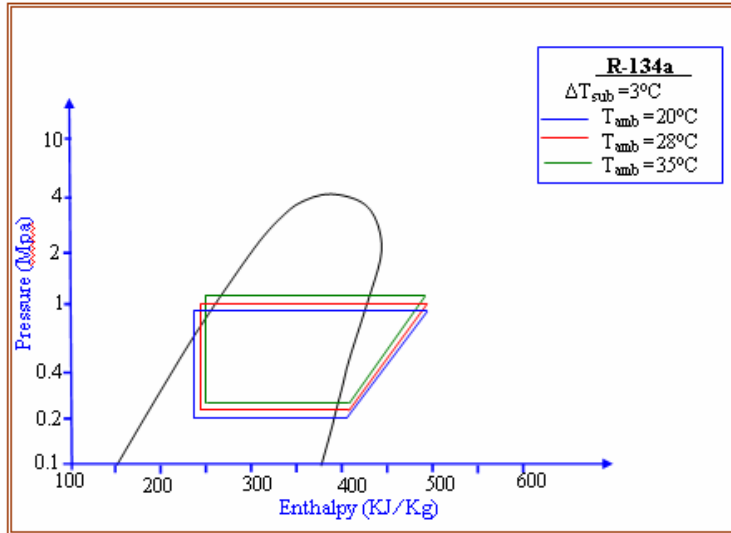


Figure (6.11): Effect of different ambient temperatures on (p-h) diagram at  $\Delta T_{sub} = 3^\circ\text{C}$  for R-134a.

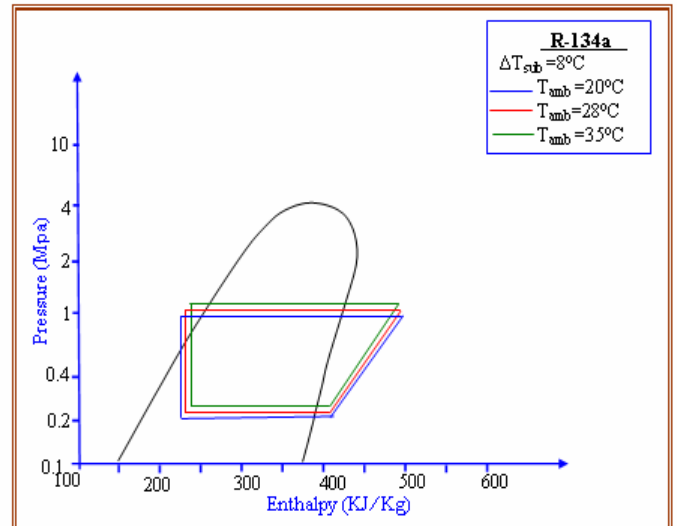


Figure (6.12): Effect of different ambient temperatures on (p-h) diagram at  $\Delta T_{sub} = 8^\circ\text{C}$  for R-134a.

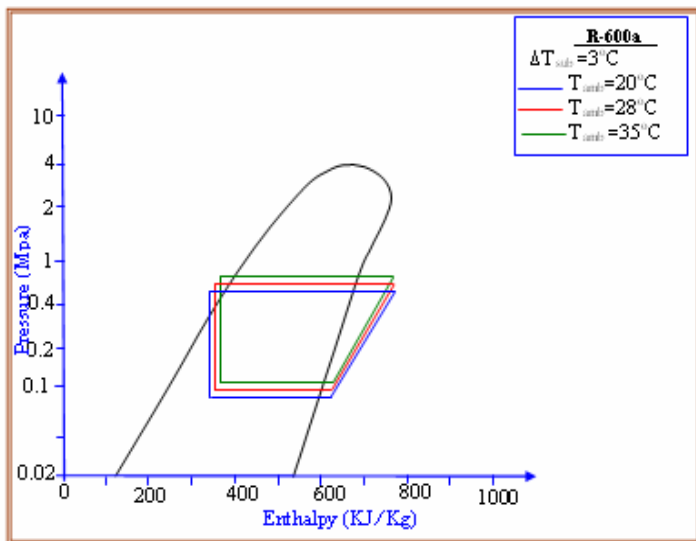


Figure (6.13): Effect of different ambient temperatures on (p-h) diagram at  $\Delta T_{sub} = 3^\circ\text{C}$  for R-600a.

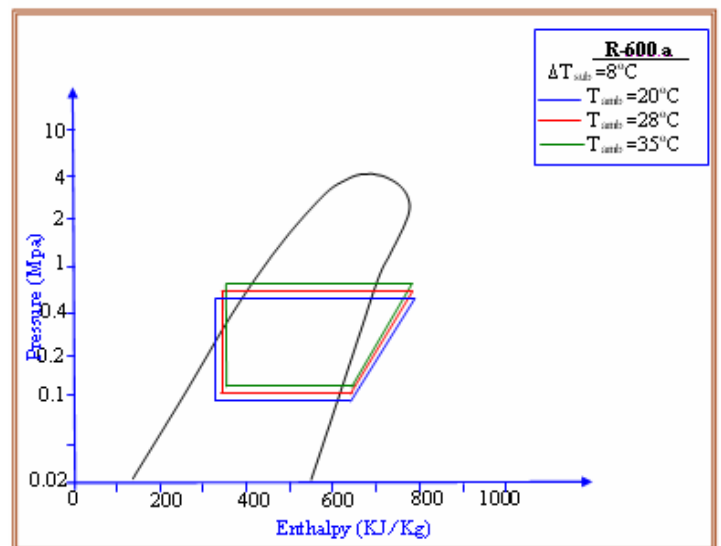


Figure (6.14): Effect of different ambient temperatures on (p-h) diagram at  $\Delta T_{sub} = 8^\circ\text{C}$  for R-600a.

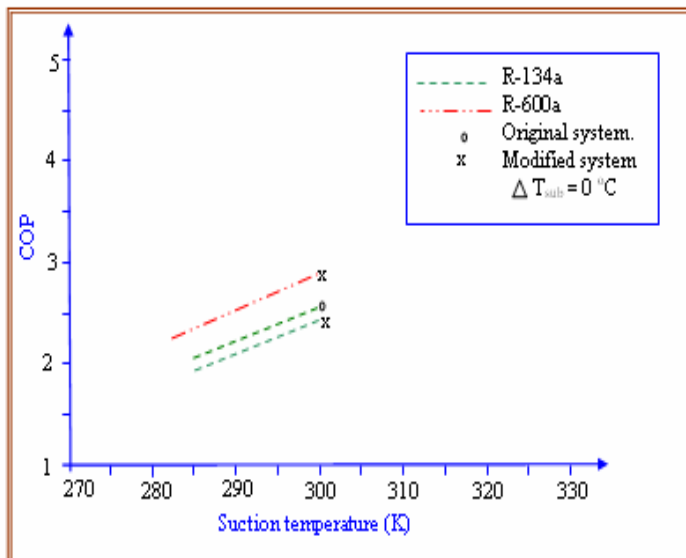


Figure (15): Effect of suction temperature on the COP.

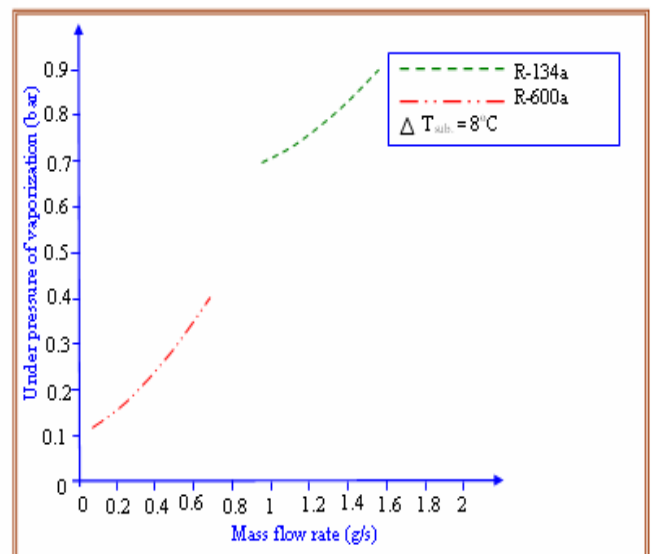
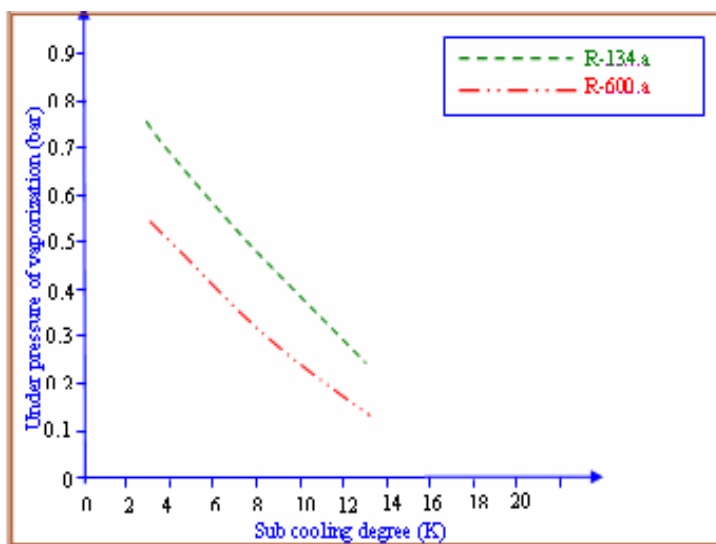
Figure (16): Relationship between underpressure of vaporization and mass flow rate,  $\Delta T_{sub} = 8^{\circ}\text{C}$ .

Figure (17): Relationship between underpressure of vaporization and subcooling.

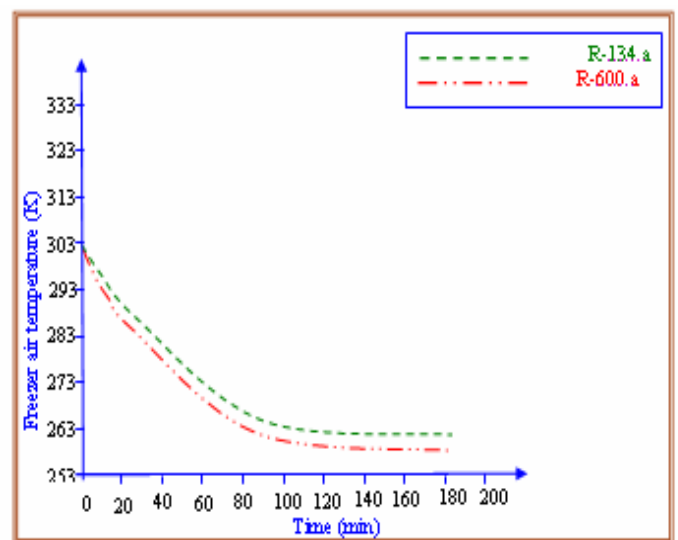


Figure (18): Change freezer air temperature with pull down time for R-134a and R-600a.



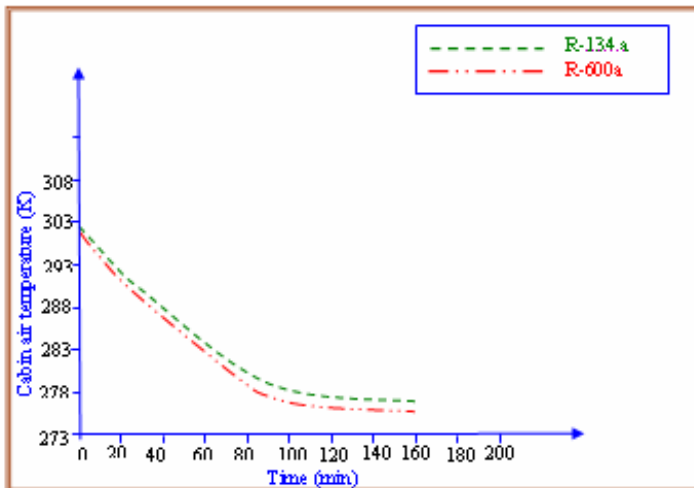


Figure (19): Change cabin air temperature with pull down time for R-134a and R-600a.

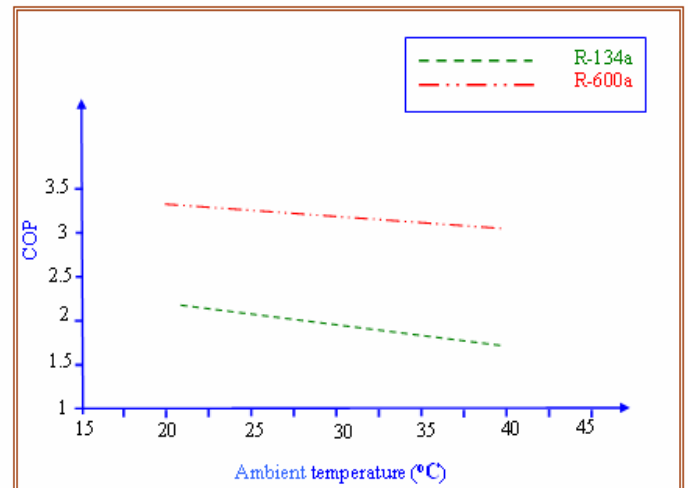


Figure (20): Effect of ambient temperature

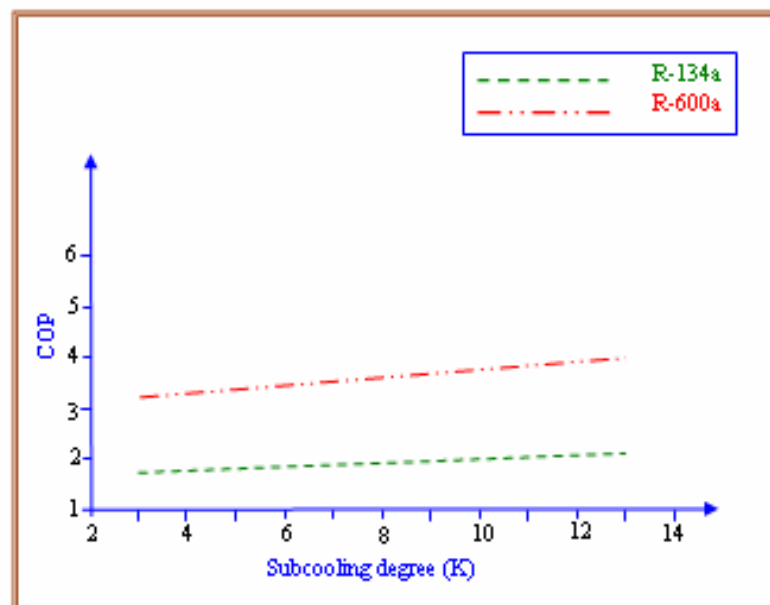


Figure (21): Effect of subcooling degree on the COP.



## Buckling Analysis of Composite Plates under Thermal and Mechanical Loading

Prof. Dr. Adnan Naji Jameel Dr. Ibtehal Abbas Sadiq M.Sc. student Hasanain Ibraheem Nsaif

ebtihalabas@yahoo.com

Univ. of Baghdad / Mech. Eng. Dept., Baghdad-Iraq

### Abstract

Buckling analysis of composite laminates for critical thermal (uniform and linear) and mechanical loads is reported here. The objective of this work is to carry out theoretical investigation of buckling analysis of composite plates under thermo-mechanical loads, and experimental investigation under mechanical loads. The analytical investigation involved certain mathematical preliminaries, a study of equations of orthotropic elasticity for classical laminated plate theory (CLPT), higher order shear deformation plate theory (HSDT), and numerical analysis (Finite element method), then the equation of motion are derived and solved using Navier method and Levy method for symmetric and anti-symmetric cross-ply and angle-ply laminated plates to obtain buckling load by solving eigenvalue problem for different boundary conditions under different thermo-mechanical loading. It also contained a verification study of these methods with those published by other researchers. The results obtained gives good agreement which shows that maximum percentage discrepancy was 7.6152 %. The experimental investigation is to find mechanical properties at room temperature of glass-polyester such as longitudinal, transverse and shear modulus under tension test. Also, to find critical load that cause buckling under buckling test. Analytical and numerical results of critical buckling load studied the effect of Boundary conditions, No. of layers, No. of half wavelengths in y-direction, lamination angle, aspect ratio, and thickness ratio on buckling load under different thermo-mechanical loading condition.

**Keyword:** thermal load, buckling analysis, composite plates, thermo-mechanical load, mechanical load, finite element

### تحليل الانبعاج للصفائح المركبة تحت تأثير الأحمال الحرارية والميكانيكية

#### الخلاصة :

يتضمن البحث دراسة وتحليل الانبعاج للصفائح المواد المركبة المعرضة للأحمال الحرارية (المنتظمة والخطية) والميكانيكية نظريا وتحليل الانبعاج لتلك الصفائح وعمليا. في الجانب النظري تم دراسة معادلات الحركة عن النظرية الكلاسيكية CLPT وعن نظرية اجهاد القص ذات الرتبة العالية HSDT وتم اشتقاق هذه المعادلات وحلها تحليليا باستخدام طريقة نافير وطريقة ليفي لجميع انواع الاسناد للصفائح المركبة المتماثلة وغير المتماثلة مع الاخذ بنظر الاعتبار نسبة طول الى عرض الصفيحة ، عدد الطبقات ، زاوية دوران

الياف الطبقات ، ونسبة نحافة الطبقات وتأثيرها على الحمل الحرج المسبب في تأثير الانبعاج بحل مسألة Eigenvalue للأحمال الحرارية والميكانيكية ، وايضا تم تحليل حمل الانبعاج الحرج عدديا باستخدام طريقة العناصر المحددة. يتضمن الجانب العملي حساب الخواص الميكانيكية (ضمن درجة حرارة الغرفة) لمادة الفايبر كلاس – بوليستر عن طريق اختبار الشد وايجاد حمل الانبعاج الحرج بواسطة اختبار الانبعاج. النتائج التي تم الحصول عليها اعطت موافقة جيدة مع النتائج المنشورة لباحثين اخرين.

## Introduction

Fiber-reinforced composites are used extensively in the form of relatively plate, and consequently the load carrying capability of composite plate against buckling has been intensively considered by researchers under various loading and boundary conditions. Thus far, there have been numerous studies on composite laminated structures which find widespread applications in many engineering fields namely aerospace, biomedical, civil, marine and mechanical engineering because of their ease of handling, good mechanical properties and low fabrication cost. They also possess excellent damage tolerance and impact resistance. The initial theoretical research into buckling analysis was Gossard et al. 1952[1] outlined an approximate method (Ritz method) based on von Karman large-deflection plate theory for calculating the deflections of flat plates subjected to thermal buckling theoretically and experimentally. This method is used to determine the deflections of a simply supported plate subjected to a temperature distribution over the plate surface. Sharma et al. 1980[2] studied the uniaxial compressive buckling response of arbitrary laminated composite plates of anti-symmetric cross-ply and angle-ply laminates for two boundary conditions (SCSC, SCSF). The differential equation governing the elastic response materials have developed using CLPT (classical laminated plate theory) that solved by using Levy method (direct

Integration). The effect of aspect ratio, lamination angle on buckling behavior has been studied. Thangaratnam K. R. et al. 1988[3] studied buckling analysis of composite laminates for critical temperature under thermal load based on finite element method using semiloof element. Results are presented for cross-ply and angle-ply laminates for simply supported, clamped and combined of them with varying ratio for coefficient of thermal expansion and different No. of layers. Liangxin S. and Zhiyu S. 1992[4] investigated bending deflection, buckling load and natural frequency for symmetric cross-ply simply supported laminated plates using Navier solution based on HSPT and Finite element method for different thickness ratio. Kam T. Y. and Chang R. R. 1993[5] studied optimal ply orientation and No. of layers of thick laminated composite plates for max. uniaxial buckling load and vibration frequency based on finite element using global optimization technique for cases of symmetric and anti-symmetric angle-ply simply supported laminated composite plates with various material properties, side to thickness ratio (b/h), aspect ratio (a/b), and different No. of layers. Prabhu M.R. and Dhanaraj R. 1994[6] analyzed thermal buckling of laminated composite plate using finite element method. Nine node elements is employed for thermal buckling analysis of symmetric cross-ply and angle-ply laminates subjected to uniform temperature distribution. The effects of modulus ratio, length to thickness ratio, fiber orientation, aspect ratio and various



boundary conditions (SSSS, CCCC) on the critical temperature are analyzed. Argyris J. and Tenek L. 1994[7], in this study, the behavior of simply supported isotropic and thin laminated composite plates under thermal loads have examined for bending, buckling and post-buckling of symmetric angle-ply square laminates. The material properties are assumed to be independent on temperature. Finite element using triangular shell element contains 3 nodes has been implemented. Ghosh A. K. and Dey S. K. 1994[8] studied buckling analysis of simply supported cross-ply laminated square plates based on finite element using four nodes with seven degree of freedom at each node for thick and thin laminated plates for different aspect ratio, modulus ratio under uniaxial loading conditions. Sun L. and Xiaoping S. 1994[9], developed higher order displacement field for the analysis of the thermo-mechanical buckling of composite plates subjected to thermal or mechanical load. Exact closed-form solutions of symmetric cross-ply laminates are obtained using Navier method including effects of transverse shear deformation on critical temperature and critical load. The effects played with side to thickness ratio, coefficients of thermal expansion ratio and different No. of layers. Simelane S. P. 1998 [10] studied thermal buckling of laminated composite plate using finite element computer package ABAQUS with five degrees of freedom in each node. The effects of lamination angle, modulus ratio, plate aspect ratio, and boundary constraints upon the critical buckling load temperature were investigated. Matsunaga H. 2005[11] presented higher order deformation theory for thermal buckling load of cross-ply laminated composite and sandwich

square plates by using Navier method which can take into account the effects of transverse shear stress of simply supports multilayered plate. Shariyat M. 2007[12] investigated thermal buckling analysis of rectangular composite plates under uniform temperature rise based on layerwise plate theory and determine the buckling temperature using Budiansky instability criterion in a computerized solution. The effects played with boundary conditions (SSSS, CCCC) and various geometric by assuming that material property is to be vary with temperature. Yu L. H. and Wang C. Y. 2008[13] studied the buckling of a rectangular plate based on an elastic foundation. Two opposite sides are simply supported and other two edges is to be (SS and CC), and Levy method (direct integration method) is used based on classical plate theory for different aspect ratio. The plate is subjected to uniaxial and biaxial compressive load. Ozben T. 2009[14] studied the critical uniaxial buckling load using finite element and Ritz methods for different plate dimensions ratio and different orientation angles with symmetric and anti-symmetric laminated plates for (SSSS, SSSC and SCSC). Rajesh et al. 2009[15] examined the random system properties on thermal buckling load of laminated composite plates under uniform temperature rise using finite element for deriving the eigenvalue problem with and without temperature dependent elastic properties. Numerical results present that the characteristics of thermal buckling load of the plate are influence by (SSSS, CCCC and SCSC), plate thickness ratio, aspects ratio. The random system properties having random change in all input material variables, thermal expansion coefficients and plate

thickness. Shiau et al. 2010[16] studied thermal buckling behavior of composite laminated plates using finite element method for cross-ply and angle-ply laminates with various degree of orthotropy, fiber angle, aspect ratio, different boundary conditions and No. of layers.

From above literature review, there are a few literatures available in thermo-mechanical field. In the present work, thermo-mechanical buckling analysis of shear deformable laminated plates with thermo-elastic properties has investigated analytically. In the present study, the temperature distribution field is assumed to be uniform and linear through the plate thickness. Thermal expansion coefficients and elastic constants is assumed to be independent of temperature. The formulations are based on Reddy's higher order shear deformation plate theory and classical laminated plate theory. Navier method of higher order shear deformation theory, Levy method of classical laminated plate theory and Finite element coded by ANSYS 13.0 is used to formulate numerical model. Many design parameters are changed to study their effects on the buckling characteristics such as No. of cross-ply and angle-ply layers, aspect ratio (a/b), thickness ratio (a/h), type of boundary conditions and number of half wavelengths.

## Theoretical Analysis

### A. Classical Laminated Plate Theory (Clpt)

#### Displacement

The displacement field of CLPT contains only three dependent variables [17]:

$$u(x,y) = u_0(x,y) + z\phi_x(x,y) \quad (1a)$$

$$v(x,y) = v_0(x,y) + z\phi_y(x,y) \quad (1b)$$

$$w(x,y) = w_0(x,y) \quad (1c)$$

where:  $\phi_x$ ,  $\phi_y$  denote rotations about y and x axes respectively, and

$u_0$ ,  $v_0$ ,  $w_0$  denote the displacement components along (x,y,z) directions respectively of a point on the mid-plane (i.e....z=0).

### Stress and Strain

The total strains can be written as follows:

$$\begin{Bmatrix} \epsilon_{xx} \\ \epsilon_{yy} \\ \gamma_{xy} \end{Bmatrix} = \begin{Bmatrix} \epsilon_{xx}^{(0)} \\ \epsilon_{yy}^{(0)} \\ \gamma_{xy}^{(0)} \end{Bmatrix} + z \begin{Bmatrix} \epsilon_{xx}^{(1)} \\ \epsilon_{yy}^{(1)} \\ \gamma_{xy}^{(1)} \end{Bmatrix} = \begin{Bmatrix} \frac{\partial u_0}{\partial x} - \alpha_x T_0 \\ \frac{\partial v_0}{\partial y} - \alpha_y T_0 \\ \frac{\partial u_0}{\partial y} + \frac{\partial v_0}{\partial x} - \alpha_{xy} T_0 \end{Bmatrix} + z \begin{Bmatrix} \frac{\partial \phi_x}{\partial x} - \alpha_x T_1 \\ \frac{\partial \phi_y}{\partial y} - \alpha_y T_1 \\ \frac{\partial \phi_x}{\partial y} + \frac{\partial \phi_y}{\partial x} - \alpha_{xy} T_1 \end{Bmatrix} \quad (2)$$

The transformed stress-strain relations of an orthotropic lamina in a plane state of stress are; for  $\bar{Q}_{ij}$ , see [17] :

$$\begin{Bmatrix} \sigma_x \\ \sigma_y \\ \sigma_{xy} \end{Bmatrix}_k = \begin{bmatrix} \bar{Q}_{11} & \bar{Q}_{12} & \bar{Q}_{16} \\ \bar{Q}_{12} & \bar{Q}_{22} & \bar{Q}_{26} \\ \bar{Q}_{16} & \bar{Q}_{26} & \bar{Q}_{66} \end{bmatrix}_k \begin{Bmatrix} \epsilon_{xx} - \alpha_x \Delta T \\ \epsilon_{yy} - \alpha_y \Delta T \\ \gamma_{xy} - 2\alpha_{xy} \Delta T \end{Bmatrix} \quad (3)$$

### Equation of Motion

The Euler-Lagrange equations are obtained by setting the coefficient of  $\delta u_0$ ,  $\delta v_0$ ,  $\delta w_0$  to zero separately [17]:

$$\delta u_0: \frac{\partial N_{xx}}{\partial x} + \frac{\partial N_{xy}}{\partial y} = 0 \quad (4 a)$$

$$\delta v_0: \frac{\partial N_{xy}}{\partial x} + \frac{\partial N_{yy}}{\partial y} = 0 \quad (4 b)$$

$$\delta w_0: \frac{\partial^2 M_{xx}}{\partial x^2} + 2 \frac{\partial^2 M_{xy}}{\partial x \partial y} + \frac{\partial^2 M_{yy}}{\partial y^2} + \hat{N}_{xx} \frac{\partial^2 w}{\partial x^2} + \hat{N}_{yy} \frac{\partial^2 w}{\partial y^2} = 0 \quad (4 c)$$

### Levy Method

Levy method, can be used to solve the governing equations of various laminated plates for which two (parallel) opposite edges are simply supported and the other two edges can have any boundary conditions.

For cross-ply rectangular laminates with edges  $y=0$  and  $y=b$  simply supported and the other two edges  $x=\pm a/2$ , having arbitrary boundary conditions. Assume the following representation of the displacement [17]:

$$u_0(x,y,t) = \sum_{m=1}^{\infty} U_m(x) \sin \beta y \dots (5 a)$$

$$v_0(x,y,t) = \sum_{m=1}^{\infty} V_m(x) \cos \beta y \quad (5 b)$$

$$w_0(x,y,t) = \sum_{m=1}^{\infty} W_m(x) \sin \beta y \quad (5 c)$$

Where:  $\beta = \frac{n\pi}{b}$ ;  $U_m(x)$ ,  $V_m(x)$ ,  $W_m(x)$  are independent of  $y$  (function of  $x$ ).

$n$  = No. of half wavelengths in  $y$ -direction ( $n=1, 2, 3$ )

$b$  = Length of the plate along  $y$ -direction.

For angle-ply rectangular laminates with edges  $x=0$  and  $x=a$  simply supported and the other two edges  $y=\pm b/2$ , having arbitrary boundary conditions. Assume the following representation of the displacement [17]:

$$u_0(x,y,t) = \sum_{m=1}^{\infty} U_m(y) \sin \alpha x \quad (6 a)$$

$$v_0(x,y,t) = \sum_{m=1}^{\infty} V_m(y) \cos \alpha x \quad (6 b)$$

$$w_0(x,y,t) = \sum_{m=1}^{\infty} W_m(y) \sin \alpha x \quad (6 c)$$

Where:  $\alpha = \frac{m\pi}{a}$ ;  $a$  = Width of the plate along  $x$ -direction.

$m$  = No. of half wavelengths in  $x$ -direction ( $m=1, 2, 3$ )

## B. Third Order Shear Deformation Plate Theory (Tsdt)

### Displacement

The displacement field of (HSDT) is of the form [17]:

$$u(x,y,z,t) = u_0(x,y,t) + z\phi_x(x,y,t) - \frac{4}{3h^2} z^3 \left( \phi_x + \frac{\partial w_0}{\partial x} \right) \quad (7 \text{ a})$$

$$v(x,y,z,t) = v_0(x,y,t) + z\phi_y(x,y,t) - \frac{4}{3h^2} z^3 \left( \phi_y + \frac{\partial w_0}{\partial y} \right) \quad (7 \text{ b})$$

$$w(x,y,z,t) = w_0(x,y,t) \quad (7 \text{ c})$$

### Stress And Strain

The total strains can be written as follows [17]:

$$\begin{Bmatrix} \varepsilon_{xx} \\ \varepsilon_{yy} \\ \gamma_{xy} \end{Bmatrix} = \begin{Bmatrix} \varepsilon_{xx}^{(0)} \\ \varepsilon_{yy}^{(0)} \\ \gamma_{xy}^{(0)} \end{Bmatrix} + z \begin{Bmatrix} \varepsilon_{xx}^{(1)} \\ \varepsilon_{yy}^{(1)} \\ \gamma_{xy}^{(1)} \end{Bmatrix} + z^3 \begin{Bmatrix} \varepsilon_{xx}^{(3)} \\ \varepsilon_{yy}^{(3)} \\ \gamma_{xy}^{(3)} \end{Bmatrix} \quad (8 \text{ a})$$

$$\begin{Bmatrix} \gamma_{yz} \\ \gamma_{xz} \end{Bmatrix} = \begin{Bmatrix} \gamma_{yz}^{(0)} \\ \gamma_{xz}^{(0)} \end{Bmatrix} + z \begin{Bmatrix} \gamma_{yz}^{(1)} \\ \gamma_{xz}^{(1)} \end{Bmatrix} + z^3 \begin{Bmatrix} \gamma_{yz}^{(3)} \\ \gamma_{xz}^{(3)} \end{Bmatrix} \quad (8 \text{ b})$$

Where:

$$\begin{Bmatrix} \varepsilon_{xx}^{(0)} \\ \varepsilon_{yy}^{(0)} \\ \gamma_{yz}^{(0)} \\ \gamma_{xz}^{(0)} \\ \gamma_{xy}^{(0)} \end{Bmatrix} = \begin{Bmatrix} \frac{\partial u_0}{\partial x} - \alpha_x T_0 \\ \frac{\partial v_0}{\partial y} - \alpha_y T_0 \\ \frac{\partial w_0}{\partial y} + \phi_y \\ \frac{\partial w_0}{\partial x} + \phi_x \\ \frac{\partial u_0}{\partial y} + \frac{\partial v_0}{\partial x} - \alpha_{xy} T_0 \end{Bmatrix} \quad (8 \text{ c})$$

$$\begin{Bmatrix} \varepsilon_{xx}^{(1)} \\ \varepsilon_{yy}^{(1)} \\ \gamma_{yz}^{(1)} \\ \gamma_{xz}^{(1)} \\ \gamma_{xy}^{(1)} \end{Bmatrix} = \begin{Bmatrix} \frac{\partial \phi_x}{\partial x} - \alpha_x T_1 \\ \frac{\partial \phi_y}{\partial y} - \alpha_y T_1 \\ 0 \\ 0 \\ \frac{\partial \phi_x}{\partial y} + \frac{\partial \phi_y}{\partial x} - \alpha_{xy} T_1 \end{Bmatrix} \quad (8 \text{ d})$$

$$\begin{Bmatrix} \gamma_{yz}^{(2)} \\ \gamma_{xz}^{(2)} \end{Bmatrix} = -\frac{4}{h^2} \begin{Bmatrix} \frac{\partial w_0}{\partial y} + \phi_y \\ \frac{\partial w_0}{\partial x} + \phi_x \end{Bmatrix} \quad (8 \text{ e})$$

$$\begin{Bmatrix} \varepsilon_{xx}^{(3)} \\ \varepsilon_{yy}^{(3)} \\ \gamma_{xy}^{(3)} \end{Bmatrix} = -\frac{4}{3h^2} \begin{Bmatrix} \frac{\partial \phi_x}{\partial x} + \frac{\partial^2 w_0}{\partial x^2} \\ \frac{\partial \phi_y}{\partial y} + \frac{\partial^2 w_0}{\partial y^2} \\ \frac{\partial \phi_x}{\partial y} + \frac{\partial \phi_y}{\partial x} + 2 \frac{\partial^2 w_0}{\partial x \partial y} \end{Bmatrix} \quad (8 \text{ f})$$

The transformed stress-strain relations of an orthotropic lamina in are:

$$\begin{Bmatrix} \sigma_x \\ \sigma_y \\ \sigma_{xy} \end{Bmatrix}_k = \begin{bmatrix} \bar{Q}_{11} & \bar{Q}_{12} & \bar{Q}_{16} \\ \bar{Q}_{12} & \bar{Q}_{22} & \bar{Q}_{26} \\ \bar{Q}_{16} & \bar{Q}_{26} & \bar{Q}_{66} \end{bmatrix}_k \begin{Bmatrix} \varepsilon_{xx} - \alpha_x \Delta T \\ \varepsilon_{yy} - \alpha_y \Delta T \\ \gamma_{xy} - 2\alpha_{xy} \Delta T \end{Bmatrix} \quad (9 \text{ a})$$

$$\begin{Bmatrix} \sigma_{yz} \\ \sigma_{xz} \end{Bmatrix}_k = \begin{bmatrix} \bar{Q}_{44} & \bar{Q}_{45} \\ \bar{Q}_{45} & \bar{Q}_{55} \end{bmatrix}_k \begin{Bmatrix} \gamma_{yz} \\ \gamma_{xz} \end{Bmatrix} \quad (9 \text{ b})$$

### Equation of Motion

The Euler-Lagrange equations are obtained by setting the coefficient of  $\delta u_0$ ,  $\delta v_0$ ,  $\delta w_0$ ,  $\delta \phi_x$ ,  $\delta \phi_y$  to zero separately [29]:

$$\delta u_0: \frac{\partial N_{xx}}{\partial x} + \frac{\partial N_{xy}}{\partial y} = 0 \quad (10 \text{ a})$$



$$\delta v_0: \frac{\partial N_{xy}}{\partial x} + \frac{\partial N_{yx}}{\partial y} = 0 \quad (10 \text{ b})$$

$$\begin{aligned} \delta W_0: & \frac{\partial Q_x}{\partial x} - c_2 \frac{\partial R_x}{\partial x} + \frac{\partial Q_y}{\partial y} - c_2 \frac{\partial R_y}{\partial y} + \\ & c_1 \left( \frac{\partial^2 R_{xx}}{\partial x^2} + 2 \frac{\partial^2 R_{xy}}{\partial x \partial y} + \frac{\partial^2 R_{yy}}{\partial y^2} \right) \\ & + \hat{N}_{xx} \frac{\partial^2 w}{\partial x^2} \\ & + \hat{N}_{yy} \frac{\partial^2 w}{\partial y^2} + 2 \hat{N}_{xy} \frac{\partial^2 w}{\partial x \partial y} = 0 \end{aligned} \quad (10 \text{ c})$$

$$\begin{aligned} \delta \phi_x: & \frac{\partial M_{xx}}{\partial x} - c_1 \frac{\partial P_{xx}}{\partial x} + \frac{\partial M_{xy}}{\partial y} - \\ & c_1 \frac{\partial P_{xy}}{\partial y} - Q_x + c_2 R_x = 0 \end{aligned} \quad (10 \text{ d})$$

$$\begin{aligned} \delta \phi_y: & \frac{\partial M_{xy}}{\partial x} - c_1 \frac{\partial P_{xy}}{\partial x} + \frac{\partial M_{yy}}{\partial y} - \\ & c_1 \frac{\partial P_{yy}}{\partial y} - Q_y + c_2 R_y = 0 \end{aligned} \quad (10 \text{ e})$$

### Navier Method

Navier method can be used to solve the governing equations of various laminated plates for which when all four edges of the laminate are simply supported.

For cross-ply rectangular laminates with edges  $y=0$  and  $y=b$  simply supported and the other two edges  $x=0$  and  $x=a$  simply supported. Assume the following representation of the displacement:

$$u_0(x,y,t) = \sum_{n=1}^{\infty} \sum_{m=1}^{\infty} U_{mn}(t) \cos \alpha x \sin \beta y \quad (11 \text{ a})$$

$$v_0(x,y,t) = \sum_{n=1}^{\infty} \sum_{m=1}^{\infty} V_{mn}(t) \sin \alpha x \cos \beta y \quad (11 \text{ b})$$

$$w_0(x,y,t) = \sum_{n=1}^{\infty} \sum_{m=1}^{\infty} W_{mn}(t) \sin \alpha x \sin \beta y \quad (11 \text{ c})$$

$$\phi_x(x,y,t) = \sum_{n=1}^{\infty} \sum_{m=1}^{\infty} X_{mn}(t) \cos \alpha x \sin \beta y \quad (11 \text{ d})$$

$$\phi_y(x,y,t) = \sum_{n=1}^{\infty} \sum_{m=1}^{\infty} Y_{mn}(t) \sin \alpha x \cos \beta y \quad (11 \text{ e})$$

$$\text{Where: } \alpha = \frac{m\pi}{a} ; \quad \beta = \frac{n\pi}{b}$$

$m$  = No. of half wavelengths in  $x$ -direction ( $m=1, 2, 3$ )

$n$  = No. of half wavelengths in  $y$ -direction ( $n=1, 2, 3$ )

$U_m$ ,  $V_m$ ,  $W_m$  are arbitrary constants to be determined;

For angle-ply rectangular laminates with edges  $y=0$  and  $y=b$  simply supported and the other two edges  $x=0$  and  $x=a$  simply supported. Assume the following representation of the displacement [17]:

$$u_0(x,y,t) = \sum_{n=1}^{\infty} \sum_{m=1}^{\infty} U_{mn}(t) \sin \alpha x \cos \beta y \quad (12 \text{ a})$$

$$v_0(x,y,t) = \sum_{n=1}^{\infty} \sum_{m=1}^{\infty} V_{mn}(t) \cos \alpha x \sin \beta y \quad (12 \text{ b})$$

$$w_0(x,y,t) = \sum_{n=1}^{\infty} \sum_{m=1}^{\infty} W_{mn}(t) \sin \alpha x \sin \beta y \quad (12 \text{ c})$$

$$\phi_x(x,y,t) = \sum_{n=1}^{\infty} \sum_{m=1}^{\infty} X_{mn}(t) \cos \alpha x \sin \beta y \quad (12 \text{ d})$$

$$\phi_y(x,y,t) = \sum_{n=1}^{\infty} \sum_{m=1}^{\infty} Y_{mn}(t) \sin \alpha x \cos \beta y \quad (12 e)$$

### C. Finite Element Method

Finite element method has been employed to analyze critical buckling load for different boundary conditions and various laminate stacking sequences, aspect ratio, thickness ratio and for different number of layers. Analyses performed are this design study utilized a finite element model of the plate. The model was developed in ANSYS 13.0 using the 900 quadrate elements. The global x coordinate is directed along the width of the plate, while the global y coordinate is directed along the length and the global z direction corresponds to the thickness direction and taken to be the outward normal of the plate surface. There are 30 elements in the axial direction and 30 along the width (i.e. 16926 DOF). A convergence study has been performed to select the particular mesh used in this study. A linear buckling analysis (eigenvalue buckling) was performed on the model to calculate the minimum buckling load of the structure. The finite element model is described via an input file using APDL ANSYS language with SHELL 281. This element is suitable for analyzing thin to moderately thick shell structures. The element has eight nodes with six degrees of freedom at each node: translations in the x, y, and z axes, and rotations about the x, y, and z axes. It may be used for layered applications for modeling composite shells. It includes the effects of transverse shear deformation. The accuracy in modeling composite shells is

governed by the first order shear deformation theory.

### Applying Load

It can be apply mechanical load on the solid model through lines. The solver expects all loads to be in terms of the finite element model. Therefore, the program automatically transfers all applied loads to the nodes and elements at the beginning of the solution.

For thermal load, the locations for temperature load is usually at the top and bottom planes called “pseudo-nodes “ as shown in Fig. (1):

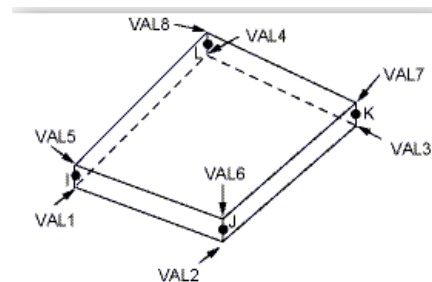


Fig. (1): thermal Load locations

### Defining the Layer Configuration

The most important characteristic of a composite material is its layered configuration. Each layer may be made of a different orthotropic material and may have its principal directions oriented differently. For laminated composites, the fiber directions determine the layer orientation. The layer configuration is defined layer-by-layer from bottom to



top. The bottom layer is designed as layer 1, and additional layers are stacked from bottom to top in the positive Z (normal) direction of the element coordinate system. It can define layered sections via the section commands and the following properties are specified:

- Material properties.
- Layer orientation angle.
- Layer thickness.

### Mesh Convergence

A convergence study was performed to determine the appropriate finite element mesh to be used in the linear buckling analysis of laminated plate model. Three meshes were developed, with increasing numbers of elements in the x and y directions.

The buckling loads for each of these models are shown in table (1). There is only a 0.7% difference between the load calculated for mesh 1 (7\*7) and mesh 2 (15\*15). A smaller difference (0.01 %) is observed between mesh 2 and mesh 3 (30\*30). This indicates that the coarsest mesh is capable of performing the analysis within a reasonable degree of accuracy.

**Table (1):** Critical buckling load convergence study for C-C-S-C laminates

No.of Elements	No.of Nodes	No.of DOF	Critical buckling load $N_{xx}(N/m)$
49	176	1056	10452
225	736	4416	10379
900	2821	16926	10378

### Computer Programming

The main computer program has been built for Levy method and Navier method to carry out the analysis required for solving the effect of mechanical and thermal loads on buckling analysis of composite laminated plate using classical and higher order shear deformation plate theory. However they involved complex calculations that are difficult to interpret physically and require considerably more computational effort. A computer code written in MATLAB (R2010a) consisting from 1400 steps approximately. This program has the following features. See Fig. (2):

1. It can solve a problem for (square, rectangular) composite laminated plate when two opposite edges are simply supported and other two edges any boundary conditions.
2. It can solve thin and thick laminated plate with any number of layers.
3. It can solve symmetric and anti-symmetric cross-ply and angle-ply composite laminated plate.
4. It can solve for critical mechanical load and critical thermal load that cause buckling and combination of these loads.

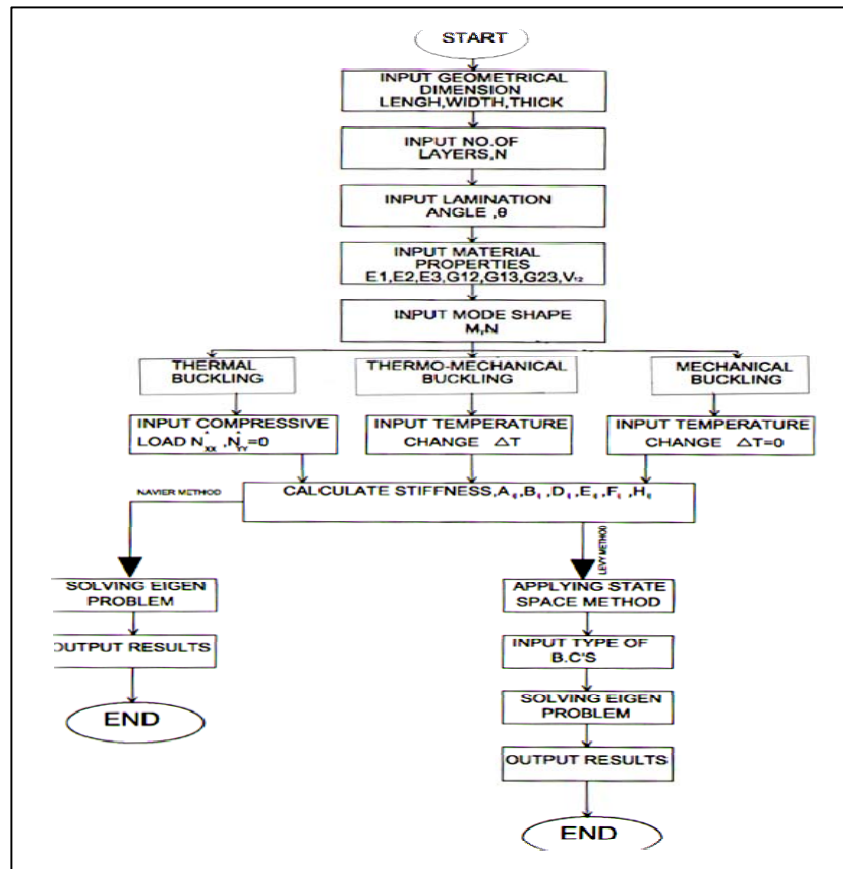


Fig. (2): MATLAB diagram

### Verification Of Computer Program

In the present study, various combinations of edge support conditions have been investigated. For example, C-S-C-S means clamped edges at  $x = (0, a)$  while simply supported at edges at  $y = (0, b)$ . To validate the present methods, thermo-mechanical buckling analysis of different boundary conditions laminated plates, the critical buckling load (thermal, mechanical) are plotted and compared below with [9], [15], and [17] as shown below. The results are compared to analytical solution (Levy and Navier) and numerical solution (Finite element method), the max. discrepancy in Fig.(3) was 4.195% when  $b/h=100$  because [9]

used analytical solution (Navier method) without include membrane stiffness (that cause large deformation) while the present study include both membrane and bending stiffness.

Table (2): Dimensionless thermal buckling of

square laminated plates  $\bar{T} = T_c \alpha_0 * 1000$

b/h	laminate	B.C'S	[15] (F.E)	ANSYS 13.0 (Discrepancy %)	
30	(45/-45) <sub>2T</sub>	S-S-S-S	1.133	1.131 (0.1765%)	$E2/E1=0.081$ $G12=G13=0.031 E1$ $G23=0.0304 E1$ $\nu12=0.21$
50	(45/-45) <sub>2T</sub>	S-S-S-S	0.443	0.44101 (3.0747%)	$\alpha1=-0.21 \alpha0$ $\alpha2=16 \alpha0$ $\alpha0=1e-6$

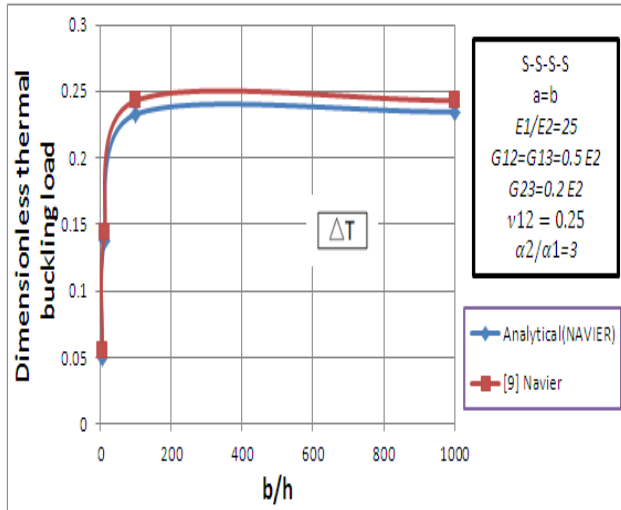


**Fig.(3):** Dimensionless critical temperature  $\bar{T} = T_{cr} \frac{a^2 h}{D_{22} \pi^2}$  of symmetric cross-ply 0/90/90/0 laminated plate

**Table. (3):** Dimensionless uniaxial buckling load  $\bar{N} = N_{xx}^0 \frac{a^2}{E_2 h^3}$  of anti-symmetric cross-ply laminates

B.C'S	b/h	[17] Levy	Present Levy (Discrepancy %)	Present Navier (Discrepancy %)
S-F-S-F	50	16.426	17.53375 (6.3178%)	-
S-F-S-S	50	17.023	18.11575 (6.032%)	-
S-F-S-C	50	19.389	20.46825 (5.272%)	-
S-S-S-S	50	35.232	36.351 (3.078%)	-
S-S-S-C	50	59.288	60.409 (1.855%)	-
S-C-S-C	50	89.770	94.216 (4.718%)	-
S-S-S-S	5	12.109	-	13.0991 (7.558%)
S-S-S-S	10	25.423	-	24.8047 (2.432%)

*E1/E2=40  
G12=G13=0.6 E2  
G23=0.5 E2  
v12=0.25  
a=b  
h=1  
N=10*

From the above results, it is obvious that the methods of solution give reasonable results for both thermal and mechanical loads respectively.

## Results And Discussions

### A. Experimental Analysis

In view of difficulty of theoretical analysis of laminated structure behavior, experimental methods have become important in solving the buckling problem of laminated composite plates. In the present work, mechanical properties (Tensile test) and compressive behavior (buckling test) of (0/90/90/0) E-glass polyester laminated composite plates are calculated experimentally at room temperature.

#### Tensile Test

Each laminate was oriented in longitudinal, transverse and  $45^\circ$  angle relative to designated  $0^\circ$  direction to determine the engineering parameters  $E_1$ ,  $E_2$ ,  $G_{12}$  according to ASTM (D 638). The mechanical properties for glass-polyester are obtained from tensile test as shown in table (4).

**Table (4):** Experimental mechanical properties of Fiber glass-Polyester

Mechanical properties	Glass-polyester
$E_1$ (Mpa)	2473.046067
$E_2$ (Mpa)	1917.178
$G_{12}$ (Mpa)	336
$v_{12}$ [10]	0.25
$V_f$	0.36

### Buckling Test

In this study, buckling load of laminated plate determined analytically, numerically and experimentally. The laminated plate length was 220 mm. The width and thickness are 110 mm and 5.2 mm respectively. The specimen was loaded in axial compression (vertical direction) using tensile test machine of 100 KN capacities. The specimen was simply supported at two ends and kept free at the other two ends. The specimen was loaded slowly until buckling. Simply supported boundary conditions were simulated along the top and bottom edges. For axial loading, the test specimen was placed between two extremely stiff machine heads of which the lower one was fixed during the test, whereas the upper head was moved downwards by servo hydraulic cylinder. The laminated plate was loaded at constant cross-head speed of 2 mm/min.

The buckling load is determined from the load-displacement curve. The vertical displacement is plotted on the x-axis and load was plotted on the y-axis as shown in Fig. (4 a). For the determination of buckling load, the point where left from the straight line is determined on the graphics and the value of this point on the y-axis is called as the buckling load. The specimen was loaded in axial compression (vertical direction) using tensile test machine of 100 KN capacities as shown in Fig. (4 b). The specimen was simply supported at two ends and kept free at the other two ends. The specimen was loaded slowly until buckling.

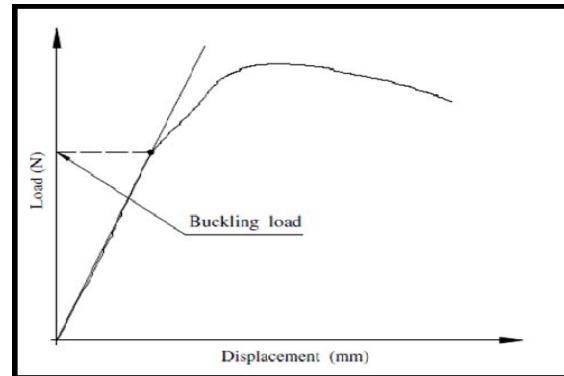


Fig. (4 a): The determination of buckling load



Fig. (4 b): Buckling test of F-S-F-S laminates

The agreement between the three methods was generally good. The max. discrepancy was 9.13% because there were bubbles and fiber glass is not straight in some portions. The critical buckling load is shown in table (5).

Table (5): Dimensionless buckling load [ $\bar{N} = N_{yy}^0 * b^2 / E_2 * h^3$ ] of F-S-F-S laminates

Laminated plate	Length b (mm)	Width a (mm)	Thick. (mm)	Levy (Discrepancy%)	Finite element (Discrepancy%)	Experimental
(0/90) <sub>s</sub>	220	110	5.2	3.4578 (7.89%)	3.4113 (9.13%)	3.75408



## B. Theoretical Analysis

The present study focused mainly on the buckling behavior of composite laminated plates subjected to thermal (uniform, linear)(see eq. 6 a and 6 b) , mechanical and thermo-mechanical loads are analyzed by analytically and numerically for different aspect ratio, thickness ratio, lamination angle and number of layers with various boundary conditions and type of load (biaxial and uniaxial).

In present work, mechanical properties for glass-polyester are obtained from experimental results as shown in table (6).

**Table. (6):** Experimental mechanical properties of Fiber glass-Polyester

Mechanical properties	Glass-polyester
$E_1$ (GPa)	6.981
$E_2 = E_3$ (GPa)	2.0566
$G_{12} = G_{13}$	0.8979
$G_{13} = G_{23}$ (GPa)(assume)	0.8979
$\nu_{12}$ [9]	0.28
$\alpha_{xx} (1/C^\circ)$ [18]	$8.6 \alpha_0$
$\alpha_{yy} (1/C^\circ)$ [18]	$22.1 \alpha_0$
$\alpha_0 (1/C^\circ)$	$10^{-6}$
$V_f$	0.34

### 1. Laminated Plate Subjected To Uniaxial Load Along Y-Axis

From Fig. (5), it can be shown that the buckling load is decrease in cases F-S-S-S and F-S-C-S because the effect of B.C'S. The buckling load is decreased with high percentage in F-S-C-S when a/b varies from 0.5 to 1. On other hand, this percentage gets smaller in F-S-S-S; F-S-C-S when a/b varies from 1 to 2.

In case F-S-F-S, the buckling load increase with small percentage when a/b varies from 0.5 to 2 because of its boundary condition.

It is worth mentioning that the decrease in buckling load in F-S-C-S is more than other case where this decrease reaches to 74.688% because the boundary effects on the middle region of the laminated plate decreases and consequently, the buckling load decreases.

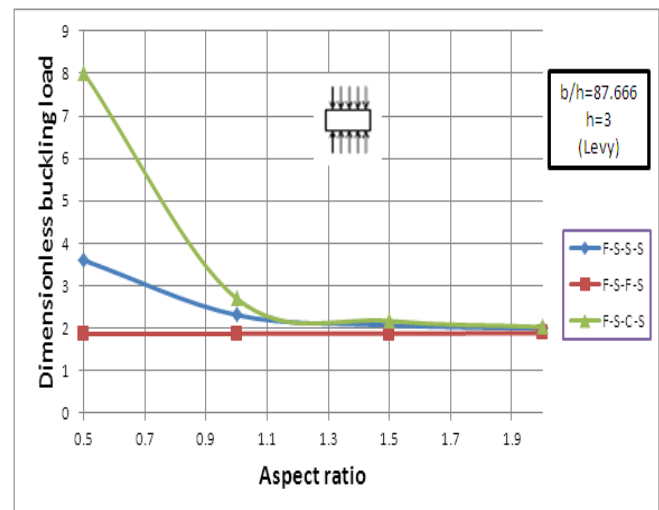


**Fig. (5):** Dimensionless uniaxial buckling load  $[\bar{N} = N_{yy} * b^2 / E_2 * h^3]$  versus aspect ratio , (a/b) of an anti-symmetric cross-ply  $(0/90/0/90)_T$  laminates

In Fig.(6), the buckling load decrease when b/h varies from 10 to 50. The max. percentage of decreasing in buckling load occurs when b/h varies from 10 to 20 where this decrease reaches to 51.876 % because the effects of boundary on the middle region of the laminated plate diminish. So that, the buckling load encounters a significant decrease.



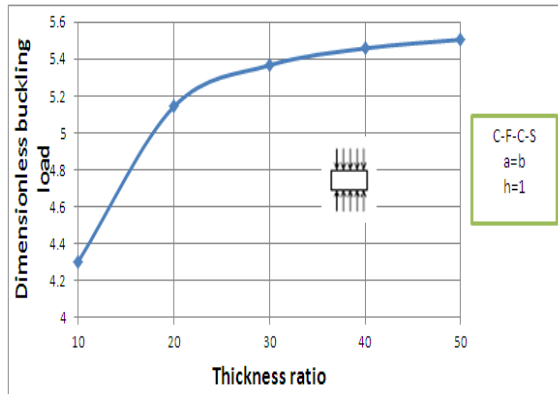


**Fig. (6):** Dimensionless uniaxial buckling load  $[\bar{N} = N_{yy}^0 * b^2 / E_2 * h^3]$  versus thickness ratio, (a/h) of an antisymmetric cross-ply  $(0/90/0/90)_T$  laminates

Figs. (7) and (8) below shows the deformation of laminated plate at critical buckling load and it's deflection at first mode.

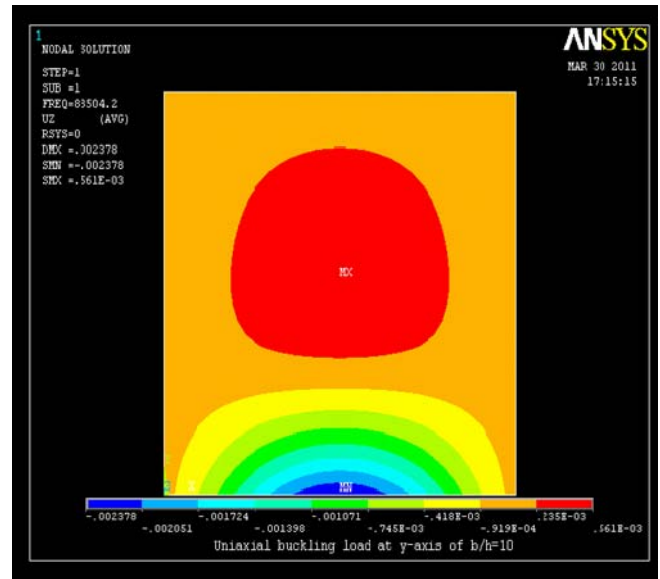


**Fig. (8):** Deflection of laminated plate for mode 1

## 2. Laminated Plate Subjected To Biaxial Load

From Fig.(9) , it can be obtained that biaxial load increase with high percentage when  $N$  varies from 2 to 4 because of the resistance of layers(that increase with increase the no. of layers) against load that cause buckling. Then, it will increase with small percentage when  $N$  varies from 4 to 10. Increasing in buckling load in case  $(0/90)_T$  is more than other case, it reaches to 16.65%. The buckling load increase asymptotically when No. of layers increase.

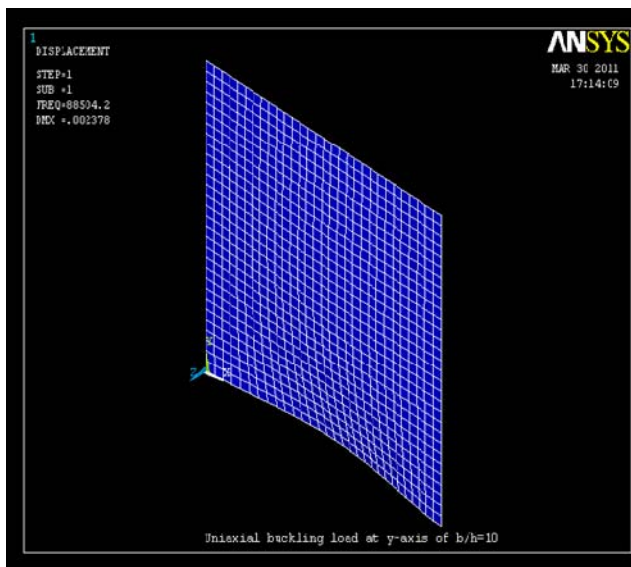


**Fig. (7):** Deformed shape of laminated plate for mode 1

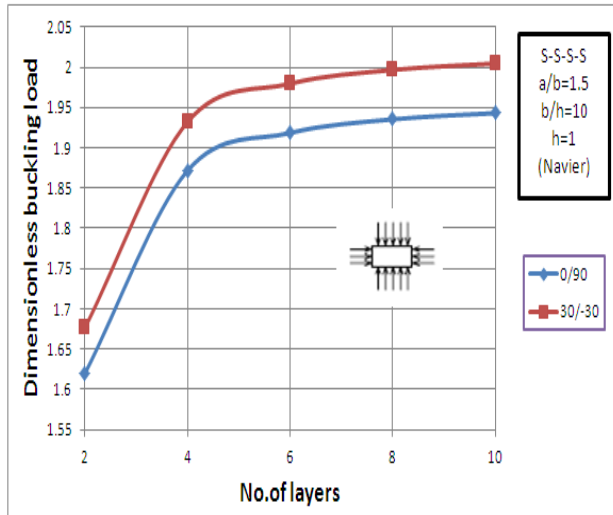


**Fig. (9):** Dimensionless Biaxial buckling load  $[\bar{N} = N_{cr} * b^2 / E_2 * h^3]$  versus No. of layer for antisymmetric laminates

From Fig.(10), the buckling load decrease when  $a/b$  varies from 0.5 to 2. The max. percentage of decreasing in buckling load occurs when  $a/b$  varies from 0.5 to 1 where this decrease reaches to 52.626%.

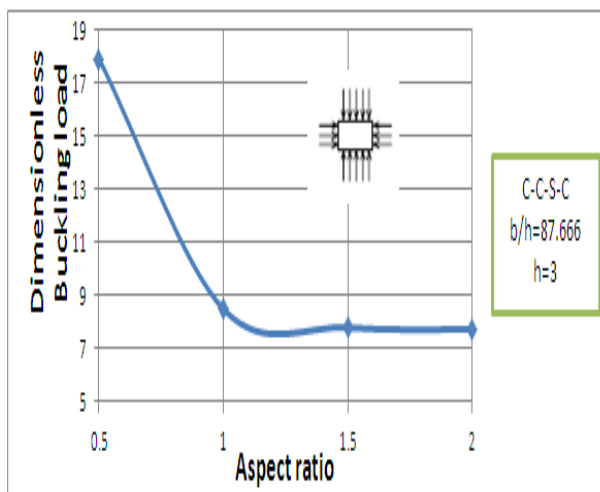


**Fig. (10):** Dimensionless biaxial buckling load  $[\bar{N} = N_{cr} * b^2 / E_2 * h^3]$  versus aspect ratio , ( $a/b$ ) of an antisymmetric cross-ply  $(0/90/0/90)_T$  laminates

Figs. (11) and (12) below shows the deformation of laminated plate at critical buckling load and it's deflection at first mode.

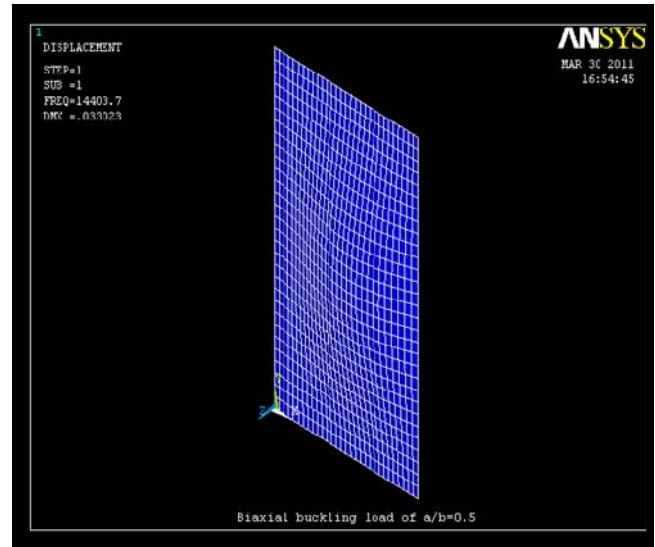


**Fig. (11):** Deformed shape of laminated plate for mode 1

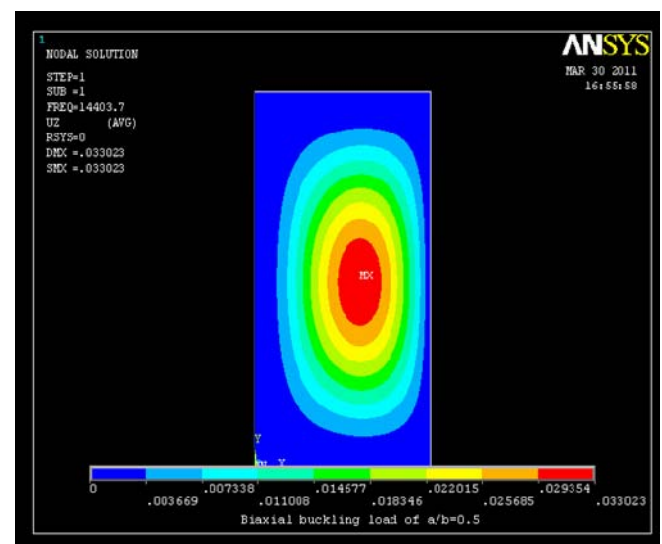


**Fig. (12):** Deflection of laminated plate for mode 1

Fig (13) shows the min. buckling load is shown when the value of half wavelengths is to be 2. Since the nearest integer value of n to critical buckling is to be when n is to be 3, then saying the right value of critical buckling load is to be when n=3.

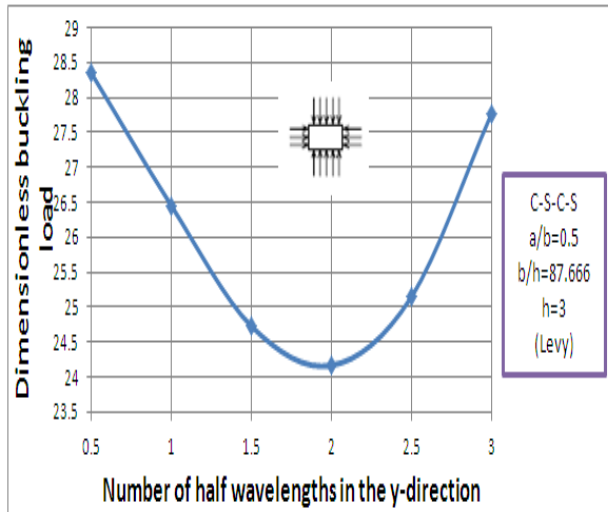


**Fig. (13):** Dimensionless Biaxial buckling load  $[ \bar{N} = N_{cr} * b^2 / E_2 * h^3 ]$  versus Number of half wavelengths in the y-direction , n of an antisymmetric cross-ply  $(0/90/0/90)_T$  laminates

### 3. Laminated Plate Subjected To Uniaxial Load Along X-Axis

From Fig (14), it should be noted that the buckling load decrease with small percentage when  $\theta$  varies because of the effect of B.C'S, while in case S-F-S-F it becomes to decrease higher when  $\theta$  varies. The decrease in buckling load in S-F-S-F is more than other cases where this decrease reaches to 69.26%. On other hand, the min. percentage of

decreasing in buckling load is to be in S-C-S-F, it reaches to 46.532%.

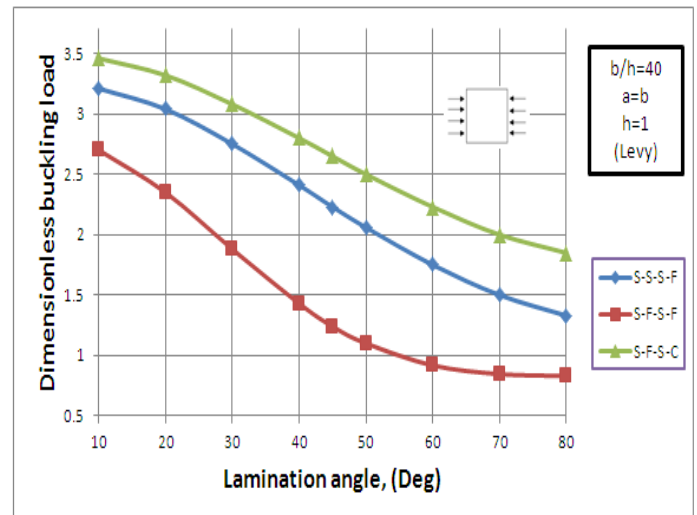


**Fig. (14):** Dimensionless uniaxial buckling load  $[ \bar{N} = N_{xxx}^0 * b^2 / E_2 * h^3 ]$  versus lamination angle , ( $\theta$ ) of an antisymmetric angle-ply  $(\theta/-\theta/\theta/-\theta)$  laminates

### 4. Laminated Plate Subjected To Thermal Load

In the Fig.(15), it can be obtained that the buckling load is decrease with high percentage when a/b varies from 0.5 to 1. On other hand, this percentage get smaller when a/b varies from 1 to 2.

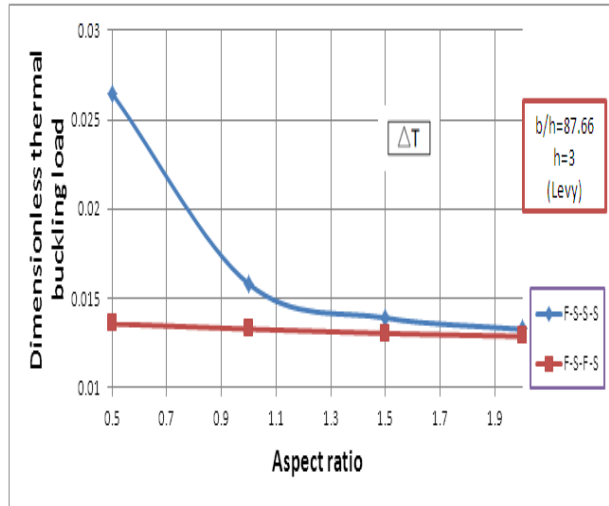


**Fig. (15):** Dimensionless Linear Thermal buckling load [  $\bar{T} = T_{cr} * \alpha_0 * 1000$ ] versus aspect ratio , (a/b) of an antisymmetric cross-ply  $(0/90/0/90)_S$  laminates

Fig.(16) shows that the buckling load was decrease with high percentage when b/h varies from 10 to 20 because the total thickness was decrease Then this percentage gets smaller when b/h varies from 20 to 50.

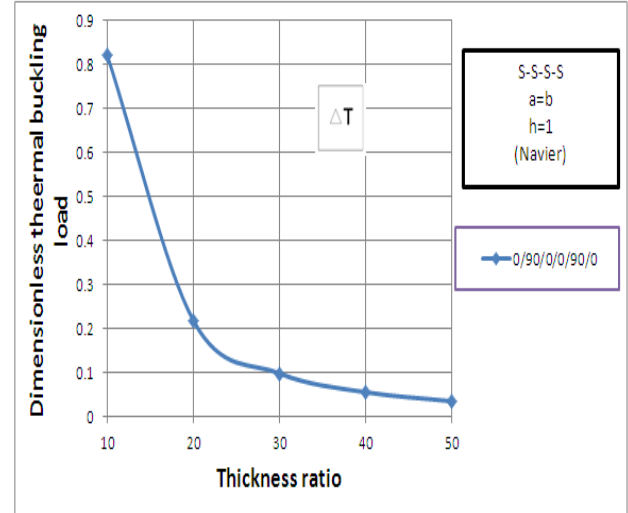


**Fig. (16):** Dimensionless Uniform Thermal buckling load [  $\bar{T} = T_{cr} * \alpha_0 * 1000$ ] versus thickness ratio , (a/h) laminates

## 5. Laminated Plate Subjected To Thermo-Mechanical Load

The uniaxial buckling load for different cases is summarized. It is important to note that the max. buckling load decreases with different percentage when  $T$  increase.

In table (7), deals with thick laminated plate; the decrease in buckling load in case  $(0/90)_S$  is more than other cases because  $(0/90)_S$  of laminated rectangular plate is less stiffness than other cases; this decrease reaches to 12.5% but the decrease in buckling load in  $(45/-45/45/-45/45)_T$  is less than other cases, it reaches to 8.15%.

**Table. (7):** Dimensionless uniaxial buckling load [  $\bar{N} = N_{xx}^0 * b^2 / E_2 * h^3$  ] of laminated plates under uniformly temperature distribution

Lamination Scheme	Boundary condition	a/b	b/h	Buckling load (Navier)			
				$\Delta T=0^\circ\text{C}$	$\Delta T=20^\circ\text{C}$	$\Delta T=40^\circ\text{C}$	$\Delta T=60^\circ\text{C}$
$(0/90)_s$	S-S-S-S	1.5	10	5.1532	4.8953	4.7	4.5049
$(0/90/90/0/0)_s$	S-S-S-S	1.5	10	6.1228	5.9302	5.7376	5.545
$(0/90)_T$	S-S-S-S	1.5	10	6.079	5.8245	5.6292	5.434
$(0/90/90/0/0)_T$	S-S-S-S	1.5	10	5.7163	5.5237	5.3312	5.1386
$(45/-45)_T$	S-S-S-S	1.5	10	7.29	7.0542	6.859	6.6638
$(45/-45/45/-45/45)_T$	S-S-S-S	1.5	10	7.6185	7.3875	7.1923	6.997

From Fig.(17), it can be obtained that the buckling load is decrease with small percentage when temperature varies from  $0^\circ\text{C}$  to  $30^\circ\text{C}$  where the percentage decreases in buckling load reaches to 10.25% along temperature variations.

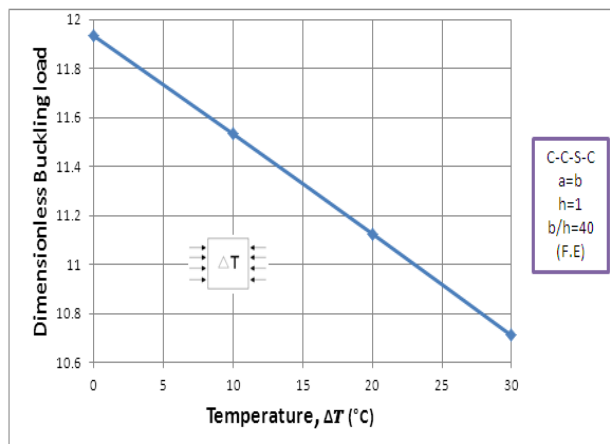


**Fig. (17):** Dimensionless uniaxial buckling load [  $\bar{N} = N_{xx}^0 * b^2 / E_2 * h^3$  ] versus temperature varying linearly of symmetric angle-ply  $(30/-30)_s$  laminates

Figs. (18) and (19) below shows the deformation of laminated plate at critical buckling load and it's deflection at first mode.

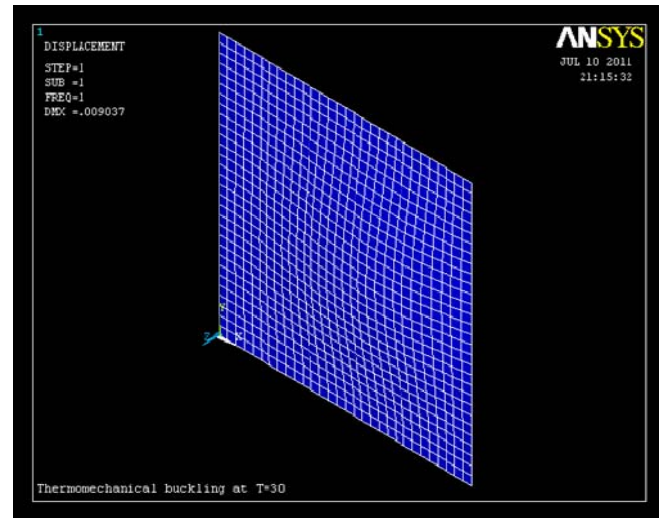


**Fig. (18):** Deformed shape of laminated plate for mode 1

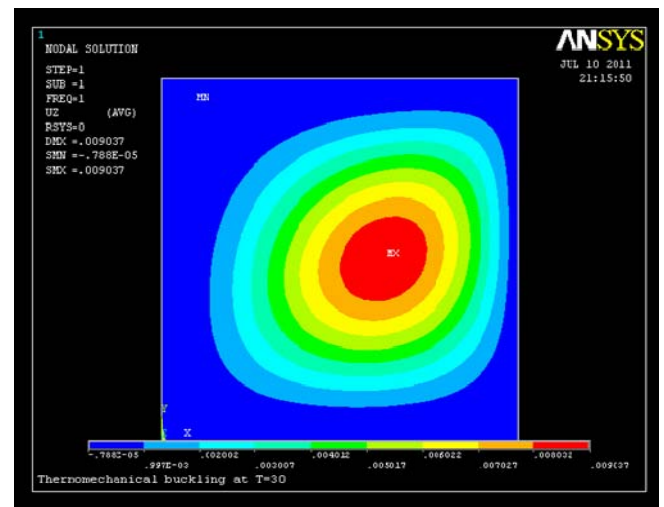


**Fig. (19):** Deflection of laminated plate for mode 1



## Conclusion

This study considers the buckling analysis of cross-ply and angle-ply laminates with various B.C's. From the present analytical study, the following conclusions can be made:

1. It was noted that different thickness ratio affected the critical buckling load. The buckling load decrease when  $b/h$  increase and reaches to min. value at  $b/h=50$ . The max. decrease in buckling load occurs when  $b/h$  varies from 10 to 20.
2. As the aspect ratio increases, the critical buckling load of laminated plate decreases and reaches to min. value at  $a/b=2$ . The max. decrease in buckling load occurs when  $a/b$  varies from 0.5 to 1.
3. It was seen that the different fiber orientation angles affected the critical buckling load. When the fiber angle increases, the buckling load decreases and reaches to min. value at  $\theta=80$ ,
4. It is clear that No. of layers affected on critical buckling load. The buckling load increase when No. of layers increase and reaches to max. value at  $N=10$ . The max. increase in buckling load occurs when  $N$  varies from 2 to 4.
5. It was seen that No. of half wavelengths affected on buckling load because critical buckling load (the value of min.

load) may not occur in the first half wavelengths. It may lie in the second or third half wavelengths.

6. The boundary conditions affect the buckling load, the buckling load increase when boundary conditions become more stiffness.

## Appendix A

### Classical laminated plate theory

The in plane force resultants are defined as

$$\begin{Bmatrix} N_{xx} \\ N_{yy} \\ N_{xy} \end{Bmatrix} = \int_{-h/2}^{h/2} \begin{Bmatrix} \sigma_x \\ \sigma_y \\ \sigma_{xy} \end{Bmatrix}_k dz = \sum_{k=1}^N \int_{z_k}^{z_{k+1}} \begin{Bmatrix} \sigma_x \\ \sigma_y \\ \sigma_{xy} \end{Bmatrix}_k dz \quad (A-1)$$

Where  $\sigma_x$ ,  $\sigma_y$  and  $\tau_{xy}$  are normal and shear stress.

$\alpha_x$ ,  $\alpha_y$  and  $\alpha_{xy}$  are thermal expansion coefficients

$$\begin{Bmatrix} N_{xx} \\ N_{yy} \\ N_{xy} \end{Bmatrix} = \begin{bmatrix} A_{11} & A_{12} & A_{16} \\ A_{12} & A_{22} & A_{26} \\ A_{16} & A_{26} & A_{66} \end{bmatrix} \begin{Bmatrix} \epsilon_{xx}^0 \\ \epsilon_{yy}^0 \\ \gamma_{xy}^0 \end{Bmatrix} + \begin{bmatrix} B_{11} & B_{12} & B_{16} \\ B_{12} & B_{22} & B_{26} \\ B_{16} & B_{26} & B_{66} \end{bmatrix} \begin{Bmatrix} \epsilon_{xx}^1 \\ \epsilon_{yy}^1 \\ \gamma_{xy}^1 \end{Bmatrix} - \begin{Bmatrix} N_x^T \\ N_y^T \\ N_{xy}^T \end{Bmatrix} \quad (A-2)$$



$$\begin{Bmatrix} M_{xx} \\ M_{yy} \\ M_{xy} \end{Bmatrix} = \int_{-h/2}^{h/2} \begin{Bmatrix} \sigma_x \\ \sigma_y \\ \sigma_{xy} \end{Bmatrix}_k dz = \sum_{k=1}^N \int_{z_k}^{z_{k+1}} \begin{Bmatrix} \sigma_x \\ \sigma_y \\ \sigma_{xy} \end{Bmatrix}_k z dz \quad (A-3)$$

$$\begin{Bmatrix} M_{xx} \\ M_{yy} \\ M_{xy} \end{Bmatrix} = \begin{bmatrix} B_{11} & B_{12} & B_{16} \\ B_{12} & B_{22} & B_{26} \\ B_{16} & B_{26} & B_{66} \end{bmatrix} \begin{Bmatrix} \varepsilon_{xx}^0 \\ \varepsilon_{yy}^0 \\ \gamma_{xy}^0 \end{Bmatrix} + \begin{bmatrix} D_{11} & D_{12} & D_{16} \\ D_{12} & D_{22} & D_{26} \\ D_{16} & D_{26} & D_{66} \end{bmatrix} \begin{Bmatrix} \varepsilon_{xx}^1 \\ \varepsilon_{yy}^1 \\ \gamma_{xy}^1 \end{Bmatrix} - \begin{Bmatrix} M_x^T \\ M_y^T \\ M_{xy}^T \end{Bmatrix} \quad (A-4)$$

Where  $\{N^T\}$  and  $\{M^T\}$  are thermal stress and bending results, respectively

$$\begin{Bmatrix} N_x^T, M_x^T \\ N_y^T, M_y^T \\ N_{xy}^T, M_{xy}^T \end{Bmatrix} = \sum_{k=1}^N \int_{-h/2}^{h/2} \begin{bmatrix} \bar{Q}_{11} & \bar{Q}_{12} & \bar{Q}_{16} \\ \bar{Q}_{12} & \bar{Q}_{22} & \bar{Q}_{26} \\ \bar{Q}_{16} & \bar{Q}_{26} & \bar{Q}_{66} \end{bmatrix} \begin{Bmatrix} \alpha_x \\ \alpha_y \\ 2\alpha_{xy} \end{Bmatrix} (1, z) \Delta T dz \quad (A-5)$$

For uniform temperature variation:  
 $\Delta T = \text{applied temperature} - \text{reference temperature}$  (A-6)

For linear temperature variation:  
 $\Delta T = T_0(x, y, t) + z * T_1(x, y, t)$  (A-7)

Here,  $A_{ij}$  are the extensional stiffness,  $B_{ij}$  the coupling stiffness, and  $D_{ij}$  the bending stiffness.

$$A_{ij} = \sum_{k=1}^N (\bar{Q}_{ij})_k (z_{k+1} - z_k) \quad (A-8)$$

$$B_{ij} = \frac{1}{2} \sum_{k=1}^N (\bar{Q}_{ij})_k (z_{k+1}^2 - z_k^2) \quad (A-9)$$

$$D_{ij} = \frac{1}{3} \sum_{k=1}^N (\bar{Q}_{ij})_k (z_{k+1}^3 - z_k^3) \quad (A-10)$$

## Appendix B

Third order shear deformation plate theory

The in-plane force resultants are defined as:

$$\begin{Bmatrix} N_{xx} \\ N_{yy} \\ N_{xy} \end{Bmatrix} = \int_{-h/2}^{h/2} \begin{Bmatrix} \sigma_x \\ \sigma_y \\ \sigma_{xy} \end{Bmatrix}_k dz = \sum_{k=1}^N \int_{z_k}^{z_{k+1}} \begin{Bmatrix} \sigma_x \\ \sigma_y \\ \sigma_{xy} \end{Bmatrix}_k dz \quad (B-1)$$

$$\begin{Bmatrix} N_{xx} \\ N_{yy} \\ N_{xy} \end{Bmatrix} = \begin{bmatrix} A_{11} & A_{12} & A_{16} \\ A_{12} & A_{22} & A_{26} \\ A_{16} & A_{26} & A_{66} \end{bmatrix} \begin{Bmatrix} \varepsilon_{xx}^0 \\ \varepsilon_{yy}^0 \\ \gamma_{xy}^0 \end{Bmatrix} + \begin{bmatrix} B_{11} & B_{12} & B_{16} \\ B_{12} & B_{22} & B_{26} \\ B_{16} & B_{26} & B_{66} \end{bmatrix} \begin{Bmatrix} \varepsilon_{xx}^1 \\ \varepsilon_{yy}^1 \\ \gamma_{xy}^1 \end{Bmatrix} - \begin{bmatrix} E_{11} & E_{12} & E_{16} \\ E_{12} & E_{22} & E_{26} \\ E_{16} & E_{26} & E_{66} \end{bmatrix} \begin{Bmatrix} \varepsilon_{xx}^{(3)} \\ \varepsilon_{yy}^{(3)} \\ \gamma_{xy}^{(3)} \end{Bmatrix} - \begin{Bmatrix} N_x^T \\ N_y^T \\ N_{xy}^T \end{Bmatrix} \quad (B-2)$$

$$\begin{Bmatrix} M_{xx} \\ M_{yy} \\ M_{xy} \end{Bmatrix} = \int_{-h/2}^{h/2} \begin{Bmatrix} \sigma_x \\ \sigma_y \\ \sigma_{xy} \end{Bmatrix}_k z dz = \sum_{k=1}^N \int_{z_k}^{z_{k+1}} \begin{Bmatrix} \sigma_x \\ \sigma_y \\ \sigma_{xy} \end{Bmatrix}_k z dz \quad (B-3)$$

$$\begin{Bmatrix} M_{xx} \\ M_{yy} \\ M_{xy} \end{Bmatrix} = \begin{bmatrix} B_{11} & B_{12} & B_{16} \\ B_{12} & B_{22} & B_{26} \\ B_{16} & B_{26} & B_{66} \end{bmatrix} \begin{Bmatrix} \varepsilon_{xy}^0 \\ \varepsilon_{xy}^0 \\ \gamma_{xy}^0 \end{Bmatrix} + \begin{bmatrix} D_{11} & D_{12} & D_{16} \\ D_{12} & D_{22} & D_{26} \\ D_{16} & D_{26} & D_{66} \end{bmatrix} \begin{Bmatrix} \varepsilon_{xx}^1 \\ \varepsilon_{yy}^1 \\ \gamma_{xy}^1 \end{Bmatrix} - c_1 \begin{bmatrix} F_{11} & F_{12} & F_{16} \\ F_{12} & F_{22} & F_{26} \\ F_{16} & F_{26} & F_{66} \end{bmatrix} \begin{Bmatrix} \varepsilon_{xx}^{(3)} \\ \varepsilon_{yy}^{(3)} \\ \gamma_{xy}^{(3)} \end{Bmatrix} \quad (B-4)$$

$$\begin{Bmatrix} P_{xx} \\ P_{yy} \\ P_{xy} \end{Bmatrix} = \int_{-h/2}^{h/2} \begin{Bmatrix} \sigma_x \\ \sigma_y \\ \sigma_{xy} \end{Bmatrix}_k z^2 dz = \sum_{k=1}^N \int_{z_k}^{z_{k+1}} \begin{Bmatrix} \sigma_x \\ \sigma_y \\ \sigma_{xy} \end{Bmatrix}_k z^2 dz \quad (B-5)$$

$$\begin{Bmatrix} P_{xx} \\ P_{yy} \\ P_{xy} \end{Bmatrix} = \begin{bmatrix} E_{11} & E_{12} & E_{16} \\ E_{12} & E_{22} & E_{26} \\ E_{16} & E_{26} & E_{66} \end{bmatrix} \begin{Bmatrix} \varepsilon_{xy}^0 \\ \varepsilon_{xy}^0 \\ \gamma_{xy}^0 \end{Bmatrix} + \begin{bmatrix} F_{11} & F_{12} & F_{16} \\ F_{12} & F_{22} & F_{26} \\ F_{16} & F_{26} & F_{66} \end{bmatrix} \begin{Bmatrix} \varepsilon_{xx}^1 \\ \varepsilon_{yy}^1 \\ \gamma_{xy}^1 \end{Bmatrix}$$

$$c_1 \begin{bmatrix} H_{11} & H_{12} & H_{16} \\ H_{12} & H_{22} & H_{26} \\ H_{16} & H_{26} & H_{66} \end{bmatrix} \begin{Bmatrix} \varepsilon_{xx}^{(3)} \\ \varepsilon_{yy}^{(3)} \\ \gamma_{xy}^{(3)} \end{Bmatrix} - \begin{Bmatrix} P_x^T \\ P_y^T \\ P_{xy}^T \end{Bmatrix} \quad (B-6)$$

$$\begin{Bmatrix} Q_{yz} \\ Q_{xz} \end{Bmatrix} = \int_{-h/2}^{h/2} \begin{Bmatrix} \sigma_{yz} \\ \sigma_{xz} \end{Bmatrix}_k dz = \sum_{k=1}^N \int_{z_k}^{z_{k+1}} \begin{Bmatrix} \sigma_{yz} \\ \sigma_{xz} \end{Bmatrix}_k dz \quad (B-7)$$

$$\begin{Bmatrix} Q_{yz} \\ Q_{xz} \end{Bmatrix} = \begin{bmatrix} A_{44} & A_{45} \\ A_{45} & A_{55} \end{bmatrix} \begin{Bmatrix} \gamma_{yz}^{(0)} \\ \gamma_{xz}^{(0)} \end{Bmatrix} - c_2 \begin{bmatrix} D_{44} & D_{45} \\ D_{45} & D_{55} \end{bmatrix} \begin{Bmatrix} \gamma_{yz}^{(2)} \\ \gamma_{xz}^{(2)} \end{Bmatrix} \quad (B-8)$$

$$\begin{Bmatrix} R_{yz} \\ R_{xz} \end{Bmatrix} = \int_{-h/2}^{h/2} \begin{Bmatrix} \sigma_{yz} \\ \sigma_{xz} \end{Bmatrix}_k z^2 dz = \sum_{k=1}^N \int_{z_k}^{z_{k+1}} \begin{Bmatrix} \tau_{yz} \\ \tau_{xz} \end{Bmatrix}_k z^2 dz \quad (B-9)$$

$$\begin{Bmatrix} R_{yz} \\ R_{xz} \end{Bmatrix} = \begin{bmatrix} D_{44} & D_{45} \\ D_{45} & D_{55} \end{bmatrix} \begin{Bmatrix} \gamma_{yz}^{(0)} \\ \gamma_{xz}^{(0)} \end{Bmatrix} - c_2 \begin{bmatrix} F_{44} & F_{45} \\ F_{45} & F_{55} \end{bmatrix} \begin{Bmatrix} \gamma_{yz}^{(2)} \\ \gamma_{xz}^{(2)} \end{Bmatrix} \quad (B-10)$$

Where

$$A_{ij}, B_{ij}, D_{ij}, E_{ij}, F_{ij}, H_{ij} = \sum_{k=1}^N \int_{z_k}^{z_{k+1}} \bar{Q}_{ij}^{(k)} (1, z, z^2, z^3, z^4, z^6) dz \quad (\text{B-11})$$

Where  $\{N^T\}$ ,  $\{M^T\}$  and  $\{P^T\}$  are thermal stress results

$$\left\{ \begin{matrix} N_x^T, M_x^T, P_x^T \\ N_y^T, M_y^T, P_y^T \\ N_{xy}^T, M_{xy}^T, P_{xy}^T \end{matrix} \right\} = \sum_{k=1}^N \int_{-h/2}^{h/2} \begin{bmatrix} \bar{Q}_{11} & \bar{Q}_{12} & \bar{Q}_{16} \\ \bar{Q}_{12} & \bar{Q}_{22} & \bar{Q}_{26} \\ \bar{Q}_{16} & \bar{Q}_{26} & \bar{Q}_{66} \end{bmatrix} \begin{Bmatrix} \alpha_x \\ \alpha_y \\ 2\alpha_{xy} \end{Bmatrix} (1, z, z^3) \Delta T dz \quad (\text{B-12})$$

## References

Gossard M.L., Seide P., and Roberts W.M. “ **Thermal buckling of plates** “. NASA TN 2771; 1952.

Sharma S., Iyengar N.G.R., and Murthy P.N. “ **Buckling of anti-symmetric cross and angle-ply laminated plates** “. Int. J. Mech. Sci. 1980; 22: 607-620.

Thangaratnam K.R., Palaninathan, and Ramachandran J. “ **Thermal buckling of composite laminated plates** “. J computers and structures 1988; 32(5): 1117-1124.

Liangxin S. and Zhiyus S. “ **The analysis of laminated composite plates based on the simple higher order theory** “. J computers and structures 1992; 43(5): 831-837.

Kam T.Y. and Chang R.R. “ **Design of laminated composite plates for maximum buckling load and vibration frequency** “. J computer

methods in applied mechanics and engineering 1993; 106: 65-81.

Prabhu M.R. and Dhanaraj R. “ **Thermal buckling of laminated composite plates** “. J computers and structures 1994; 53(5): 1193-1204.

Argyris J. and Tenek L. “ **High-temperature bending, buckling and postbuckling of laminated composite plates using the natural mode method** “. J computer methods in applied mechanics and engineering 1994; 117: 105-142.

Ghosh A.K. and Dey S.K. “ **Buckling of laminated plates – a simple finite element based on higher-order theory** “. J finite elements in analysis and design 1994; 15: 289-302.

Sun L. and Xiaoping S. “ **Thermo-mechanical buckling of laminated composite plates with higher-order transverse shear deformation** “. J computers and structures 1994; 53(1): 1-7.

Simelane S. P. “ **Thermal buckling of laminated composite Plates** “. M.Sc thesis; South Africa; 1998.

Matsunaga H. “ **Thermal buckling of cross-ply laminated composite and sandwich plates according to a global higher-order deformation theory** “. J composite structures 2005; 68: 439-454.

Shariyat M. “ **Thermal buckling analysis of rectangular composite plates with temperature-dependent properties based on a layerwise**



theory “. J thin-walled structures 2007; 45:439-452.

Yu L.H. and Wang C.Y. “ **Buckling of rectangular plates on an elastic foundation using the Levy method** “. J AIAA 2008; 46(12):3163-3166.

Ozben T. “ **Analysis of critical buckling load of laminated composites plate with different boundary conditions using FEM and analytical methods** “. J computational materials science 2009; 45:1006-1015.

Rajesh K., Lal A., and Singh B.N. “ **Effects of random system properties on the thermal buckling analysis of laminated composite plated** “. J computers and structures 2009; 87:1119-1128.

Shiau L., Kuo S., and Chen C. “ **Thermal buckling behavior of composite laminated plates** “. J composite structures 2010; 92: 508-514.

Reddy J.N. “ **Mechanics of laminated composite plates and shells: theory and analysis** “. 2ed; CRC Press 2004.

Zaffer G. “ **Design and optimization of laminated composite materials** “. Canada; John Wiley & Sons 1999.

Hasanain I. N. “ **Buckling analysis of composite plates under thermal and mechanical loading** “. M.Sc. thesis; University of Baghdad; 2011

## Nomenclature

Symbol	Description	Units
a	Dimension along x-coordinate	m
b	Dimension along y-coordinate	m
$A_{ij}, B_{ij}, D_{ij}, E_{ij}, F_{ij}, H_{ij}$	Extensional, bending extensional coupling, bending and additional stiffness	-
$E_1, E_2, E_3$	Elastic modulus components	Gpa
$G_{12}, G_{23}, G_{13}$	Shear modulus components	Gpa
h	Thickness	m
m, n	No. of half wavelengths in x and y directions	-
N	Total number of plate layers	-

Symbol	Description	Units
$N_{xx}, N_{yy}, N_{xy}$	In-plane force resultant	N/m
$M_{xx}, M_{yy}, M_{xy}$	Moment resultant per unit length	N.m/m
$P_{xx}, P_{yy}, P_{xy}$	Resultant force per unit length	N/m
$Q_{xz}, Q_{yz}$	Transverse shear force resultant	N
$R_{xz}, R_{yz}$	Transverse shear force resultant (HSDT)	N
$\bar{Q}_{ij}^{(k)}$	Transformed lamina stiffness	N/m
$z$	Distance from neutral axis	m
$x, y, z$	Cartesian coordinate system	m
$Z_k, Z_{k+1}$	Upper and lower lamina surface coordinates along z-direction	m
$\alpha_{xx}, \alpha_{yy}, \alpha_{xy}$	Transformed thermal coefficients of expansion	$1/^\circ\text{C}$
$\epsilon_{xx}, \epsilon_{yy}, \epsilon_{xy}, \epsilon_{xz}, \epsilon_{yz}, \epsilon_{zz}$	Strain components	m/m
$\Delta T$	Temperature increment	$^\circ\text{C}$
$\gamma_{xz}, \gamma_{yz}$	Transverse shear strain	m/m
$\nu_{12}$	Poisson's ratio component	-



Symbol	Description	Units
$\sigma_{xx}, \sigma_{yy}, \sigma_{xy}, \sigma_{xz}, \sigma_{yz}$	Stress components	Gpa
C-S-C-S	Clamped at x-axis and simply supported at y-axis	-
$N_{xx}^T, N_{yy}^T$	Thermal stress resultant	N/m
$N_{xx}^0, N_{yy}^0$	Applied edge forces	N/m
$\theta$	Fiber orientation angle	Degree
$U_{mn}, V_{mn}, W_{mn}, X_{mn}, Y_{mn}$	Arbitrary constant	-
u, v, w u, v, w	Displacement component	M
T	Temperature	$^{\circ}\text{C}$
1, 2, 3	Principal material coordinate system	-
$(0/90)_S$	Symmetric cross-ply laminate	-
$(0/90)_T$	Anti Symmetric cross-ply laminate	-
$(\theta/-\theta)_T$	Anti symmetric angle-ply laminate	-
$(\theta/-\theta)_S$	Symmetric angle-ply laminate	-
S	Simply supported edge	-
C	Clamped edge	-`
F	Free edge	-

**Prof. Dr. Adnan Naji Jameel**  
**Dr. Ibtehal Abbas Sadiq**  
**Hasanain Ibraheem Nsaif**

**Buckling Analysis of Composite Plates under  
Thermal and Mechanical Loading**



## Effect of Oscillatory Motion in Enhancing the Natural Convection Heat Transfer from a Vertical Channel

Lecturer: Saad Mohammed Jalil

Mechanical Engineering Department- University Of Anbar

Email: saadmj79@gmail.com

### Abstract

This paper reports an experimental study regarding the influence of vertical oscillations on the natural convection heat transfer from a vertical channel. An experimental set-up was constructed and calibrated; the vertical channel was tested in atmosphere at 25°C. The channel-to-ambient temperature difference was varied with the power supply to the electrical heater ranging between 15W to 70W divided into five levels. Data sets were measured under different operating condition from a test rig under six vibrating velocities (VVs) levels ranging from (5-30 m/s) in addition to the stationary state. The results show that the maximum heat transfer enhancement factor (E) occurs at Rayleigh number ( $Ra=2.328 \times 10^3$ ) and vibrational Reynolds number ( $Re_v=6.365 \times 10^3$ ); this enhancement reached to (7.685%). The results also illustrated that the temperature gradient along the channel wall length was enhanced by inducing the oscillatory motion to the channel. Rayleigh and vibrational Reynolds numbers were ranging between ( $2.306 \times 10^3 - 5.564 \times 10^3$ ) and ( $0.0 - 19.86 \times 10^3$ ) respectively. Finally, A correlation which summarized the effects of both Ra and Rev was determined for the Nusselt numbers.

**Keywords :** Oscillatory Motion, Enhancing, Natural Convection, Vertical Channel.

### تأثير الحركة الاهتزازية في تحسين انتقال الحرارة بالحمل الحر من قناة عمودية

المدرس : سعد محمد جليل  
قسم الهندسة الميكانيكية - جامعة الانبار

### الخلاصة

يهدف البحث الحالي إلى إجراء دراسة عملية حول تأثير الاهتزاز العمودي على انتقال الحرارة بالحمل الحر من قناة عمودية. تم تصنيع ومعايرة المنشأ التجريبي المستخدم في الدراسة، وفي ظروف جوية وعند درجة حرارة (25°C) للمحيط الخارجي تم اختبار القناة المستخدمة لعدة سرعات اهتزازية الفرق في درجة الحرارة بين القناة العمودية والمحيط الخارجي تغير وفقاً لمقدار القدرة الكهربائية المجهزة للسطح والتي تراوحت بين (15W - 70W). القراءات المسجلة من التجارب للقناة قيست تحت تأثير سرعات اهتزاز عمودية مختلفة تراوحت بين (5-30 m/s) بالإضافة إلى الحالة المستقرة (غير مهتزة). من خلال النتائج تبين أن أعلى قيمة لمعامل تحسين انتقال الحرارة بالحمل الحر (E) حصل عند عدد رالي ( $Ra = 2.328 \times 10^3$ ) و عدد رينولد الاهتزازي ( $Re_v = 6.365 \times 10^3$ ) ونسبة زيادة (7.685%) مقارنة بالحالة المستقرة. كذلك بينت النتائج أن تدرج درجات الحرارة على طول جدران القناة قد تحسن بتأثير الحركة الاهتزازية المجهزة للقناة. خلال جميع التجارب فإن عدد رالي و رينولد الاهتزازي تراوحت بين ( $2.306 \times 10^3 - 5.564 \times 10^3$ ) و ( $0.0 - 19.86 \times 10^3$ ) على الترتيب. العلاقة التجريبية المستنتجة من النتائج لخصت تأثير كل من عدد رالي و رينولد الاهتزازي على عدد نسلت عند كل حالة.

**الكلمات الرئيسية:** الحركة الاهتزازية ، تحسين ، الحمل الحر ، قناة عمودية.

## 1. Introduction

Natural convection heat transfer with air as the working fluid is a highly important cooling mechanism that is currently implemented across a broad spectrum of systems. It is simple, efficient, dependable, quiet operation and poses no hazards to human users, makes it the preferred method of cooling especially in devices where heat transfer rates are at low levels (**Yeh LT,1995, Incropera FP and DeWitt DP,1996, Sathe S,1998, Incropera FP,1999 and Tou SKW et al.,1999**). Also it concerns a number of applications, ranging from the cooling of electronic equipment to the heating of buildings. Laminar heat transfer by natural convections has been studied extensively for different geometries (**Ramanathan S and Kumar R,1991, Vafai K and Etefagh J, 1990a, Vafai K and Etefagh J,1990b, Daloglu A and Ayhan T,1999, and Khanafer K and Vafai K,2000**).

Vertical channels are frequently encountered configuration in natural convection cooling where the flows are induced by the buoyancy of thermal diffusion alone. A significant domain of natural convection flow has relatively small velocity magnitudes and contain almost unnoticeable turbulence levels. Spaces cooled by natural convection flows vary from one application to another. Natural convection inside vertical channels had received an increase attention in the past decade. There are only few works that dealt with heat transfer and flow induced by natural convection inside vibrating geometries. As an example, (**Fu and Shieh,1993**) studied the effect of buoyancy and vertical vibrations at the four walls of a square closed cavity. (**Kwak et al.,1998**) discussed the effects of having vibrations on the temperature of one plate of a closed cavity to the natural convection inside the cavity. (**Oronzio Manca et al.,2003**) experimentally introduced air natural convection in an asymmetrically heated channel with unheated extensions. The addition of downstream unheated extensions improves the thermal performance of the channel for some configurations, longer extension and the lower the aspect ratio the lower the wall temperature in the channel. (**X.R. Zhang et al.,2004**) described a numerical study of the laminar natural convection on a periodically oscillating vertical flat plate heated at a uniform temperature. Of particular interest of the paper was the heat transfer characteristics when the oscillatory velocity being close to the flow velocity in the velocity boundary layer under non-oscillation

conditions. The results showed that the heat transfer of the problem under consideration significantly depends on the dimensionless oscillation velocity, a relative size between the oscillation velocity and the flow velocity in the velocity boundary layer of a stationary plate. The heat transfer enhancement was found to be increased with the dimensionless oscillation frequency, amplitude, the Prandtl number, but decreased with the Grashof number.

(**N. Bianco,T and S. Nardini,2005**) investigated numerically the natural convection in air in a convergent channel. An extended computational domain was adopted, which allowed to take the account of diffusion by both momentum and energy outside the channel. Temperature profiles were strongly affected by the convergence angle at low Rayleigh numbers. At the lower minimum gap, streamlines and isotherms show a low pressure region in the channel due to a choked flow in its upper end. (**Wu-Shung Fu and Chien-Ping Huang,2006**) performed a numerical simulation to study effects of a vibrational heat surface on natural convection in a vertical channel flow. The results showed that for the same Rayleigh number, natural convection of a vibration heat plate with a certain combination of frequency and amplitude was possibly smaller than that of a stationary state. (**L. A. Florio and A. Harnoy,2006**) investigated a dynamic means of locally enhancing laminar natural convection cooling in a vertical channel through the localized application of fluid oscillations numerically. The two-dimensional system considered for these purposes was a vertical channel with a small transversely oscillating plate placed near a constant heat flux channel wall. The flow and heat transfer in the system resulting from the combined effects of the natural convection and the oscillating plate were determined. The results indicated that for displacement amplitudes of at least one-third of the mean spacing and with dimensionless frequencies ( $Re/\sqrt{Gr}$ ) of at least  $2\pi$ , the local heat transfer coefficient could be enhanced as much as 41%.

(**N. Kasayapanand and T. Kiatsiriroat,2007**) presented numerically the electrohydrodynamic effect to natural convection inside the vertical channels by the use of computational fluid dynamics technique. The relation between channel aspect ratio and number of electrodes that performs the

maximum heat transfer was expressed incorporating with the optimum concerning parameters. (Subhrajit Dey, Debapriya Chakraborty, 2009) implemented a numerical methods (finite volume) to study the effects of an oscillating fin in enhancing heat transfer. It is conclude that there are benefits in Nu for an oscillating fin over a conventional static fin because of contraction and disturbances imported to the thermal boundary layers. The benefits improved with higher frequencies and amplitudes of oscillation.

(L. Cheng et al.,2009) proposed a novel approach to enhance the heat transfer by using the flow-induced vibration of a new designed heat transfer device. Thus the flow-induced vibration is effectively utilized instead of strictly avoiding it in the heat exchanger design. The vibration and the heat transfer of these devices were studied numerically and experimentally. It was found that the new designed heat exchanger can significantly increase the convective heat transfer coefficient and decrease the fouling resistance. Therefore, a lasting heat transfer enhancement by the flow-induced vibration can be achieved. (P. Poskas et al.,2011) presented the results of experimental investigation of local opposing mixed convection heat. The analysis of the results revealed significant increase in the heat transfer with the increase of air pressure (Gr number). Also a sharp increase in heat transfer was noticed in the region with vortex flow as comprised with the turbulent flow region.

In the above mentioned research it is noted that much of the work have been carried out on natural convection inside different geometries and that related to behavior of vertical channel subjected to the effect of oscillation have not been fully investigated. The present investigation mainly attempt to shed light on the oscillation induced heat transfer enhancement , the base plate of a vertical channel and its walls are allowed to have oscillatory motion in vertical direction. The experiments are carried out at constant heat flux with various frequencies. Accordingly, an investigation is done for better understanding about performance of natural convection inside vibrated vertical channel.

## 2. Experimental Set-Up And Data Reduction

The main objective of the experimental setup was to assist in development of natural

convection requirements in a vertically oriented channel subjected to influence of oscillatory motion. A summary information about the experimental apparatus, devices used and procedure are described below.

### 2.1 Experimental Set-Up

A schematic view of the experimental setup is presented in fig.1. The essential components of the setup include a wood room of 2×1.5m dimensions with 2m height, experiment testing model was represented by a vertical channel, instrumentation for measurements temperatures (channel and ambient temperatures), power supply to the heater, and the frequencies supply to the experiment model by the exciter. Tests were carried out under constant heat flux condition with various frequencies and amplitude, which lead to various vibrating velocities (VVs) for the channel in ambient temperature controlled at 25°C for all experiments by a thermostat/heater unit as shown in fig.1. Five levels of heat flux ranging between (15-70W) were considered to study the natural convection behavior from the channel. At each level, the channel subjected to six values of VVs ranging between (5-30 m/s) in addition to the stationary state.

Fig.2 illustrates the dimensions and the parts of the experiment model. The channel was made from Aluminum as one part. The channel configuration was produced from rectangular Aluminum bar with dimensions 100×75×20mm by milling a longitudinal groove of dimensions 10×60mm in the center of the bar. The bar constructed by casting an appropriate amount of Aluminum inside a stainless steel ground container and then grained and polished to have the required dimensions for the bar. Aluminum was selected as the channel material because of its high thermal conductivity ,low emissivity ,structural strength, and durability. Nickel-chrome wire heater used for heating the channel base consists of nickel-chrome wire wound round a thin mica plate and insulated on both sides by two mica sheets. A 5mm thick asbestos slab was glued to the bottom surface of the lower mica sheet to reduce heat loss. The rear surface of the asbestos and the lateral surface of the channel base were insulated by a wooden case of 15mm thickness. Hence, all five sides of the test section except the upper surface were insulated. The aim of which was to reduce the heat loss and

To keep the temperature of the boundary around ambient temperature.

The channel base temperature was measured by the average of four temperatures measurements at the back of the base. Four k-type thermocouples were installed at equal spacing in grooves along the bottom surface of the channel. Furthermore, two k-type thermocouples were attached to the rear surface of the wooden case to calculate the conductive dissipated heat transfer. The temperature distribution for the channel walls was collected by installing five k-type thermocouples along the channel wall length with 10mm between them. This indicates a clear temperature gradient along the channel wall length under the effect of the oscillatory motion. All thermocouples were connected to a k-type selector switch and the output of the selector was supplied to a digital thermometer. From the calibration test of the thermocouples used the accuracy of averaged steady state temperature measurements haven't exceed  $\pm 0.5^\circ\text{C}$ . The heater was supplied by stabilized AC power through a regulator which maintains a constant voltage during the data reading. The output of the regulator is fed to a variable transformer (variac) so that the necessary heating level can be selected. The current flow and voltage drop are measured by an ammeter-voltmeter combination. The power input is measured by a calibrated wattmeter. The measurements of wattmeter are verified by the readings of voltmeter and ammeter.

The channel was fixed vertically in a position between two horizontal arms of an iron frame; the frame supported the wooden case, which was connected to the exciter. The oscillatory motion was induced by the exciter-power amplifier unit as shown in fig.1. The oscillatory motion of the channel measured as a vibrating velocity by the vibration meter, which is sensing the signal of vibration sent by the electro-dynamics pick-up. After completion the experiments in non-vibrating condition the desired vibrating velocity was set according to the vibration meter reading by adjusting the power amplifier unit to import vibration to the test section by the exciter. The experimental data of temperatures, vibrating velocities, and the electric power, were measured when the system operates under steady state conditions.

## 2.2 Processing Of The Experimental Data

The experimental data includes the values of temperatures, velocities of vibration, voltage drop across the electrical heater and electrical current. Using these values, the Nusselt number is calculated by definition (M. Dogan , M. Sivrioglu, 2010):

$$Nu = \frac{h.S}{k_{air}} \quad (1)$$

Where  $k_{air}$  is the conduction heat transfer coefficient for air at film temperature ( $T_f$ ) which is calculated as below:

$$T_f = \frac{T_b + T_\infty}{2} \quad (2)$$

Where  $T_b$  is the base temperature of the channel which is represented the average temperature of the thermocouples that placed in the base plate of the channel. Then the temperature difference ratio TDR is given by:

$$TDR = \frac{\Delta T_v}{\Delta T_{unv}} \quad (3)$$

It is computed at six locations along the channel wall length represented by the non-dimensional channel length ( $X=x/L$ ).

The Convection heat transfer from the channel ( $Q_{conv}$ ) is calculated from an energy balance:

$$Q_{total} = Q_{conv} + Q_{cond} + Q_{rad} \quad (4)$$

The total dissipated energy is determined from Ohm's law,  $Q_{total} = VI$  at the heater source. The voltage drop (V) and current (I) are measured during the experiment.

The heat loss through the insulation of test section is calculated from :

$$Q_{cond} = k_{ins} \times A_{ins} \times \frac{\Delta T_{ins}}{\Delta y_{ins}} \quad (5)$$

Where  $k_{ins}$  is the thermal conductivity of the insulation and  $\Delta T_{ins}$  is the difference between internal and external surface temperatures of the insulation.

For the heated surface represented by the vertical channel, radiative heat transfer was also taken into account using the flowing equation:

$$Q_{rad} = \varepsilon \sigma A F (T_b^4 - T_\infty^4) \quad (6)$$

Where the view factor F between the channel and its surrounding was taken to be unity, (see e.g. (C.G. Rao et al.,2002 & E. Kchoc et al.,2003)), The results of experiments showed that the radiation losses never exceeded 2% of the total power supplied. Now the heat transfer coefficient can be calculated and expressed as:

$$h = \frac{Q_{conv}}{A(T_b - T_\infty)} \quad (7)$$

Other dimensionless numbers affecting the heat transfer are:

The Rayleigh number

$$Ra = Gr \cdot Pr = \frac{g \cdot \beta \cdot (T_b - T_\infty) \cdot S^3}{\alpha \nu} \quad (8)$$

Where  $\beta = \frac{1}{T_f}$ , and the characteristic length was taken as the space between the channel walls (M. Dogan , M. Sivrioglu, 2010).

The vibrational Reynolds number

$$Re_v = \frac{U_v S}{\nu} \quad (9)$$

The correlation between Nusselt number and both above dimensionless numbers eq.(8&9) is defined as below:

$$Nu = c Ra^m Re_v^n \quad (10)$$

The constants (c,m,n) are calculated and listed in Table (1) for each case .Also all thermophysical of air appearing in equations above were calculated at film temperature eq.(2)

### 3. Results and Discussion

The convection heat transfer from vertical oscillated channel under constant heat flux conditions has been experimentally investigated. Tests were conducted under various heat flux and oscillating velocities conditions. the stationary state of the vertical channel was investigated to assess the validity of the

experimental results with previous work and used as a reference to compare heat transfer results which generates under six vibrating velocities condition ranging (5-30 m/s) . the air around the base and walls is oscillating because of channel vibration.. Oscillatory motions generally enhance the heat and mass transfer in fluid.

The oscillatory motion of the channel is defined as:

$$d_x = \text{constant} \quad (11)$$

$$d_y = B \sin(2\pi f t) \quad (12)$$

Where B and f are the amplitude and the frequency of oscillation respectively. The experimental data are analyzed by the procedure that described previously in section 2.2. the temperatures distribution along the channel wall length, heat transfer coefficients and the non-dimensional numbers are calculated at different velocities of vibration under various heat flux levels.

The experimental results obtained in the current study indicate that the oscillation in general enhanced the heat transfer coefficient but in a fluctuating manner. For temperatures distribution the behavior was expected with cooling the base plate by decreasing the base temperature difference.

#### 3.1 Temperature distribution

Plotting the Temperature Difference Ratio (TDR) versus the vibrating velocities (VVs) for non-dimensional channel wall length helps to understand the effect of vibrating velocity variation ,for each heat flux value, on the temperatures distribution along the channel wall length and gives a good indication about the percentage of enhancement.

Figs. 3-8 present the variations of TDR with (VVs) at all power levels and for each non-dimensional channel wall length ( $X = x/L = 0.0, 0.2, 0.4, 0.6, 0.8$  and  $1.0$ ). As can be seen from these figures, there is a positive effect on TDR with (VVs) increase for all values of (X) These figures show that the temperature difference ( $\Delta T_{unv} = T_x - T_\infty$ ) at each location along the channel wall length for stationary case is higher than the

temperature difference ( $\Delta T_v = T_x - T_\infty$ ) for vibrating state. Evidently, the ratio of the temperature difference between vibrating and stationary condition doesn't exceed (1) in most of the states.

Fig.3 shows the effect of increasing VV on TDR at  $X=0$ , which represents the base plate location, for the five power levels. From this figure, it can be seen that the heat transfer enhancement at the channel base depends on increasing or decreasing VV at each power level relative to stationary case. The best enhancing appears at the lowest power level (15W) and VV equal to (10m/s). The TDR ratio for this case decreases by (7.14%), that means there is enhancement in heat transfer. But, when the vibrating velocity is more than 10m/s; the heat transfer enhancement decrease and the TDR ratio at the maximum VVs decreases by (1.43%), but never take over the stationary state. This variation occurs for all power levels else the last point of the maximum power which is increased over the stationary state by (1.94%) that means an increase in channel base temperature at these conditions.

As can be seen from figures (3-8), the behavior of the relation between TDR and VV almost remains constant along the channel wall length. This variation in enhancing TDR along the channel wall length as can be seen from these figures is due to the fact that the buoyancy driven forces become more strong or weak with increasing in VVs and heat flux. For example, at power (50W) it can be seen that the enhancing increases with VVs and then decreases at the maximum VV. That is a result of the effect of oscillating in an increase of the buoyancy driven forces and therefore these phenomenon of enhancing at the beginning increases the enhancement magnitudes by decreasing TDR along the channel length at a specific VVs ranges.

On the other hand it can be seen from the figures that the transfer from decreases to increasing in TDR with VVs depends on the power level. These changes in its path is attributed to the buoyancy driven forces increase with slow oscillations and then becomes weak by the impeded in boundary layer with variation of the air density which is bounded the channel. It leads to slow the hot air circulation and rise but stay all points along the channel wall and its base cooler then the non-vibrated state. Also the

figures show that the decreases in TDR for the maximum power occurs at minimum VVs and return to increase with VVs until to be greater than the stationary state only at maximum VVs for all location except the channel edge ( $X=1$ ). That is occurs as a result of the rising temperature around the walls and the impeding created by the oscillation at these conditions. This behavior considers non-favorite results so it is best to working in previous ranges only with appropriate application for this ranges of temperatures or heat flux.

The same figures, illustrate that there is fluctuating enhancement in TDR with VVs represented by the two power levels (30W & 40W), it is clear that the variation in TDR decreased and then increased slowly and return to decreased at high VVs in opposite manner of the other powers. That is mean the buoyancy force has an effect on the hot air depended on the amount of heat supplied and VVs provided to the channel.

### 3.2 Heat transfer enhancement factor (E)

The rate of heat transfer at the surface of stationary vertical channel is controlled by the natural convection boundary layer created by the density difference due to temperature change near its surface. When an oscillatory motion is created between the channel and the adjacent fluid; the heat transfer coefficient at the vibration state increases with increasing VVs in most of studied conditions. Fig. 9 shows the effects of oscillation on average heat transfer rate expressed in terms of the enhancement factor (E) which is defined by the following form:

$$E = \frac{Nu_v - Nu_{unv}}{Nu_{unv}} \quad (13)$$

Where  $Nu_v$  and  $Nu_{unv}$  represents Nusselt numbers under oscillating and stationary conditions respectively. As seen from the figure, the factor E increased in various rates depending on the power levels and VVs. Here we couldn't refer to Grashof number instead of the power supplying to the channel because we have at each power level different values of Grashof number depending on the VVs supplied. The oscillation plays an important role in enhancing Nu at various VVs.

Also we can notice that the maximum enhancement occurs at the first power level



under vibrating velocity equal to (10m/s), from the results its reached to (7.685%) and then decreases with VVs but remain over the non-vibrated state. It is appear in the figure for the maximum power supplying the enhancement factor increases to (2.835%) and then it is decreased to reach under the stationary state only at the maximum VVs causing reducing in heat transfer rate by (2.42%). From Fig. 9 which shows the variation of E with VVs, it can be seen that the behavior of its variation to yield to the power level in addition to the supplying oscillations. As seen the oscillations increases E with extent of enhancement being most pronounced from small values of power and VVs.

### 3.3 Influence of Ra and Re<sub>v</sub> on Nusselt number

Fig. 10 represents the effect of Ra on Nu for the cases where the channel is vibrating vertically with various VVs. As the Ra increases the Nu increased for all velocities. From the figure it is clear that the non-vibrating case has a lowest values of Nusselt number for the most rang of Ra if it is contrasts with the oscillated cases else the last point at maximum power and VVs. Fig. 11 displays the influence of Re<sub>v</sub> for all Ra ranges ( $2.306 \times 10^3$  -  $5.564 \times 10^3$ ). It is noticed that the changing in Nusselt numbers are greater when the vibrational Reynolds increase at low VVs and then fluctuating with Re<sub>v</sub> in a different manner with that of Ra.

This increasing in Nu is due to the effect of the vertical vibrations in both buoyancy forces and the slow flow induced by the motion of the channel yet vertical vibrations affected mainly the working fluid adjacent the channel which is heated as a result of temperature differences between the channel and air. The interaction between vibrations and the oscillatory buoyancy forces resulted from vibrations in the channel cause the trend of Nu to change as Re<sub>v</sub> increases. Also the temperature of adjacent fluid inside the channel are expected to decrease as Ra increase due to the enhancements in thermal convections. Therefore, Nusselt numbers at vibrated channel increase as Re<sub>v</sub> increases but when the fluctuating increases depending on the Rayleigh number.

Based on experimental results, an empirical equation relates Nusselt number, vibrational Reynolds number and Rayleigh number has been obtained. The software (DGA-V1) is used to

synthesize above equation. The percentage error between the theoretical and empirical equation is not exceed (3%). Based in stationary state with all power levels and oscillated states at each power supplying for all vibrating velocities and by using the above software the equation is deduced different coefficients for empirical equation. This will donated us more than equation as specified in table (1).

### 4. Conclusions

Natural convection from vertical channel under vertical vibration motion was investigated experimentally. The variation of Re<sub>v</sub> and Ra were considered and the results were examined in detail. The main conclusions could be summarized as follows.

1. For the same Ra natural convection from a vertical channel subject to a vibration motion under various VVs is larger than that of the stationary state.
2. The temperature gradient along the channel wall length under vibrating state in general decreases to more cooling surfaces.
3. The increasing in Nusselt number changes with vibrational Reynolds number in fluctuating manner depending on the Rayleigh number.
4. A maximum value of the heat transfer enhancement factor (E) is (7.685%) and then decreases to minimum positive value by (2.835%)
5. Only one point leads to non-favorite results represented by decreasing E to a negative value by (2.42%) at maximum Ra and Re<sub>v</sub>.

### 5. References

C.G. Rao, C. Balaji, S.P. Venkateshan, "Effect of surface radiation on conjugate mixed convection in a vertical channel with a discrete heat source in each wall", *Int. J. Heat Mass Transfer* 45 (2002) 3331–3347.

Daloglu A, Ayhan T, "Natural Convection in a Periodically Finned Vertical Channel", *International Communication Heat Mass Transfer* 26 (1999) 1175–1182.

E. Kchoc, M. Davics, D. Newport, "Mixed convection cooling of horizontally mounted



printed circuit board", IEEE Trans. Comp. Packag. Technol. 26 (2003) 126–133.

Fu WS, Shieh WJ ,” Transient Thermal-Convection in an Enclosure Induced Simultaneously by Gravity and Vibration”, International Journal of Heat and Mass Transfer 36 (1993) 437–452.

Incropera FP ,”Liquid cooling of electronic devices”, Wiley, New York, (1999) 1–14.

Incropera FP, DeWitt DP ,”Introduction to heat transfer”, Wiley, New York (1996).

Khanafar K, Vafai K ,” Buoyancy-driven flow and heat transfer in an open-ended enclosures: elimination of the extended boundaries”, International Journal of Heat and Mass Transfer 43 (2000) 4087–4100.

Kwak HS; Kuwahara K, Hyun JM,” Resonant Enhancement of Natural Convection Heat Transfer in a Square Enclosure”, International Journal of Heat and Mass Transfer 41 (1998) 2837–2846.

L. A. Florio ,A. Harnoy,” Analysis of dynamic enhancement of natural convection cooling by a discrete vibrating plate”, Heat Mass Transfer (2006) 43: 149–163.

L. Cheng , T. Luan, W. Du, M. Xu,” Heat transfer enhancement by flow-induced vibration in heat exchangers”, International Journal of Heat and Mass Transfer 52 (2009) 1053–1057.

M. Dogan , M. Sivrioglu, "Experimental investigation of mixed convection heat transfer from longitudinal fins in a horizontal rectangular channel", International Journal of Heat and Mass Transfer 53 (2010) 2149–2158.

N. Bianco,T , S. Nardini ,” Numerical analysis of natural convection in air in a vertical convergent channel with uniformly heated conductive walls”, International Communications in Heat and Mass Transfer 32 (2005) 758–769.

N. Kasayapanand , T. Kiatsirirot ,” Numerical modeling of the electrohydrodynamic effect to natural convection in vertical

channels”, International Communications in Heat and Mass Transfer 34 (2007) 162–175.

Oronzio Manca , Marilena Musto , Vincenzo Naso ,” Experimental analysis of asymmetrical isoflux channel-chimney systems”, International Journal of Thermal Sciences 42 (2003) 837–846.

P. Poskas , R. Poskas, A. Sirvydas, A. Smaizys,” Experimental investigation of opposing mixed convection heat transfer in the vertical flat channel in a laminar–turbulent transition region”, International Journal of Heat and Mass Transfer 54 (2011) 662–668.

Ramanathan S, Kumar R ,”Correlations for Natural Convection between Heated Vertical Plates”, Journal of Heat Transfer 113(1991) 97–107.

Sathe S ,”A review of recent developments in some practical aspects of air-cooled electronic packages”, J. Heat Transfer 120 (1998) 830–838.

Subhrajit Dey ,Debapriya Chakraborty,”Enhancement of convective cooling using oscillating fins”, International Journal of Heat and Mass Transfer 36 (2009) 508–512.

Tou SKW, Tso CP, Zhang X ,”3-D numerical analysis of natural convective liquid cooling of a 3×3 heater array in rectangular enclosures”, Int. J. Heat Mass Transfer 42 (1999) 3231–3244.

Vafai K, Etefagh J ,”The Effects of Sharp Corners on Buoyancy-Driven Flows with Particular Emphasis on Outer Boundaries”, International Journal of Heat and Mass Transfer 33(1990a) 2311–2328.

Vafai K, Etefagh J,” Thermal and Fluid Flow Instabilities in Buoyancy-Driven Flows in Open-Ended Cavities”, International Journal of Heat and Mass Transfer 33(1990b) 2329–2344.

Wu-Shung Fu , Chien-Ping Huang,” Effects of a vibrational heat surface on natural convection in a vertical channel flow”, International Journal of Heat and Mass Transfer 49 (2006) 1340–1349.

X.R. Zhang , S. Maruyama, S. Sakai,” Numerical investigation of laminar natural convection on a heated vertical plate subjected to a periodic oscillation”, International Journal of Heat and Mass Transfer 47 (2004) 4439–4448.



Yeh LT, "Review of heat transfer technologies in electronic equipment", J. Electron Package Trans ASME 117 (1995) 333–337.

## NOMENCLATURE

### LATIN SYMBOLS

<i>Symbols</i>	<i>Description</i>	<i>Units</i>
$a$	Channel wall thickness	m
$A$	Exposed area of the channel	m <sup>2</sup>
$A_{ins}$	Area of the insulations	m <sup>2</sup>
$B$	Oscillation displacement amplitude	m
$d_x$	Displacement of oscillating in x direction	m
$d_y$	Displacement of oscillating in y direction	m
$c$	Constant	
$E$	Enhancement factor	
$f$	Frequency	Hz
$F$	View factor	
$g$	Acceleration due to gravity	m <sup>2</sup> /s
$Gr$	Grashof number	
$h$	Convective heat transfer coefficient	W/m <sup>2</sup> .°C
$k_f$	Fluid thermal conductivity	W/m °C
$k_{ins}$	Insulation thermal conductivity	W/m °C
$L$	Channel wall length	m
$m$	Constant	
$n$	Constant	
$Nu$	Nusselt number	
$Pr$	Prandtl number	
$Q_{total}$	Total power supply	W
$Q_{cond.}$	Heat transfer by conduction	W

<i>Symbols</i>	<i>Description</i>	<i>Units</i>
$Q_{rad.}$	Heat transfer by radiation	W
$Q_{conv.}$	Heat transfer by convection	W
$Ra$	Rayleigh number	
$Re_v$	Vibrational Reynolds number	
$S$	Characteristic length	m
$t$	Time, (s)	
$T_f$	Film temperature	°C
$T_b$	Base temperature	°C
$T_x$	Temperature at position (x)	°C
$T_\infty$	Ambient temperature	°C
$U_v$	Vibrating velocity	m/s
$W$	Channel width	m
$x$	Coordinate along the channel length	m
$X$	Dimensionless channel length (x/L)	
$y$	Coordinate along the channel width	m

### GREEK SYMBOLS

$\beta$	Coefficient of thermal expansion	K <sup>-1</sup>
$\nu$	Kinematic viscosity	m <sup>2</sup> /s
$\varepsilon$	Emissivity	
$\sigma$	Stefan-Boltzmann constant	W/m <sup>2</sup> .K <sup>4</sup>
$\alpha$	Thermal diffusivity	m <sup>2</sup> /s

Table 1 Coefficients and ranges of governing empirical equations of the studied cases

Case		c	m	n	Ra	Re <sub>v</sub>
Stationary (15-70)W		0.08335	0.4688	0	2.437×10 <sup>3</sup> - 5.421×10 <sup>3</sup>	0
Oscillatory Case (5-30) m/s	15 W	49.761	-0.3726	-0.01685	2.306×10 <sup>3</sup> - 2.420×10 <sup>3</sup>	2.918×10 <sup>3</sup> - 1.986×10 <sup>4</sup>
	30 W	0.01311	0.6427	0.01206	3.469×10 <sup>3</sup> - 3.536×10 <sup>3</sup>	2.788×10 <sup>3</sup> - 1.9108×10 <sup>4</sup>
	40 W	104.851	-0.4285	-0.00164	4.052×10 <sup>3</sup> - 4.146×10 <sup>3</sup>	2.743×10 <sup>3</sup> - 1.8751×10 <sup>4</sup>
	50 W	2.8024	0.001143	0.01055	4.241×10 <sup>3</sup> - 4.423×10 <sup>3</sup>	2.627×10 <sup>3</sup> - 1.7991×10 <sup>4</sup>
	70 W	20.8042	-0.19155	-0.02205	5.174×10 <sup>3</sup> - 5.564×10 <sup>3</sup>	2.544×10 <sup>3</sup> - 1.7212×10 <sup>4</sup>
	(15-70) W	0.0975	0.4161	-0.00515	2.306×10 <sup>3</sup> - 5.564×10 <sup>3</sup>	2.544×10 <sup>3</sup> - 1.9860×10 <sup>4</sup>

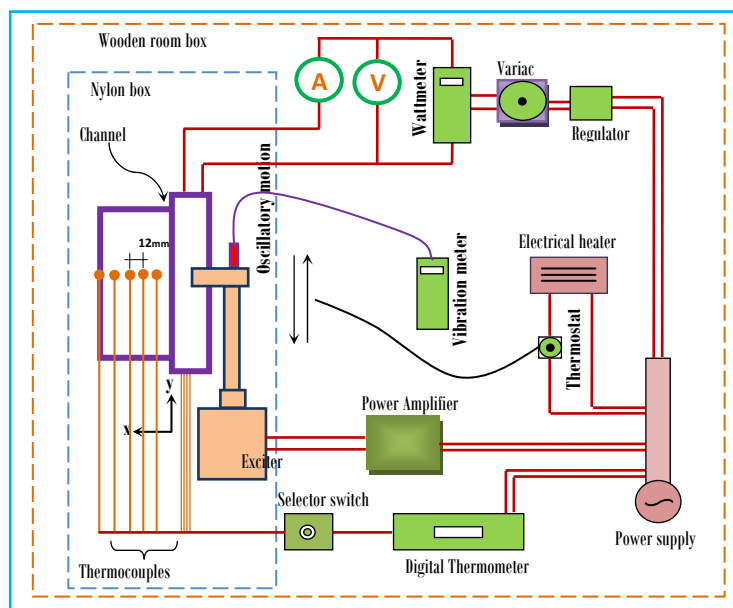


Fig. 1 Schematic diagram of the experimental setup

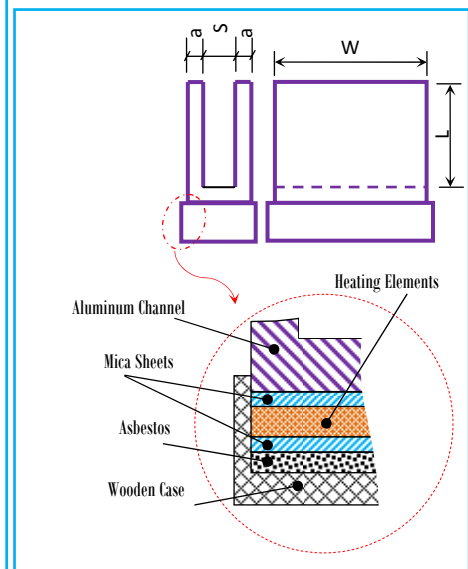
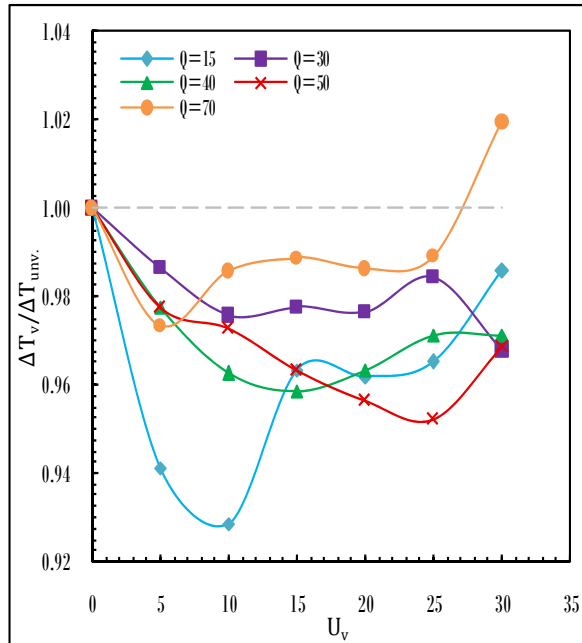
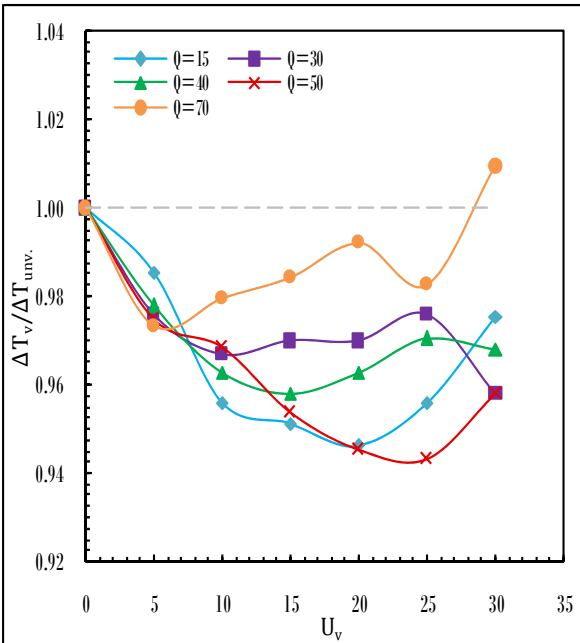


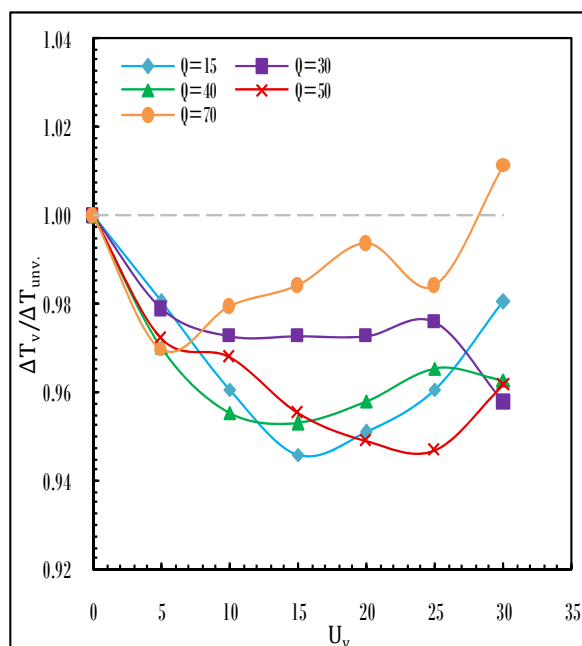
Fig. 2 Dimensions and components of the channel in (mm) (W=100, L=60, a=5, S=10)



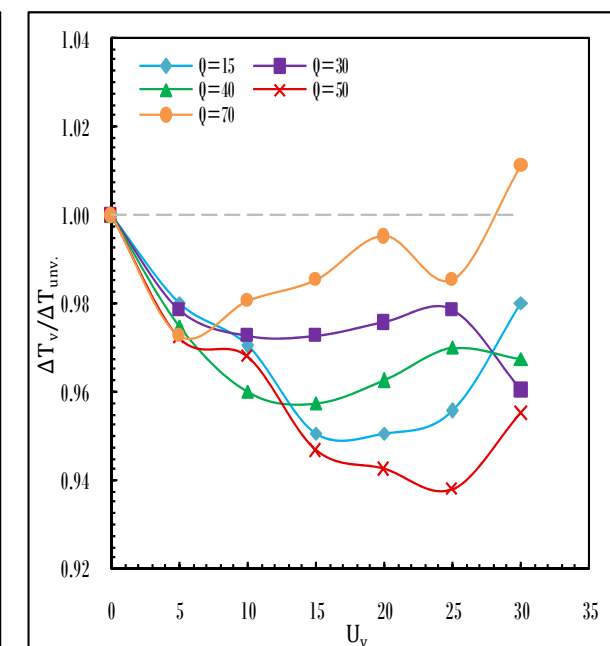
**Fig.3** Variations of temperature difference ratio with vibrating velocity at  $X=0.0$



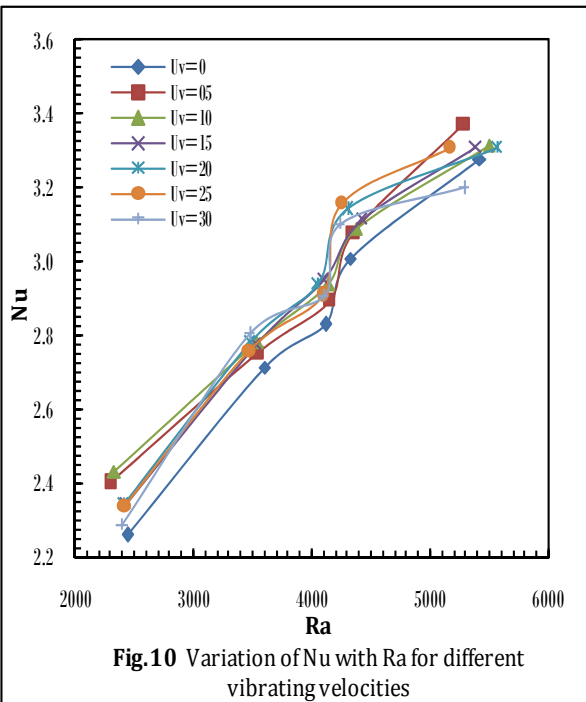
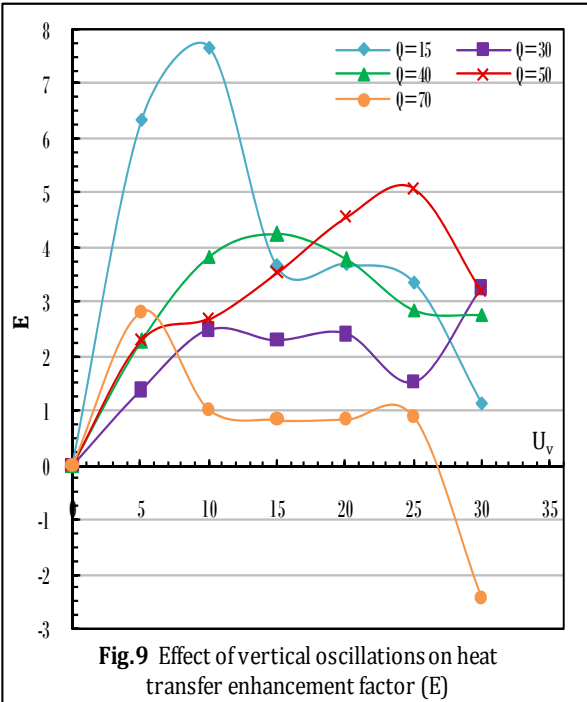
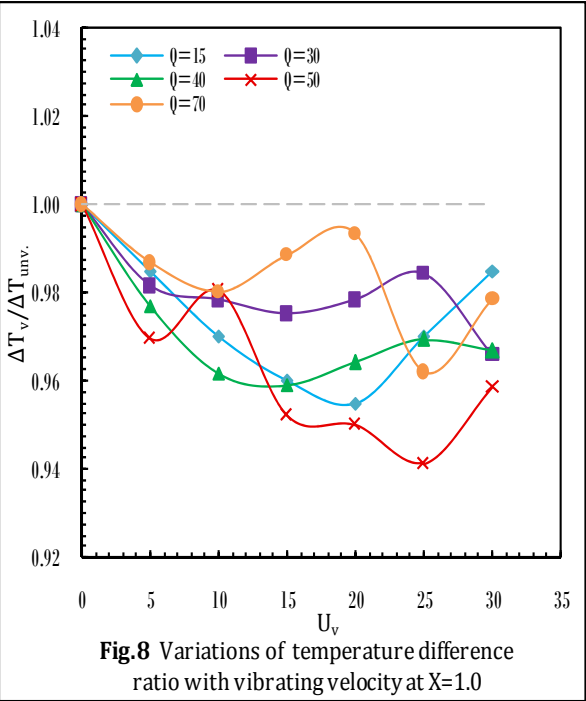
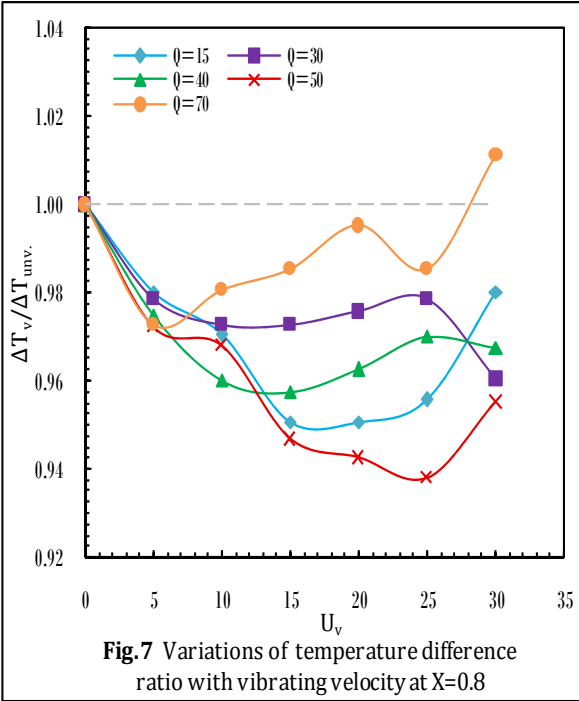
**Fig.4** Variations of temperature difference ratio with vibrating velocity at  $X=0.2$

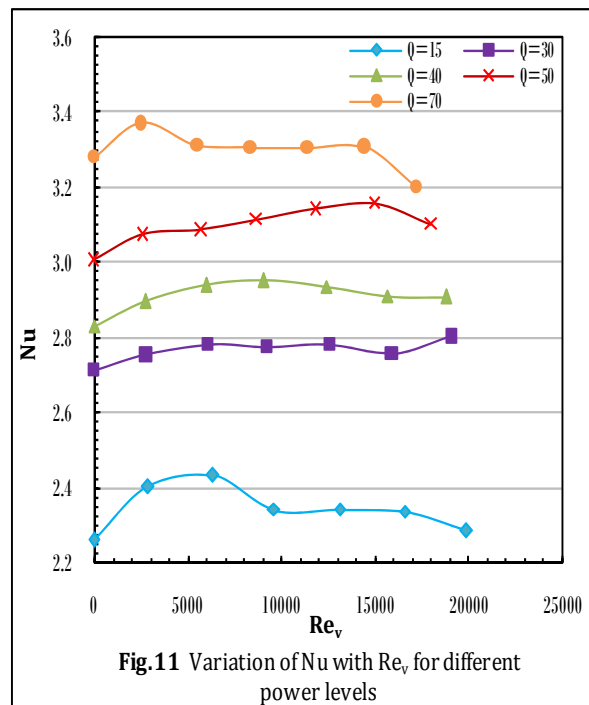


**Fig.5** Variations of temperature difference ratio with vibrating velocity at  $X=0.4$



**Fig.6** Variations of temperature difference ratio with vibrating velocity at  $X=0.6$





# Optimized Zero and First Order Design of Micro Geodetic Networks

By

Prof.dr. Riyadh Z. Al zubaidy

Mr. Hussien A. Mahdi

Hind Sabah Hanooka

University of Baghdad – College of Engineering

## Abstract

Precision is one of the main elements that control the quality of a geodetic network, which defines as the measure of the network efficiency in propagation of random errors.

This research aims to solve ZOD and FOD problems for a geodetic network using *Rosenbrock* Method to optimize the geodetic networks by using MATLAB programming language, to find the optimal design of geodetic network with high precision.

ZOD problem was applied to a case study network consists of 19 points and 58 designed distances with a priori deviation equal to  $5mm$ , to determine the best points in the network to consider as control points. The results showed that P55 and P73 having the minimum ellipse of error and considered as control points.

FOD problem was applied to three cases of selected network to analyzed using the objective function of A-Optimality and D-Optimality, with selected range of movement of  $300m$  to each point in each direction. The first case was a free network, the second case was with P55 and P73 as control points, and the third case was with P42 and P44 as control points. The results showed that the third case was the optimal design with high precision.

**Key Words:** Micro – Geodetic networks – Optimization – Precision – Zero order design – First order design – Rosenbrock method – A-optimality – D-optimality.

تعتبر الدقة من العوامل الرئيسية التي تتحكم في جودة أو نوعية الشبكات الجيوديسية، وتعد الدقة قياساً لفاعلية الشبكة في توزيع الأخطاء العشوائية.

تهدف هذه الدراسة إلى حل مسألة التصميم من الرتبة الصفريّة ومسألة التصميم من الرتبة الأولى لشبكة جيوديسية باستخدام طريقة Rosenbrock لإيجاد التصميم الأمثل للشبكة الجيوديسية باستخدام لغة MATLAB البرمجية. حيث تم تطبيق مسألة التصميم من الرتبة الصفريّة على شبكة الدراسة التي تتألف من 19 نقطة و 58 مسافة تصميمية وبانحراف معياري مقداره 5 ملم، لتحديد أفضل نقاط الشبكة التي يمكن اعتبارها كنقاط ضبط. فأظهرت النتائج أن النقطتين P55 و P73 تمتلك أصغر منحني خطأ وبالتالي يمكن اعتبارها كنقاط ضبط.

ثم تم تحليل ثلاث حالات من شبكة الدراسة من خلال تطبيق مسألة التصميم من الرتبة الأولى وباستخدام دالتي الهدف A-Optimality و D-Optimality لتحديد التصميم الأمثل لشبكة الدراسة الذي يحقق أعلى دقة، وتم تحديد حيز الحركة لنقاط الشبكة بمقدار 300 متر لكل نقطة وفي كل اتجاه. الحالة الأولى هي باعتبار الشبكة هي شبكة حرة (بدون نقاط ضبط)، الحالة الثانية هي اعتبار الشبكة بنقطتي ضبط P55 و P73، والحالة الثالثة هي اعتبار الشبكة بنقطتي ضبط P42 و P44.

وأظهرت نتائج تطبيق مسألة التصميم من الرتبة الأولى على الحالات الثلاثة، بأن الحالة الثالثة من شبكة الدراسة تعتبر التصميم الأمثل الذي يحقق أعلى دقة.



## Introduction

A geodetic network provides a frame work for setting out the main elements of (dams, bridges, power plants, tunnels ports, etc.) and for monitoring the position and deformation of these elements after construction, they can also be used to monitor crystal deformation, these networks are called local or micro networks, which are generally designed for a limited and specific purposes, but when used for multi-purposes, they are defined as national control networks, or reference networks which are play an important role when preparing the coverage maps of the country. The goal of designing, computing, measuring and adjusting procedure is to find the proper and optimal design of a geodetic network then establishing the points of the geodetic network by expressing their positions by (E, N) coordinates. To achieve the best network design, there are different techniques which are triangulation, trilateration, and combined control survey. The optimization problems of geodetic networks are classified into, Zero Order Design problem, ZOD, which define as searching for an optimal datum. First Order Design problem, FOD, which is define as the determination of the optimal position of the network points. Second Order Design problem, SOD, which is defined as weight problem, and Third Order Design problem, TOD, which is the optimal improvement of an existing network or an existing design. Sometimes FOD and SOD problems can be solved simultaneously; in this case the design problem is called a combined design problem, COMD. This research aims to solve ZOD problem and FOD problem of geodetic networks in order to find the optimal design of geodetic network in sense of high precision using least squares adjustment and Rosenbrock Method which solves nonlinear optimization problems, and using the objective function of A-Optimality and D-Optimality, with a constraint of the limits of movement for each point in each direction.

## Preparation of Geodetic Network

Any geodetic project involved three steps which are: design (precision and reliability), adjustment (determination of geometry) and testing (validation of geometry), **Teunissen, P. J. G., 2006**, and the preparation of geodetic network contain design procedure, planning for survey, and optimization procedure.

## Design Procedure

The approximate positions for stations must be determined to be included in the survey. These positions can be determined from topographic maps, photo measurements, or previous survey data. The approximate locations of the control stations should be dictated by their desired locations, the surrounding terrain, vegetation, soils, sight-line obstructions, and so on. Field reconnaissance at this phase of the design process is generally worthwhile to verify sight lines and accessibility of stations. Moving a station short distance from the original design location may greatly enhance the inter visibility between stations, but not change the geometry of the network significantly. By using topographic maps in the process, clearances of sight-line can be checked by constructing profiles between stations. In the design process, considerations should be given to the abilities of the field personal, quality of the equipment, and observational procedures. After the design is completed, specifications for field crews can be written based on these parameters. These specifications should include the type of the used instrument, number of turnings for angle observations, accuracy of instrument leveling and centering, misclosure requirements, and many other items. When approximate station coordinates are determined, a stochastic model for the observational system can be designed. Once the stochastic model is designed, simulated observations are computed from the station coordinates, and a least squares adjustment of the observations is to be done. Since actual observations have not been made, their values are computed from the station coordinates. When the adjustment has been completed, the network can be checked for geometrically weak areas, unacceptable error ellipse sizes or shapes and so on. This inspection may dictate the need of any or all of the following, **Ghilani, C. D., and Wolf, P. R., 2006**:

1. More observations.
2. Different observational procedure.
3. Different equipment.
4. More stations.
5. Different network geometry and so on.

## Planning for Survey

In past, the planning of survey based on empirical standards, experience and intuition. This procedure depends on its validity on the pattern of new work conforming closely to that of the past

experience. Any deviation in design can only be assessed intuitively and may have adverse effects on the precision of survey. By classical methods, the observational precision may be assessed by examining triangle and other miscloses. The size of the corrections to the observations after an adjustment is also of assistance in this assessment. The actual implicit requirement of the survey is that stations be coordinated to some specified positional accuracy. In order to assess the positional accuracy, error ellipses may be calculated for each station and their dimensions to compare with the specification, related to the adjustment reveal any weaknesses, the field part must revisit the scheme to take additional measurements, and this is an expensive proposition. Some recent articles suggested the use of simulated observations to analyze a proposed scheme of survey. All these requirements to analyze the scheme need the knowledge of three components:

1. The approximate coordinates of stations.
2. The type of the proposed observations (Distances, Directions, Azimuths, etc.) and their position in the network.
3. The anticipated precision for each type of observation.

With this information, it is possible to calculate the error ellipses for the stations, and verify the desired accuracy can be attained. The effect of additional or fewer measurements and changes in observational accuracy can also be assessed, by repeating the above procedure varying requirements 2 and 3. In this way, the most economical method to achieve the desired accuracy may be determined before any field measurements have been taken. In other words, the network has been "Optimized", **Allan, J. S., and Hoar, G. J., 1973.**

### Optimization Procedure

The optimization and design of a geodetic control network play an important role in network analysis. Optimization means maximizing or minimizing an objective function which represents the criteria adopted to define Quality of a Geodetic Network. Generally, the quality of a geodetic network is characterized by precision, reliability, and economy. Precision may be expressed by the covariance matrix of the coordinates, displacement or deformation parameters, etc. So, the precision is the measure of the network characteristics in propagation of random errors, while reliability describes the ability of the redundant observation to check

observation errors. Finally, economy is expressed in terms of the observation program, e.g., the cost of observation, transport...etc, **Kuang, S. L., 1991.**

A network can be designed in such way that, **Schmitt, G., 1982:**

- The postulated precision of the network elements, e.g. coordinates or displacement of points, can be realized,
- It becomes sensitive against statistical testing carried in measurements, and it resists against undetected gross errors, and
- The construction of the points and the performance of the measurements satisfy some cost criteria.

In mathematical terms the quality of geodetic network means, **Amiri-Simkooei, A. R., 1998:**

$$\alpha_p(\text{precision}) + \alpha_r(\text{Reliability}) + \alpha_c(\text{cost})^{-1} \rightarrow \max \quad (1)$$

where:

$\alpha_p$ ,  $\alpha_r$  and  $\alpha_c$  are the weight coefficients for precision, reliability and cost, respectively.

There are two methods that can be used to solve the design problem:

1. Trial and error method: which can be summarize in the following steps, **Amiri-Simkooei, A. R., 2007:**
  - a. Specify precision and reliability criteria (e.g. ellipse of error).
  - b. Select an observation scheme (stations, observations and their precision).
  - c. Compute the values of the quantities specified as precision and reliability criteria (e.g. covariance matrix and redundancy numbers).
  - d. If the computed criteria are close to those specified in (a), then go to the next stage; otherwise alter the observation scheme (by adding the observations or increasing the weight if they are not satisfied, or by removing the observations or decreasing the weights if they are too optimistic) and return to (c).
  - e. Compute the cost of the network and restart from (b) with completely different scheme (e.g. Trilateration instead of triangulation).
  - f. Stop when it is believed that the optimum (minimum cost) network has been found.

In other words – in trial and error method, the objective function is computed with a suggested solution for the problem, and if the suggested solution does not satisfy the objective function, the solution is changed a bit and the objective function is computed again. This process is

repeated until the requirement is satisfied. The solution in the trial and error method depends on the experience of the designer. However, in some cases the solution might not even be found, but what might be interesting is its ease of use and lack of complicated mathematical models in its solution, **Sahabi, et al., 2006**.

2. **Analytical method:** which offer specific algorithms for the solution of particular design, which are used to describe a method that solves a particular design problem by a unique series of mathematical steps, **Kuang, S. L., 1991**. The analytical approach gives some advantages rather than other existing methods for network optimization, as follows:

- Any type of geodetic observable can be considered.
- Any condition or constraint can be considered.
- All the criteria of precision, reliability and cost can be considered simultaneously in the optimal design.
- The optimization procedure can be performed in the sense of FOD and SOD separately or simultaneously.
- This methodology can be used for the optimal design of one, two, or three dimensional networks.

The main disadvantage of the analytical method is: the proper formulation of the mathematical model can be difficult. This also holds for solution of the problem in an analytical way, **Simkoeei, A. R., 2007**.

## Adjustment Computations by Least Squares

The development of the theory of least squares adjustment is based on the variance law for independent observations. The mathematical concept of weights is presented as a function of the variance (squares of standard deviations), while the use of weights, in conjunction with the variance law, leads to the idea of the variance factor. The square root of the variance factor is usually referred to as the standard deviation of an observation having unit weight, **Gale, L. A., 1965**.

The principle and the equations of least squares and adjustment with constraints are explained in, **Mikhail, E. M., 1976**.

## Variance - Covariance Matrix

Variance – covariance matrix of coordinates of the analyzed network is a basis for

calculations of the relative positional errors. They allow the calculations of the following quantities that are frequently used in describing the positional accuracies which is called *post analysis process*, **Moffitt, F. H., and Bourchard, H., 1987**. The following symbols will be used:

$(\sigma_E, \sigma_N)$  = standard deviation of coordinates.

$(\sigma_{\max}, \sigma_{\min})$  = semi – major and semi – minor axes of standard error ellipse.

$(\sigma_d, \sigma_a, \sigma_A)$  = standard deviations of observed distance, directions (azimuths) and angles.

The covariance of a pair of coordinate values belonging to one or two points denoted by  $(\sigma_{E_i N_i}, \sigma_{E_j N_j})$  is a measure of statistical dependence of the two values, if the two coordinates or two observation values are uncorrelated then their covariance equals zero. The algorithm for computing the variance – covariance matrix is as follows:

$$\sigma_0^2 = \frac{v^t w v}{r} \quad (2)$$

$$\sum_{xx} = \sigma_0^2 (B^t w B)^{-1} \quad (3)$$

where:

$\sum_{xx}$  = variance-covariance matrix of adjusted unknowns,

$\sigma_0^2$  = variance of unit weight,

$B$  = the coefficients matrix,

$w$  = the weight matrix, and

$r$  = redundancy.

It is important to know that  $\sum_{xx}$  is square and symmetrical. For instant, for two points  $i$  and  $j$  in a network,  $\sum_{xx}$  will be a matrix of the form:

$$\sum_{xx} = \begin{bmatrix} \sigma_{E_i}^2 & \sigma_{E_i N_i} & \sigma_{E_i E_j} & \sigma_{E_i N_j} \\ \sigma_{E_i N_i} & \sigma_{N_i}^2 & \sigma_{N_i E_j} & \sigma_{N_i N_j} \\ \sigma_{E_i E_j} & \sigma_{N_i E_j} & \sigma_{E_j}^2 & \sigma_{E_j N_j} \\ \sigma_{E_i N_j} & \sigma_{N_i N_j} & \sigma_{E_j N_j} & \sigma_{N_j}^2 \end{bmatrix} \quad (4)$$

## Ellipse of Error

The variance or standard deviation are measures of precision for the one dimensional case like an angle or a distance, but in the case of two dimensional problems, such as the horizontal position of a point, error ellipses may be established around the point to designate precision regions for a different probabilities. The orientation of the ellipse relative to the E, N axes system, **Fig. 1**, depends on the correlation between E and N. If they are uncorrelated, the

ellipse axes will be parallel to E and N. If the two coordinates and of equal precision, or  $\sigma_E = \sigma_N$ , the ellipse becomes a circle. Considering the general case where the covariance matrix for the position of point p is given as, **Davis, et al., 1981**:

$$\Sigma = \begin{bmatrix} \sigma_E^2 & \sigma_{EN} \\ \sigma_{EN} & \sigma_N^2 \end{bmatrix} \quad (5)$$

The semi major and semi minor axes of the corresponding ellipse are computed as in the following:

$$\sigma_{\max}^2 = \frac{1}{2} \left( \sigma_N^2 + \sigma_E^2 + \sqrt{(\sigma_N^2 - \sigma_E^2)^2 + 4\sigma_{EN}^2} \right) \quad (6)$$

$$\sigma_{\min}^2 = \frac{1}{2} \left( \sigma_N^2 + \sigma_E^2 - \sqrt{(\sigma_N^2 - \sigma_E^2)^2 + 4\sigma_{EN}^2} \right) \quad (7)$$

The orientation of the ellipse is determined by computing  $(\theta)$  between the E axis and the semi major axis from:

$$\tan 2\theta = \frac{2\sigma_{EN}}{\sigma_E^2 - \sigma_N^2} \quad (8)$$

where:

$\theta$  = is laid off counter clockwise from the positive E-axis.

### Mathematical Model in Adjusting Horizontal Geodetic Network

The adjustment of geodetic networks still one of the most important problems in surveying for many applications such as designed for monitoring. With advance development of computers, the method of adjusting the geodetic networks by "variation of coordinates" technique become the most preferred one, **Jabiry, J. M., 2007**. The variation of coordinates is the most common method to adjusting the traditional geodetic networks such as triangulation networks, trilateration networks, intersection, resection, hybrid networks and traversing as well as in engineering applications such as displacement computation of heavy structures like dams and towers. The reason for the prevalence of using this method is its suitability for computer programming because it taken specific pattern depending on the type of observations and their relation to the fixed and unknown points, and it is based on assumption coordinates for unknown points, calculated by lengths and observed

directions by error does not exceed 1/4000 for lengths and 1 minute for directions to be solve with minimum iteration, **AL-Joboory, B. S., 2010**. The following equation is the final linearized observation equations for an observed distance see **Fig. 2**, where coordinates of  $i, j$  are known.

$$v_s = \left( \frac{E_i^\circ - E_j^\circ}{S_{ij}} \right) \times \delta E_i + \left( \frac{N_j^\circ - N_i^\circ}{S_{ij}} \right) \times \delta N_i \\ + \left( \frac{E_i^\circ - E_j^\circ}{S_{ij}} \right) \times \delta E_j - \left( \frac{N_i^\circ - N_j^\circ}{S_{ij}} \right) \times \delta N_j \quad (9) \\ + (S_{comp} - S_{obs})$$

### Free Net Adjustment or Inner Constraints

The datum problem is very important in geodetic networks and there are various methods for defining a datum. The definition of the best datum for a geodetic network can be called as the ZOD. There exist three methods for obtaining the adjusted coordinates of net points. If the datum is not defined for a geodetic network, one can say that there exists infinite number of solution for the coordinates of the net points, in other word, the points can get infinite values as coordinates. In order to restrict the values, some constraints should be included in our adjustment process, so that they convert our infinite number of solutions to finite number. These constraints should be defined so that the network becomes translation-free, rotation-free, and free of expansion or contraction. These characteristics can be included in adjustment process using minimum constraint, inner constraint, or even over constraint least squares adjustment. There are various literatures for mathematical description of these methods like (Teunissen, P.J.G., 1982), **Eshagh, M., 2006**.

In a free network adjustment the system of normal equation is singular because of the rank defect (no external datum). Different approaches for the solution of a free net are available, but the solution is always chosen where the trace of the covariance matrix of the estimated parameters is a minimum. The geometric interpretation of the minimum trace is that there should not be any translation, rotation or scaling changes from the given approximate values of the unknown parameters. One of the advantages of free net adjustment is the fact that it can better identify the existence of certain unmodeled systematic error in the system, as the solution is not influenced by external factors, **Remondino, F., 2006**. If a square, symmetric matrix, such as  $N$ , is of full

rank, then all of its eigenvalues are nonzero, and it's eigenvectors form an orthogonal basis for the row space. If it is not full rank, it has order  $u$ , rank ( $h < u$ ), and therefore defect ( $u-h$ ). Such as matrix will have ( $u-h$ ) zero eigenvalues. The  $h$  eigenvectors associated with nonzero eigenvalues will form an orthogonal basis for the row space, and the ( $u-h$ ) eigenvectors associated with the zero eigenvalues will form an orthogonal basis for the null space. The locus of solutions to the rank – deficient equations and the intersection point of the solution space and the row space are shown schematically **Fig. 3**. This strategy will have the following characteristics:

1. It will resolve the deficiency from the datum defect and it will therefore permit a unique solution to the system of equations.
2. Of all the possible solutions to the rank – deficient system, it will select the one with minimum magnitude and minimum variance.

This solution is known in the geodetic and photogrammetric literature as the inner constraint solution, or sometimes as the free net solution.

This presentation is useful for understanding the geometry of the problem, but there are easier ways to construct the needed constraint matrix. The eigenvectors just described provide a basis of the null space of the rank – deficient matrix. But, as with any vector space, there are many (an infinite number of) such bases. In the adjustment of geodetic nets, the relationships between the observations and the point coordinate parameters are expressed by condition equations: for example, the angle or the distance condition equations in geodetic applications. These equations all contribute relative information rather than absolute information about the point positions. The usual procedure to introduce absolute information is by constraining (fixing) certain point coordinate components. These points are referred to as control points. Without such control points, or other constraints, the system of normal equations would be rank deficient and hence not uniquely solvable. The rank deficiency is equal to the minimum number of constraints that would be needed to bring the system to full rank. In the case of a horizontal network with only angle observations, the rank deficiency is four. In the case of a horizontal network with at least one distance observation, the rank deficiency is three. The rank deficiencies are referred to as datum defect, since the presence of the necessary control points would define the datum. Of course, there may be other causes of rank deficiency, such as

insufficient observations to define a point, these are another matter altogether, and are referred to as configuration defects. In one introduces just enough constraint equations to satisfy the datum defect, and then these are known as minimal constraints. Different sets of minimal constraints have the interesting property that, although the point coordinate estimate may vary, the observation residuals are invariant. Thus, for residual analysis only any minimal set of control points is as good as another. However, in practice the choice of control point is very important. The new network must be consistent with existing networks at shared points. There are many mathematical techniques that could be used to solve for the generalized inverse, they are:

1. Orthogonal bordering.
2. Pseudo inverse.
3. Singular value decomposition (SVD).
4. Orthogonalization (QR).
5. There is another common approach is, **AL-Joboory, B. S., 2010:**

$$N^+ = (B^t w B + C^t C)^{-1} - C^t (C C^t C C^t)^{-1} C \quad (10)$$

For the purpose of illustration, consider the geodetic horizontal triangle network in **Fig. 4**, as an example. If only the three angle observations shown are made and no control points are introduced, then the resulting normal equations, of size  $[6 \times 6]$  have rank two and rank deficiency of four. The fixing of two control points, or four point coordinates, would resolve this datum defect. These constraints can be implemented very simply by eliminating the effect by replacing the unknowns with numerical constant. However, for generality we assume that the constraints are implemented by the general method of bordering, (Helmert Method), where:

$$\begin{bmatrix} -N & C^t \\ C & 0 \end{bmatrix} \begin{bmatrix} \Delta \\ k_c \end{bmatrix} = \begin{bmatrix} -t \\ g \end{bmatrix} \quad (11)$$

In which  $N$  and  $t$  pertain to the normal equations, where  $N=B^t w B$  and  $t=B^t w f$ .

For the horizontal 2-D network in **Fig. 4**, with no distance observations, the following constraint matrix will have the same effect as the (harder to compute) eigenvectors:

$$C = \begin{bmatrix} 1 & 0 & 1 & 0 & 1 & 0 \\ 0 & 1 & 0 & 1 & 0 & 1 \\ y_i^o & -x_i^o & y_j^o & -x_j^o & y_k^o & -x_k^o \\ x_i^o & y_i^o & x_j^o & y_j^o & x_k^o & y_k^o \end{bmatrix} \quad (12)$$

in which approximate coordinates  $x^o$ ,  $y^o$  of three points are used. If distance observation were present then the datum defect would be one less, and the fourth row of the matrix in eq. (3) will be canceled. In order to demonstrate the plausibility of this solution, it will be shown that the rows of the matrix in eq. (3) are orthogonal to the coefficients of the angle condition equation. This condition equation represents the one most widely used in two dimensional, horizontal triangulation networks. For the clockwise angle at point ( $i$ ), in **Fig. 3**, from point ( $j$ ) to point ( $k$ ), the following row vector represents the coefficients of the linearized angle condition equation, **Mikhail, et al., 2000**.

$$B = \left[ \frac{\partial F_\theta}{\partial x_i} \quad \frac{\partial F_\theta}{\partial y_i} \quad \frac{\partial F_\theta}{\partial x_j} \quad \frac{\partial F_\theta}{\partial y_j} \quad \frac{\partial F_\theta}{\partial x_k} \quad \frac{\partial F_\theta}{\partial y_k} \right] \quad (13)$$

If one takes the inner product of  $B$  with the rows of  $C$ , the result is a vector of zeros. In other words, the rows of  $C$  are orthogonal to  $B$ .

$$BC^t = [0 \quad 0 \quad 0 \quad 0 \quad 0 \quad 0] \quad (14)$$

The development will summarize for the two dimensional case, a simple extension can be to make the adjusted coordinate the approximate coordinates,  $X^o$ .

$$X_a = T + (1+k)R_\alpha \cdot X^o \quad (15)$$

in which  $T$  is the translation vector,  $(1+k)$  is the scale factor, and  $R_\alpha$  is the matrix of a small angle. Written as:

$$\begin{bmatrix} x_a \\ y_a \end{bmatrix} = \begin{bmatrix} t_x \\ t_y \end{bmatrix} + (1+k) \begin{bmatrix} \cos \alpha & \sin \alpha \\ -\sin \alpha & \cos \alpha \end{bmatrix} \begin{bmatrix} x^o \\ y^o \end{bmatrix} \quad (16)$$

Assuming a small angle and scale vector near unity, and assuming that products of small quantities may be disregarded, we obtain:

$$\begin{bmatrix} x_a \\ y_a \end{bmatrix} = \begin{bmatrix} t_x \\ t_y \end{bmatrix} + \begin{bmatrix} x_o \\ y_o \end{bmatrix} + \alpha \begin{bmatrix} y^o \\ -x^o \end{bmatrix} + k \begin{bmatrix} x^o \\ y^o \end{bmatrix} \quad (17)$$

So this represents a step in the iterative solution.

$$\begin{bmatrix} x_a \\ y_a \end{bmatrix} = \begin{bmatrix} x^o + dx \\ y^o + dy \end{bmatrix} \quad (18)$$

The last two equations can be combining to obtain:

$$\begin{bmatrix} dx \\ dy \end{bmatrix} = \begin{bmatrix} t_x \\ t_y \end{bmatrix} + \alpha \begin{bmatrix} y^o \\ -x^o \end{bmatrix} + k \begin{bmatrix} x^o \\ y^o \end{bmatrix} \quad (19)$$

Rearranging in a matrix form yields:

$$\begin{bmatrix} dx \\ dy \end{bmatrix} = \begin{bmatrix} 1 & 0 & y^o & x^o \\ 0 & 1 & -x^o & y^o \end{bmatrix} \begin{bmatrix} t_x \\ t_y \\ \alpha \\ k \end{bmatrix} \quad (20)$$

The above equations can be written for every point in the network as:

$$\begin{bmatrix} d_{x1} \\ d_{y1} \\ d_{x2} \\ d_{y2} \\ \vdots \\ d_{xn} \\ d_{yn} \end{bmatrix} = \begin{bmatrix} 1 & 0 & y_1^o & x_1^o \\ 0 & 1 & -x_1^o & y_1^o \\ 1 & 0 & y_2^o & x_2^o \\ 0 & 1 & -x_2^o & y_2^o \\ \vdots & \vdots & \vdots & \vdots \\ 1 & 0 & y_n^o & x_n^o \\ 0 & 1 & -x_n^o & y_n^o \end{bmatrix} \begin{bmatrix} t_x \\ t_y \\ \alpha \\ k \end{bmatrix} \quad (21)$$

By considering this to be over determined system of equations, then:

$$f \approx B\Delta \quad (22)$$

Then it could be solved in the least squares sense by the usual normal equations:

$$\Delta = (B^t B)^{-1} B^t f \quad (23)$$

Now suppose that we would like to enforce the condition between the point coordinates before and after the iterative correction where will be no net shift, rotation, or scale change.

In other words,

$$\Delta = \begin{bmatrix} t_x \\ t_y \\ \alpha \\ k \end{bmatrix} = 0 \quad (24)$$

This can be done by setting

$$B^t f = 0 \quad (25)$$

or, it can be written as,

$$\begin{bmatrix} 1 & 0 & \dots & 1 & 0 \\ 0 & 1 & \dots & 0 & 1 \\ y_1^o & -x_1^o & \dots & y_n^o & -x_n^o \\ x_1^o & y_1^o & \dots & x_n^o & y_n^o \end{bmatrix} = \begin{bmatrix} d_{x1} \\ d_{y1} \\ \vdots \\ d_{xn} \\ d_{yn} \end{bmatrix} = \begin{bmatrix} 0 \\ 0 \\ 0 \\ 0 \end{bmatrix} \quad (26)$$

The geometric interpretation of the inner constraint solution is that when advancing from one iteration to the next, there will be no net shift, rotation, or scale change between the approximate and refined coordinate positions. Thus, rather than arbitrarily fixing two points (four coordinate components) out of many, one fixes four geometric relationships. All points then equal play roles in connecting the network to the coordinate system. This can have dramatic effects upon the a posteriori confidence ellipse of the network points. If a point is fixed, then its confidence ellipse vanishes. For a three point network, after fixing two points, all of the error is cast into the uncertainty of the third point. With the inner constraint or free net solution, however, each point has a finite confidence ellipse that reflects its strength of determination in the network.

### First Order Design problem (FOD)

Determination of the optimum geometric design for geodetic network is one of the classical design problems in geodesy, known as the first-order design problem, **Berné, J. L., and Baselga, S., 2004**. When trying to define the best geometric configuration of a new geodetic network, the range of situation can vary from the case where the possible location of the station is so constrained by exterior conditions - visibility, natural features, private properties, etc. - that there is almost no choice for the most adequate location because there is no margin of movement, to the case where any possible location within an area is acceptable. As the margin of choice grows, there is an increasing need for reliable criteria to determine the most appropriate network design. Criteria for appropriateness should rely on the minimum in determination at the defined points, considering both the type and the number of observations to be done. Some mathematical methods are required to search for the best design.

One of the most rigorous approaches is to determine the position of all the stations to be located by means of minimizing the hyper volume of error hyper ellipsoid inherent to the solution. The system of equations for the parametric least squares method in its parametric form, and for any kind of observations (angles, distance, etc.) can be used and as the aim is to minimize the hyper volume of the hyper ellipsoid define by  $\sum_{xx}$  this involves minimizing its determined

$$\begin{aligned} &\text{Min. det. } (\sum_{xx}) \\ &\text{or} \\ &\text{Max. det. } (\sum_{xx})^{-1} \end{aligned} \quad (27)$$

The question of finding optima for the determinant function (and even to calculate the determinant function itself) is far from being a trivial problem. Moreover, if the desired solution has to be not a local but the global optimum, the solution is almost unattainable, at least from the classical mathematical point of view.

### Measures and Criteria for Precision

The precision measures and criteria of a geodetic network are based on the covariance matrix of estimated coordinates. One measure of precision takes the form of scalar function of the elements of the covariance matrix of the coordinates varieties. The purpose is to fill the need for an overall representation of the precision of a network, **Kuang, S. L., 1991**.

A scalar function (objective function) may be one of the following, **Berné, J. L., and Baselga, S., 2004**.

#### 1. A – Optimality

This refers to minimizing the trace in the covariance matrix. As a result, the average variances of the parameter estimates are minimized.

$$f = \text{trace } (\sum_{xx}) \rightarrow \min \quad (28)$$

#### 2. D – Optimality

This seeks to minimize the covariance matrix determinant. It has the statistical significance of minimizing the volume of the error hyper ellipsoid.

$$f = \det (\sum_{xx}) \rightarrow \min \quad (29)$$

#### 3. E – Optimality



This aims to minimize the largest eigenvalue of the covariance matrix for the parameter estimates.

$$f = \lambda_{\max} \rightarrow \min \quad (30)$$

#### 4. S – Optimality

This related to network stiffness and supposes an eigenvalue and eigenvector approach to the problem of optimization in terms of network stiffness, i.e. the maximum flattening of the eigenvalue spectrum.

$$f = \lambda_{\max} - \lambda_{\min} \rightarrow \min \quad (31)$$

#### 5. Criterion Matrices

These consist of defining a desired matrix for the result – the criterion matrix – and then finding the solution that is closest to this ideal assumption. They sometimes appear together with some of the other methods.

### Rosenbrock Method for Unconstrained Optimization Problems

Rosenbrock Method falls within the numerical category of optimization methods. The method, due to, **Rosenbrock, H. H., 1960**, uses a direct search technique making use of the Orthogonalization principle of Gram-Schmidt in order to give an acceleration in both the direction and the step length. The method is fully explained in many references, **Rosenbrock, H. H., 1960**, **Kuester, J. L., and Mize, J. H., 1973**, **Bazaraa, M. S., and Shetty, C. M., 1979**, **AL-Fahdawi, D. KH., 2000**, **Al-Hity, A. A., 2006**. It can be reviewed by the following algorithm:

1. Choose initial values for the design variables and set of step sizes ( $\lambda_1, \lambda_2, \lambda_3, \dots, \lambda_n$ ) (where  $n$  is the number of independent variables). Also choose a set of search directions ( $S_1^j, S_2^j, S_3^j, \dots, S_n^j$ ) which are usually selected as being parallel to the basic axes when  $j=1$ , and evaluate the function.
2. Sequentially search parallel to each of the  $n$  directions in turn, adopting the new point if the move is successful (objective function is less than or equal to the previous one) and retaining the last point if the move is unsuccessful. If a move is successful the step length is multiplied by a factor ( $\alpha$ ), ( $\alpha > 1$ ) then this direction is next searched in its turn. If the move is unsuccessful then the step length to be used for the next search is ( $\beta$ ) times the previous length ( $0 < \beta < 1$ ) and the

direction of move is reversed. However Rosenbrock recommended the use of ( $\alpha = 3$ ) and ( $\beta = 0.5$ ) as suitable values.

3. The search of step (2) continues until at success is followed by a failure in every direction, **Himmelblau, D. M., 1972**.
4. Compute the new set of direction ( $S_1^{j+1}, S_2^{j+1}, S_3^{j+1}, \dots, S_n^{j+1}$ ) for use in next ( $j+1$ )<sup>th</sup> stage of method by using the Gram-Schmidt Orthogonalization procedure.
  - a. Compute a set of independent direction ( $P_1, P_2, P_3, \dots, P_n$ ) as

$$P_{(n,n)} = [P_1 \ P_2 \ P_3 \dots P_n] \quad (32)$$

$$= \begin{bmatrix} S_1^j & S_2^j & S_3^j & \dots & S_n^j \end{bmatrix} \begin{bmatrix} a_1 & 0 & . & 0 \\ a_2 & a_2 & . & 0 \\ . & . & . & . \\ a_n & a_n & . & a_n \end{bmatrix}$$

where:

$a_i$  = The algebraic sum of the all the successful step length in the corresponding direction.

$S_i^j$  = The direction and  $i=1,2,3,\dots,n$

$P_1$  = The vector joining the starting point and the final obtained after the sequence of the searches in the ( $j$ )<sup>th</sup> stage.

$P_2, P_3, \dots, P_n$  = The algebraic sum of the successful step length in the all directions except the first one, and so on these linearly independent vector  $P_2, P_3, \dots, P_n$  can be used to generate a new set of orthogonal directions.

$$b. \text{ Set } D_1^j = P_1^j \quad (33)$$

with:

$$S_1^j = \frac{D_1^j}{\sqrt{(D_1^j)^t \cdot D_1^j}} \quad (34)$$

$$c. \text{ Compute } D_i^j = P_i^j - \sum_{m=1}^{i-1} [(P_{m+1}^j)^t \cdot S_m^j] \cdot S_m^j \quad (35)$$

with:

$$S_i^j = \frac{D_i^j}{\sqrt{(D_i^j)^t \cdot D_i^j}}$$

5. Take the best point obtained in the present stage, and repeat the same procedure of searching from step (2).

$$\text{i.e. } new [x_{L,i}^j] = old [x_{L,i}^j] + \lambda_i [S_{L,i}^j] \quad (36)$$

where:

$L$  = variable index,  $L=1,2,\dots,n$

$i$  = direction index,  $i=1,2,\dots,n$

$j$  = stage index.

6. The procedure terminates when the convergence criterion between initial and final value of the objective function is satisfied.

### Case Study Geodetic Network

A trilateration network part of Mosul Dam Network was selected as a case study for the purpose of application of the proposed optimization network technique. The network consists of 19 points, six of the observations pillars are on the dam body, and 58 designed distance with standard deviation equal to 5mm as shown in **Fig. 5**, **Table 1** lists the initial coordinates of the network points. This initial coordinates were based on the epoch 36. **Table 2**. lists the designed distances of the network. The designed distances were derived from the observed distances of Mosul Dam Network in epoch 36 from **AL-Kanani, Y. H., 2009**. The designed distances difference slightly from the observed distance for study purpose. Additional designed distances were added to make a difference in the original network and to strengthen the network to get the more realistic control points. These distances were from P44 to P54, P55 to P3, P42 to P52, P42 to P61, P01 to P71, P61 to P71, and from P71 to P73.

### ZOD Application to the Case Study

During the design stage of the geodetic networks, a selection of some control points must be made. The ZOD used to select the best points which can be detected to be the control points for the network of the case study. A program using MATLAB language was prepared to solve ZOD as shown in **Fig. 6**. which shows a flow chart describing the steps of free network program, this program has a capability of:

1. Compute the free network adjustment by calculating the general inverse or the so-called false inverse through Helmert Method.
2. Compute the post-analysis for the adjustment including variance-covariance matrix and compute the elements of ellipse of error.
3. Plot of the points and the ellipse of errors for each point in the network.

The results of application of the ZOD, semi-major, semi-minor axis and area of the ellipse of errors, for each point presented in **Table 3**. **Fig. 7** presents the ellipses of error for each point in the network exaggerated by a factor of 30000. The ellipse of error for the network points varies

between 24.50mm<sup>2</sup> and 146.24 mm<sup>2</sup>. Points P66, P55, and P73 have the smallest ellipse of error compared to the other points. Because of, Point P66 is lie on the dam body, therefore; points P55 and P73 considered as the best points and selected as control points.

### FOD with High Precision

First Order Design problem is one of the classical design problems that face surveyors. By using FOD one can determinate the optimum geometric design for a geodetic network through optimizing station positions. The variables in FOD problem are the observations "design matrix" or (B-Matrix geometry of the network). To solve FOD problem, one of the optimization methods was selected that is "Rosenbrock Method". A program was prepared using MATLAB language to solve FOD with precision using Rosenbrock Method based on the equations from (32) to (36), and using least square techniques. The two objective functions to solve FOD with high precision are:

1. A-Optimality:

$$\text{Objective function} = \text{Min. trace } (Q_{xx}) \quad (37)$$

$$\text{Constraint:} \quad \begin{aligned} E_L &\leq E_i \leq E_U \\ N_L &\leq N_i \leq N_U \end{aligned}$$

2. D-Optimality:

$$\text{Objective function} = \text{Min. det. } (Q_{xx}) \quad (38)$$

$$\text{Constraint:} \quad \begin{aligned} E_L &\leq E_i \leq E_U \\ N_L &\leq N_i \leq N_U \end{aligned}$$

where:

$$\Sigma_{xx} = \sigma_o^2 Q_{xx},$$

$$Q_{xx} = (B^T W B)^{-1},$$

$$\sigma_o^2 = 1 \text{ in design stage,}$$

$E_i$  and  $N_i$  = coordinates of points,  
 $i$  = number of point,

$E_L$  and  $E_U$  = lower and upper limit in X-direction for each point, and

$N_L$  and  $N_U$  = lower and upper limit in Y-direction for each point.

A program was prepared using MATLAB language to solve A-Optimality and D-Optimality. FOD applying to the network of case study after applying ZOD and selecting the points P55 and P73 as control points, then the FOD was applied to the network of case study in three cases. The case which satisfies the best condition of precision

will be identified as the optimal design of the micro geodetic network. These cases are:

- The 1<sup>st</sup> case: considering the dam points are fixed, and the other points are moving.
- The 2<sup>nd</sup> case: fixing the dam points, and using the resulting points from the ZOD results as control points, these points are P55 and P73.
- The 3<sup>rd</sup> case: fixing the dam points, and using the points which are used by the general directorate for survey as control points, these points are P42 and P44.

In FOD, different values of range of movement of 50, 100, and 300m were tried. It was found that when the range of movement of 50 and 100m, the movements in the points of the network were not clear. 300m as a range of the movement in each direction for each point was selected and assuming no obstacles to exist. The upper and lower limits of movement for each point can write as:

$$E_i^o - 150\text{ m} \leq E_i \leq E_i^o + 150\text{ m}$$
$$N_i^o - 150\text{ m} \leq N_i \leq N_i^o + 150\text{ m}$$

The limits of movement for each point of the network in E and N directions computed and presented in **Table 7**. The final coordinates of network points obtained according to the FOD will be compared to the lower and upper limits, obtained below. If the final coordinates within the limits of movement, the solution continue to the next step of calculation of FOD until exceeding the limits of movement of all points. FOD with high precision, high reliability, and high precision and high reliability were applied to the three cases, mentioned above.

### FOD with High Precision Application to The Case Study

In FOD with high precision computations, The initial coordinates of points were used to calculate the initial value of the objective function. Then the prepared program of FOD with high precision applied to each case to compute the final coordinates of the points that satisfy the range of movement. The final value of the objective function of each case was computed. To make sure that the errors in the final positions of points are less than the errors in the initial positions and the errors not distributed between points of the network, area of the ellipse of errors has been added to the computations. The results of applying FOD with high precision to the three cases were as follows:

1. The 1<sup>st</sup> case: the initial value of the objective function was  $905348144335858 \times 10^{-17}$ , which is equal the trace of  $Q_{xx}$  matrix with  $[26 \times 26]$  and the final value of the objective function was  $672977706671926 \times 10^{-17}$ . This indicates that there was an improvement in the value of the objective function. **Table 4**, lists the initial and final easting and northing coordinates for each point with their standard deviations and area of ellipse of error for each point. It can be noticed that the improvement in the standard deviation in most of points and this lead to improvement the area of the ellipse of error and all that indicates the improvement in precision, see **Fig. 8**.
2. The 2<sup>nd</sup> case: the initial value of the objective function, A-Optimality, was  $767947323337789 \times 10^{-17}$ , for a trace of  $Q_{xx}$  matrix with  $[22 \times 22]$  and the final value of the objective function was  $558262174843364 \times 10^{-17}$ . **Table 5** presents the results of application of the FOD with high precision. The value of the objective function and the results of application of the FOD indicated that there was an enhancement in the value of the objective function, in the standard deviation in most of points, and in the area of the ellipse of error. All of these enhancements of sure will be reflected on the improvement of precision, see **Fig. 9**.
3. The 3<sup>rd</sup> case: the initial value of the objective function, A-Optimality, was  $68147035762434 \times 10^{-17}$ , which is equal the trace of  $Q_{xx}$  matrix with  $[22 \times 22]$  and the final value of the objective function was  $496224444075659 \times 10^{-17}$ . The results of applying FOD with high precision to the 3<sup>rd</sup> case are list in **Table 6**, that lists the final coordinates of network points, the standard deviation, and area of ellipse of error for each point. There was an improvement in the value of the objective function, in the standard deviation in most of points, and in the area of the ellipse of error. With these enhancements the network becomes more precision than the initial network, see **Fig. 10**.  
The objective function values of the 2<sup>nd</sup> case and the 3<sup>rd</sup> case was better than the objective function values of the 1<sup>st</sup> case. The results of FOD with high precision of the 3<sup>rd</sup> case were better than that of the 2<sup>nd</sup> case. Therefore, the 3<sup>rd</sup> case network

was considered as optimal design due to its high precision.

Different values of the constants  $\alpha$  and  $\beta$  of the Rosenbrock Method than the used values of 3 and 0.5 respectively, in the above analysis were investigated. These values were  $\alpha=1, 1.5$ , and 2, and  $\beta=0.1$  and 0.25. Results showed that these values gave almost similar results of that when  $\alpha=3$  and  $\beta=0.5$  were used. The precision of all cases were analyzed by using D-Optimality as objective function, which means the determinates of  $Q_{xx}$  matrix. The results of applying FOD with high precision to all cases using D-Optimality indicate that there was an improvement in the precision. The obtained improvement is exactly as that obtained by applying FOD with high precision using A-Optimality.

## REFERENCES

- AL-Fahdawi, D. KH., 2000, "*Optimum Design of Communication Towers*", M. Sc. Thesis, College of Engineering, University of Baghdad, Department of Civil Engineering.
- Al-Hity, A. A., 2006, "*Water Resources Management and Economics Lectures*", College of Engineering, Al-Anbar University.
- AL-Joboory, B. S. A., 2010, "*Adjustment in Surveying: Theory and Practice*", University of Baghdad, College of Engineering, Iraq, in Arabic.
- AL-Kanani, Y. H., 2009, "*Displacement Computation of Mosul Dam by Using Free Geodetic Network Adjustment*", M. Sc. Thesis, College of Engineering, University of Baghdad, Department of Surveying Engineering.
- Allan, J. S., and Hoar, G. J., 1973, "*Optimization of Geodetic Networks*", Survey reviews XXII, 167, University of New South Wales, Sydney, Australia, January.
- Amiri-Simkooei, A. R., 1998, "*Analytical Methods in Optimization and Design of Geodetic Networks*", M. Sc. Thesis, Department of Surveying Engineering, University of Technology, Iran.
- Amiri-Simkooei, A. R., 2007, "*Analytical First Order Design of Geodetic Network*", Iranian Journal of Engineering Sciences, Vol.1, No.1, December.
- Bazaraa, M. S., and Shetty, C. M., 1979, "*Nonlinear Programming: Theory and Algorithms*", John Wiley and Sons.
- Berné, J. L., and Baselga, S., 2004, "*First-Order Design of Geodetic Networks using the Simulated Annealing Method*", Journal of Geodesy, Vol.78, and p.p.:47-54.
- Davis, R. E., Foote, F. S., Anderson, J. M., and Mikhail, E. M., 1981, "*Surveying Theory and Practice*", 6<sup>th</sup> edition, McGraw-Hill Book Company.
- Eshagh, M., 2006, "*Scalar Risk Functions As Criteria for Datum Definition in Geodetic Networks*", National Cartographic Center of Iran, Tahrán, Iran.
- Gale, L. A., 1965, "*Theory of Adjustment by Least Squares*", the Canadian surveying, Vol. XTX, No. 1, p.p. 42-60, March.
- Ghilani, C. D., and Wolf, P. R., 2006, "*Adjustment Computation: Spatial Data Analysis*", 4<sup>th</sup> edition, John Wiley and sons.
- Himmelblau, D. M., 1972, "*Applied Nonlinear Programming*", McGraw-Hill Book Company.
- Jabiry, J. M., 2007, "*Blunder Detection Techniques in Adjustment Computations*", M. Sc. Thesis, College of Engineering, University of Baghdad, Department of Surveying Engineering.
- Kuang, S. L., 1991, "*Optimization and Design of Deformation Monitoring Schemes*", Department of Geodesy and Geomatics Engineering, University of New Brunswick, Canada, p.p. 179, September.
- Kuester, J. L., and Mize, J. H., 1973, "*Optimization Techniques with FORTRAN*", the Computer Journal, McGraw-Hill Book Company.
- Mikhail, E. M., 1976, "*Observations and Least Squares*", 1<sup>st</sup> edition, Donnelly publisher, New York.
- Mikhail, E. M., Bethel, J. S., Glone, J. C., and Wiely, J., 2000, "*Introduction to Modern Photogrammetry*", 6<sup>th</sup> edition, Donnelly publisher, New York.



Moffitt, F.H., and Bourchard, H., 1987, "Surveying", 7<sup>th</sup> edition, Harper and Row, Publisher, New York.

Remondino, F., 2006, "Image-Based Modeling of Object and Human Reconstruction", Doctoral thesis ETH No. 16562, Aristotle University, Greece, Zurich

Rosenbrock, H. H., 1960, "An Automatic Method for Finding the Greatest or Least Value of a Function", the Computer Journal, Vol. 3, p.p. :( 175-184).

Sahabi, H., Rajabi, M.A., and Blais J.A.R., 2006, "Optimal Design of Deformation Monitoring Networks using Genetic Algorithm".

Schmitt, G., 1982, "Optimization of Geodetic Networks", geodetic institute, University of Karlsruhe, Germany.

Teunissen, P.J.G., 2006, "Network Quality Control", First edition published by VSSD, <http://www.Vssd.nl/hlf>.

### List Of Symbols

Symbol	Symbol
$B$	Coefficient matrix.
$C$	Constraints matrix.
COMD	Combined Design.
$E_L$ and $E_U$	Lower and upper limit in X-direction for each point
FOD	First Order Design.
$g$	Constant terms in constraint equation.
GDS	General Directorate for Survey.
$n$	No. of observations.
$N_L$ and $N_U$	Lower and upper limit in Y-direction for each point
$Q_{xx}$	Covariance matrix
$S_i^j$	The direction and $i = 1, 2, 3, \dots, n$
SOD	Second Order Design.
TOD	Third Order Design.
$v_s$	Residual of observation.
$w$	The weight matrix.
ZOD	Zero Order Design
$\sum_{xx}$	Variance-covariance matrix of adjusted unknowns.
$\alpha_p, \alpha_r$ and $\alpha_c$	Weight coefficients for precision, reliability and cost.
$\theta$	The angle of ellipse orientation.
$\rho''$	206265
$\sigma_0^2$	Variance of unit weight.

**Table 1.** The initial coordinates of the network points.

Point	Easting, <i>m</i>	Northing, <i>m</i>	Notes
P61	70384.0000	49113.0000	on Dam body
P62	70795.0000	48989.0000	on Dam body
P63	71178.0000	48873.0000	on Dam body
P64	71571.0000	48754.0000	on Dam body
P65	71963.0000	48636.0000	on Dam body
P66	72272.0000	48402.0000	on Dam body
P51	69547.0000	49265.0000	
P52	69856.0000	48865.0000	
P53	70582.0000	48516.0000	
P54	71138.0000	47976.0000	
P55	71754.0000	47914.0000	
P71	69904.0000	49524.0000	
P72	70620.0000	49999.0000	
P73	72344.0000	48898.0000	
P01	68672.0000	49162.0000	
P32	71705.0000	50937.0000	
P03	73417.0000	47589.0000	
P42	70191.3921	48310.7710	
P44	71851.7091	47153.8040	

**Table 2.** The designed distances.

Station Occupied	Station Sighted	Distance, <i>m</i>	Station Occupied	Station Sighted	Distance, <i>m</i>
P42	P53	441.8518	P53	P62	518.6125
P42	P66	2083.2556	P53	P63	694.6583
P42	P55	1612.8824	P53	P66	1693.9374
P42	P54	1004.4418	P53	P55	1317.6971
P44	P55	766.7708	P53	P54	774.9212
P44	P66	1317.3135	P54	P55	619.3717
P44	P03	1625.3395	P54	P63	897.8043
P03	P44	1625.3431	P54	P64	890.3940
P03	P66	1404.1610	P54	P65	1056.1644
P03	P73	1692.5980	P54	P66	1211.3027
P72	P51	1299.9509	P55	P53	1317.6951
P72	P32	1434.6604	P55	P64	860.3537
P72	P61	916.6018	P55	P65	751.2943
P72	P63	1256.2973	P55	P66	711.2337
P72	P52	1367.2003	P61	P62	429.9238
P73	P32	2137.0400	P62	P63	400.1617
P73	P63	1166.4082	P63	P64	409.8950
P73	P64	786.8815	P64	P65	410.0221
P73	P65	462.5056	P65	P66	388.0540
P73	P66	501.2474	P32	P63	2130.4762
P52	P62	946.6672	P32	P66	2598.0246
P52	P61	582.6254	P71	P72	859.0721
P52	P72	1367.1868	P44	P54	1088.1253
P52	P51	505.5532	P55	P03	1694.8752
P52	P01	1221.3664	P42	P52	647.2145
P51	P01	881.4129	P42	P61	825.4356
P51	P71	441.1126	P01	P71	1284.3542
P51	P61	849.7613	P61	P71	631.4236
P51	P53	1277.4954	P71	P73	2519.5667

**Table 3.** The semi-major, semi-minor axis and area of ellipse of errors for each point in the network.

Point	Semi-major axis, <i>m</i>	Semi-minor axis, <i>m</i>	Area of ellipse of error, <i>mm</i> <sup>2</sup>	Point	Semi-major axis, <i>m</i>	Semi-minor axis, <i>m</i>	Area of ellipse of error, <i>mm</i> <sup>2</sup>
P61	0.0043	0.0034	45.93	P55	0.0034	0.0028	29.91
P62	0.0064	0.0035	70.37	P71	0.0057	0.0030	53.72
P63	0.0036	0.0030	33.93	P72	0.0055	0.0030	51.84
P64	0.0046	0.0035	50.58	P73	0.0035	0.0030	32.99
P65	0.0041	0.0036	46.37	P1	0.0133	0.0035	146.24
P66	0.0030	0.0026	24.50	P32	0.0058	0.0031	56.49
P51	0.0044	0.0029	40.09	P3	0.0068	0.0032	68.36
P52	0.0038	0.0034	40.59	P42	0.0044	0.0030	41.47
P53	0.0046	0.0026	37.57	P44	0.0056	0.0033	58.06
P54	0.0039	0.0029	35.53				

**Table 4.** The results of FOD with high precision in 1<sup>st</sup> case.

Point	Easting, <i>m</i>		Northing, <i>m</i>		$\sigma_E, m$		$\sigma_N, m$		Area of ellipse of error, <i>mm</i> <sup>2</sup>	
	Initial	Final	Initial	Final	Initial	Final	Initial	Final	Initial	Final
P51	69547.0000	69631.8139	49265.0000	49258.8553	0.0036	0.0036	0.0070	0.0058	73.26	65.94
P52	69856.0000	69748.9006	48865.0000	48763.9506	0.0033	0.0033	0.0049	0.0048	49.44	50.71
P53	70582.0000	70485.2286	48516.0000	48422.7215	0.0027	0.0027	0.0037	0.0036	32.41	32.76
P54	71138.0000	71047.7465	47976.0000	47888.4522	0.0031	0.0031	0.0032	0.0032	29.86	30.47
P55	71754.0000	71668.9221	47914.0000	47831.2088	0.0032	0.0032	0.0028	0.0027	28.98	28.95
P71	69904.0000	69823.3478	49524.0000	49649.1831	0.0042	0.0040	0.0066	0.0060	81.60	78.61
P72	70620.0000	70645.6995	49999.0000	50049.1453	0.0062	0.0060	0.0034	0.0033	65.01	62.17
P73	72344.0000	72491.2871	48898.0000	49042.3992	0.0027	0.0029	0.0035	0.0032	30.56	33.10
P01	68672.0000	68813.7930	49162.0000	49208.4240	0.0041	0.0042	0.0186	0.0129	239.93	171.91
P32	71705.0000	71842.0263	50937.0000	50869.5914	0.0077	0.0073	0.0030	0.0031	73.96	71.95
P03	73417.0000	73350.6781	47589.0000	47719.5048	0.0053	0.0044	0.0081	0.0072	95.12	83.26
P42	70191.3921	70319.8802	48310.7710	48247.4835	0.0032	0.0032	0.0042	0.0039	41.69	41.27
P44	71851.7091	71841.3424	47153.8040	47276.6001	0.0068	0.0057	0.0035	0.0037	76.29	67.45



**Table 5.** The results of FOD with high precision in 2<sup>nd</sup> case.

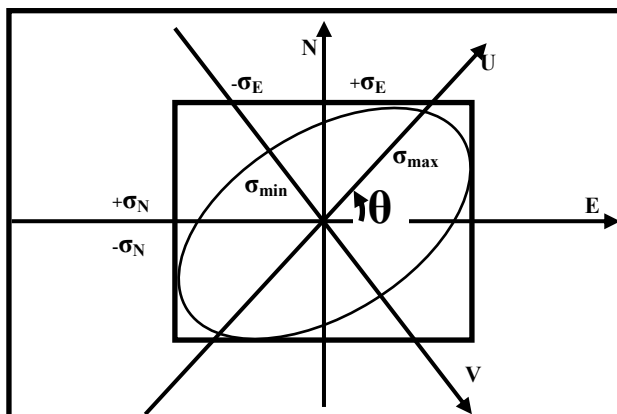
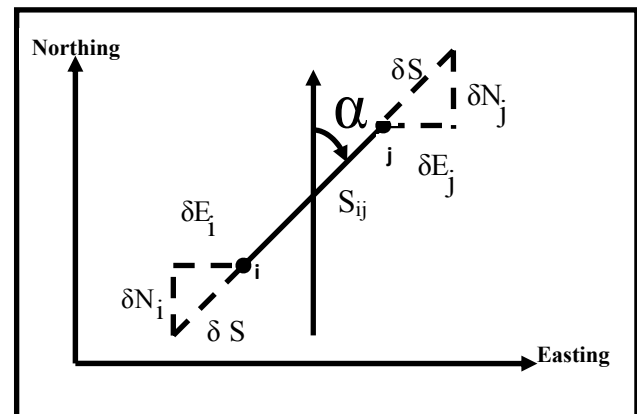
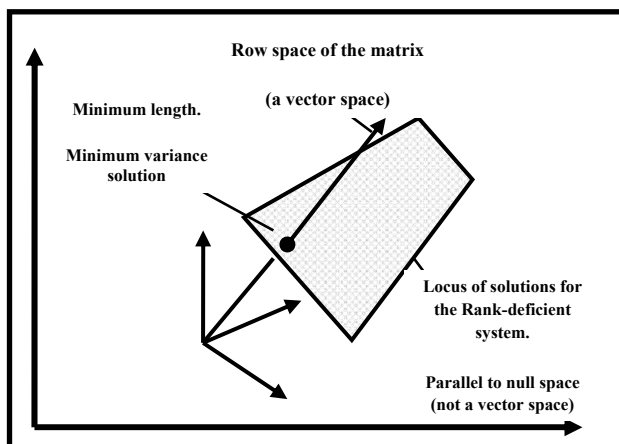
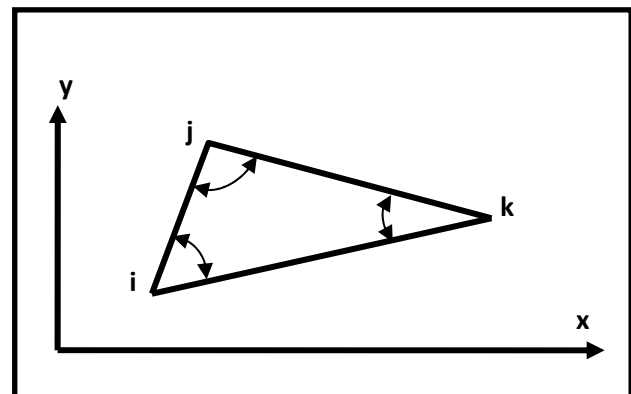
Point	Easting, <i>m</i>		Northing, <i>m</i>		$\sigma_E, m$		$\sigma_N, m$		Area of ellipse of error, <i>mm</i> <sup>2</sup>	
	Initial	Final	Initial	Final	Initial	Final	Initial	Final	Initial	Final
P51	69547.0000	69632.2526	49265.0000	49258.8593	0.0036	0.0035	0.0066	0.0054	66.97	60.10
P52	69856.0000	69753.4218	48865.0000	48768.4718	0.0033	0.0033	0.0047	0.0047	46.28	47.01
P53	70582.0000	70489.7498	48516.0000	48427.2428	0.0024	0.0023	0.0034	0.0033	24.96	25.08
P54	71138.0000	71052.2678	47976.0000	47892.9734	0.0026	0.0025	0.0030	0.0030	23.71	24.07
P71	69904.0000	69904.0369	49524.0000	49648.8212	0.0039	0.0042	0.0066	0.0056	73.87	67.92
P72	70620.0000	70543.8264	49999.0000	49998.9320	0.0061	0.0056	0.0034	0.0033	62.33	58.10
P01	68672.0000	68817.0506	49162.0000	49303.9264	0.0041	0.0041	0.0181	0.0125	229.83	161.93
P32	71705.0000	71844.1505	50937.0000	50868.6863	0.0072	0.0069	0.0029	0.0029	64.91	63.73
P03	73417.0000	73349.9212	47589.0000	47720.7375	0.0045	0.0039	0.0070	0.0066	71.32	65.48
P42	70319.8802	70320.8827	48247.4835	48247.0789	0.0028	0.0028	0.0041	0.0038	35.32	34.81
P44	71841.3424	71977.0182	47276.6001	47277.1503	0.0059	0.0051	0.0033	0.0034	60.65	55.65

**Table 6.** The results of FOD with high precision in 3<sup>rd</sup> case.

Point	Easting, <i>m</i>		Northing, <i>m</i>		$\sigma_E, m$		$\sigma_N, m$		Area of ellipse of error, <i>mm</i> <sup>2</sup>	
	Initial	Final	Initial	Final	Initial	Final	Initial	Final	Initial	Final
P51	69547.0000	69632.2357	49265.0000	49258.8599	0.0036	0.0036	0.0063	0.0053	65.01	58.55
P52	69856.0000	69754.1618	48865.0000	48769.2118	0.0031	0.0031	0.0043	0.0042	40.00	41.33
P53	70582.0000	70490.4898	48516.0000	48427.9827	0.0024	0.0023	0.0034	0.0036	26.21	26.88
P54	71138.0000	71052.0077	47976.0000	47892.7134	0.0025	0.0025	0.0028	0.0027	21.65	21.61
P55	71754.0000	71674.1833	47914.0000	47926.5815	0.0026	0.0023	0.0026	0.0027	21.27	21.07
P71	69904.0000	69828.2941	49524.0000	49671.9188	0.0041	0.0042	0.0065	0.0058	78.22	74.23
P72	70620.0000	70595.8732	49999.0000	49998.9351	0.0060	0.0056	0.0034	0.0033	61.31	57.25
P73	72344.0000	72482.8647	48898.0000	49034.1665	0.0027	0.0027	0.0035	0.0035	29.88	31.43
P01	68672.0000	68805.7023	49162.0000	49293.4201	0.0041	0.0044	0.0176	0.0121	226.34	157.64
P32	71705.0000	71834.2848	50937.0000	50873.3644	0.0075	0.0071	0.0031	0.0031	71.94	69.54
P03	73417.0000	73354.3575	47589.0000	47712.3250	0.0027	0.0027	0.0055	0.0051	45.82	43.88

**Table 7.** The limits of movement for points of the network.

Point	Limits of $E_i^0, m$		Limits of $N_i^0, m$	
	Lower	Upper	Lower	Upper
P51	69397	69697	49115	49415
P52	69706	70006	48715	49015
P53	70432	70732	48366	48666
P54	70988	71288	47826	48126
P55	71604	71904	47764	48064
P71	69754	70054	49374	49674
P72	70470	70770	49849	50149
P73	72194	72494	48748	49048
P1	68522	68822	49012	49312
P32	71555	71855	50787	51087
P3	73267	73567	47439	47739
P42	70041.3921	70341.3921	48160.7710	48460.7710
P44	71701.7091	72001.7091	47003.8040	47303.8040


**Figure 1.** ellipse of error

**Figure 2.** Distance observation.

**Figure 3.** Intersection of solution space and row space for a rank-deficient system, *after Mikhail, et al., 2000.*

**Figure 4.** Triangle network with only angle observation

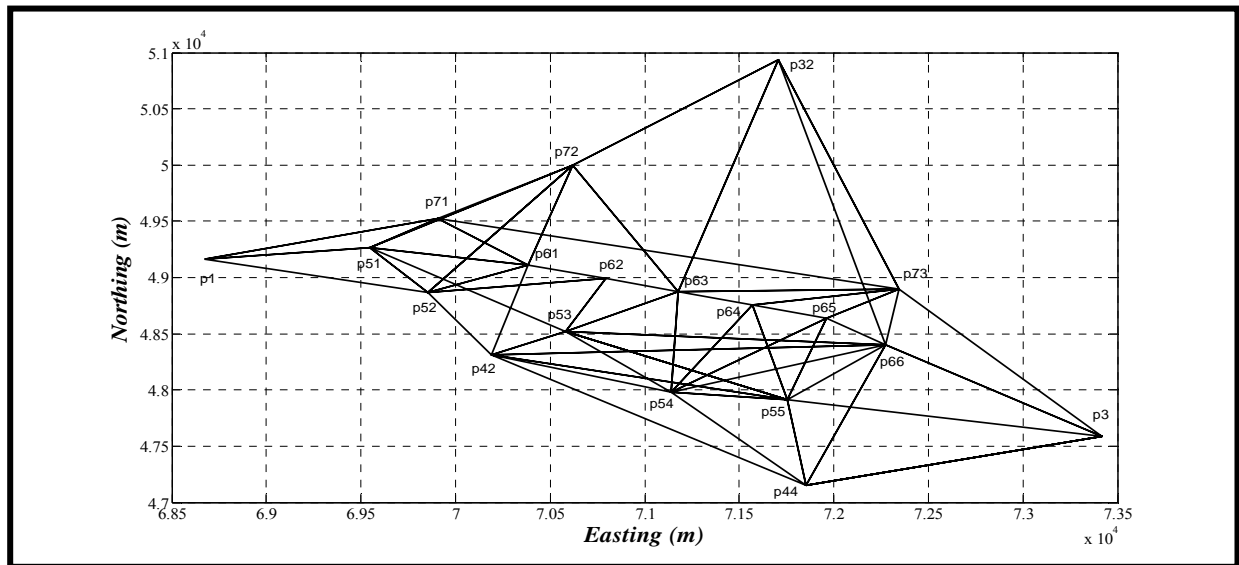


Figure 5. The selected network as a case study

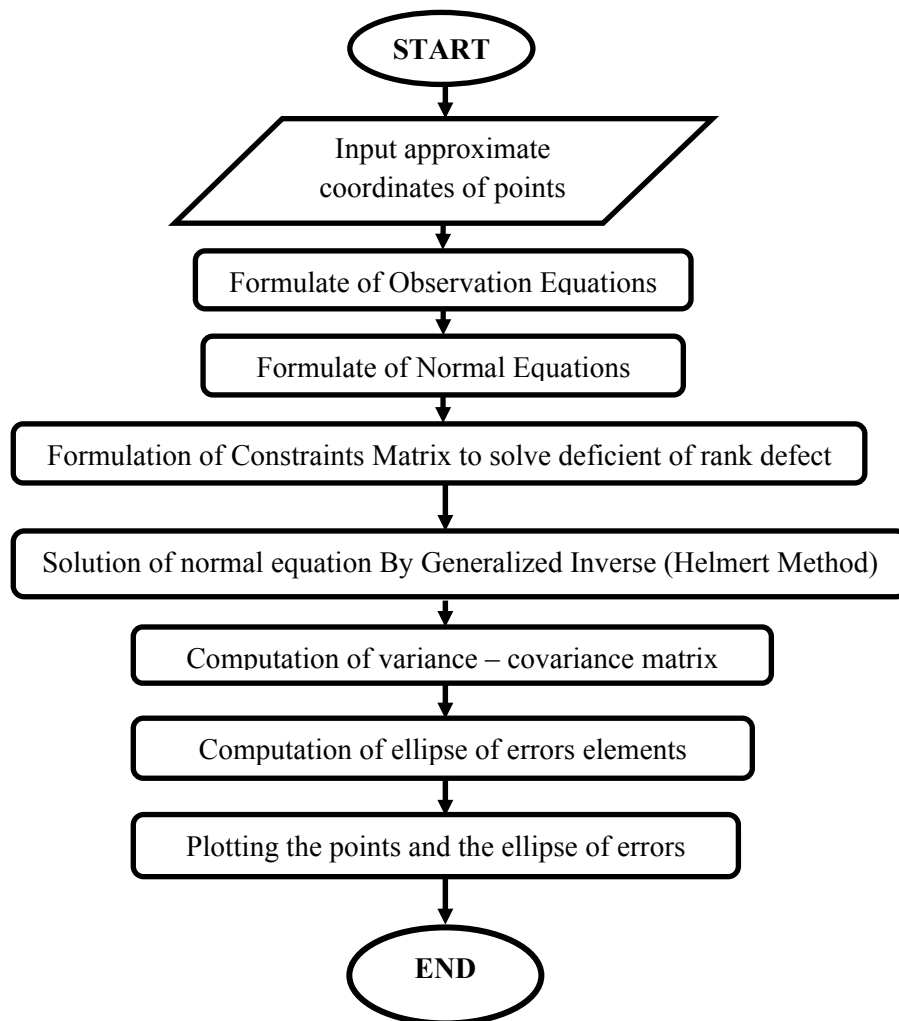
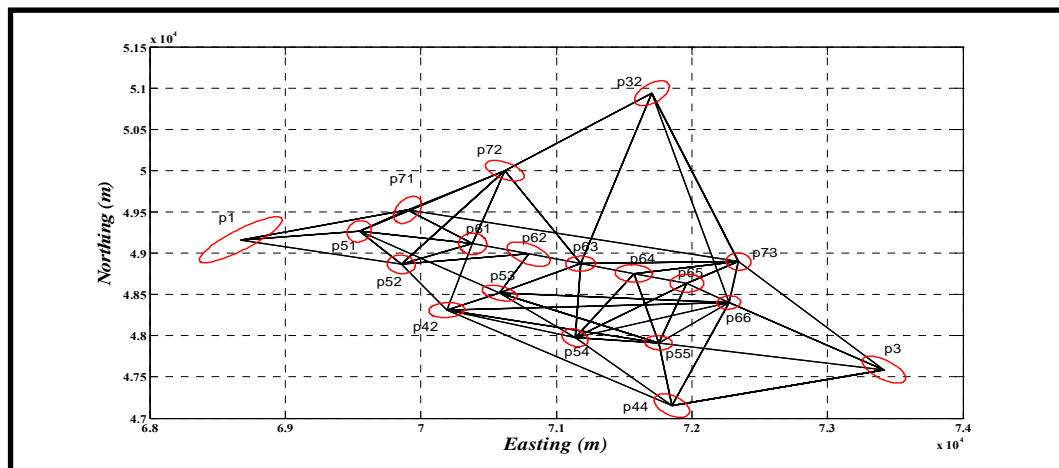
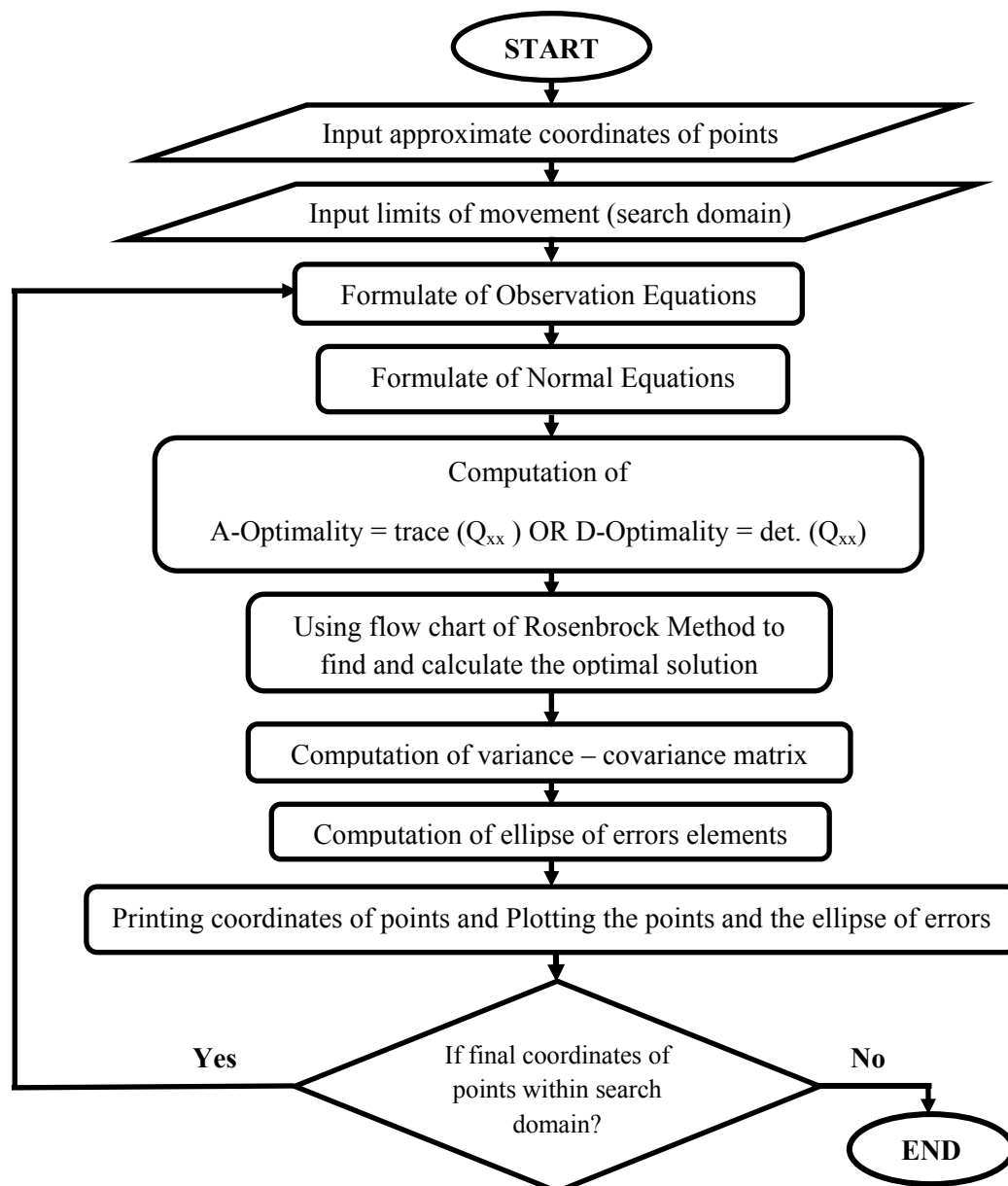


Figure 6. Flow chart of ZOD program.



**Figure 7.** The ellipses of error for each point in the network.



**Figure 8.** Flow chart of FOD with high precision program.

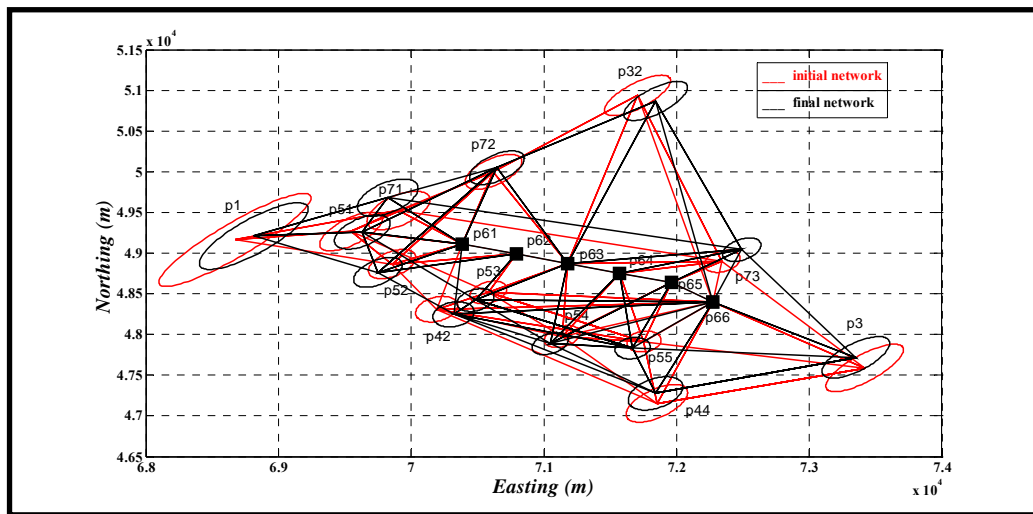


**Figure 9.** The initial and final network of the 1<sup>st</sup> case.

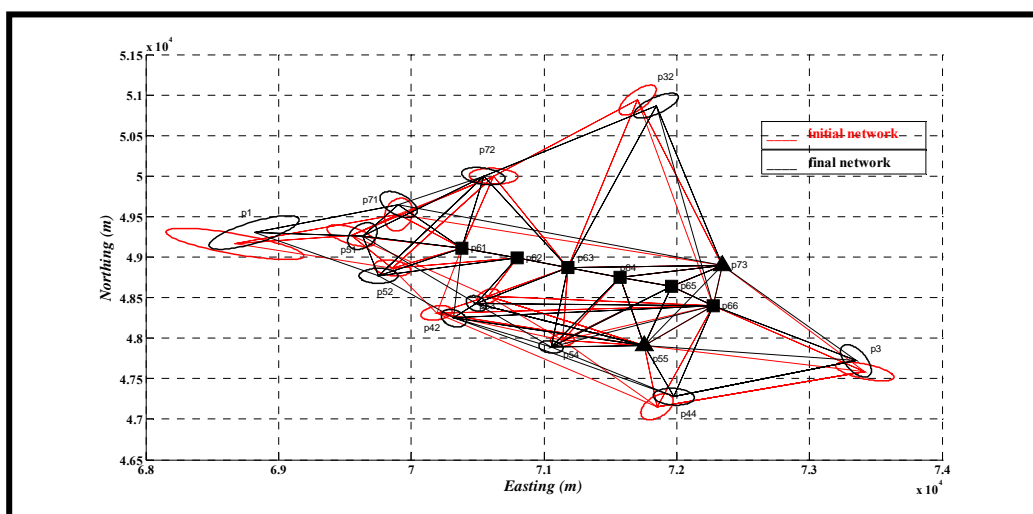


**Figure 10.** The initial and final network of the 2<sup>nd</sup> case.

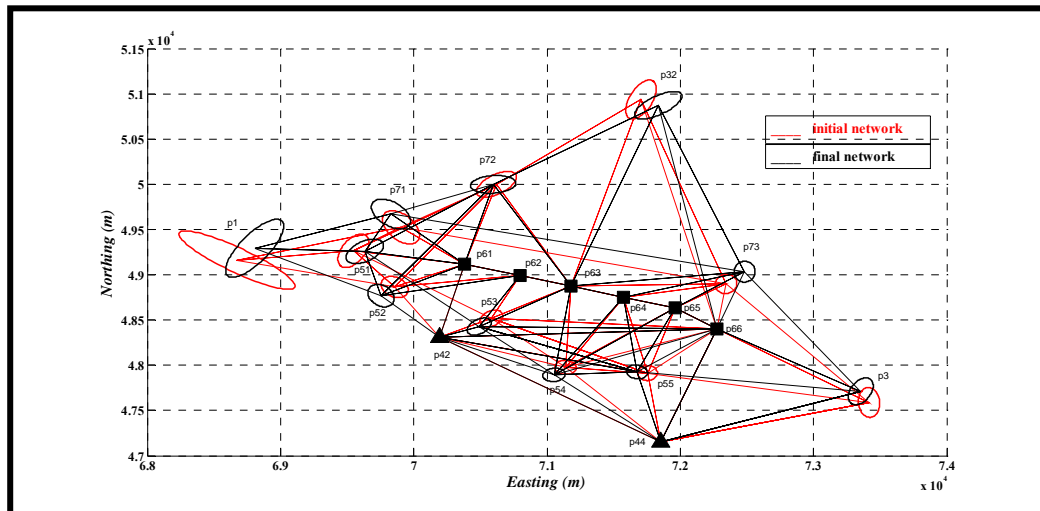


Figure 11. The initial and final network of the 3<sup>rd</sup> case.